Development of a H_2-driven enzymatic cascade to produce *N*-heterocycles in *C. necator*

Von der Fakultät für Mathematik, Informatik und Naturwissenschaften der RWTH Aachen University zur Erlangung des akademischen Grades einer Doktorin der Naturwissenschaften genehmigte Dissertation

vorgelegt von

M. Eng. Itzel Andrea Castro González

aus

Aguascalientes, Mexiko

Berichter: Prof. Dr. Lars Lauterbach, RWTH Aachen University

Prof. Dr. Stéphane Guillouet, INSA Toulouse

Tag der mündlichen Prüfung: 30.07.2025

Declaration of oath

I, Itzel Andrea Castro González, declare on oath that this thesis and its contents are my own and have been generated independently as a result of my own original research.

I hereby declare on oath:

1. This thesis was written and produced in its entirety during my time as a doctoral student at this faculty and university;

2. If any part of this thesis has previously been used for an academic degree or other qualification at this or any other institution, this has been clearly indicated;

3. If other own or public publications have been used, this has been clearly indicated;

4. If other own or public publications have been used, the source of this has been clearly indicated. This thesis is entirely my own work, with the exception of such citations;

5. All relevant sources of support have been acknowledged;

6. If any part of this thesis is based on the collaboration of others, I have clearly indicated what has been worked on by others and what has been worked on by myself;

7. Parts of this work have been previously published, as indicated below:

Aachen, June 1st, 2025

Itzel Andrea Castro González

List of Publications

- Castro González I., Pijpstraa P. , Gorret N., Lauterbach L., Guillouet S.E. 2025. Glycerol-supplemented medium promotes transition of Cupriavidus necator from heterotrophic to lithoautotrophic growth: Implications for putrescine toxicity studies. Manuscript submitted
- Schoenmakers P., Calabrese D., Hattemer J-L., Çildiroğlu G., Castro González I.A., de la Asunción Vest D., Nestl B., Lauterbach L.,H2-driven synthesis of chiral N-heterocycles with novel imine reductases in vitro and in vivo. Manuscript in preparation.
- Alhafiz H.A , Di Bisceglie F, Meier H. P. F, Weickardt I, Castro González I. A, Garcia Navarro J, Schoenmakers P, Oyen S. J, Lettau E, Lombard E, Cordero P. R.F , Konarzycka-Bessler M, Gorret N, Schmidt S, Schillberg S, Mann M, Guillouet S, Kratzer R, Lauterbach L. 2025. Cupriavidus necator as a model organism for CO_2-based biotechnology. Methods in Enzymology httpx://doi.org/10.1016/bs.mie.2025.01.017.

Acknowledgments

First of all, I would like to thank Prof. Dr Lars Lauterbach as my thesis supervisor. Thank you, Lars, for receiving me at the Synthetic Microbiology group, and trusting me with such a competitive program as the MSCA ITN project. Thank you for your professional support, and sharing your curiosity in the interesting world of biotransformations, for introducing me to various collaborators, and encouraging me to participate in conferences.

Thank you to Prof. Dr. Stefan Schillberg, Prof. Dr. Lothar Elling, Assoc. Prof. Alvaro R. Lara, Dr. Fadhel Ben Chaabane, and Dr. Petra Heidinger for the prolific scientific discussion.

As part of this PhD adventure, I encountered many researchers in institutes around Europe, and I will take a (long) moment to remember each of the places where I had the pleasure to work.

I would like to thank Prof. Stéphane Guillouet from INSA Toulouse, my second thesis supervisor. Merci beaucoup, Stéphane, pour tous les bons moments que nous sommes passés ensemble. Merci pour ta patiente, et pour ton support tout au long du projet. J'ai appris énormément pendant nos réunions, et j'ai toujours apprécie ton enthousiasme et dédication pour tes étudiants et la science. Merci aussi pour rigoler avec moi au travail et dehors. Merci à tout l'équipe TBI pour m'avoir accueilli si chaleureusement. Du coup, on se verra à nouveau avec Nathalie et tout le monde pour un apéro au bord de la Garonne.To everyone at the iAMB institute, Vielen Dank for welcoming our research group and helping us settle in. Thank you, Prof. Dr. Lars Blank, for leading with innovation, and for sharing your passion for playing Kicker after a working day. I am also deeply grateful to Gisela, Isabel, Annette, Kalle, the technical team, as well as Julia and Manja from the secretary team, without your immense effort and support, the lab simply would not function.

Thank you so much to the Blankitos and iAMB amigos for warmly adoptiming me in Aachen. Thank you, Carina, Philipp, Greta, Sebastian, Gina, Selina, Andreas, Makarius, Alex, Caro, Fred, Katrin, Jana, Aziz, Amila, for all the meals, beer, cakes, hugs, and science shared. Y por supuesto que muchas gracias a mis dramáticos latinos de mi alma y de mi corazón, words are not enough to describe these lovely people who always brighten my days and made me feel in home in another country: Ale, Vale, Loren, Pedro, Nono, Ricci, and Montse (la adoptada) … Latinos, assemble!

The PhD journey would not have been possible without the wonderful amiguitos that built the Synmicro lab from scratch. Thank you so much to Dr. Paul Cordero. Paul, I appreciate your great mentorship these years. You always listened to my scientific and personal questions with a smile, and accompanying me with your bright ideas, and kindness. Your scientific spark, and enthusiasms are truly valuable. To Domenic, Ela, Kalle, Pierre, Kyu, Donta, Halima, Kary, Meryem, Claudi, David, Jeena, thank you so much for your amazing friendship, and all the beautiful moments inside and outside the lab. Together, we always achieved the impossible, and we found joy both in the successful, and frustrating moments of science.

I am also very grateful to Assoc. Prof. Sandy Schmidt for warmly welcoming me into her group. Thank you for your kindness, and all the supportive and encouraging conversations. I truly enjoyed a wonderful Dutch summer at the University of Groningen, where I had the chance to make very nice friends.

This PhD odyssey will not be complete without all the members of the ConCO2rdini team that made this a wonderful experience. Thank you to the organizers and professors for being part of this fruitful network. I sincerely admire the Cupri-fighters: Matteito, Franzi, Ricci (yes, again, best flatmate ever), Javi, Donato A., Sandrone, Isa, Paulien, Federico, Halima, and Filip. It was a real pleasure to work

alongside brilliant, kind-hearted people such as you. See you soon at Fifi's mansion to enjoy a well-deserved break with tacos and cocktails from my Carreta.

Thank you to my friends in Aachen who are training me in martial arts. You helped me maintain the equilibrium between science and sports, and canalize my explosive energy to become a ninja-scientist.

We can't forget the friends that accompanied me from previous chapters of my life, and throughout this PhD decision. Merci à tous mes amis en Suisse, France, et ailleurs qui m'ont sauvé quand j'avais besoin d'un respire de la pluie d'Aachen : toute la team de Lausanne, Rueil, et même à Viènne et Frankfurt. Gracias a todos los latinos que sobreviven en estos rumbos conmigo, y me dan un amoroso hogar cuando lo necesito: María, Paul, Franco, Alejo, Adrien, Mónica, Balthazar, Sarah, Jorge. Por supuesto, a Estefi y Guillaume, muchísimas gracias por haberme elegido a mí en vez del gato para vivir con ustedes, y gracias por ese épico concierto de Céline Dion.

Están también, todos mis amigos de México quienes siempre me reciben con el corazón y los brazos abiertos. No importa cuánto tiempo pasemos lejos, los abrazos y las risas nunca faltan con ustedes. No se preocupen, ya estoy más cerca de ser millonaria y mantenerlos a todos, lo merecemos.

Finalmente, mi más sincera gratitud y todo mi amor a mi familia en México. Su corazón de oro ha estado conmigo todos estos años. Desde Aguascalientes, pasando por Guadalajara y hasta Morelia, siempre me han apoyado y acompañado en todas mis aventuras. Exploran el mundo conmigo a través de llamadas, videos y fotos. Siempre escuchan las historias bizarras que traigo del extranjero, me apapachan, me consienten y arman la pachanga para mí, aunque me quede dormida. A mis abuelitos, quienes, con sus fascinantes historias y sus ocurrencias, me inspiran a vivir la vida con una sonrisa. A mi papá, mi mamá y mi hermana, la chamacada más hermosa del mundo, gracias por siempre recibirme en el aeropuerto con una chaska y el amor más puro que hay….

Funding

This project has received funding from the European Union's Horizon 2020 research and innovation program under the Marie Skłodowska Curie ConCO2rde grant agreement No 955740. This presentation reflects only the author´s view, the Agency is not responsible for any use that may be made of the information it contains.

This project is part of a co-tutelle between RWTH Aachen University (Germany) and INSA Toulouse (France). Thesis prepared at RWTH Aachen University.

Funded by
the European Union

Abstract

The increasing CO_2 emissions require sustainable alternatives to repurpose this abundant yet undervalued carbon source. A promising approach is using CO_2 as carbon source to sustain autotrophic organisms, while performing biosynthesis of products of interest. Autotrophic organisms naturally assimilate CO_2 as a carbon source while using light or inorganic compounds as energy sources. However, autotrophic systems still require genetic engineering to meet industrial productivity and efficiency demands. Among autotrophic microorganisms, *Cupriavidus necator* is a facultative chemolithotroph which uses CO_2 as sole carbon source, H_2 as energy source, and O_2 as electron acceptor. Although this metabolic versatility allows *C. necator* to produce diverse molecules of commercial interest, few studies have focused on using its H_2-driven metabolism for obtention of fine chemicals.

In this study, a new process was explored to obtain high-value molecules in *C. necator* using a H_2-driven enzymatic cascade. Production of Nitrogen heterocycles (*N*-heterocycles) was selected because of their relevance across the chemical industry, notably as building blocks in pharmaceuticals. The thesis builds upon previous works with three different oxidoreductases, and extends them to establish a functional *in vivo* enzymatic cascade in *C. necator*. The enzymatic cascade consists of heterologous variants of O_2-dependent putrescine oxidase (PuOx), NADH-dependent imine reductase (IRED), and the native NAD^+-dependent soluble hydrogenase (SH) from *C. necator* for cofactor recycling.

C. necator was engineered for the heterologous production of PuOx and IRED variants, and protein production was evaluated under heterotrophic conditions with minimal media. Several strains were tested to improve protein production, and enzymatic assays were performed, confirming that IRED was active in the soluble extract of *C. necator*. Moreover, PuOx and IRED production was observed in individual *C. necator* strains in both heterotrophic and lithoautotrophic conditions.

In parallel, the transition from heterotrophy to lithoautotrophy was compared using fructose or glycerol in the preculture medium. A three-step culture with glycerol in the last preculture medium resulted in an optimized protocol to transition to lithoautotrophic growth in *C. necator*. The optimized cultivation protocol was used to assess the effect of putrescine, a potential substrate for the enzymatic cascade. Growth and cytometry analyses revealed that putrescine is not toxic for *C. necator* in lithoautotrophic conditions, tolerating up to 100 mM putrescine with minimal impact in specific growth rate, but causing an extended lag phase and changing cell's morphology. The optimized protocol was retained to evaluate the assembled enzymatic cascade in *C. necator* engineered strains.

C. necator was further engineered to combine PuOx and IRED, and assemble the enzymatic cascade. Initial experiments with the enzymatic cascade revealed challenges in the step catalyzed by PuOx. Nonetheless, further analysis confirmed that the IRED-catalyzed reaction proceeded within *C. necator*, reaching 0.8 % conversion from 2-methyl-1 pyrroline to 2-methylpyrrolidine after 48 h of biotransformation under lithoautrophic conditions. Focusing on this step, IRED expression was optimize, and biotransformation performance was compared under both heterotrophic and

lithoautotrophic conditions. An increase to 67 % conversion was observed after 24 h of lithoautotrophic biotransformation with safe-gas mixture, being faster than in heterotrophic conditions.

This study established the basis for a robust biotransformation strategy in *C. necator*, demonstrating its potential as a sustainable microbial host for *N*-heterocycle production. Future work will focus on optimizing productivity, improving PuOx expression, and downstream product extraction. By integrating oxidoreductases with *C. necator*'s H_2-driven metabolism, this research highlights the potential of lithoautotrophic biotransformations, and positions *C. necator* as a key microorganism in the transition towards a CO_2-based bioeconomy.

Zusammenfassung

Die steigenden CO_2-Emissionen erfordern nachhaltige Alternativen zur Wiederverwendung dieser reichlich vorhandenen, aber unterschätzten Kohlenstoffquelle. Ein vielversprechender Ansatz ist die Verwendung von CO_2 als Kohlenstoffquelle zur Erhaltung autotropher Organismen bei gleichzeitiger Biosynthese interessanter Produkte. Autotrophe Organismen nehmen CO_2 auf natürliche Weise als Kohlenstoffquelle auf und nutzen Licht oder anorganische Verbindungen als Energiequelle. Autotrophe Systeme erfordern jedoch noch immer gentechnische Veränderungen, um den Anforderungen der industriellen Produktivität und Effizienz gerecht zu werden. Unter den autotrophen Mikroorganismen ist *Cupriavidus necator* ein fakultativer Chemolithotroph, der CO_2 als einzige Kohlenstoffquelle, H_2 als Energiequelle und O_2 als Elektronenakzeptor nutzt. Obwohl diese metabolische Vielseitigkeit es *C. necator* ermöglicht, verschiedene Moleküle von kommerziellem Interesse zu produzieren, gibt es nur wenige Studien, die sich mit der Nutzung seines H_2-getriebene Stoffwechsels zur Gewinnung von Feinchemikalien befassen.

In dieser Studie wurde ein neues Verfahren untersucht, um mithilfe einer H_2-getriebenen enzymatischen Kaskade hochwertige Moleküle in *C. necator* zu gewinnen. Die Produktion von Stickstoffheterocyclen (*N*-Heterocyclen) wurde aufgrund ihrer Bedeutung für die chemische Industrie, insbesondere als Bausteine für Arzneimittel, ausgewählt. Die Arbeit baut auf früheren Arbeiten mit drei verschiedenen Oxidoreduktasen auf und erweitert diese, um eine funktionelle *in vivo*-lithoautotropher Enzymkaskade in *C. necator* zu etablieren. Die enzymatische Kaskade besteht aus heterologen Varianten der O_2-abhängigen Putrescin-Oxidase (PuOx), der NADH-abhängigen Imin-Reduktase (IRED) und der nativen NAD^+-abhängige Hydrogenasen (SH) aus *C. necator* für die Cofaktor-Recycling.

C. necator wurde für die heterologe Produktion von PuOx- und IRED-Varianten entwickelt, und die Proteinproduktion wurde unter heterotrophen Bedingungen mit Minimalmedien bewertet. Zur Verbesserung der Proteinproduktion wurden mehrere Stämme getestet und enzymatische Assays durchgeführt, die bestätigten, dass IRED im löslichen Extrakt von *C. necator* aktiv war. Darüber hinaus wurde die Produktion von PuOx und IRED in einzelnen *C. necator*-Stämmen sowohl unter heterotrophen als auch unter lithoautotrophen Bedingungen beobachtet.*C. necator* wurde für die heterologe Produktion von PuOx- und IRED-Varianten gentechnisch verändert, und die Proteinproduktion wurde unter heterotrophen Bedingungen evaluiert. Nachdem eine heterologe Proteinproduktion beobachtet wurde, wurde *C. necator* weiter gentechnisch verändert, um PuOx und IRED zu kombinieren und die enzymatische Kaskade unter lithoautotrophen Bedingungen zusammenzufügen. Parallel dazu wurde der Übergang von Heterotrophie zu Lithoautotrophie unter Verwendung von Fructose oder Glycerin im Vorkulturmedium verglichen. Eine dreistufige Kultur mit Glycerin im letzten Vorkulturmedium führte zu einem optimierten Protokoll für den Übergang zum lithoautotrophen Wachstum in *C. necator*. Das optimierte Kultivierungsprotokoll wurde verwendet, um die Wirkung von Putrescin, einem potenziellen Substrat für die enzymatische Kaskade Wachstums- und Zytometrieanalysen zeigten, dass Putrescin unter lithoautotrophischen Bedingungen für *C.*

necator nicht toxisch ist. Es toleriert bis zu 100 mM Putrescin mit minimalen Auswirkungen auf die spezifische Wachstumsrate, verursacht jedoch eine verlängerte Lag-Phase und verändert die Zellmorphologie. Das optimierte Protokoll wurde beibehalten, um die assemblierte Enzymkaskade in gentechnisch veränderten *C. necator*-Stämmen zu evaluieren.

C. necator wurde weiterentwickelt, um PuOx und IRED zu kombinieren und die enzymatische Kaskade zusammenzufügen. Erste Experimente mit der enzymatischen Kaskade zeigten Herausforderungen in dem von PuOx katalysierten Schritt. Dennoch bestätigten weitere Analysen, dass die IRED-katalysierte Reaktion in *C. necator* ablief und nach 48 Stunden Biotransformation unter lithoautotrophen Bedingungen eine Umwandlung von 2-Methyl-1-pyrrolin zu 2-Methylpyrrolidin von 0,8 % erreichte. Mit Fokus auf diesen Schritt wurde die IRED-Expression optimiert und die Biotransformationsleistung unter heterotrophen und lithoautotrophen Bedingungen verglichen. Nach 24 Stunden lithoautotropher Biotransformation wurde eine Umwandlung von 67 % beobachtet mit sicheres Gasgemisch, was schneller war als unter heterotrophen Bedingungen.

Diese Studie schuf die Grundlage für eine robuste Biotransformationsstrategie in *C. necator* und demonstrierte dessen Potenzial als nachhaltiger mikrobieller Wirt für die Produktion von *N*-Heterocyclen. Zukünftige Arbeiten werden sich auf die Optimierung der Produktivität, die Verbesserung der PuOx-Expression und die Produktextraktion optimieren. Durch die Integration von Oxidoreduktasen in den H_2- getriebene Stoffwechsel von *C. necator* unterstreicht diese Forschung das Potenzial lithoautotropher Biotransformationen und positioniert *C. necator* als einen wichtigen Mikroorganismus im Übergang zu einer CO_2-basierten Bioökonomie.

Résumé

L'augmentation des émissions de CO_2 nécessite des alternatives durables pour réutiliser cette source de carbone abondante mais sous-exploitée. Une approche prometteuse pour convertir le CO_2 en composés utiles est de l'utiliser comme source de carbone pour soutenir les organismes autotrophes, tout en réalisant la biosynthèse des produits d'intérêt. Les organismes autotrophes assimilent naturellement le CO_2 comme source de carbone tout en utilisant la lumière ou des composés inorganiques comme sources d'énergie. Cependant, les systèmes autotrophes nécessitent encore le recours au génie génétique pour répondre aux exigences de productivité et d'efficacité industrielles. Parmi les microorganismes autotrophes, *Cupriavidus necator* est une bactérie chimio-lithotrophe facultative qui utilise le CO_2 comme seule source de carbone, l'H_2 comme source d'énergie et l'O_2 comme accepteur d'électrons. Bien que cette polyvalence métabolique permette à *C. necator* de produire diverses molécules d'intérêt commercial, peu d'études ont porté sur l'utilisation de son métabolisme de l'H_2 pour obtenir des produits chimiques fins.

Dans cette étude, un nouveau procédé a été exploré pour obtenir des molécules à haute valeur ajoutée chez *C. necator* à l'aide d'une cascade d'enzymes alimentée en H_2. La production d'hétérocycles azotés (*N*-hétérocycles) a été choisie en raison de leur importance dans l'industrie chimique, en particulier comme composants de base dans les produits pharmaceutiques. La thèse s'appuie sur des travaux antérieurs portant sur trois oxydoréductases différentes afin d'établir une cascade enzymatique fonctionnelle in vivo dans C. necator. La nouvelle cascade enzymatique se compose de variants hétérologues de la putrescine oxydase (PuOx) dépendante de l'O_2, de l'imine réductase (IRED) dépendante du NADH et de l'hydrogénase soluble dépendant à le NAD^+ (SH) qui est native de *C. necator* et est utilisée pour le recyclage des cofacteurs.

C. necator a été modifié génétiquement pour la production hétérologue de variants de PuOx et d'IRED, et la production de protéines a été évaluée dans des conditions hétérotrophes avec un milieu minimal. Plusieurs souches ont été testées afin d'améliorer la production de protéines, et des tests enzymatiques ont été réalisés, confirmant que l'IRED était active dans l'extrait soluble de *C. necator*. De plus, la production de PuOx et d'IRED a été observée dans des souches individuelles de *C. necator* dans des conditions hétérotrophes et lithoautotrophes.

En parallèle, la transition de l'hétérotrophie à la lithoautotrophie a été comparée en utilisant du fructose ou du glycérol comme milieu de préculture. Une culture en trois étapes utilisant du glycérol dans le dernier milieu de préculture a optimisé la croissance en réduisant la phase de démarrage des cultures lithoautotrophes de *C. necator*. Des analyses de croissance et de cytométrie ont révélé que la putrescine n'est pas toxique pour *C. necator* dans des conditions lithoautotrophes, tolérant jusqu'à 100 mM de putrescine avec un impact minimal sur le taux de croissance spécifique, mais provoquant une phase de latence prolongée et une modification de la morphologie cellulaire. Le protocole a été conservé pour évaluer la cascade enzymatique assemblée dans des souches génétiquement modifiées de *C. necator.*

C. necator a ensuite été modifié pour combiner PuOx et IRED et assembler la cascade enzymatique. Les premières expériences avec la cascade enzymatique ont révélé des difficultés dans l'étape catalysée par PuOx. Néanmoins, des analyses plus approfondies ont confirmé que la réaction catalysée par l'IRED se déroulait dans *C. necator*, avec une conversion de 0,8 % de 2-méthyl-1 pyrroline en 2-méthylpyrrolidine après 48 heures de biotransformation dans des conditions lithoautotrophes. En se concentrant sur cette étape, l'expression de l'IRED a été optimisé, et les performances de biotransformation ont été comparées dans des conditions hétérotrophes, ainsi que dans des conditions lithoautotrophes. Une augmentation de la conversion à 67 % a été observée après 24 heures de biotransformation lithoautotrophe avec un mélange de gaz non explosif, ce qui été plus rapide que dans des conditions hétérotrophes.

Cette étude a établi les bases d'une stratégie de biotransformation robuste chez *C. necator*, démontrant son potentiel en tant qu'hôte microbien durable pour la production de *N*-hétérocycles. Les travaux futurs se concentreront sur l'optimisation de la productivité, l'amélioration de l'expression de PuOx et le traitement en aval. En intégrant des oxydoréductases dans le métabolisme à base d'H_2 de *C. necator*, cette recherche met en évidence le potentiel des biotransformations lithoautotrophes et positionne *C. necator* comme un micro-organisme clé dans la transition vers une bioéconomie basée sur le CO_2.

Content

List of figures

Supplementary Figures

List of tables

Supplementary Tables

List of Abbreviations

ALE	Adaptive laboratory evolution	**$NADP^+$**	Nicotinamide adenine dinucleotide phosphate, oxidized form
ATP	Adenosine triphosphate	**NADPH**	Nicotinamide adenine dinucleotide phosphate, reduced form
BSA	Bovine serum albumin	**O_2**	Molecular oxygen
CBB	Calvin-Benson-Bassham cycle	**OD**	Optical density
C. necator	*Cupriavidus necator* H16, formerly known as Ralstonia eutropha/Alcaligenes eutrophus	**PCR**	Polymerase chain reaction
CO_2	Carbon dioxide	**PuOx**	Putrescine oxidase
DNA	Deoxyribonucleic acid	**SH**	Soluble NAD^+ hydrogenase
E. coli	*Escherichia coli*	***M. stipitatus***	*Myxococcus stipitatus*
Figure S	Figure in Supplementary	***R. erythropolis***	*Rhodococcus erythropolis*
H_2	Molecular hydrogen	**RNA**	Ribonucleic acid
IRED	Imine reductase	**SD**	Standard deviation
MBH	Membrane-bound hydrogenase	**SDS-PAGE**	Sodium dodecyl sulfate–polyacrylamide gel electrophoresis
GC	Gas chromatography	**SEM**	Standard error of the mean
GHG	Greenhouse gas	**TAE**	Tris-Acetate-EDTA
NAD^+	Nicotinamide adenine dinucleotide, oxidized form	**Tris**	Tris(hydroxymethyl)-aminomethane
NADH	Nicotinamide adenine dinucleotide, reduced form	**UV**	Ultra-violet

Introduction and General context.

The global temperature has increased of 1.1°C between 2011-2020, leading to environmental disasters, threatening natural ecosystems and human settlements around the world. In response, the Intergovernmental Panel on Climate Change (IPCC) has emphasized the need for immediate climate action by adhering to the Paris Agreement and limiting the global temperature rise to below 2°C (H. Lee et al., 2023). To achieve this target, the Agreement mandates a reduction in greenhouse gas (GHG) emissions, particularly carbon dioxide (CO_2): a reduction of 42% by 2030, and global net-zero emissions by 2050 (UNFCCC, 2016). McGlade & Ekins (2015) stressed that reduction of CO_2 emissions requires limiting fossil fuel exploitation, estimating that one-third of oil reserves, half of gas reserves, and more than 80% of coal reserves must remain untapped between 2010 and 2050 to meet the 2°C limit. Furthermore, these climate goals also limit projects involving Arctic resources and unconventional oil. Urgent action is needed to transition away from fossil fuels to sustainable alternatives for industrial production while mitigating CO_2 emissions.

The chemical sector is identified as the third-largest source of direct CO_2 emissions, and the largest energy consumer in the world (International Energy Agency, IEA, 2023). Traditional chemical synthesis methods often rely on non-renewable resources and energy-intensive conditions, exacerbating environmental concerns. To address the intensive GHG emissions of the chemical industry, and align with the sustainability goals and perspectives, a new economic model has emerged : the bioeconomy (McCormick, 2014).

The bioeconomy represents a transformative framework for chemical production that promotes the use of renewable biological resources, such as agricultural biomass, microbial processes, and enzymatic pathways, to establish sustainable value chains. Unlike traditional fossil fuel-based methods, the bioeconomy prioritizes the regeneration and the efficient use of natural resources, contributing to lower GHG emissions and reducing environmental degradation (European Commission, 2024; European Commission: Directorate-General for Research and Innovation, 2018; OECD, 2009). At EU level, various projects have been developed to demonstrate the feasibility of local bioeconomies and their implementation across different economic sectors (European Commission: Directorate-General for Research and Innovation, 2018; IEA, 2021). Implementing bioeconomy strategies has the potential to redefine current industrial systems, support sustainable development goals and “decouple economic growth from environmental harm” (Noonan & Vrizzi, 2020).

Addressing CO_2 emissions has become a central objective within the bioeconomy, and three main strategies can be identified: CO_2 removal, CO_2 reduction, and CO_2 utilization. Strategies for CO_2 removal focus on extracting the gas from the atmosphere through technologies such as direct air capture and natural solutions such as afforestation and soil carbon sequestration (Fuss et al., 2018; Minx et al., 2018). Strategies for CO_2 reduction aim to prevent emissions at their source, employing measures such as energy efficiency improvements, transition to renewable energy, and carbon capture and storage at industrial facilities (Gibbins & Chalmers, 2008; Haszeldine, 2009). The strategies for CO_2 utilization have gain increasing attention in recent years and involve converting captured

carbon dioxide into value-added products, including fuels, chemicals, and materials, using processes such as electrochemical reduction and enzymatic transformation (Hepburn et al., 2019; Z. Zhang et al., 2020). Together, these complementary strategies offer a path to mitigate climate change and support sustainable industrial practices (Godoy et al., 2020; McCormick, 2014; Meylan et al., 2015).

Among the various approaches under the bioeconomy framework and CO_2 utilization, biorefineries represent a key strategy to transform and valorize CO_2. Biorefineries are facilities that transform feedstocks into a spectrum of bio-based products and bioenergy (de Jong et al., 2020; de Jong & van Ree, 2009). Traditionally, biorefineries used biomass as feedstocks, such as crops, lignocellulose, oil crops, and organic waste. In Europe, several biorefineries have progressed going from laboratory research through pilot plants and commercial initiatives. The IEA regularly reports on the progress made by its member countries in this area (de Jong & van Ree, 2009). Despite the advancements in traditional biorefineries, challenges remain including feedstock competition with the food sector, limited biomass availability, low energy conversion, and low productivities. In response to feedstock limitations and supply, CO_2 has emerged as an alternative carbon source, leading to the development of CO_2-based biorefineries (Z. Liu et al., 2020, 2023).

The emerging CO_2-based biorefineries come with their own obstacles, particularly related to CO_2 fixation, energy capture and productivity (Z. Liu et al., 2020, 2023).To address these obstacles, the development of CO_2-based biorefineries is increasingly shifting towards the use of autotrophic microorganisms. The metabolism of autotrophic microorganisms offer a potential solution to CO_2 fixation , as these microorganisms naturally assimilate CO_2 as a carbon source while using energy from light or inorganic electron donors (Claassens et al., 2016). To enhance productivity in autotrophic microorganism, significant advances in genetic engineering have been made over the past decade, however, further optimization is still possible (Z. Liu et al., 2023).

Among the autotrophic candidates, *Cupriavidus necator* has emerged as a particularly promising candidate due to its versatile metabolism. *C. necator* is a facultative chemolithotroph and it is able to grow using CO_2 as sole carbon source and H_2 as an energy source. Historically, *C. necator* has been widely studied for bioplastic production, and over the last decade other products have been explored. A non-exhaustive list of examples can be found in literature and patents (Garrigues et al., 2020; Ibrahim, 2023; Morlino et al., 2023; Santolin et al., 2024; R. Tang et al., 2020; Y. Wang et al., 2024). While these advances are encouraging, most of these applications have focused on the production of bulk compounds. In contrast, the potential of *C. necator* to perform H_2-driven biotransformations for the synthesis of fine chemicals with high-value, continues to offer opportunities. The few available examples often rely on purified enzymes from *C. necator* (Al-Shameri et al., 2019; Lim et al., 2024) or *C. necator* resting cells (Jämsä et al., 2024; Teetz et al., 2022); and even fewer studies have explored *C. necator* as an integrated whole-cell biocatalyst under autotrophic conditions for fine chemicals (Assil-Companioni et al., 2019).

In this study, we aim to explore the production of fine chemicals through H_2-driven biotransformations in genetically modified strains of *C. necator*. Our approach combines the advantages of microbial

autotrophy and biocatalysis to develop *C. necator* as a CO_2-production platform, where the high-value of the products compensates for the typically lower productivity of autotrophic systems. The fine chemicals that were selected as a case study are Nitrogen heterocycles (*N*-heterocycles) because of their relevance across the chemical industry, notably as building blocks in pharmaceuticals.

Our H_2-driven biotransformation builds upon previous works that demonstrated the production of *N*-heterocycles under different conditions. First versions of an enzymatic cascade were developed and assessed *in vivo* in *E. coli* by Borlinghaus et al. (2019) using two enzymes: Putrescine oxidase (PuOx) and Imine reductase (IRED). These enzymes were coupled *in vitro* with the purified Soluble Hydrogenase (SH) of *C. necator* as a cofactor regeneration system by Al-Shameri et al. (2019). Our study combines these previous works, and extends them by assembling variants of PuOx and IRED directly inside *C. necator*, because this bacterium contains the necessary metabolism to power a new enzymatic cascade under CO_2, H_2 and O_2 -growing conditions. The adapted enzymatic cascade in *C. necator* contains three oxidoreductases: the variants of PuOx and IRED, which are heterologously expressed in *C. necator* for the first time; and the native SH of *C. necator,* which represents the crucial element for cofactor regeneration and ensures the cascade's functionality.

The novelty of this work lies in developing a CO_2-based process within *C. necator* to access *N*-heterocycles. This is achieved by introducing new enzymes as biocatalyst tools in *C. necator* and establish a H_2-driven biotransformation. Ultimately, the process is entirely fed by lithoautotrophic cultivations using CO_2 as sole carbon source, H_2 as energy donor, and O_2 ad electron acceptor.

The manuscript is structured as follows:

Section 1. Literature review: this section is divided in three chapters. The first chapter provides an overview of the properties of *N*-heterocycles, highlighting their relevance in the pharmaceutical industry. The main industrial production strategies are presented alongside the emerging biotechnological advancements. Special focus is given to biocatalysis and enzymatic cascades, and their impact on microbial biotransformations. The second chapter presents *C. necator,* its lithoautrophic metabolism and current biotechnological products. The third, and final chapter, describes the individual enzymes which are required for the enzymatic cascade: IRED, PuOx, and SH.

Section 2. Materials and Methods: this section contains a detailed description of the methodologies, reagents and equipment used during experimentation.

Section 3. Results and Discussion: Presents findings across the different chapters:

> Chapter 1: different *C. necator* strains were developed to evaluate the heterologous production of IRED and PuOx variants under heterotrophic conditions. Characterization of the proteins and evaluation of enzymatic activity were performed on the selected strains.
>
> Chapter 2: focuses on evaluating the interaction of PuOx, IRED and SH in *C. necator* under lithoautotrophic conditions. Several *C. necator* strains were developed for the combination of

PuOx and IRED within *C. necator.* Lithoautotrophic growth was evaluated in the strains and biotransformation of putrescine and 2-methyl-1-pyrroline was evaluated.

Section IV. Overall Discussion, Conclusion and Perspectives: compares the results to the state of the art of H_2-driven biotransformations, demonstrating the potential of CO_2-based biorefineries with *C. necator* and reflecting on the transition to a bioeconomy model.

Section 1: Literature review

Chapter 1: *N*-heterocycles, small molecules with powerful properties.

Nitrogen heterocycles (*N*-heterocycles) are cyclic molecules containing carbon atoms and at least one nitrogen atom. In his article, cleverly titled "Nature loves nitrogen heterocycles", Walsh (2015) highlights the ubiquitous presence and relevance of *N*-heterocycles in nature. They are fundamentally part of essential biomolecules, such as DNA, RNA and protein-synthesizing ribosome, and participate in the storage and transmission of genetic information. Their pivotal role in the biochemistry of life was further evidenced by Rodriguez (et al., 2019). They simulated prebiotic conditions, reporting possible pathways and conditions under which *N*-heterocycles could have reacted to promote the formation of genetic precursors on early Earth.

Beyond their roles in genetic material, *N*-heterocycles rings are prevalent in a vast array of bioactive natural products. This bioactivity is largely attributed to their unique chemical characteristics. In particular, the presence of nitrogen atoms in cyclic rings introduces regions of high electron density that allows *N*-heterocycles to act as suitable proton donors or acceptors. They are also capable of forming weak interactions, including hydrogen bonding and aromatic interactions, as well as other non-covalent interactions. These interactions are essential for stabilizing molecular structures and enabling crucial biological processes, such as protein-nucleic acid recognition (Chopra et al., 2020; Jena et al., 2022). In addition to their ability to form diverse molecular interactions, *N*-heterocycles also present aromaticity. This combination enhances their compatibility with biological systems and contributes to their functions in various biochemical pathways.

A prominent group of *N*-heterocycles with significant biological properties are alkaloids. Alkaloid derivatives are especially abundant in plants and fungi, where they act in chemical signaling, growth regulation, and defense mechanisms. For instance, plants produce indole-3-acetic acid as a hormone to regulate growth, while certain bacteria and fungi synthesize indole alkaloids to deter predators or compete with other microbes in their environment. Additionally, alkaloids such as reserpine and vinblastine exhibit potent pharmacological activities and are used in treatments for hypertension and cancer, respectively (Zulak et al., 2006).

The significance of *N*-heterocycles extends beyond their natural occurrence, as they are synthesized both naturally and synthetically for a wide array of applications in the food, chemical or textile industries. According to the Observatory of Economic Complexity, OEC (2023), *N*-heterocycles represent a significant segment of the global chemical industry. In 2022, they were the 32nd most traded product worldwide, with a total trade value of $103 billion. Trade in *N*-heterocycles compounds accounted for 0.43% of total world trade, reflecting their extensive application across multiple fields. The prominence of *N*-heterocycles in the pharmaceutical industry is particularly notable and has been well-documented through extensive research in drug discovery. For example, Abdelshaheed et al. (2021) explored their application in antimicrobial agents, while Gordon et al. (1994) and Kerru et al.

(2020) highlighted their role in designing anticancer drugs. Similarly, Yan et al., (2021) and Zhang & Studer(2015) focused on their use in synthetic methodologies, showcasing the broad spectrum of their pharmaceutical relevance. Marshall et al. (2024) presented their most recent update on pharmaceutical composition, emphasizing the exceptional presence of *N*-heterocycles in approved drugs (Figure 1). Over a 10-year period, the Federal Drug Administration (FDA) approved 321 new small-molecule drugs, of which 82% contained at least one *N*-heterocycle. This high percentage underscores the critical role of *N*-heterocycles in modern pharmacology and therapeutic development.

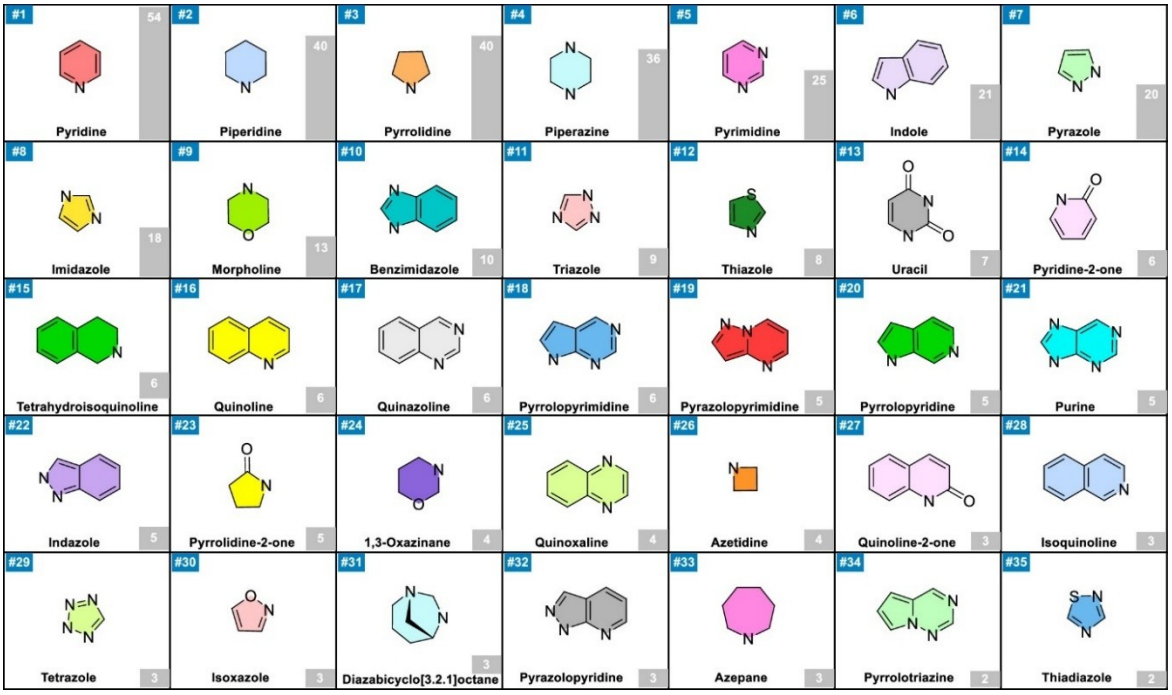

Figure 1. Most frequently *N*-heterocycles in pharmaceuticals : The top 35 *N*-heterocycles approved by the Federal From 2013 to 2023(Marshall et al., 2024)

1.1.1 Commercial production.

Nitrogen compounds were firstly extracted from natural sources and they gradually transition towards synthetic chemistry. Historically, pyridine, one of the most relevant *N*-heterocycles in industry, was isolated from the basic fraction that remained after the distillation of coal tar (ATSDR Agency for Toxic Substances and Disease Registry, 1992; Scriven, 2013). The growing demand started to deplete the natural deposits and prompted the development of synthetic methods in the 1950s to supplement the production. Most of the commercial processes to produce pyridines are based in the condensation of ammonia (NH_3) with aldehydes or ketones in vapor, or liquid phase (Chichibabin, 1905, 1924; Lazdin'sh & Avots, 1979). Pyridine serves as the base to obtain other *N*-heterocycles. Piperidine can be produced through the hydrogenation of pyridine using catalysts such as platinum, palladium, or Raney nickel in liquid-phase reactions. High yields of completed saturated rings are obtained at room temperature by using nickel-aluminum alloys with 0.5 M KOH to ensure an alkaline medium (Adkins

& Billica, 1948). Many variations of these methods have been created with several patents in the field (Balasubramanian, 2013; Frolov & Vereshchagin, 2023; Scriven & Murugan, 2005).

The growing demand for nitrogen products in the early 20th century also prompted the quest for new nitrogen sources, encouraging the development of nitrogen fixation technologies. The Haber-Bosch process emerged from this period and became the most commercialized process. This process is currently used to produce ammonia (NH_3) through the reaction of atmospheric nitrogen gas (N_2) with hydrogen gas (H_2) in the presence of an iron-based catalyst under high temperatures and pressures (~ 400–500°C, 100–200 bar). Ammonia is then available to produce nitrogen-containing molecules by reacting with carbon sources, often derived from petrochemicals. The Haber-Bosch process is regarded pivotal in meeting the global demand for ammonia and nitrogen-based compounds of our industrial era (Erfani et al., 2024; Smil, 1999). Despite its success, the Haber-Bosch process remains an energy- intensive method that relies heavily on fossil fuels, particularly natural gas as H_2 source, and generates substantial CO_2 emissions to the atmosphere (International Fertilizer Industry Association, 2014; Royal Society, 2020; Smil, 2000).

Other industrially relevant *N*-heterocycle; such as quinoline, pyrrolidine, and their derivatives, are also produced through resource-demanding processes. Pyrrolidine, is synthesized by reacting 1,4-butanediol with ammonia in the presence of hydrogen and a metal-containing catalyst under liquid-phase conditions at 140–220 bar and 160–230°C (Chedid et al., 2016). Quinoline production is traditionally achieved via methods like the Skraup synthesis and requires high temperatures (200–220°C) and pressures (up to 19 bar) along with strong acids like sulfuric acid. This generates toxic byproducts and consumes substantial energy (Yamashkin & Oreshkina, 2006). Some advancements were done to improve quinoline production and efficiency. Saggadi et al. (2015), developed a microreactors utilizing microwave-assisted synthesis. While their method still operated under high temperatures (200–220°C) and pressures (up to 19 bar), they achieved overall greater efficiency by regulating the power absorbed from the reaction medium, and reduced t unwanted byproducts. Their system also supported a continuous chemical synthesis at a pilot scale using glycerol as a renewable feedstock. Further process improvement can be achieved by rigorous control of reaction conditions and solvents, to obtain high-purity quinoline derivatives for pharmaceutical applications (Nakamura et al., 2021).

Although innovations have been made, heavy dependence on fossil fuels, high-energy demands and the associated environmental impacts remain significant barriers to a fully sustainable nitrogen chemistry. As Chen et al. (2018) have emphasized, there is an urgent need for alternative technologies that not only reduce energy consumption, but also address greenhouse gas emissions, advocating for innovative and sustainable approaches that conciliate nitrogen compound production and environmental priorities.

1.1.2 Advancements in *N*-heterocycle production.

New methods to reduce environmental impacts and increase efficiency are attracting widespread interests in the synthesis of *N*-heterocycles. Three approaches can be identified: optimization of NH_3

production, alternative nitrogen sources, and optimization of catalytic systems. The first approach focuses on the innovations for NH_3 production. Lin et al. (2023) provides an overview of the modifications at the Haber-Bosch process and progress in other thermocatalytic processes. Additionally, new solvents and methods to produce "green ammonia" in solid phase have different degrees of scalability and environmental impacts, and their insights can be found elsewhere in literature (Candeias et al., 2009; J. Li et al., 2024). The second approach explores alternatives to ammonia as nitrogen source. Weber et al. (2024) applied a boron-mediated reduction of N_2, allowing the direct functionalization into *N*-heterocycles and circumventing the need for NH_3 intermediate and transition metals. The potential of waste animal biomass was also demonstrated by extracting *N*-heterocycles from bovine skin through a one-step thermochemical conversion process with KOH and Al_2O_3 as catalysts (Tang et al., 2023).

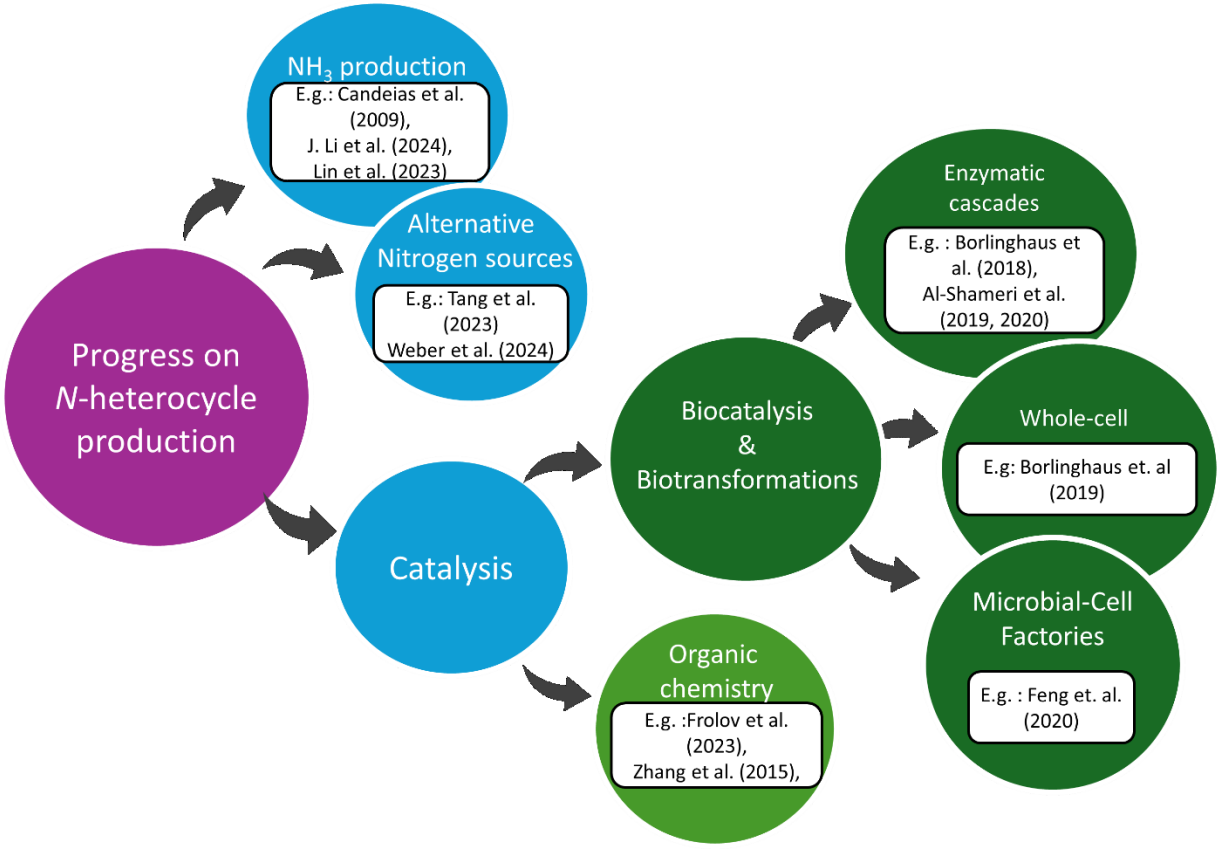

Figure 2. Progress on *N*-heterocycles production focuses on three main areas : NH_3 production, alternative nitrogen sources and catalysis. In the field of catalysis, approaches relying on enzymes such as biocatalysis and biotransformations, are highlighted in dark green. Some examples are indicated for each approach.

Among these approaches for modern *N*-heterocycle production, the catalysis field has attracted a growing interest over the years with its versatile and wide strategies. Progress was achieved in

synthesizing *N*-heterocycles through cascade reactions with isonitriles as radical acceptors. Zhang & Studer (2015), summarized the advantages of these radicals under mild or metal-free conditions. Moreover, organic chemistry offers diverse intra- and intermolecular reactions tailored to produce piperidine derivatives. Frolov & Vereshchagin (2023), presented the numerous advances in reactions such as hydrogenation, cyclization and multicomponent cascade reactions; while addressing "green reactions", which can take place in non-toxic iron catalysis, or water-mediated synthesis.

The advancements in the chemical-based synthesis of *N*-heterocycles have been notable, however, certain limitations remain, such as selection of an appropriate catalyst and obtention of complex molecules with determined chirality. Enzymes have emerged as indispensable tools in the field of biocatalysis to overcome these challenges and meet the principles of green chemistry (Anastas & Warner, 1998). Enzymes are highly preferred as catalyst because they operate under mild conditions, exhibit high chemo-, regio-, and enantioselectivity, and, generally, reduce the reliance for toxic components. Significant scientific milestones have demonstrated the transformative potential of enzymes, further fueling their development and application across diverse disciplines such as industrial processes, chemical synthesis, and medicine (Heckmann & Paradisi, 2020). Additionally, enzymes offer flexibility, as they can be engineered to improve their efficiency, expand substrate acceptance, and refine reaction specificity (Gao et al., 2022). This versatility has driven an intensive development of biocatalysis for the sustainable production of *N*-heterocycles.

1.1.2.1 Bio-power: Biocatalysis and Enzymatic Cascades to obtain N-heterocycles.

In this manuscript we adopt the broad definition of biocatalysis as the use enzymes to carry out chemical conversions (Lau & Grosse, 2013). We further classify biocatalytic strategies for the synthesis of *N*-heterocycles into two main categories: *in vitro* biocatalysis, and *in vivo* biocatalysis.

We use the term *in vitro* biocatalysis to describe the techniques that involve purified enzymes or soluble cell extracts (France et al., 2017). This approach commonly relies on enzymes that naturally synthesize or modify specific *N*-heterocycles. Some of these enzymes, such as non-ribosomal peptide synthases, cyclodipeptide synthase, and Pictet-Spenglarase; are responsible for the direct synthesis of five or six-membered *N*-heterocycles skeletons (Feng et al., 2022; Gao et al., 2022). Other enzymes, such as imine reductases (IREDs); reduce cyclic imines to produce the *N*-heterocycles. Since the first IRED characterization and purification (Mitsukura et al., 2010, 2011, 2013), IREDs have attracted much attention because of their ability to catalyze the enantioselective reduction of imines. All of the above enzymes, can be combined and arranged into sequential reactions with other enzymes that are not part of the same pathway in nature (Gao et al., 2022). Such artificially assembled sequences are referred to as enzymatic cascades. Enzymatic cascades that include IREDs have gained popularity for efficiently producing chiral substituted pyrrolidines, piperidines, piperazines, and other complex *N*-heterocycles (Borlinghaus et al., 2018; Cárdenas-Fernández et al., 2023; Heath et al., 2016). The potential of enzymatic cascades with IREDs have been demonstrated by their application in pharmaceutical processes and patents (France et al., 2018; IP.com Prior Art Database, 2017a; Schober et al., 2019).

When designing an *in vitro* enzymatic cascade, one of the main challenges is the addition of stoichiometric amounts of cofactors (Sperl & Sieber, 2018). These molecules are essential for enzymatic reactions but can significantly increase production costs due to their high price. For example, one mol of NADH have reached a price of $3000, and for NADP around $5000 (Faber, 2011). The continuous addition of cofactor limits the broader application of enzymatic cascades in industrial settings.

To address the issue when using cofactors and IREDs in enzymatic cascades, Al-Shameri et al. (2019, 2020) proposed to include the purified soluble hydrogenase from *C. necator* as a mechanism to recycle NADH, and produce *N*-heterocycles. The *in vitro* cascades developed by Al-Shameri et al. (2019, 2020) combine an engineered putrescine oxidase (PuOx) for substrate oxidation, an engineered NADH-dependent IRED (Borlinghaus & Nestl, 2018) for reduction of the imine intermediate, and the soluble hydrogenase (SH) for continuous NADH cofactor regeneration. They obtained 97% product formation of substituted pyrrolidines and piperidines in one-pot reaction of 1 mL reaction volume (Al-Shameri et al., 2019). The system was further developed and coupled with an electrolysis platform and applied for the production of labelled *N*-heterocycle isotopes.(Al-Shameri et al., 2020). While this H_2-driven *in vitro* system demonstrated potential for *N*-heterocycle production, it relies on purified enzymes. The use of purified enzymes could pose scalability challenges for industrial applications, particularly when large quantities of enzyme are required.

In vivo biocatalysis is another strategy that involves the use of living cells, mainly microbial cells, to carry out enzymatic reactions. In this category, we distinguish biotransformations from bioconversions. Biotransformations, or whole-cell biotransformations, refer to the use of intact microbial cells to convert an externally added substrate into a desired product. Bioconversions refer to the use of a desired product from basic nutrients provided to the microorganism (Oehlenschläger et al., 2024; Wierckx, 2009). Both strategies may include endogenous and/or heterologous enzymes, and can rely on engineered metabolic pathways or assembled enzymatic cascades.

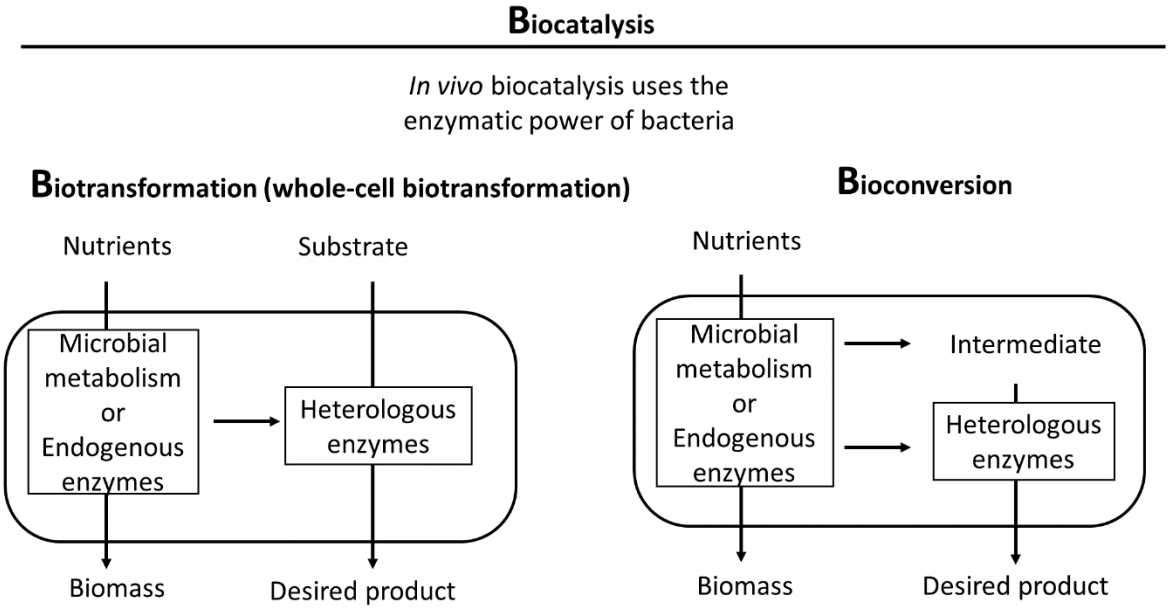

Figure 3. The 3 B of Catalysis: Biocatalysis, Biotransformation and Bioconversion. *In vivo* biocatalysis uses microbial cells through biotransformation or bioconversion to produce diverse chemical (Adapted from Wierckx, 2009).

The main advantage of assembling enzymatic cascades directly inside microorganisms instead of using purified enzymes, is that the microbial cells can offer an optimal environment for complex biosynthetic pathways, which in turn can result in high selectivity and compound recycling(B. Lin & Tao, 2017). For such reasons, the production of *N*-heterocycles using whole-cell biotransformations and IRED enzymatic cascades has been widely explored and some examples are presented below.

One contribution was made by Hussain et al. (2015), who employed *E. coli* whole cells harboring IREDs to achieve asymmetric reduction of imines. Their work demonstrated the applicability of biocatalysis in the synthesis of optically pure chiral *N*-heterocycles. Another representative example is the hybrid *in vivo* /*in vitro* approach developed by France et al. (2016), which combined whole-cell biotransformation with purified enzymes. In their system, two recombinant *E. coli* cells, one containing a carboxylic acid reductase and other an IRED, where mixed with cell lysate preparation of a transaminase. The enzyme interaction resulted in high isolated yields of piperidines and pyrrolidines.

An industrially relevant example was presented by Borlinghaus et al. (2019), who designed a biotransformation process for the production of 3-methylpiperidine using *E. coli* whole-cells. They combined the enzymatic reactions of PuOx and IRED enzyme using an *E. coli* strains that co-expressed both genes. As a result, they were able to transform the diamine 1,5 diamino2 methyl pentane into 3-methylpiperidine in 20 mL reaction vessel. The process was further optimized and successfully scaled up to a 20 L bioreactor, achieving a product yield of 67%.

The previous examples show the utility of *E. coli* whole-cell systems, and particularly those using IRED, as recurring systems for the production of *N*-heterocycles. However, the biotransformations in *E. coli*

remain disconnected from CO_2-based or H_2-driven process, highlighting the need for alternative microbial platforms that can couple enzymatic cascades with lithoautotrophic metabolism.

1.1.2.2 Microbial Cell Factories and C. necator as an alternative for CO_2 bioproduction

When model microorganisms are systematically engineered to optimize chemical production, they are often referred to as Microbial Cell Factories (MCFs). The main workhorses for MCFs are *E. coli* and *Saccharomyces cerevisiae* because they have genetic adaptability and well-established molecular tools that allows them to be intensively modified to achieve high production (G. B. Kim et al., 2025; Valle & Bolívar, 2021). With the advances in molecular tools, other microorganisms such as *Corynebacterium glutamicum*, *Pichia pastoris*, *Pseudomonas putida*, *Yarrowia lipolytica*, and *Bacillus subtilis* have also been developed as MCFs. Comprehensive reviews have covered the design and optimization of these MCFs, including advances in metabolic engineering (Cho et al., 2022); and the metabolic analysis in the production of particular chemicals (G. B. Kim et al., 2025; S. Y. Lee et al., 2019).

Among the MCFs, *C. necator* is another recognized chassis. Although *C. necator* is less genetically developed than traditional heterotrophic microbial hosts, it offers unique advantages for CO_2 biotransformations. However, the development of *C. necator* as a MCFs has faced obstacles due to the limited availability of standardized genetic tools, lower transformation efficiencies, and difficulty in fine-tuning heterologous gene expression (R. Tang et al., 2023). Moreover, the redundancy of *C. necator'*s genome often complicates pathway design and limits overall efficiency (Jahn et al., 2024).

In the last decade, significant progress has been made to overcome the genetic limitations of *C. necator,* and ongoing research is expanding its synthetic biology toolbox. For example, efforts has been made to optimize plasmid based expression and optimize promoters for *C. necator* (Alagesan et al., 2018; Sydow et al., 2017). Other study focused on improving electrophoresis efficiencies (Azubuike et al., 2021), implement CRISPR-based techniques (Xiong 2018), and knockdown strategies using broad-host range synthetic small RNA (Cho et al., 2023). Recently, Vajente et al. (2024) proposed a species-independent method using natively methylated DNA and Golden Gate assembly, achieving a 70-fold increase in electroporation efficiency.

Metabolic engineering was applied in *C. necator* to integrate a synthetic pathway for glycine biosynthesis while growing on formate and CO_2 (Claassens, Bordanaba-Florit, et al., 2020), and yields were improved by genomic integration (Dronsella et al., 2025). Further synthetic biology tools available for *C. necator* are described in detail by Santolin et al. (2024).

Together, these examples demonstrate the efforts towards establishing genetic accessible tools for *C. necator*. As the synthetic biology toolbox continues to expand, the feasibility of integrating engineering cascades for CO_2-based process in *C. necator* increases. In the following section, we examine the key characteristics of *C. necator,* with a particular focus on the lithoautotrophic metabolism, and the enzymes necessary to serve as a platform for a H_2-driven enzymatic cascade for the production of *N*-heterocycles

Chapter 2 : *C. necator*, more than a plastic bacterium:

1.2.1 General characteristics of *C. necator*

C. necator is a Gram-negative, non-pathogenic β-proteobacterium renowned for its exceptional metabolic versatility. As a facultative chemolithoautotroph, it can grow heterotrophically in diverse carbon sources, or derive energy from inorganic compounds, utilizing hydrogen (H_2) as an electron donor and carbon dioxide (CO_2) as its sole carbon source under autotrophic conditions (Enrich-Prast et al., 2014). When organic carbon is available, *C. necator* can switch to heterotrophic growth, yet retaining the ability to assimilate inorganic substrates in the absence of organic sources (Reinecke & Steinbüchel, 2009). *C. necator* is also able to adapt to both aerobic and anaerobic environments. For aerobic conditions the electron transport chain and terminal respiratory complexes are used; while under anaerobic conditions, denitrification enzymes are produced, reducing nitrate or nitrite to N_2 gas (Cramm, 2009; Cramm et al., 1997, 1999; Pohlmann et al., 2000, 2006).

The taxonomic classification of *C. necator* has encountered many changes over the decades. The species was initially named *Hydrogenomonas eutropha* (Wittenberg & Repaske, 1958), for the capacity of oxidizing H_2 gas as energy source. At the time, the classification was primarily based on physiological traits, and the species was reassigned as *Alcaligenes eutrophus* (Davis et al., 1969) after several structural and biochemical studies. Further advances in molecular biology and genomic sequencing gave rise to new reclassifications: first *Ralstonia eutropha* (Yabuuchi et al., 1995), then to *Wautersia eutropha* (Vaneechoutte et al., 2004), and ultimately to its current designation as *C. necator* (Vandamme & Coenye, 2004).

The most extensively studied strain, H16 ,was isolated from activated sludge in Germany (Schlegel, Kaltwasser, et al., 1961). Today, *C. necator* H16 is considered a model "knallgas" bacterium, extensively investigated for the ability to accumulate polyhydroxyalkanoates (PHAs), and perform efficient autotrophic metabolism via H_2 oxidation and CO_2 fixation (Schlegel, Gottschalk, et al., 1961).

1.2.2 Genome

The genome of Cupriavidus necator H16 is composed of three circular replicons: two chromosomes (chromosome 1 and chromosome 2) and one megaplasmid (pHG1), with a total of 7.4 Mbp. Chromosome 1 (4 Mbp) contains most of the essential housekeeping genes involved in central metabolism, DNA replication, transcription, and translation, containing 66.4% GC content (Pohlmann et al., 2006). The genes responsible for alternative metabolic function, including lithoautotrophy, denitrification, or substrate uptake are distributed among the other replicons (Fricke et al., 2009; Jahn et al., 2021; Pohlmann et al., 2006). Chromosome 2 (2.6 Mbp), contains 66.7% GC content, encodes specialized genes involved in sugar metabolism, particularly those associated with the Entner-Doudoroff pathway through 2-keto-3-deoxy-6-phosphogluconate (KDPG), pathways for catabolism of aromatic compounds, and assimilation of nitrogen sources. Chromosome 2 also contains the *cbb* operon, which encodes the enzymes of the Calvin-Benson-Bassham (CBB) carbon reduction

cycle, required for CO_2 fixation and autotrophic growth (Pohlmann et al., 2006). The pHG1 megaplasmid (0.45 Mbp) encodes multimer resolution systems to ensure plasmid stability, along with a putative type II restriction-modification system that may protect against foreign DNA (Schwartz et al., 2003). In addition, pHG1 carries a second *cbb* operon with high sequence and regulatory homology to the chromosomal copy, although it lacks two genes present in chromosomal copy (Bowien & Kusian, 2002; Pohlmann et al., 2006). The genomic distribution reflects the metabolic versatility and ecological adaptability of *C. necator*.

1.2.3 Metabolism

1.2.3.1 Heterotrophic metabolism

Under heterotrophic conditions, *C. necator* H16 is capable of utilizing a variety of organic carbon sources. Fructose is transported into the cell via an ATP-binding cassette (ABC) transporter and metabolized through the Entner-Doudoroff- (ED) pathway (Gruber et al., 2014; Pohlmann et al., 2006). Recent studies have demonstrated that when the ED pathway is disrupted, alternative metabolic routes can enable fructose catabolism. These pathways rely on the Calvin-Benson-Bassham (CBB) cycle, where fructose is processed via the non-oxidative pentose phosphate pathway and subsequently fixed by Rubisco, thereby redirecting carbon into central metabolism (Ding, 2025).

In addition, *C. necator* can utilize N-acetylglucosamine through a phosphotransferase system (PTS)-type transporter (Pohlmann et al., 2006). Interestingly, strain H16 is unable to metabolize glucose, likely due to the absence of a dedicated glucose transporter (Raberg et al., 2011). Glycerol can also serve as a carbon source, supported by the presence of genes encoding putative glycerol kinases and glycerol dehydrogenases (Fukui et al., 2014; Pohlmann et al., 2006). However, the growth rate on glycerol is considerably slow and resembles the metabolic profile observed under autotrophic conditions (Schwartz et al., 2009). The limited growth in glycerol may promote a metabolic shift toward CO_2 fixation, even in the absence of H_2, due to the upregulation of *cbb*X genes and hydrogenase expression under mixotrophic conditions (B. Friedrich & Schwartz, 1993; Strittmatter et al., 2022). *C. necator* encodes four formate dehydrogenases (FDHs) distributed across chromosome 1 and 2 , enabling it to use formate as both as carbon and energy source (Pohlmann et al., 2006). A soluble FDH catalyzes the oxidation of formate to CO_2, generating NADH, supplying reducing power while the released CO_2 is assimilated via the CBB cycle (Jahn et al., 2024; Oh & Bowien, 1998; Yu et al., 2017). Recent advances in metabolic engineering have targeted formate metabolism to improve growth efficiency and carbon assimilation (Calvey et al., 2023; Claassens, Bordanaba-Florit, et al., 2020; Rowaihi et al., 2018) In addition, *C. necator* is natively capable of metabolizing a range of volatile fatty acids (VFAs), including acetate, propionate, butyrate, hexanoate, and valerate (Jawed et al., 2022; J. Wang et al., 2010). To enhance fatty acid catabolism, several genetic strategies have been developed, including adaptive evolution and targeted mutations in regulatory and transport genes (Holmes et al., 2024)

C. necator is widely known for the natural ability to accumulate polyhydroxyalkanoates (PHAs), particularly poly-3-hydroxybutyrate (PHB). These intracellular storage polymers are synthesized under

various nutritional conditions and serve as carbon and energy reserves, reaching almost 80 % of dry weight mass in PHB.

PHB accumulation is typically triggered under nutrient-limited conditions, such as nitrogen or phosphorus deficiency, in the presence of excess carbon sources. This metabolic strategy enables *C. necator* to store carbon and energy for future use. The regulation of PHA biosynthesis involves a network of genes and environmental signals. The key enzymes responsible for PHB synthesis include β-ketothiolase (PhaA), acetoacetyl-CoA reductase (PhaB), and PHB synthase (PhaC). The expression of these enzymes is tightly regulated by factors such as the availability of nutrients, and the intracellular concentration of PHB (Grousseau et al., 2014; Panich et al., 2021; Santin et al., 2024; Schlegel, Gottschalk, et al., 1961; Weldon & Euler, 2025).

An overview of C necator metabolism, with focus on PHA biosynthesis is presented in Figure 4.

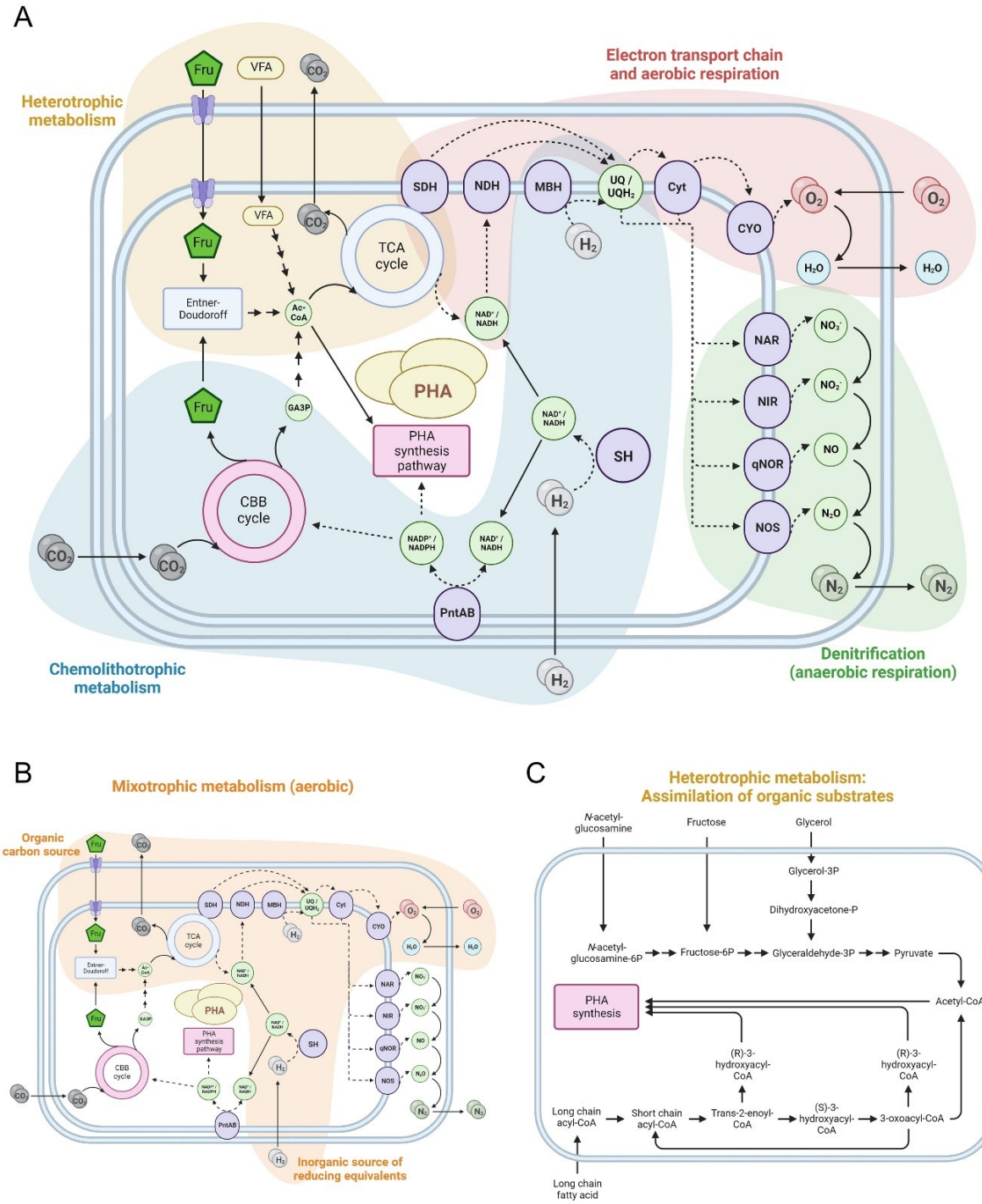

Figure 4. Overview of *C. necator* metabolism : main carbon and energy metabolism in *C. necator* (A). Pathways involved in mixotrophic metabolism are highlighted in orange Fructose and CO_2 are used as heterotrophic and autotrophic carbon sources, respectively. (B). PHA synthesis from *N*-acetyl-glucosamine, fructose and glycerol (C). Symbols code: electron flows indicated with dotted arrows, metabolite/carbon flows with solid arrows. Color code: Violet for oxidoreductases, light blue for catabolic pathways, red for anabolic pathways. Abbreviations: Fru, fructose; Ac-CoA, acetyl-coenzyme A; TCA, tricarboxylic acid; SDH, succinate dehydrogenase; SH, soluble hydrogenase; MBH, membrane-bound hydrogenase; PntAB, transhydrogenase; CBB, Calvin-Benson-Bassham; GA3P, glyceraldehyde-3-phosphate; NDH, NADH dehydrogenase; UQ, ubiquinone, Cyt, b/c-type cytochrome; CYO,

cytochrome oxidase; NAR, nitrate reductase; NIR, nitrite reductase; NOR, nitric oxide reductase; NOS, nitrous oxide reductase. (Morlino et al., 2023)

1.2.3.2 Lithoautotrophic metabolism

Carbon fixation

Under autotrophic conditions, *C. necator* utilizes CO_2 as a carbon source, H_2 as an electron donor, and O_2 as the terminal electron acceptor (Lauterbach & Lenz, 2019). *C. necator* fixes CO_2 primarily via the CBB cycle, catalyzed by 11 distinct enzymes distributed across three phases: carboxylation, reduction and regeneration (Nelson & Cox, 2009).

In the carboxylation phase, one molecule of CO_2 is added to ribulose-1,5-bisphosphate (RuBP) in a reaction catalyzed by ribulose-1,5-bisphosphate carboxylase/oxygenase (Rubisco). Rubisco is the central enzyme of the CBB cycle, and in *C. necator* the enzyme is classified as a Form IC, composed of large (CbbL) and small (CbbS) subunits (Badger & Bek, 2008; Baker et al., 1998). During the carboxylation reaction, two molecules of 3-phosphoglycerate (3-PGA) are formed and can be further metabolized into pyruvate or other intermediates of central metabolism (Brigham et al., 2013).

In the reduction phase, 3-PGA is phosphorylated to 1,3-bisphosphoglycerate by phosphoglycerate kinase, and then reduced by glyceraldehyde-3-phosphate dehydrogenase using NADPH to produce glyceraldehyde-3-phosphate (GAP). GAP is further converted into fructose-6-phosphate through the actions of an aldolase, and fructose-1,6-bisphosphatase.

In the regeneration phase, ribose-5-phosphate is produced via the reversible reactions of the reductive pentose phosphate pathway. Ribose-5-phosphate (Ru5P) is then isomerized to ribulose-5-phosphate, by the ribose-5-phosphate isomerase. Finally, Ru5P is phosphorylated to regenerate RuBP, allowing the cycle to start again (Brigham et al., 2013; Nelson & Cox, 2009; Schwartz et al., 2009). The CBB cycle in *C. necator* is presented in Figure 5.

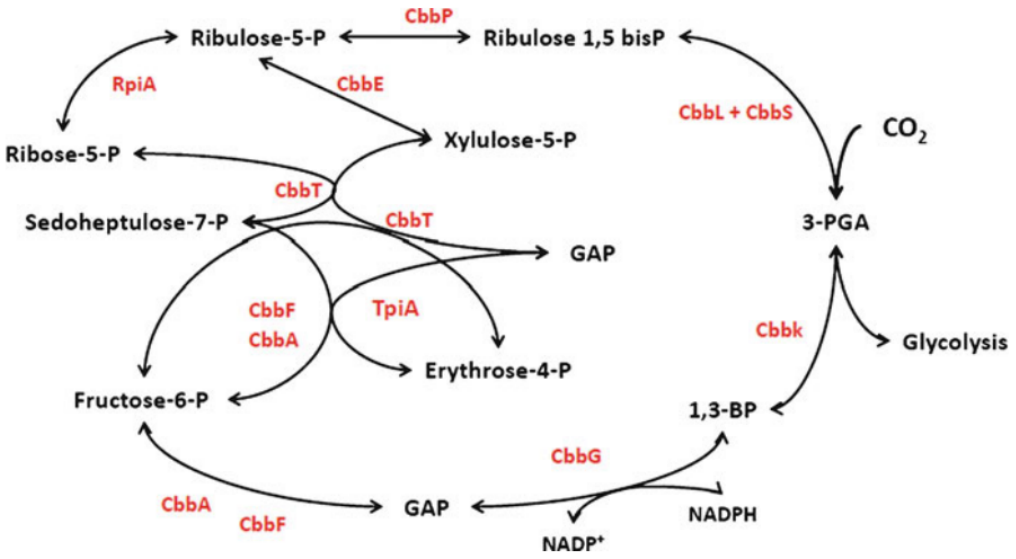

Figure 5. Calvin-Benson-Bassham cycle in *C. necator* . Abbreviations: ribulose -5-P, Ribulose5-phosphate; CbbP, phosphoribulose kinase; CbbL + CbbS, RuBisCO ,ribulose-1,5-bisphosphate carboxylase/ oxygenase; CbbK, phosphoglycerate kinase; CbbG, glyceraldehyde-3-phosphate dehydrogenase; CbbA, aldolase; CbbF, fructose bisphosphatase; erythrose-4-P, erythrose-4-phosphate; fructose-6P,fructose-6-phosphate; sedoheptulose-7P, sedoheptulose -7-phosphate; xylulose-5P, xylulose-5-phosphate; CbbT, transketolase; CbbA, fructose-bisphosphate aldolase; CbbF, fructose/sedoheptulose bisphosphatase; CbbE, ribulose-5-epimerase; TpiA, triosephosphate isomerase; RpiA, ribose-5-phosphate isomerase. (Brigham et al., 2013)

Although RuBisCO is central to CO_2 fixation, it is a relatively slow carboxylase and exhibits competing oxygenase activity, which can limit efficiency (Prywes et al., 2023). *C. necator* is capable of fixing CO_2 at ambient concentrations, reaching a doubling time of approximately 21 hours under autotrophic conditions (Claassens, Scarinci, et al., 2020). To improve Rubisco performance in *C. necator*, strategies such as directed evolution (Satagopan & Tabita, 2016), or heterologous Rubisco overexpression (S. Kim et al., 2022; Z. Li et al., 2020) have been explored. Other autotrophic organisms have evolved strategies to compensate for the low catalytic efficiency and dual activity of Rubisco by increasing CO_2 concentrations near the enzyme. These strategies are known as carbon-concentrating mechanisms (CCMs) and typically include bicarbonate transporters, carboxysomes, and carbonic anhydrases (CAs) (Kerfeld & Melnicki, 2016; Scott et al., 2020). CAs are metalloenzymes that catalyze the rapid and reversible interconversion of CO_2 and bicarbonate (HCO_3^-), facilitating CO_2 delivery to RuBisCO, and enhancing carboxylation efficiency (Lindskog, 1997). While *C. necator* lacks other classical CCM, it encodes four CA-like proteins that may contribute to intracellular inorganic carbon balance (Gai et al., 2014). Additionally, HCO_3^-concentration has been shown to enhance initial growth under autotrophic conditions (Repaske et al., 1971), and replenish metabolic intermediates (Panich et al., 2024).

The *cbb* operon in *C. necator* encodes all essential enzymes of the CBB cycle, with the exception of triose-phosphate isomerase, and ribose-5-phosphate isomerase (Panich et al., 2021). *C. necator* harbors two functionally redundant *cbb* operons, one located on chromosome 2 and the other on the pHG1 megaplasmid. Although both operons are nearly identical and actively transcribed (Gruber et al., 2017; Li et al., 2020), deletion of a single operon does not significantly impair autotrophic growth or CO_2 fixation, reflecting the organism's genome redundancy (Jahn et al., 2021).

Energy metabolism.

A key element for the lithoautotrophic metabolism in *C. necator*, is the presence of hydrogenases. Hydrogenases are oxidoreductases that use hydrogen as electron donor to reduce diverse substrates (EC 1.12 class, BRaunschweig ENzyme Database, BRENDA), they are metalloenzymes classified according to their active metal center: [NiFe], [FeFe], and [Fe] hydrogenases (Lubitz & Ogata, 2013; Vignais & Billoud, 2007).

C. necator contains four active O2-tolerant [NiFe] hydrogenases that support its lithoautotrophic metabolism by catalyzing the reversible H_2 oxidation ($H_2 \leftrightarrow 2H^+ + 2e^-$). Recent reviews have provided an overview of the main roles for each enzyme, and a brief summary is presented in Table 1 (Panich et al., 2021; Wei et al., 2023; Weldon & Euler, 2025).

Table 1. *C. necator* [NiFe] hydrogenases.

Hydrogenase	Characteristics	Further references
Membrane-bound hydrogenases (MBH)	Localized in the cellular membrane along with the respiratory chain. Formed by HoxG, HoxK and HoxZ. Reduces ubiquinone, transferring the electrons from H_2 oxidation to cytochrome *a* while generating proton force for ATP synthesis.	(Buhrke et al., 2004; Cramm, 2009; Lenz & Friedrich, 1998)
Soluble hydrogenase (SH)	Localized in the cytoplasm. Formed by hydrogenase module (HoxH and HoxY), and diaphorase module (HoxF and HoxU) Catalyzes the oxidation of H_2 and reducing NAD^+ to NADH. O2-tolerant.	(Buhrke et al., 2004; Cramm, 2009; Lauterbach et al., 2013; Lenz & Friedrich, 1998)
Regulatory hydrogenase (RH)	Formed by subunits HoxB and HoxC, which interact with the kinase HoxJ. The complex reacts with the regulator, HoxA, to mediate the hydrogen- sensing and transcription	(Buhrke et al., 2004; Burgdorf et al., 2005; Lenz et al., 2002;

		Lenz & Friedrich, 1998)
Actinobacterial hydrogenase (AH)	Presents slow consumption rates, presumably active at low H_2 concentrations. Requires further characterization.	(Jugder et al., 2015; Panich et al., 2021; Schäfer et al., 2016)

The MBH and SH are the main energy-converting enzymes in *C. necator.* The MBH feeds electrons directly into the respiratory chain, which are used by the ATP-synthase to generate ATP. In contrast, the SH couples H_2 with reduction of NAD^+ to NADH, playing a major role for cofactor generation in biosynthetic pathways. The SH will be described in detail in a separate section

The interaction between these hydrogenases and metabolic pathways in *C. necator* is illustrated in Figure 6.

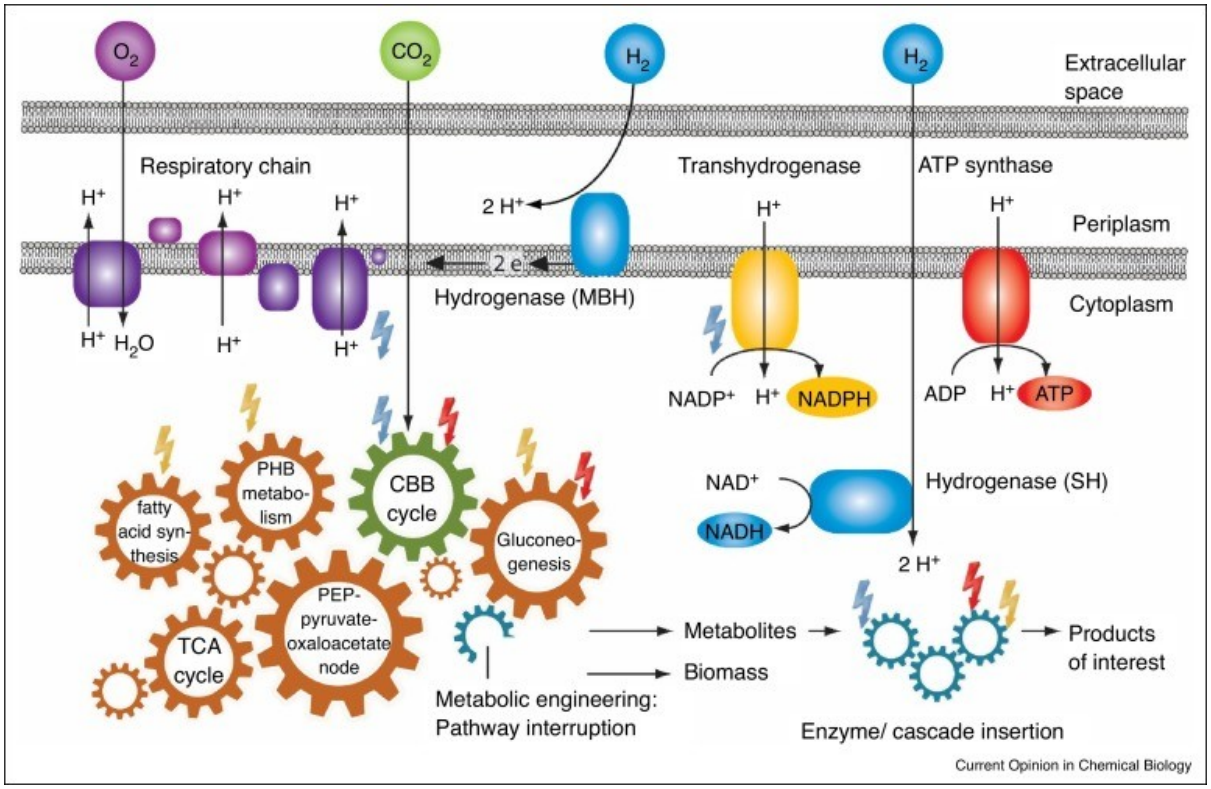

Figure 6. Lithoautotrophic metabolism in *C. necator* : *C. necator* uses CO_2 as carbon source through the CBB cycle, H_2 as electron donor for energy conversion, and O2 as final electron acceptor in the respiratory chain. Color code: NADH, blue bolt; NADPH, yellow bolt; and ATP, red bolt. Abbreviations: TCA, tricarboxylic acid cycle; CBB, Calvin-Benson-Bassham; PHB, polyhydroxybutyrate; PEP, 2-phosphoenolpyruvate. (Lauterbach & Lenz, 2019).

Four putative transhydrogenases are present in *C. necator* genome. Transhydrogenases transfer hydrides through the cellular membrane from NADH and NADPH, contributing to the redox balance. (Cramm, 2009)

1.2.4 Bioproducts diversity.

Since the discovery of *C. necator*'s ability to accumulate PHAs, and particularly PHB, these biopolymers attracted significant attention due to their unique characteristics in flexibility, resistance, and biodegradability (Zhila et al., 2021). *C. necator* can accumulate remarkably high PHB yields under various trophic conditions, both heterotrophic and lithoautotrophic. PHB production is largely driven by nutrient availability, particularly nitrogen starvation, and excess carbon sources, redirecting carbon flux toward storage mechanism (Jahn et al., 2021).

PHB production has been a longstanding focus in research, especially due to its relevance for sustainable bioplastics. For years, efforts concentrated on achieving high-cell-density cultivations to maximize PHB yield (Ishizaki & Tanaka, 1991; Tanaka et al., 1995)(Tanaka, Ishizaki). Between 1990 and 2000, several companies successfully scaled up PHB production and began engineering *C. necator* for commercial use. Notable examples include Kaneka (Japan), Monsanto (USA), Tianjin Northern Food and Zhejiang Tian An (China), and Zeneca Bio Products (UK) (G.-Q. Chen, 2009; S. Y. Lee, 1996; Palmeiro-Sánchez et al., 2022). More recently, continued efforts have aimed at enhancing PHB production from CO_2. This topic has been extensively reviewed, with numerous examples reported in the literature (S. Kim et al., 2022; Vlaeminck et al., 2024; L. Zhang et al., 2022).

The development of advanced genetic tools over the past decade has enabled the exploration of a broader range of bioproducts derived from *C. necator*, particularly under autotrophic conditions. Today, *C. necator* is recognized as a promising chassis for the CO_2-based production of a growing portfolio of value-added compounds. Examples of CO_2-based products and heterotrophic-based products are listed in Table 2.

Table 2. Examples of products synthesized from autotrophic or heterotrophic sources in *C. necator.*

Carbon source	Product	Concentration g/L	Reference
CO_2	1,3-butanediol	2.97	(Gascoyne et al., 2021)
	2,3 butanediol	32	(Bommareddy et al., 2020)
		0.04 g/L/h	(Weiler et al., 2024)
	Isopropanol	7.7	(Bommareddy et al., 2020)
		0.25	(Marc et al., 2017a)
		3.25	(Garrigues et al., 2020)
		0.6	(C. Liu et al., 2016)
	Isobutanol	0.8	(H. Li et al., 2012)
	3-Methyl-1-butanol	0.6	(H. Li et al., 2012)
	D-mannitol	3.9	(Hanko et al., 2022)

	Alka(e)ne	0.0044	(Crépin et al., 2016)
	Trehalose	0.47	(Löwe et al., 2021)
	Mevalonate	10	(Garavaglia et al., 2024)
	α-humulene	0.01	(Krieg et al., 2018)
	L-isoleucine	0.01	(L. Wang et al., 2024)
	L-valine	0.03	
	Myo-inositol	1.05	(X. Wang, Wang, et al., 2023)
	Sucrose	0.18	(Nangle et al., 2020)
	Lipochitooligosaccharides	0.0014	(Nangle et al., 2020)
	2-hydroxyisobutyrate	3.2	(Przybylski et al., 2015)
	N-acetylglucosamine	0.08	(X. Wang, Chang, et al., 2023)
	Fatty acids	0.06 mg/g	(Z. Li et al., 2019)
Fructose	Isopropanol	15.1	(Boy et al., 2023)
	Isobutanol	14	(Lu et al., 2012)
	Alka(e)ne	1.5	(Crépin et al., 2018)
	2-hydroxyisobutyrate	6.4	(Hoefel et al., 2010)
	Cyanophycin	31.3	(K. Lin et al., 2012)
Butyrate	2-hydroxyisobutyrate	0.2	(Przybylski et al., 2013)

Autotrophic bioproduction in *C. necator* involves the use of H_2 and O2 as gaseous substrates, and requires safety measures due to the potential formation of explosive mixtures. In air, hydrogen is flammable at concentrations between 4% and 74%, and becomes explosive at concentrations between 19% and 57% (Shapiro & Moffette, 1957). This poses a significant challenge, as optimal growth for *C. necator* typically requires gas mixtures with H_2/O2/CO_2 ratios of 7:1:1, 7:2:1, or 6:2:1 (Ishizaki & Tanaka, 1991; Takeshita & Ishizaki, 1996; Volova et al., 2013). Explosive conditions are reached when gaseous hydrogen exceeds 4 % and oxygen exceeds 6 %(Garrigues et al., 2020). To address safety during autotrophic *C. necator* cultivations, various strategies have been proposed, including the development of explosion-proof bioreactors, reactor configurations, and non-explosive gas supply (Aliyu Alhafiz et al., 2025; Lambauer & Kratzer, 2022; Miyahara et al., 2022).

Chapter 3 : Union is strength, assembling an enzymatic cascade with oxidoreductases.

Oxidoreductases are versatile biocatalysts widely used in biotransformation processes. These enzymes belong to the EC 1 class and catalyze reduction-oxidation reactions. During the reaction electrons are transferred from a reducing agent, which donates electrons and becomes oxidized; to an oxidizing agent, which accepts the electrons and becomes reduced. According to the BRENDA database, oxidoreductases account for approximately 30% of all registered active enzymes, and contains over 20 subclasses. Notably, more than 50% of oxidoreductases utilize NAD^+/NADH or $NADP^+$/NADPH as redox cofactors (Sellés Vidal et al., 2018)

Oxidoreductases have gained significant industrial relevance due to their catalytic versatility and selectivity. Among the most relevant types for biotechnological applications are oxidases, dehydrogenases, reductases, dismutases, and oxygenases (Espina et al., 2021; Martínez et al., 2017a). A market analysis published in 2022 by Allied Market Research estimated the global enzyme market at USD 5.8 billion in 2021, with projections reaching USD 10.2 billion by 2031. Enzymes derived from microbial sources represent the largest market share, while oxidoreductases are the second most prominent group, surpassed only by hydrolases (Sajeev & Deshmukh, 2022). These trends highlight the growing opportunities for oxidoreductase development in industrial biocatalysis and multi-enzyme cascades.

In this context, the present study describes the development of a novel lithoautotrophic process for the production of *N*-heterocycles, using engineered microorganisms to host an enzymatic cascade. The cascade is implemented in *C. necator*, a bacterium with a unique metabolism capable of autotrophic growth using CO2 as carbon source, H_2 as electron donor, and O2 as terminal electron acceptor. The pathway involves three key oxidoreductases: heterologously expressed variants of putrescine oxidase (PuOx) and imine reductase (IRED), introduced for the first time into *C. necator*; and the native soluble hydrogenase (SH), which is essential for cofactor regeneration and overall cascade functionality. The enzymatic cascade is illustrated in Figure 7, and each enzyme is described in detail in the next sections.

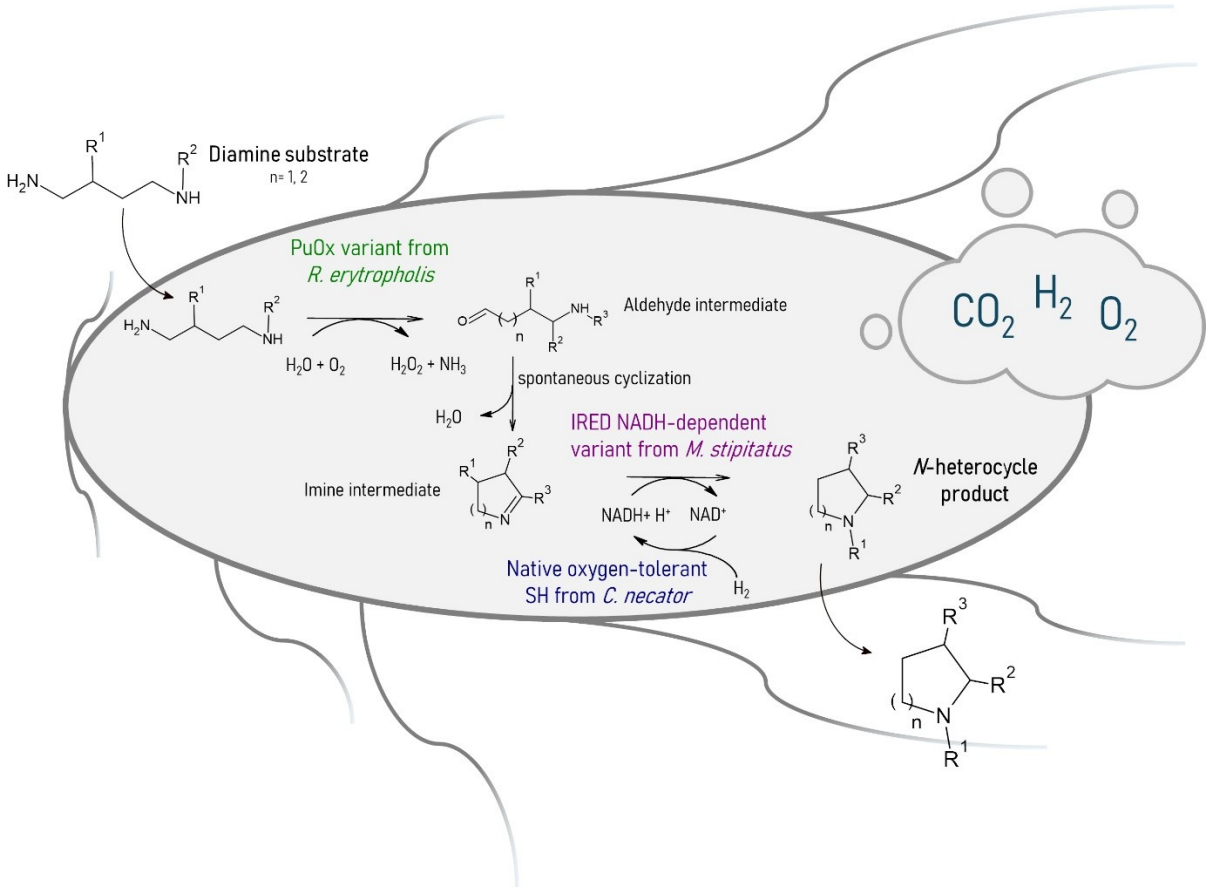

Figure 7. H_2-driven enzymatic cascade for production of *N*-heterocycles in *C. necator* : the desired enzymatic cascades start with a diamine substrate that enters *C. necator* cell. The substrate is oxidized via the putrescine oxidase variant from *Rhodococcus erythropolis* ($PuOx_{M1}$), and reduced via the NADH-dependent imine reductase variant from *Myxococcus stipitatus* ($IRED_{V8}$). Cofactor regeneration is guarantee by the oxygen-tolerant soluble hydrogenase natively present in *C. necator* (SH). Lithoautotrophic metabolism in *C. necator* relies on CO_2 as the sole carbon source, H_2 as the electron donor, and O_2 as the terminal electron acceptor. Image adapted (Al-Shameri et al., 2019) with ChemSketch and Powerpoint.

1.3.1 Imine Reductases (IREDs) and NADH-dependent $IRED_{V8}$

Imine reductases (IREDs) are oxidoreductases classified under EC 1.5.1, which catalyze the reversible transfer of electrons during imine reduction, resulting in chiral amines. To drive the reduction, the majority of IREDs require NADPH, and they are stereoselective towards *R*- or *S*-enantiomers (BRENDA database). The reaction is illustrated in Figure 8.

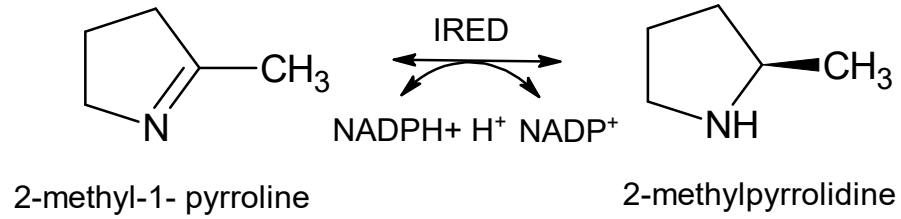

Figure 8. IRED reaction with the model substrate 2-methyl-1-pyrroline

IREDs were first described in a patent filed in 2009 (Nagasawa et al., 2011), and subsequently isolated and characterized by Mitsukura et al. (2010, 2011, 2013). Since then, IREDs structure and reaction mechanism have been analyzed.

IREDs share conserved structural features across a wide range of organisms. They typically function as homodimers, with each monomer binding one molecule of NADPH through a characteristic Rossmann-fold motif located in the N-terminal domain. This domain is connected to a C-terminal helical bundle via a long interdomain α-helix, forming a stable and functionally active architecture. The active site is generally composed of hydrophilic residues, such as aspartate or tyrosine, which contribute to substrate binding and catalysis (Gilio et al., 2022; Huber et al., 2014; Rodríguez-Mata et al., 2013; Schrittwieser et al., 2015).

The proposed reaction mechanism suggest that the imine is protonated by the amino acid in the catalytic site, followed by hydride transfer from NADPH to the imine (Rodríguez-Mata et al., 2013). During transition states, the stereoselectivity could be controlled through electrostatic interaction caused by the orientation of the iminium cation (Wu et al., 2024). Stereoselectivity in IREDs can be altered from *R*- to *S*- with site mutation mutagenesis (Stockinger et al., 2021). Moreover, structural and evolutionary studies have provided deeper insight into the origin and control of IREDs stereoselectivity. Through ancestral sequence reconstruction, six historical mutations were identified that collectively modulate stereoselectivity by reshaping the substrate-binding pocket. These mutations are located in flexible loop regions surrounding the NADPH binding pocket and influence how substrates are positioned during catalysis (Zhu et al., 2024). Understanding IRED structural basis enables rational protein engineering strategies to fine-tune stereoselectivity for synthetic applications.

Despite the growing catalog of characterized and engineered IREDs, the native physiological role in bacteria remains partially elucidated (Schrittwieser et al., 2015). As IREDs present activity towards the synthesis of primary, secondary, and tertiary chiral amines, it is suggested that they play a role in the

synthesis of secondary metabolites in bacteria (Cárdenas-Fernández et al., 2023; Montgomery et al., 2020).

Since their discovery, industrial interest in IREDs grew rapidly due to their selectivity, tunability, and scalability. At GlaxoSmithKline (GSK), directed evolution was applied to engineer an IRED in an enzymatic cascade, and produce the lysine-specific demethylase-1 inhibitor GSK2879552 (Schober et al., 2019). Other pharmaceutical companies such as Novartis and Pfizer have also developed multienzyme cascades incorporating IREDs for the stereoselective synthesis of amines (France et al., 2018; Kumar et al., 2021; E. J. Ma et al., 2021). Recently, Aleku et al. (2024) discussed a broad panel of IREDs, including the subclass reductive aminases (RedAms), highlighting ongoing academic-industrial collaborations.

The diversity of IREDs and their applications continue to expand through enzyme discovery and protein engineering, enabling the synthesis of complex *N*-heterocycles (Borlinghaus, 2019; Borlinghaus et al., 2018; Scheller, 2016). Among the most interesting examples, the *R*-selective IRED from *Myxococcus stipitatus* was engineered to shift its preference from NADPH to NADH (Borlinghaus & Nestl, 2018). The cofactor change was achieved using the "Cofactor Specificity Reversal-Structural Analysis and Library Design" (CSR-SALAD), combined with site-directed mutagenesis of the residues surrounding the NADPH-binding pocket. The resulting mutant library was screened, identifying key amino acids that enhanced NADH-dependent activity. The most effective variant was $IRED_{V8}$ with changes in amino acid N32E/R33Y/T34E/K37R/L67I/T71V, exhibiting improved kinetics with NADH while retaining moderate activity with NADPH. $IRED_{V8}$ was further coupled with NADH-dependent enzymatic cascades for the *in vitro* production of methylated *N*-heterocycles (Al-Shameri et al., 2020).

$IRED_{V8}$ enables broader applications for *in vivo* enzymatic cascades with the NADH-dependent soluble hydrogenase from *C. necator*, and was selected for this study (Figure 9).

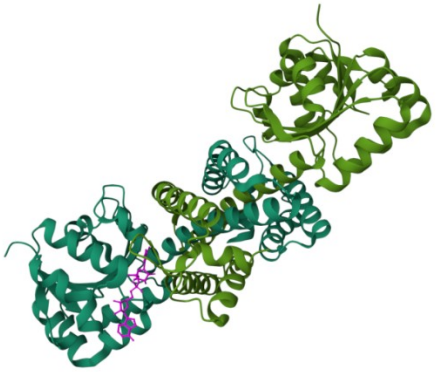

Figure 9. Structure of NADH-dependent $IRED_{V8}$: Each IRED monomer is colored with dark or light green, and NAP^+ is colored in purple in one monomer. Structure from PDB data bank, accession number 6TOE (Stockinger et al., 2021)

1.3.2 Putrescine oxidases (PuOx) and variant $PuOx_{M1}$

Putrescine oxidases (PuOx) belongs to the enzyme class EC 1.43.10, acting on CH-NH_2 group donors with O2 as acceptor. PuOx catalyze the oxidative deamination of amines using O2 as co-substrate, and require flavin adenine dinucleotide (FAD^+) as cofactor (BRENDA database) (Figure 10).

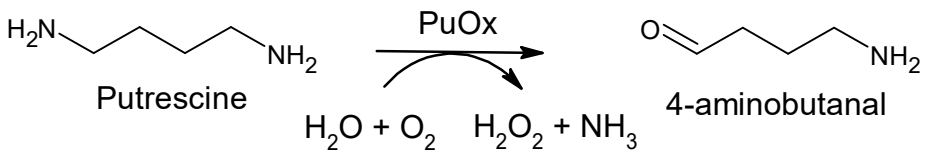

Figure 10. Reaction catalyzed by PuOx.

PuOx was first identified and partially characterized in *Micrococcus rubens* (DeSa, 1972; Yamada, 1971; Yamada et al., 1965), and its structure was further analyzed in subsequent work (Ishizuka et al., 1993). A homologous enzyme from *Rhodococcus erythropolis* was later characterized (van Hellemond et al., 2008), enabling detailed investigations of structure, and catalytic mechanisms.

Structurally, PuOx is a soluble cytoplasmic homodimer protein with a narrow, negatively charged active site. The active site is mainly shaped by the amino acid Glu324. The enzyme demonstrates strict substrate specificity, requiring diamines with two primary amino groups spaced by at least four carbon atoms, such as putrescine and cadaverine. Furthermore, a lysine and a tryptophan are involved in non-covalent FAD binding (van Hellemond et al., 2008). (Figure 11)

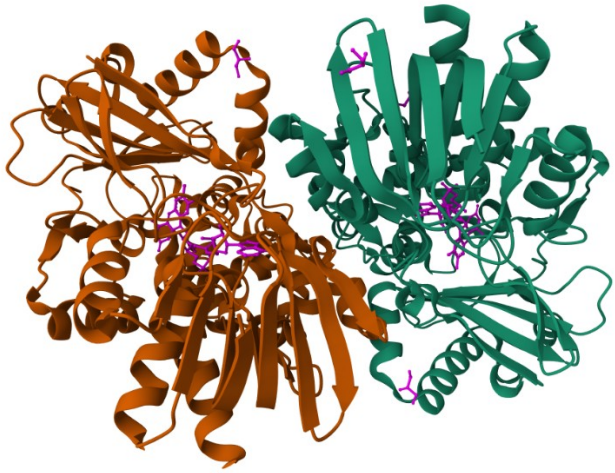

Figure 11. Structure of PuOx : wild-type structure from *R. erythropolis*, each monomer is colored with dark green or orange, and FAD^+ is colored in purple. Structure from PDB data bank, accession number 2YG3 (Kopacz et al., 2011).

The suggested catalytic mechanism of PuOx proceeds via two half-reactions. In the reductive half-reaction, the enzyme rapidly and irreversibly oxidizes putrescine, transferring a hydride directly

to the FAD cofactor via a bifurcated mechanism. In the oxidative half-reaction, the reduced $FADH_2$ is reoxidized by O_2, producing hydrogen peroxide (H_2O_2) as a by-product (Kopacz et al., 2014). The overall reaction yields 4-aminobutanal, NH_3, and H_2O_2.

Compared to IREDs, PuOx enzymes are less extensively studied, and current research is focused on specialized applications. Recent work includes their use in biosensor platforms (Xia et al., 2017), and enzyme immobilization strategies for integrated biocatalytic systems (Kamathewatta et al., 2021).

An interesting advance was done in *N*-heterocycle biocatalysis, engineering the PuOx from *R. erythropolis*, to broaden the substrate scope beyond natural diamines. An initial variant containing the E203G mutation in the substrate access channel exhibited increased oxidation activity toward longer, non-natural diamines (Al-Shameri et al., 2019). Further engineering three additional amino acid substitutions (L200I, E203S, I206L) within a loop region adjacent to the active site, resulting in the $PuOx_{M1}$ variant. This enzyme demonstrated improved activity toward C5 diamines while retaining catalytic efficiency with putrescine (Borlinghaus et al., 2019).

$PuOx_{M1}$ was selected for our study due to the broadened substrate, to support the synthesis of *N*-heterocycles in a whole-cell enzymatic cascade.

1.3.3 Soluble hydrogenase (SH) from *C. necator*.

Hydrogenases catalyze the reversible oxidation of H_2 into protons and electrons (Figure 12). The soluble hydrogenase (SH) of *C. necator* is a [NiFe]-hydrogenase classified under EC 1.12.1.2, and plays an important role in redox balancing in the bacterium.

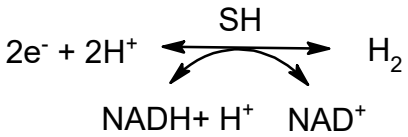

Figure 12. Reaction catalyzed by SH.

SH is a heterohexameric enzyme composed of six subunits: $HoxHYFUI_2$ (Figure 13). The subunits are organized into two modules: hydrogenase and diaphorase. The hydrogenase module is formed by HoxHY, and contains the [NiFe] active site which is responsible for H_2 oxidation. The diaphorase module is formed by HoxFU, and contains several iron-sulfur clusters [4Fe-4S] and [2Fe-S], which facilitates electron transfer across the subunits, oxidizing NADH. In *C. necator*, the reaction is favored towards the reduction of NAD^+ to NADH (Lauterbach et al., 2013). Both the HoxF and HoxY subunit contains flavin mononucleotide FMN, which are intricately linked to the Fe-S clusters, enabling the efficient electron transfer within the SH subunits (Lenz et al., 2015). Moreover, HoxI subunits form a homodimer, potentially involved in regulatory functions (Burgdorf et al., 2005).

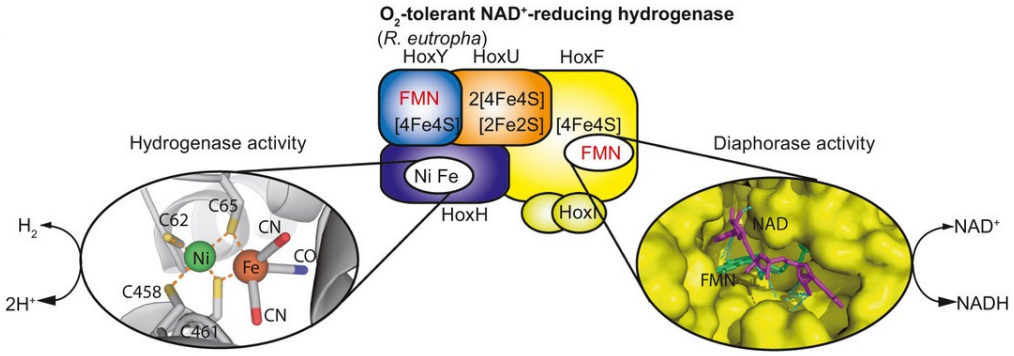

Figure 13. Diagram of the structure of SH from *C. necator* . Imaged adapted (Lauterbach et al., 2013)

The genes encoding SH expression are located in the plasmid pHG1, organized in the operon *hoxFUYHWI* (Schwartz et al., 2003). The *hoxF* gene plays an important role in SH expression, as its inactivation disrupt transcription of the entire SH operon (Jahn et al., 2024). The genes *hoxW* and *hoxI* encode for accessory proteins, and *hoxJ* couples SH expression to ATP levels, modulating enzyme production based on energy availability (Burgdorf et al., 2005; Lenz et al., 1997; Lenz & Friedrich, 1998). Moreover, SH maturation is a complex process requiring the biosynthesis of metal cofactors and the involvement of several maturation proteins encoded by the *hyp* and *hoxMLOQRTVW* operons (Burgdorf et al., 2001; Cramm, 2009).

Normally, SH would be expressed during lithoautotrophic growth, where H_2 serves as the energy source. However, in the wild-type strain *C. necator* H16 the protein HoxJ is mutated, and results in SH production even under heterotrophic conditions (Lenz & Friedrich, 1998). This additional expression imposes a protein cost in heterotrophy (Jahn et al., 2024).

Unlike many other hydrogenases that are sensitive to oxygen, the SH from *C. necator* exhibits remarkable oxygen tolerance: activity is retained even at atmospheric O2 concentrations, and shows only a 20% activity decrease at 60% O2 (Schneider & Schlegel, 1981). In biotechnological applications, O2-tolerance and the ability to produce NADH, make SH an attractive candidate for cofactor recycling systems. Notably, SH has been successfully coupled with IREDs, and PuOx *in vitro* for the production of *N*-heterocycles, demonstrating its potential in multi-enzyme cascades (Al-Shameri et al., 2019, 2020). The O_2-tolerant SH, combined with the lithoautotrophic capacity of *C. necator*, provide a promising platform for implementing the designed enzymatic cascade and access *N*-heterocycles.

Section 2: Materials and methods

Chapter 1 Bacterial strains and plasmids

Table 3. Strains used within this work.

Strain	Characteristics and plasmid contained	Name in manuscript	Reference
C. necator			
H16	Wild type strain of *C. necator*, with mega plasmid pHG1, SH+ MBH+ RH+ $HoxJ^-$	WT	DMS 428, Leibniz Institute DSMZ-German Collection of Microorganisms and Cell Cultures GmbH
lls365	Strain producing $IRED_{V8}$ with plasmid pAA56	WT + IRED	Previously designed by A. Al-Shameri
ll377	Strain with two plasmids: $IRED_{V8}$ with plasmid pAA56, and overexpression of native *Cn*GroESL with plasmid pEG19	WT + IRED + GroESL	This work
lls196	Strain producing $PuOx_{M1}$ with plasmid pDA2	WT + PuOx	This work
lls14	*C. necator*, with mega plasmid pHG1, SH^+ MBH^+ RH^+ $HoxJ^-$, Δlon	Δlon	P. Schoenmakers, 2022
lls380	Δlon producing $PuOx_{M1}$ with plasmid pDA2	Δlon + PuOx	This work
lls378	Strain producing $IRED_{V8}$ and $PuOx_{M1}$ together with plasmid pDA4	WT + IRED +PuOx	This work
lls379	Strain producing $IRED_{V8}$ with plasmid pAA56, and $PuOx_{M1}$ in plasmid pDA5	WT + IRED + PuOx-2	This work
lls345	Strain producing $IRED_{V8}$ with plasmid pDA6	WT+ $IRED_{pcat}$	This work

lls372	Strain producing $PuOx_{M1}$ with plasmid pDA5	WT + PuOx-2	This work
lls370	Strain producing IRED WT from *M. stipitatus* (NADPH dependent) with plasmid pDA7	WT + $IRED_{NADPH}$	This work
E. coli			
AA44	pCB28a (+), Cm^R, IPTG induction, containing $IRED_{V10}$ - NAD^+ dependent (N32E/R33Y/T34E/K37A/L67I/T71V)	*E. coli* + $IRED_{V10}$	Previously designed by A. Al-Shameri
HW 191	MC 1000 *pho*R- Δ*ara* 714 leu^+		Arne Rietsch/Jon Beckwith (Harvard Medical School)
lls173	BL21 derivative producing $PuOx_{M1}$ in plasmid pBAD_$PuOx_{M1}$.		(Al-Shameri et al., 2019)
DH10β	*ara*D139 Δ(*ara-leu*)7697 *fhu*A *lac*X74 *gal*K (Φ80Δ(*lac*Z)M15) *mcr*A *gal*U *rec*A1 *end*A1 *nup*G *rps*L (StrR) Δ(*mrr-hsd*RMS-BC)		(Grant et al., 1990)
S17-1	Tra^+, *rec*A pro^-,th^-,chr:RP4-2		(Simon et al., 1983)
BL21	F^- *ompT gal dcm lon hsdS_B(*rB^- mB^-*)*; $\Delta lon\ \Delta ompT$, lacks restriction-modification system; optimized for recombinant protein expression.		(Jeong et al., 2009; Studier & Moffatt, 1986)

Table 4. Plasmids used within this work

Plasmid	Characteristics	Reference
pAA56	pKRrha, Tet^R, RSF1010 mob and origin of replication, par. L-Rhamnose inducible: rhaR, rhaS, $rhaP_{BAD.}$ N-terminal StrepTagII- $IRED_{V8}$ from *M. stipitatus* (NADH-dependent) (N32E/R33Y/T34E/K37R/L67I/T71V)	Previously designed by A. Al-Shameri
pBAD18_$PuOx_{M1}$	pBAD, pBR322 origin, $Amp^{R.}$ L-Arabinose inducible system P_{Bad}. N-terminal HisTag-$PuOx_{M1}$ from *R. erythropolis* (L200I/E203S/I206L)	(Borlinghaus et al., 2019)
pDA2	pKRrha, Tet^R, RSF1010 mob and origin of replication, par. L-Rhamnose inducible: rhaR, rhaS, $rhaP_{BAD.}$ N-terminal HisTag-$PuOx_{M1}$ (L200I/E203S/I206L)	This work
pDA4	pKRrha, Tet^R, RSF1010 mob and origin of replication, par. L-Rhamnose inducible: rhaR, rhaS, $rhaP_{BAD}$. Contains N-terminal StrepTagII-$IRED_{V8}$ and N-terminal-HisTag-$PuOx_{M1}$	This work
pEG19	pBBR1MCS-2 derivative, Kan^R. L-Arabinose inducible system P_{Bad}. (pBBAD), P_{LAC}-RBS-GroESL inserted after the MCS.	(Marc et al., 2017b)
pDA5	N-terminal-HisTag-$PuOx_{M1}$ exchanged for GroESL in pEG19	This work
pCAT201	Empty backbone of pBBR1MCS-2, OriV origin of replication, Kan^R	(Azubuike et al., 2020) Addgene #134878
pDA6	pCAT201, Kan^R. L-Arabinose inducible system. N-terminal StrepTagII- $IRED_{V8}$ (N32E/R33Y/T34E/K37R/L67I/T71V)	This work
pDA7	pCAT201, Kan^R. L-Arabinose inducible system. N-terminal StrepTagII- IRED WT from *M. stipitatus* (NADPH dependent).	This work

For Results section 1.1.4, synthetic genes were ordered on pBAD plasmids with ampicillin resistance and L-arabinose inducible system. IRED sequences from different microorganisms were provided by B. Nestl and the partner Innophore. All sequences were tagged with HisTag. Plasmids were stored in *E. coli* DH10β and proteins were produced in HW191.

Details of plasmid construction are indicated on Supplementary section.

Chapter 2 Cloning and transformation

2.2.1 DNA cloning

Amplification of selected DNA fragments and plasmid linearization were made with the polymerase chain reaction (PCR) in a thermocycler using different enzymes: Phusion® High Fidelity DNA Polymerase, Q5® High Fidelity DNA Polymerase or Q5® High-Fidelity 2X Master Mix (New England Biolabs®, NEB, Germany), following the manufacturer's indications. To amplify *C. necator*'s DNA, 3% DMSO was used in the PCR-mix. PCR amplicons were treated with DpnI (NEB, Germany) to digest DNA template. Amplicons were further purified with the Monarch PCR and DNA Cleanup Kit according to the manufacturer's instructions.

To construct the different plasmids, DNA fragments and plasmid backbones were ligated using either enzymatic restriction and ligation, or Gibson assembly, following manufacturers recommendations.

For the enzymatic restriction, appropriate enzymes were chosen from NEB or Thermo Fisher suppliers to digest the DNA fragments, and ligation was performed in a 20 µL reaction containing T4 DNA Ligase in T4 DNA Ligase Buffer (NEB, Germany). The ligation reaction contained a ratio 5:1 insert to plasmid, and was incubated 2 h at room temperature. Challenging constructs were incubated overnight at 16°C. Where necessary, a 5'-terminal phosphate modification was added to the PCR fragments. For this purpose, the fragments were incubated with the T4 polynucleotide kinase in the T4 DNA Ligase Buffer (NEB, Germany) at 37°C for 30 min, and this enzyme was heat-inactivated at 65°C for 20 min, before ligation with the T4 DNA Ligase. Ligated plasmids were transformed into *E. coli* DH10β or BL21 chemical competent cells.

For the Gibson assembly, linear DNA fragments were generated by PCR containing flanking homologies. Amplified fragments were assembled using 2x Gibson Assembly Master Mix® from NEB (Germany). The reaction contained 200 ng of plasmid and the mass of the inserts was calculated with the NEBuilder Assembly Tool. The reaction was incubated in a thermoblock at 50°C during 1 h, and transformed into *E. coli* DH10β or BL21 chemical competent cells.

Plasmid pDA2 was constructed by amplifying a first version of the pKR backbone containing $puox_{M1}$ with primers PKRnewRham_Reverse-1 and PKRnewRham_Forward-1 without amplifying *rhaS* and *rhaR* (SupplementarySupplementary A.). Separately, the correct sequence of *rhaS* and *rhaR* (PNewRham) was amplified with primers Rhamnose-Forward-1 and Rhamnose_Reverse-1 from plasmid pECcas9 (SupplementarySupplementary A.). Both, vector and insert containing the corrected promoter sequence were joined via Gibson assembly (de la Asunción Vest, 2023).

Plasmid pDA4 was constructed using pDA2 and pAA56. Both plasmids have a pKR-backbone and the *puox$_{M1}$* gene was transferred from pDA2 to pAA56. Plasmid pDA2 contains one digestion site for the restriction enzyme XbaI, and a second restriction site was added by PCR amplification with the primers oIC78/oIC79 (SupplementarySupplementary A.). The new XbaI recognition site was added in 5'-terminal. The amplified segment was digested with XbaI as described before. The plasmid pAA56 presents already a XbaI site in C-terminal of *ired$_{V8}$* and was digested with the XbaI enzyme. The two digestion were ligated with T4 DNA using an excess 5:1 DNA mass from PCR-amplified fragment.

Plasmid pDA5 was obtained exchanging the *groEL* gene from pEG19 (Figure 19) with the *puox$_{M1}$* gene from pBAD18_PuOx$_{M1}$ (Borlinghaus et al., 2019). The exchange was done using the restriction sites EcoRI and HindIII present in both constructs. Each plasmid was digested with the two restriction enzymes, and fragments were loaded for agarose electrophoresis separation. Different fragments were extracted from the gel: from pEG19 digestion, the band at 6.9 kbp was extracted (backbone, containing mobility region and origin compatible for *C. necator*); and from pBAD18_PuoxM1 the band at 1.3 kbp was extracted (PuOXM1-fragment with His-tag). The gel extraction was performed using the Monarch® DNA Gel Extraction Kit; NEB following manufacturers recommendations. The backbone and Puox$_{M1}$-fragment were quantified with Nanodrop. Both segments were ligated using T4 Ligase, and a 5:1 excess of fragment mass. The plasmid pDA5 was electroporated simultaneously with pAA56 in *C. necator,* and colonies were screened and isolated on FN plates containing Kan, and Tet resistance.

Plasmid pDA6 was constructed as following: primers oIC99/oIC100 (SupplementarySupplementary A.)were used to amplify the backbone of pCAT201 and primers oIC101/oIC102 to amplify *ired$_{V8}$* from pAA56. Fragments were joined via Gibson assembly following manufacturer's recommendations.

After transformation, bacterial colonies were analyzed by colony-PCR. Individual colonies were picked with a sterile toothpick and resuspended in a 15 µL reaction with appropriate primers using the OneTaq® Quick-Load® 2X Master Mix with Standard Buffer (NEB, Germany). Single colonies were streaked out on a LB plate with the corresponding antibiotic.

2.2.2 Agarose gel electrophoresis

Buffer composition of 10 x Tris-phosphate-EDTA buffer (10 x TPE) is described in Table 5. The PCR products were analyzed with gel electrophoresis in a flat-bed gel chamber. Gels were prepared containing 1 % agarose in 1 x TPE buffer.

Table 5. Buffer composition for agarose gel.

Buffer	Components	Final Concentration
10 x TPE	Tris base	108 g/L
	H_3PO_4 (85% v/v)	25 mL/L
	EDTA disodium salt	29.8 g/L

The gel was dissolved by heating 60 s and Midori Green Advance DNA Stain (Nippon genetic, Japan) was added for gel staining. The mix was poured into the gel chamber and different ladders were used to identify DNA sizes: 1 kb Plus DNA ladder, Quick-Load® 1 kb Extend DNA Ladder or 1 kb Ladder from NEB (Germany). PCR products were mixed with NEB 6 x Gel Loading dye and loaded on the gel. The gel was set to run at constant 90 V for 30 min-45 min. After electrophoresis, the gels were analyzed using the BioRad Gel Doc XR.

2.2.3 Sequencing

Final verification of genetic constructs was performed with full-plasmid sequencing, gene sequencing or *E. coli* colony sequencing using the services from Microsynth Seqlab GmbH, Göttingen.

2.2.4 Preparation of chemically competent *E. coli* cells

Preculture of *E. coli* cells were grown in 5 mL of LB medium and incubated over night at 37 °C while shaking at 60 rpm. A 500 mL Erlenmeyer flask containing 100 mL LB-medium was inoculated with 1 mL of the overnight preculture. The culture was incubated at 37 °C and harvested after 1.5-2 hours when the OD_{600} reached 0.5. The culture was centrifuged at 4000 x g for 5 minutes at 4 °C. The supernatant was discarded, and the pellet was gently resuspended in 30 mL TBF-1 buffer and kept on ice for 90 min. Then the cells were washed by centrifugation at 4000 x g for 5min at °C and gently resuspended in 4 mL of TBF-2 buffer. Cells suspension was divided in aliquots of 50 µL and frozen using liquid N_2. Aliquots were stored at -80 °C until further used. Buffer composition is described in Table 6.

Table 6. Buffers used for *E. coli* competent cells

Buffer	**Component**	**Final concentration**
TFB-1	potassium acetate pH 5.8	30 mM
(Filter sterilized)	CaCl2	10 mM
	MnCl2	50 mM
	RbCl2	100 mM
	Glycerol	15% (v/v)
TFB-2	MOPS pH 7	10 mM
(Filter sterilized)	CaCl2	75 mM
	RbCl2	100 mM
	Glycerol	15% (v/v)

2.2.5 *E. coli* transformation.

Aliquots of chemically competent *E. coli* cells were thawed on ice, and 100 ng of plasmid was gently mixed with the cells by pipetting up and down. Cells were then kept on ice for 30 minutes and heat shocked at 42 °C for 30 seconds. Cells were chilled on ice for 5 minutes. Cells were regenerated by

adding 950 µL of LB medium and incubated at 37 °C for 1 h in agitation at 250 rpm. After regeneration, 100 µL of transformed cells were plated on LB agar plates with appropriate antibiotics. The remaining 900 µL of the cell suspension was centrifuged at 8000 rpm for 2 min, and 800 µL of the supernatant was discharged. The pellet was resuspended in the remaining 100 µL supernatant to concentrate the transformed cells. The concentrated cell solution was plated on another LB agar plate with antibiotic.

2.2.6 Preparation of electro-competent *C. necator* cells

C. necator competent cells were prepared by adapting the protocol from Tee et al. (2017) as follows: 10 mL of fructose-ammonia (FN) medium was inoculated with the desired strain in a 100 mL Erlenmeyer flask, and incubated for 48 h at 30°C. Then, 50 mL of FN was inoculated with 2% of the preculture and grown at 30°C until an OD_{600} between 0.4-0.6 was reached. The cells were recovered in a 50 mL tube and incubated during 10 min on ice. Cells were centrifugated at 4000 rpm for 10 min at 4°C. Cell pellets were resuspended with 1 ml of 10 % sterile Glycerol and filled up to 50 mL. Cell suspension was centrifuged at 3400 rpm for 10 min at 4 °C. Cells were resuspended again in 1 ml of 10 % Glycerol and filled up to 25 mL. The cells were centrifugated with the same previous conditions. Finally, the pellet was resuspended in 1 mL of 10% Glycerol and aliquoted in 50-100 µL. The tubes containing the competent cells were flash-frozen with liquid N_2 and stored at -80°C.

2.2.7 *C. necator* transformation

2.2.7.1 *C. necator* electroporation

For the electroporation, *C. necator* competent cells were thawed on ice and mixed with the plasmid. Typically, between 70-200 ng of plasmid was added to the cells and mixed gently with the pipette. The mix was transferred to a 2 mm-gap electroporation cuvette and shocked with 25 kV, 25 µF, 200 Ω and 50 ms. Immediately after the shock, 900 µL of LB containing 0.5% fructose was added to the cuvette. The cell suspension was transferred to a sterile Eppendorf tube and incubated at 37°C for 2 h at 300 rpm. Transformed cells were plated on LB agar plates containing the appropriate antibiotic. To obtain individual colonies, two cell concentrations were plated: non-diluted, and concentrated. For the non-diluted samples, 100 µL of cell suspension was directly plated. The concentrated sample was prepared by centrifuging the remaining cell suspension at 2000 rpm for 2 min, and removing 800 µL of supernatant. Cell pellet was resuspended in the remaining 100 µL and plated. Plates were incubated for 48h-72h at 37°C until colonies were observed. Clones were isolated in FN agar plates with appropriate antibiotic and evaluated by Colony PCR.

2.2.7.2 *C. necator* conjugation

For conjugation, target plasmids were first transformed into *E. coli* S17-1 (donor strain). The donor strain and *C. necator* (recipient strain) were grown in 10 mL LB medium overnight at 37 °C. The cells were harvested in falcon tubes and centrifuged for 10 min at 4000 x g. The supernatant was discharged and each pellet was resuspended in 5 ml sterile H16 buffer (25 mM Na_2HPO_4 x 12 H_2O and 11 mM $KH_2(PO_4)$ pH 7.0). The cells were centrifuged again for 10 min at 4000 x g. The supernatant was discharged and the resulting pellets were resuspended in 1 ml sterile H16 buffer. Donor and recipient strains were mixed together by plating 0,2 ml of each cell solution directly into a LB agar plate without

antibiotic. The plate was incubated for 6 h at 37°C. The bacterial film was removed by gentle scratching with an inoculation loop and resuspended in 5 ml sterile H16 buffer. The cell solution was centrifuged for 10 min at 4000 x g. The supernatant was discharged and the cells were resuspended one last time with 1 ml sterile H16 buffer. To obtain individual colonies, the cells in H16 buffer were diluted at 10^{-1}, 10^{-2} and 10^{-3}. An aliquot of 100 µL from each diluted and non-diluted cell suspension was plated on FN agar plates containing appropriate antibiotic.

Chapter 3 Bacterial cultivation

2.3.1 Cultivation media

Table 7. Media used for cultivations in this work

Medium	Component	Concentration
Rich medium		
LB liquid	Yeast extract	10 g/L
	Tryptone	5 g/L
LB agar	LB liquid	
	Agar	1.3 % w/v
TSB without dextrose, liquid	Dextrose-free Bacto™ Triptic Soy Broth (TSB, Becton Dickinson, Sparks, MD, USA)	27.5 g/L
TSB without dextrose, solid	TSB without dextrose liquid	
	Agar	1.3 % (w/v)
TB	K2HPO4	72 mM
	KH_2PO4	18 mM
	Bacto tryptone	1.2 % (w/v)
	Bacto yeast extract	2.4% (w/v)
	Glycerol	2.4% (w/v)
Minimal medium		
AUT	Na_2HPO_4 x 12 H_2O	25 mM
	KH_2PO_4	11 mM
	$MgSO_4$ x 7 H_2O	0.81 mM
	$CaCl_2$ x 2 H_2O	0.068 mM
	$FeCl_3$ x 6 H_2O (prepared in 0.1 N HCl)	18 µM
	NiCl2 x 6 H_2O	1 µM
	NH_4Cl	37.4 mM
FN	AUT	

	Fructose	4 g/L
FGN	AUT	
	Fructose	2 g/L
	Glycerol	2 g/L
FGN_{mod}	AUT	
	Fructose	0.5 g/L
	Glycerol	4 g/L

E. coli strains were cultivated in rich medium, liquid or solid (Table 7), supplemented with appropriate antibiotic: 50 µg/mL kanamycin (Kan), 35 µg/mL chloramphenicol (Cm), 100 µg/mL carbenicillin or ampicillin. Cultures were cultivated at 37 °C.

C. necator were cultivated in rich or minimal medium, both liquid or solid (Table 7), supplemented with appropriate antibiotic: 10 µg/mL gentamycin (Gen, natural resistance), 200 µg/mL kanamycin (Kan), 10 µg/mL tetracycline (Tet). For challenging transformations or with higher contamination risk, antibiotic concentrations were doubled.

To prepare *C. necator* minimal media, a 10 x H16 buffer was first prepared by dissolving 90 g/L of Na_2HPO_4 x 12 H_2O and 15 g/L of KH_2PO_4, and adjusting to pH 7 with phosphoric acid. This stock solution was diluted 1:10 with Millipore water, to obtain working H16 buffer. H16 buffer served as the base for minimal media to which sterile components were added according to the desired formulation.

2.3.2 Storage

C. necator strains were placed in glycerol stocks for long-term storage. Single colonies were picked to inoculate 10 mL of liquid FN or TSB without dextrose, with appropriate antibiotic and incubated at 30 °C under agitation. After growth, one mL of culture was transferred to a 1.5 mL cryotube and 0.5 mL of 50 % glycerol (v/v) was added. Cryotubes were flash-frozen with liquid N_2 and stored at -80 °C.

2.3.3 *E. coli* cultivation

E. coli strains were grown either in LB or TB medium, in liquid or solid agar plates with appropriate antibiotic. For the preparation of agar plates., 1.5% agar-agar or Bacto™ Agar was added to the medium and sterilized in autoclave. *E. coli* cultures were incubated at 37 °C.

2.3.4 *C. necator* cultivation in heterotrophic conditions and biotransformation.

C. necator was grown either in rich or minimal medium.

Liquid cultures in rich media were prepared in TSB without dextrose, TB, LB or LB without salt. For minimal growth the media FN, FGN or FGN_{mod} were used.

C. necator strains were streaked from a 1 mL cryostock on rich or minimal medium agar plates and incubated at 30 °C for 2-3 days. For liquid precultures, a single colony was picked and incubated on 10 mL medium contained in 100 mL Erlenmeyer. Precultures were placed at room temperature during 72 h or 30°C for 48 h at approximately 110 rpm.

Main cultures were inoculated with appropriate volumes of preculture into baffled Erlenmeyer flasks. Depending on the experimental objectives (growth assessment, protein production, protein purification, or biotransformation), Erlenmeyer flasks of 250 mL, 500 mL, 1 L, or 5 L were used. Each flask was filled to one-fifth of its total volume with culture medium. Main cultures were incubated at 30°C under agitation at 150 rpm.

Growth monitoring was performed using the Cell Growth Quantifier (CGQ) from Aquila Biolabs (Scientific Bioprocessing), an analytical device designed for automatic and noninvasive online biomass measurement in shake flasks. The CGQ sensor plate was positioned under each cultivation flask. The sensor emitted light through the flask wall and quantified the amount of scattered light, which increased proportionally with cell density. Growth monitoring data was retrieved using the DOTS software, and the backscatter signal data was used to determine the growth rate.

For FN characterization, cultures were initiated at an OD_{600} of 0.1, while cultivations with putrescine started at an OD_{600} of 0.05 in FN medium. Optical measurements were done with the Cary 60 UV-Vis Spectrophotometer (Agilent) in cuvettes with 1 cm optical length path. Main cultures were placed at 30°C in an Infors HT Ecotron incubator at 150 rpm.

To evaluate the biotransformation of 2-methylpyrroline to 2-methylpyrrolidine under heterotrophic conditions, *C. necator* strains were cultivated in TB medium. Cultivations were performed in 500 mL baffled Erlenmeyer flasks, each containing 60 mL of TB medium. Main cultures were inoculated with sufficient preculture to achieve an initial OD_{600} of 0.1. *C. necator* strains containing pCAT backbones were induced with a final concentration of 0.2 % (v/v) arabinose once they reached an OD_{600} around 0.8-1. Simultaneously, biotransformation was started with a final concentration of 10 mM 2-methyl-1-pyrroline. Supernatant samples were collected throughout the cultivation to monitor both cell growth and biotransformation progress. Growth was assessed by measuring the optical density at 600 nm using 1-cm path length polystyrene cuvettes. Biotransformation samples were stored at -20 °C until further analysis with gas chromatography.

2.3.5 *C. necator* gas fermentation and biotransformation.

2.3.5.1 Gas fermentation protocol performed at INSA Toulouse

To prepare the strains for the chemolithoautotrophic cultivation, a series of seed cultivations was carried out as illustrated Figure 14, and described in Table 8. Precultures and main culture were prepared as previously described by Di Bisceglie et al. (2025), with modifications in the described MIT medium. The media FN, FGN_{mod}, and AUT were used and adapted during the protocol. Each seed

culture with the appropriate antibiotics was incubated at 30°C, 140 rpm, and 10 % (vol/vol) was used inoculating the culture at an initial OD_{600} of 0.1. For all cultivation steps 10 µg/L gentamicin was added.

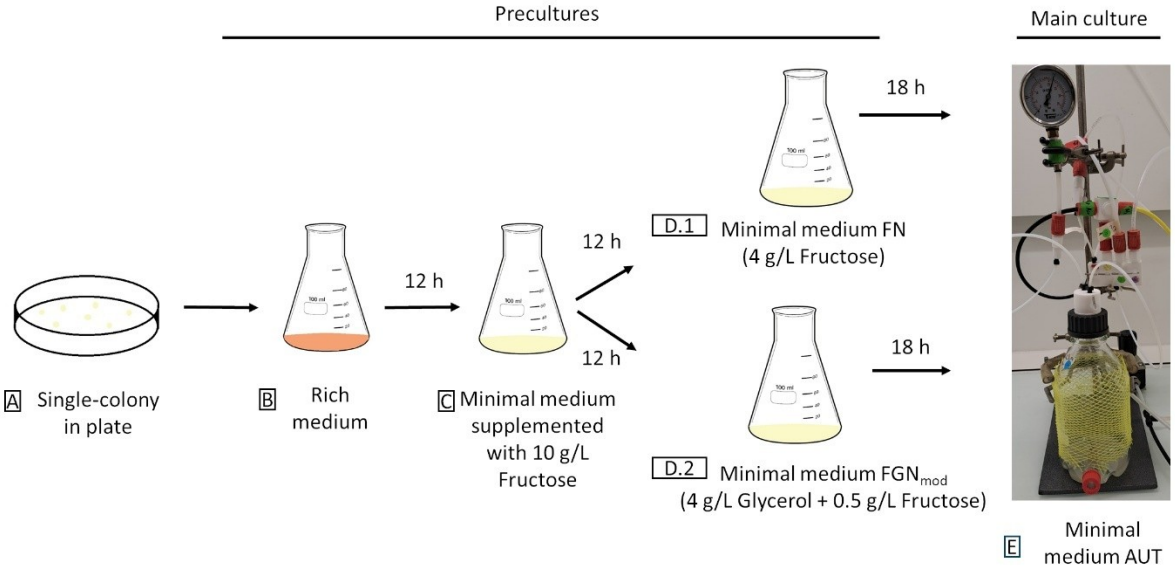

Figure 14. Seed train before gas fermentation: *C. necator* strains are cultivated in 3 liquid precultures form a single colony before inoculation in AUT medium for gas fermentation.

Table 8. Seed train before gas fermentation.

Step	Description and media	Time
1	Strains were streaked in agar plates (FN, LB or TSB agar) with appropriate antibiotic using a 10 µL inoculation loop.	2-3 days at 30°C, until isolated colonies were obtained.
2	A single colony was inoculated in 10 mL of TSB without dextrose, in a 100 ml baffled Erlenmeyer flask.	12 h
3	25 ml of AUT modified with 1 g/L NH_4Cl and supplemented with 10 g/L fructose was inoculated in a 100 mL baffled Erlenmeyer flask.	12 h
4	50 mL of FN or FGN_{mod} was inoculated in a 250 mL baffled Erlenmeyer flask.	17-18 h

Once the seed train was completed, residual fructose or glycerol from FN or FGN_{mod} media (Step 4-Table 8) was removed. A sufficient volume was harvested and centrifuged at 2057 x g for 10 minutes. The supernatant was discarded, and the pellet was resuspended in AUT medium before inoculating the main culture.

Gas fermentations were conducted in 250 mL or 1 L baffled Schott glass bottles (custom made by Verres Vagner, Toulouse, France), each containing a final volume of 50 mL of AUT medium and appropriate antibiotic. Cultures were started at an OD_{600} of 0.1. The bottles were sealed using a distributor with stoppers GL 45; UNF1/4" 28G; Ø 1.6 (Bohlender GmbH, Grünsfeld, Germany) and covered with a high-density polyethylene net (HDPE).

After inoculation, the air from the headspace was removed using a vacuum generator (VN-05-H-T3-PQ2VQ2-RQ2, Festo AG & Co. KG, Esslingen am Neckar, Germany). To ensure complete removal of atmospheric air, the headspace was flushed once using a gas mixture of H_2: O_2: CO_2–70:12:18 (%) and emptied again using the vacuum generator. Bottles were subsequently filled with the corresponding gas mixtures.

For chemolithoautotrophic conditions, a commercial mix of H_2: CO_2 (80:20 %) (AirLiquide, Bagneux, France) was used to pressurize the bottles up to 1.3 bar, and completing to 1.5 bar with pure O_2 allowing to reach a H_2: CO_2: O_2 -70.4: 17.6: 12 (%) mixture. Overpressure was monitored using a manometer, and the bottles were refilled whenever the overpressure dropped to approximately 0.5 bar. To refill the bottles, vacuum was applied in the headspace to remove the older atmosphere, and replaced with a fresh gas mixture. For 1 L bottles, the refreshed gas composition consisted of H_2: CO_2: O_2 -70.4: 17.6: 12 (%), achieved by filling the bottles with the commercial mix of H_2: CO_2 (80:20 %) up to 1.2 bar, and completing with pure O_2 to 1.5 bar. The increased O_2 concentration (12%) was used to ensure enough sufficient availability during the biotransformation. Gas compositions are summarized in Table 9.

Table 9. Gas composition in bottles in overpressure.

Bottle	**Commercial mix 80%H_2/20%CO_2 Pressure (bar)**	**O_2 Pressure (bar)**	**Over pressure**	**Gas composition headspace H_2: CO_2: O_2 (%)**
1 L - starting composition)	1.3	0.2	1.5	73.6: 18.4: 8
1 L -refills	1.2	0.3	1.5	70.4: 17.6: 12
250 mL	1.2	0.3	1.5	70.4: 17.6: 12

The bottles were incubated at 30°C under agitation at 140 rpm in an Infors HT Ecotron incubator (INFORS HT, Bottmingen, Switzerland). For protein production, *C. necator* strains containing pkr backbones were induced with a final concentration of 12 mM of rhamnose once they reached and OD_{600} between 0.5-0.7. After 16 h of protein production, the biotransformation assays were started by adding 10 mM putrescine or 2-methyl-1-pyrroline, according tested strain.

Cultures were harvested 48 h after the start of the biotransformation. The remaining gas was carefully released under a flow-hood and the cultures were collected in a tube. Cells were centrifuged at 4 °C, at 15 000 x g for 10 min. The supernatant was removed and cells were flash-frozen in liquid N_2, and stored at -70°C for further protein analyses.

During the gas fermentation, culture samples were collected to monitor cell growth and biotransformation. Growth was monitored by measuring optical density at 600 nm using a Hach Lange Spectrophotometer DR3900 (Hach Lange, Berlin, Germany) and 2mm path length glass cuvettes. The correlation between CDW and OD was previously established as CDW = 2 x OD, under this specific measurement conditions (Di Bisceglie et al., 2025). Biotransformation samples were stored at -20 °C and further analyzed with gas chromatography.

The specific growth rates were determined as the slope of ln (OD) = f(t) in the linear section of the curve with R^2 =0.99. Errors were calculated as the standard deviation of the slope.

2.3.5.2 Gas fermentation protocol performed at RWT Aachen University

To prepare the strains for the chemolithoautotrophic cultivation, *C. necator* strains were precultured with a simplified version of the seed train (Table 10). Precultures were incubated at 30°C, approximately at 150 rpm, and 10 % (vol/vol) was used to inoculate each step.

Table 10. Simplified seed train prior to gas fermentation.

Step	Description and media	Time
1	Strains were streaked in agar plates (FN, LB or agar) with appropriate antibiotic using a 10 µL inoculation loop.	2-3 days at 30°C, until isolated colonies were obtained.
2	A single colony was inoculated in 10 mL of LB without salt, in a 100 ml baffled Erlenmeyer flask.	12 h
3	10 mL of FGN_{mod} was inoculated in a 100 mL of baffled Erlenmeyer flask.	17-18 h

Gas fermentation was conducted in 500 mL baffled Erlenmeyer flasks with screw cap, containing a final volume of 60 mL of AUT medium. To make the flaks air tight, the bottle caps were drilled

beforehand to fit bottle stoppers DURAN®-GL 45. Cultures were started with sufficient preculture to reach an OD_{600} of 0.1.

For chemolithoautotrophic conditions, the gases were supplied through a gas mixing station from HTK® Hamburg with air-tight tubing (Festo, Germany). To introduce the gas mixture, sterile needles BD Microlance TM 3 27G x3/4''-Nr 20 0.4 x 19 mM were adapted to the tubes and inserted through the bottle stoppers. A second needle was inserted in the bottle stopper for gas release, and air exchange. Non-explosive gas mixture was supplied in the headspace with a flow of 100 mLn/min during 8 min, ensuring sufficient time to exchange the atmosphere with the desired gas mixture. After 8 min, the gas-releasing needle was removed, and the gas mixture was kept flowing during 1 additional minute to create a saturated atmosphere with slight overpressure in the flask. The gas composition and settings of the gas mixing station are described in Table 11.

Table 11. Non-explosive gas composition in flasks. Total flow in the gas mixing station was set to 100 mL_n/min and is considered as reference 100 %. (mL_n/min means volumetric flow at normal conditions).

Gas	**Flow (mL_n / min)**	**Composition (%)**
H_2	80	80 %
N_2	6	6 %
O_2	4	4 %
CO_2	10	10 %

Inoculated bottles with the gas mixture were incubated at 30°C, approximately at 150 rpm. *C. necator* strains containing pCAT backbones were induced with a final concentration of 0.2 % (v/v) arabinose once they reached and OD_{600} around 1. Simultaneously, biotransformation was started with a final concentration of 10 mM 2-methyl-1-pyrroline.

Cultures were harvested 48 h after induction/biotransformation. Cells were centrifuged at 4 °C, at 15000 x g for 10 min. The supernatant was removed and cells were flash-frozen in liquid N_2, and stored at -80°C for further protein analyses.

During the gas fermentation, supernatant samples were collected to monitor both cell growth and biotransformation. Growth was assessed by measuring optical density at 600 nm using a Cary 60 UV-Vis Spectrophotometer (Agilent) with 1- cm path length polystyrene cuvettes. Biotransformation samples were stored at -20 °C until further analysis with gas chromatography.

2.4.1 Protein production

Proteins intended for characterization, purification, or activity assays were produced by cultivating *C. necator* strains under heterotrophic conditions using minimal medium. Precultures were made inoculating a single colony in 100 mL of FN medium with the corresponding antibiotic in 250mL baffled flask at 30°C for 48 h.

To produce IRED from the respective *C. necator* strain, 1 L of FN medium with 20 µg/mL tetracycline was inoculated from the preculture in a 5 L baffled shake flask at an initial OD_{600} of 0.1. The cultures were placed in a shaker at room temperature and once they reached an OD_{600} 0.3-0.7, 0.2% L-rhamnose was added to induce IRED production (final concentration 12 mM). For the strains containing the chaperonin GroESL, an extra 5 mL of L-arabinose was added at the moment of induction (final concentration 6.6 mM). Cultures were incubated for 44-48 hr at room temperature in agitation at 150 rpm. Cells were harvested by centrifugation at 4°C, 4500 rpm for 30 min. The supernatant was discarded, the pellet was weighted, and flash- frozen with liquid N_2. Pellets were used immediately for cell lysis and protein analysis, or stored at -80 °C.

To produce PuOx from the respective *C. necator* strain, the main cultures were inoculated with the entire preculture volume into 5 L baffled flask. Flasks were filled to 4/5 of their total volume with FGN medium supplemented with 20 µg/mL tetracycline. Cultures were incubated at 30° under agitation at 100 rpm for either 48 h or 120 h. Cultures were induced with 0,2% L-rhamnose (final concentration 12 mM) at two distinct time points to assess the impact of the induction time, either at the same moment of inoculation, or 24 h after inoculation. Cells were harvested at 4000 rpm for 20 min at 4° C (Thermo Scientific Multifuge X3R). The supernatant was discharged, the pellet was weighted flash-frozen with liquid N_2. Pellet was used immediately for cell lysis and protein analysis, or stored at -80 °C.

2.4.2 Cell lysis

Frozen cells were thawed and resuspended with Resuspension Buffer (50mM potassium buffer (K_iPO_4) pH 7, 5% glycerol and cOmplete™, EDTA-free Protease Inhibitor Cocktail) at a ratio 1:2 per gram of cell pellet. Cells were lysed using two techniques: high-cell pressure homogenizer or sonication.

High-cell pressure homogenizer was used to obtain soluble extract and purify proteins. Two rounds of the One-Shot Cell Disrupter (Constant Systems Ltd) at 1.3 kBar were applied to cells. After disruption, the samples were centrifugated at 4°C 40000 x g in an ultracentrifuge for 1 hr. The supernatant was recovered and kept on ice for subsequent purification and analysis.

Sonication was only used for experiments which required soluble extract. Cell suspensions were transferred to a 15 mL tube and kept on ice. Samples were sonicated with 10 cycles of 45 s at 50% intensity, and incubated during 1 min of on ice in between of each cycle.

2.4.3 Protein purification

Proteins were purified using gravity columns. The corresponding resin for each protein was loaded into 2.5 mL or 5 mL columns with lower filters of 90 µm pore size from MoBiTec GmbH. The resin was incubated in the column during. All purifications were performed at 4 °C.

IRED was purified using the Strep-Tactin®XT 4Flow® from IBA Lifesciences GmbH, adapting the manufacture's recommendations. The buffers were modified from the protocol as follows: Binding Buffer contained 50 mM K_iPO_4 pH 7 with 300mM KCl, and the Elution Buffer contained 50 mM K_iPO_4 pH 7 with 300mM KCl and 50 mM Biotin. Purification process including equilibration and washing steps were performed according to the "Protein purification with Strep-Tactin®XT resins protocol" from IBA. During the purification, 1-2 mL of the flow through and washing steps were collected for further analysis. Three elution fractions were collected as recommended by IBA's protocol and analyzed on SDS-Page gel. Fractions showing a band were pooled and the buffer was exchanged and concentrated using an Amicon® Ultra-15, PLTK Ultracel-PL Membrane, with 30 kDa cut-off. Three cycles of exchange buffer were done by adding Storage buffer (50 mM K_iPO_4 pH 7 with 5% Glycerol) and centrifugation 20 min at 4000 rpm, 4°C. A final concentration step was done at 30 min at 4000 rpm, 4°C without extra addition of buffer, reaching a volume approximately of 500 µl. The concentrated protein was distributed in aliquots, flash frozen with liquid N_2 and stored at -80 °C. The protein was divided in 50 µl aliquots, subsequently shock frozen and stored at -80° C.

PuOx was purified via affinity chromatography using a nickel nitrilotriacetic acid (Ni-NTA) column. The resin volume was set to 3 ml. The column was equilibrated using three column volumes (CV) of Equilibration buffer (20 mM Na_3PO_4, 300 mM NaCl, 10 mM imidazole, pH 7.4) which were pipetted from the top. The soluble extract was mixed with an equal volume of Equilibration buffer and pipetted into a 100 ml syringe. The syringe was then placed on top of the column and the valve was opened. The flow of the protein solution was naturally controlled by gravity, making this a gravity flow column. 1 ml of flow through were collected and the rest were discharged. The column was washed with two CV of Wash buffer (20 mM Na_3PO_4, 300 mM NaCl, 25 mM imidazole, pH 7.4). All 6 ml of Wash buffer were collected into 2 ml Eppendorf tubes. Finally, 2 CV of Elution buffer (20 mM Na_3PO_4, 300 mM NaCl, 250 mM imidazole, pH 7.4) were added to the column and collected afterwards. The column was then regenerated adding 10 CV of Regeneration buffer (20 mM 2-(N-morpholine)-ethanesulfonic acid, 100 mM NaCl, pH 5), 10 CV of ultrapure water and 2 CV of 20% ethanol. For PuOx storage buffer contained 0.3 M phosphate buffer with pH 7. The protein was concentrated using an Amicon Ultra15 Centrifugal Filter 10K while centrifuging at 4000 rpm at 4° C for 15 min (Beckman L-60 Ultracentrifuge). Three ml of Storage buffer was added and centrifuged again at 4000 rpm at 4° C for 15 min. This process was repeated until a final concentration of 500 µl was reached. The protein was divided in 50 µl aliquots, subsequently shock frozen and stored at -80° C.

2.4.4 Protein quantification

Protein concentration in the soluble extract and purified proteins was determined using the standard bicinchonic acid (BCA) Protein Assay Micro Kit from SERVA Electrophoresis GmbH, according to the manufacturer's instructions with slight modifications. A standard curve was prepared using a dilution series of bovine serum albumin (BSA) ranging from 0 mg/mL to 1000 mg/mL. A volume of 25 µL was used for standards and samples. Duplicates were pipetted into a 96-well microtiter plate and 200 µL of BCA working reagent was used. The plate was incubated at 37 °C for 30 min and read in the Infinite 200 Pro M nano plate reader (Tecan) at 550 nm.

Protein concentration was calculated from the BSA standard curve. Samples analyzed from the soluble extract were diluted to fit in the range of the standard curve. Typically, dilutions of 1/4, 1/10, 1/50 or 1/100 were used.

2.4.5 Sodium dodecyl-sulfate polyacrylamide gel electrophoresis (SDS-PAGE)

Buffers and solutions are listed in Table 12. Enough sample volume was resuspended in 1x SDS sample buffer and heated at 95°C for 15 min. Samples were loaded into the gel wells 4-20% Tris-Glycine gels from Mini Protean ^{R} TGX Stain Free ^{TM} gel (Bio-Rad). For crude and soluble extract 20 µg of protein were loaded into the wells, whereas for the purified protein, 4 µg were loaded. The Color Prestained Protein Standard, Broad Range from NEB was used for size estimation. Electrophoresis was performed at constant 110 V for 45-60 min in SDS running buffer.

Table 12. Buffers and solutions for SDS-PAGE

Buffer	Component	Final concentration
5x SDS-PAGE Sample Buffer	Distilled H_2O	Up to 8.1 mL
	0.5 M Tris-HCl (pH 6.8)	62 mM
	Glycerol	10 % (v/v)
	10% SDS	2% (v/v)
	β-mercaptoethanol	5 % (v/v)
	1 % bromophenol Blue	0.05 % (v/v)
10x SDS Running Buffer	Tris base	30 g/L
	SDS	10 g/L
	Glycine	14.2 g/L
	Adjusted with distilled H_2O	-
Coomassie Staining Solution	Coomassie Brilliant Blue G-250	0.08 mg/mL
	37% HCl	0.3 % (v/v)
	Adjusted with distilled H_2O	
Destaining Solution	Millipore water	-

After electrophoresis, gels were washed in distilled water three times during 5 min. In between each washing-step, gels were heated 30 s in the microwave. Coomassie Staining Solution was added to gels and incubated under mild agitation at room temperature until bands became visible. For destaining, gels were incubated overnight in water.

2.4.6 Western blot analysis

Buffers and solutions are listed in Table 13. After SDS-PAGE, gels were transferred to nitrocellulose membranes using the Trans-Blot Turbo Transfer System from Bio-Rad according to the manufacturer's instructions. After transfer, the nitrocellulose membranes were incubated briefly in Ponceau S solution to verify blotting. The membrane was washed under running water. Detection of Strep-tag®II was performed with an antibody conjugated with alkaline phosphatase (Strep-Tactin® AP, IBA), following the protocol for Western Blot with Strep-Tactin® or StrepMAB conjugates from IBA Lifesciences GmbH. For detection of His6-tagged proteins, the same procedure was used, changing the antibody to the 6x-His Tag Monoclonal Antibody with AP (Invitrogen ™). Briefly, the nitrocellulose membrane was incubated under gently agitation in 20 mL of TBS-blocking buffer for 1 h at room

temperature or overnight at 4 °C. The membrane was washed 3 times with TBS-Tween buffer for 5 min at room temperature under agitation. After the last washing, the membrane was incubated with 10 mL of TBS-Tween buffer and 2.5 µL of the corresponding antibody under gently agitation for 1 h at room temperature. Antibody excess was removed by washing 2 times with TBS-Tween buffer for 1 min at room temperature in agitation, and two additional times with TBS buffer for 1 min at room temperature under agitation. The membrane was revealed with 30 ml of reaction buffer, 10 µL NBT solution and 60 µL BCIP in the dark without shaking until bands were visible. The reaction was stopped by washing several times with distilled water.

Table 13. Buffers for Western blot. Protocol from IBA.

Buffer	**Components and Concentration**
TBS buffer	50 mM Tris/HCl, pH 7.4 140 mM NaCl
TBS-blocking buffer	TBS buffer 3% BSA 0.1% w/v Tween 20
TBS-Tween buffer	TBS buffer 0.1% w/v Tween 20
Reaction buffer	100 mM Tris/HCl, pH 8.8 100 mM NaCl 5 mM MgCl2
NTB	7.5% w/v nitrotetrazolium blue in 70% v/v dimethylformamide
BCIP	5% w/v 5-bromo-4-chloro-3-indolyl-phosphate in dimethyl-formamide

2.4.7 Enzymatic assay with soluble extract and purified proteins

The assay was carried out using 3 mL quartz cuvettes from Hellma Analytics, with a final reaction volume of 2 mL. Activity Buffer (50 mM K_iPO_4, pH 7) was warmed at 30 °C and added to the cuvette along with 0.5 mM of NADH as cofactor. Cuvettes were sealed with rubber stoppers. Spectrophotometric lectures were carried-out using the Cary 60 UV-Vis (Agilent) at 30 °C at 365 nm.

When analyzing soluble extract, the activity buffer and the cuvette containing the reaction mixture were first gassed with N_2 using a needle to create semi-anaerobic conditions. A second needle was use for gas-release. After gassing for a few minutes, the gas-releasing needle was removed, the cuvette was place on the Cary 60, and the measurement was started. Different volumes of soluble extract were tested (50, 100, 200 and 400 µL) during IRED activity assays to determine reaction saturation (SupplementarySupplementary A. -Materials and Methods,Figure S. 1). Volumes below the saturation were used, typically 50, 100 or 200 µL. After 1-2 minutes, the soluble extract was added to the cuvette and the reaction was followed. Between minute 2-3 10 mM of the corresponding substrate was added and the cofactor consumption was measured during 20-30 min at 365 nm.

For purified proteins no N_2 gassing was needed and 0.1, 0.2, 0.4 and 0.8 µM of enzyme were tested.

Slopes were measured with the Cary WinUV Software, in the linear region of the curve during the 30 s after addition of each component. Negative slopes are considered as substrate decreases over time. The slope was used to calculate an apparent specific activity for soluble extract (NADH-oxidoreductase activity), or specific activity for purified proteins. When analyzing soluble extract, the NADH-oxidoreductase activity of each sample was calculated using the difference between slopes: the slope obtained after adding the soluble extract was considered as background activity of native *C. necator* oxidoreductases, and it was subtracted from the slope obtained after substrate addition. When analyzing purified proteins, the slope after substrate addition was used directly for calculations.

Specific activities were calculated according to the formula:

$$Specific\ Activity = \frac{Slope \times Vol_{total}}{Vol_{enzyme} \times c_{enzyme} \times \varepsilon_{NADH} \times l}$$

Where:

Slope (min^{-1}): slope directly recorded using the Cary WinUV Software.
Vol_{total} (µL): total volume reaction (2,000 µL)
Vol_{enzyme} (µL): volume of soluble extract or purified protein used in the test.
C_{enzyme} (mg/mL): concentration of soluble extract or purified protein, determined from BCA assay.
l (cm): optical pathway of the cuvette (1 cm)
ε_{NADH} at 365 nm: 3.3/mM x cm

Chapter 5 Analytical methods

2.5.1 Gas chromatography

C. necator supernatant samples were collected during gas fermentations to analyze biotransformations. From each sample, 200 µL of supernatant was transferred to a clean 1.5 mL Eppendorf tube, and 20 µL 10M NaOH was added. Derivatization was performed by adding 220 µL of derivatization mix (1 M acetic anhydride in dichloromethane). The samples were vortexed for 1 min and centrifuged 2 min at 14 000 g in a benchtop centrifuge. The lower phase was extracted and transferred to a clean GC-vial with insert.

Serial dilutions from commercially available pyrrolidine products were made ranging from 0-10 mM. These solutions were used as standards and treated in the same way as supernatant samples for derivatization and extraction. Samples and standards were injected in a gas-chromatography instruments. Standards were used to establish calibration curves and calculate the product concentration in *C. necator* samples.

Detection and quantification of 2-methylpyrrolidinewas conducted on ThermoScientific™ Trace™ GC Ultra instrument coupled with a flame ionization detection (FID). The apolar Zebron ZB-5ms column was used with a constant flow of 1 or 2 ml/min. Helium was used as a carrier gas (35 mL/min). The injector temperature was 250°C and the split mode was used with a split flow 10 ml/min. Program is described in Table 14.

Table 14. Oven temperature program for GC-FID.

Rate [°C min^{-1}]	Final temperature [°C]	Hold [min]
0	100	3
5	170	0
50	280	0

Additionally, detection 2-methylpyrrolidinewas conducted on a Thermo Scientific GC coupled with mass spectrometer (MS), using an Agilent VF-5MS column (30 m × 0.25 mm × 0.25 µm) with hydrogen as a carrier gas (30 cm s-1). The injector temperature was set to 250 °C and the detector temperature was set to 330°C. The injection volume of the auto sampler was set to 1 mL and a spitless mode was used. Oven program is shown below in Table 15.Table 15. Oven temperature program for 2-methyl

Table 15. Oven temperature program for 2-methyl pyrrolidine in GC-MS.

Rate [°C min^{-1}]	Final temperature [°C]	Hold [min]
-	100	1
40	150	-
2,5	170	-
20	200	-
50	260	2

Quantification and peak integration were done with the software Chromaleon 7.2.

2.5.2 Cytometry

A BD Accuri C6® flow cytometer (BD Biosciences BD Biosciences, Franklin Lakes, NJ, USA) was used for measurements of cellular morphology and membrane integrity via propidium iodide staining. The device was equipped with blue (488 nm) and red (640 nm) excitation lasers. Light scatter was collected from two angles: forward (FSC: 0° ± 13) and side (SSC: 90° ± 13) scatter. FSC and SSC signals are

respectively correlated to cell size and granularity. The width (duration or time of flight) of the pulse from the forward scatter light was also analyzed in order to estimate the length of cells. Fluorescence intensity was measured by four detectors (Photomultipliers/PMT): FL1 (533 ± 30 nm), FL2 (585 ± 40 nm), FL3 (>670 nm), and FL4 (675 ± 25 nm) bandpass/long pass optical filter/photomultiplier detector systems. Propidium iodide (PI) (Molecular probes, Invitrogen, USA) was used to evaluate membrane permeability. Commercial solution of 1mg mL^{-1} Propidium iodide (PI) in water (Molecular probes, Invitrogen, USA) was used to evaluate membrane permeability. First, culture samples were diluted in NaCl 0.9% to reach approximately a cell concentration of 10^6 cells mL^{-1}. Then, cells were stained by 2 µL of PI working solution and incubated for 20 min at room temperature in the dark. A 100 % permeabilized–cell control was prepared by incubating cells in 70 % isopropanol for at least 1 h at room temperature. Sample runs were performed at the slow flow-rate setting (14 µL/min) using Milli-Q grade water (18.2 mΩ-cm resistance) as sheath fluid. For all sample analysis, the FSC signal (threshold: 12, 000) and SSC signal (threshold: 2, 000) were used as trigger channels. Data acquisition was performed with BD Accuri CFlow® software and data processing was achieved with FlowJo software (Becton Dickinson, Sparks, MD, USA).

Chapter 6 *In silico* analysis and software.

Genome alignments and homologous gene searches were performed using National Center for Biotechnology Information (NCBI) Blastn services (Altschul et al., 1990; Camacho et al., 2023). The SnapGene software was used for in-silico plasmid construction and sequencing analysis. Protein sequences were obtained from UniProt data base. Genome and protein data were searched in the Kyoto Encyclopedia of Genes and Genomes data base (KEGG) (Kanehisa, 2019; Kanehisa et al., 2025; Kanehisa & Goto, 2000). Protein searches were performed using the NCBI Blastp service (Camacho et al., 2023; Mahram & Herbordt, 2015). Protein structures were generated using Chimera (Pettersen et al., 2004) or retrieved from RCSB Protein Data Bank (RCSB PDB) (Berman et al., 2000).

In-silico analysis of protein-protein interaction and modelling was executed through the HDOCK server (Y. Yan et al., 2020). Models were assessed with the Confidence Score determined in the server.

The software GraphPad Prism 8.0.2 and Origin 2024 were used for data treatment, statistical analysis and graph design.

Artificial intelligence (AI) tools were used in the manuscript: ChatGPT was used for text edition, grammar correction, and overall text cohesivity. Research Rabbit, ORKG Ask and Perplexity were used for expanding bibliography research.

Figures from article sources were reproduced with permission, and licenses were obtained through Rightslink® by Copyright Clearance Center. (Lauterbach et al., 2013, license number 6040301289918) (Brigham et al., 2013, license number 6035351000657) (Lauterbach & Lenz, 2019, license number 6030330701642).

Section 3: Results and Discussion

Chapter 1: *C. necator* produces heterologous oxidorreductasas.

This section was performed at RWTH Aachen University, with the participation of the following people:

- **I.A. Castro González**: strain development and testing, sample and data analysis.
- C. Kunth: Bachelor student under I.A. Castro-Gonzalez supervision, Bachelor thesis on putative novel IREDs in *E. coli*, strain transformation and analysis of enzymatic activity in model substrate and bulky *N*-heterocycles.
- D. De la Asunción Vest: Bachelor student under I.A. Castro-Gonzalez supervision, Bachelor thesis on the expression and production of PuOx in *C. necator,* strain development with diverse genetic strategies and evaluation of protein production.
- P. Schoenmakers: PhD student, development of Δlon strain.

Oxidoreductases are enzymes that catalyze redox reactions by transferring electrons from an electron donor (reducing agent) to an electron acceptor (oxidizing agent). They represent a broad and diverse class of enzymes (Enzyme Commission number EC 1) with numerous subclasses and biological functions. Due to their versatility, oxidoreductases have gained increasing attention as biocatalysts for developing sustainable and selective pathways in the chemical industry. Oxidoreductases from different organisms have been applied in sectors such as pharmaceuticals, dyes, polymers, and agrochemicals, and numerous examples have been described elsewhere (Espina et al., 2021; Martínez et al., 2017b).

Among oxidoreductases, putrescine oxidases (PuOx) and imine reductases (IREDs) have been explored for the production of *N*-heterocycles, valuable intermediates in pharmaceutical production. Engineered variants of both enzymes have been successfully applied in biocatalytic cascades. In *E. coli*, *in vivo* production of *N*-heterocycles was achieved using the $PuOx_{M1}$ variant from *R. erythropolis*, optimized to accept larger diamine substrates, in combination with an a R-selective IRED from *S. roseum* (Borlinghaus et al., 2019). Al-Shameri et al. (2019) later demonstrated an *in vitro* system using the variant $PuOx_{E203G}$, and the IRED from *S. roseum*, coupled to an engineered NADPH-dependent soluble hydrogenase from *C. necator* for cofactor regeneration (Preissler et al., 2020). This system was later expanded into an electrolysis platform that combined an engineered NADH-dependent IRED from *M. stipitatus* ($IRED_{V8}$) (Borlinghaus & Nestl, 2018) with the NADH-soluble hydrogenase from *C. necator* (SH) (Al-Shameri et al., 2020).

This work aimed to establish a new enzymatic cascade into a whole-cell system using the lithoautotrophic bacterium, *C. necator.* Specifically, we focused on incorporating the heterologous oxidoreductases, $PuOx_{M1}$ and $IRED_{V8}$, into *C. necator'*s metabolism for the biotransformation of diamine substrates towards *N*-heterocycles. This strategy integrates our broader objective of establishing *C. necator* as microbial-cell factory using its native SH for *in vivo* NADH regeneration under autotrophic conditions

In Chapter 1, we focused on the individual production and characterization of $IRED_{V8}$ and $PuOx_{M1}$ in *C. necator*. These engineered enzymes were cloned into the host strain, and their heterologous production was evaluated using different genetic strategies

Subchapter 3.1.1 describes the heterologous expression of $IRED_{V8}$ and efforts to enhance its production through co-expression with the chaperonin GroESL and deletion of the Lon protease. We analyzed the effect of these modifications in two genetic backgrounds: the wild-type *C. necator* H16 strain and the Δ*lon* mutant. We further assessed IRED activity in both the soluble extract and purified protein

In Subchapter 3.1.2 , we applied a similar approach to $PuOx_{M1}$. We studied protein production in two different *C. necator* backgrounds, wild-type and Δ*lon* mutant. In addition, we evaluated the effect of varying culturing conditions on $PuOx_{M1}$ production and purification.

3.1.1 *C. necator* produces an active NADH-dependent Imine Reductase ($IRED_{V8}$).

Borlinghaus & Nestl (2018) engineered the enzyme $IRED_{V8}$ from *M. stipitatus* by shifting its native cofactor specificity from NADP(H) to NADH. This modification makes $IRED_{V8}$ a suitable candidate for interacting with the soluble hydrogenase (SH) in *C. necator*, facilitating the establishment of our desired enzymatic cascade in whole-cells. In this cascade, $IRED_{V8}$ oxidizes NADH to NAD^+, and SH reduces NAD^+ into NADH using H_2, thus continuously regenerating the cofactor required for the IRED reaction. By utilizing NADH as a cofactor, we directly coupled the reaction to the SH without involving transhydrogenases, which typically convert reversibly NADPH to NADH. Although transhydrogenases in *C. necator* play a role in maintaining the cellular redox balance by facilitating the transfer of reducing equivalents between NADH and $NADP^+$, its precise mechanism and function remain not fully understood (Lauterbach & Lenz, 2019; Morlino et al., 2023). In contrast, the SH is a widely-studied enzyme and its application as a cofactor regeneration system *in vitro* and coupled with whole-cell was previously proven (Andersson et al., 1998; Ratzka et al., 2011; Holzer et al., 2015; Lonsdale et al., 2015). For these reasons, we first focused our efforts in investigating $IRED_{V8}$ production in *C. necator*, to later understand its interaction in the enzymatic cascade through SH.

3.1.1.1 $IRED_{V8}$ production: *in -silico* analysis between GroESL and $IRED_{V8}$.

The GroESL protein complex, composed of the molecular chaperones GroEL and GroES, belongs to the chaperonin class of the heat shock protein family (HSP60 and HSP10, respectively). This complex has emerged as a critical tool to enhance the robustness and productivity of microbial platforms for biotechnological applications. Studies across various bacterial systems have demonstrated its role in improving stress tolerance, extending metabolic activity, and boosting product yields. In *E. coli*, overexpression of GroESL improved tolerance to several alcohols leading to an increase growth under ethanol stress (Zingaro & Papoutsakis, 2013). Similarly, in *Clostridium acetobutylicum,* this strategy

increased solvent production through transcriptional and metabolic changes which resulted in higher tolerance to butanol and accelerated adaptation in further solvent growth (Mann et al., 2012; Tomas et al., 2003). Protection against other stressor elements such as heat-shock treatments and high salt concentrations were also improved by overexpressing GroESL in *Lactococcus lactis* and *Lactobacillus paracasei* (Desmond et al., 2004).

Building from these examples of GroESL's improving stress tolerance and productivity across various bacterial systems, we aimed to evaluate the effects in *C. necator*. We adopted a strategy inspired by the work of Marc et al. (2017), who overexpressed the native *groEL* and *groES* genes from *C. necator* in an isopropanol-producing strain. In their study, GroESL overexpression had two effects. From one side, the strain presented an improved tolerance towards exogenous isopropanol. From the other side, GroESL overexpression led to higher specific enzymes activities of the heterologous enzymes acetoacetate decarboxylase (ADC) and alcohol dehydrogenase (ADH), which redirected the carbon flux towards isopropanol and ultimately increased isopropanol yields.

We firstly hypothesized that GroESL could directly participate in the folding and stability of $IRED_{V8}$, improving its specific activity, and overall functionality. GroESL is typically known to assist the folding of proteins of a size between 20 to 60 kDa (Hartl, 1996; Horwich et al., 1993; Martin et al., 1992; Sigler et al., 1998; Viitanen et al., 1992). The active dimer of IRED being around 60 kDa, is close to this upper limit. However, studies have demonstrated that GroESL is also able to accommodate proteins larger than 80 kDa *in vivo* (Dubaquié et al., 1998; Houry et al., 1999), with other examples reported in literature exceeding the size of the inner chaperonin cavity (Marchenkov & Semisotnov, 2009).

To explore a possible interaction between IRED and GroESL, we first conducted an *in-silico* analysis using the HDOCK server as docking software (Y. Yan et al., 2020). Initial challenges arose due to the size of the protein complexes, particularly from GroEL. GroEL is a homo-oligomer composed of two rings, each containing 7 subunits, with each subunit having theoretical mass of approximately 57 kDa (Braig et al., 1993, 1994; Saibil & Ranson, 2002). To address this, the complexes were divided into smaller portions to facilitate the docking process. The monomeric form of $IRED_{V8}$ was paired with a segment of GroEL, as the GroEL rings form the cavity that enters in contact with the unfolded protein (Horovitz & Willison, 2005; Saibil et al., 2013). A representation of the full GroESL multimer is represented in Figure 15.

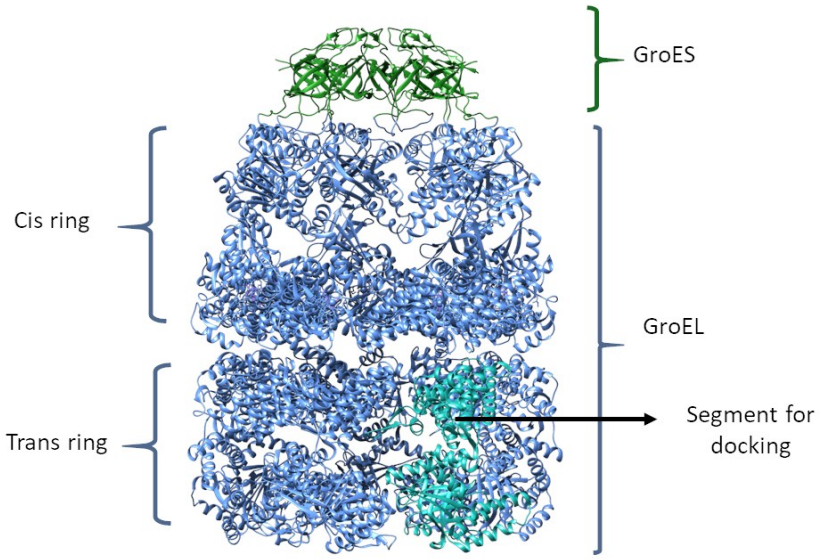

Figure 15. GroESL complex : GroES is depicted in green, while GroEL oligomer is dark blue. A segment of the GroEL ring was selected for the docking study and it is highlighted in lighter color. The structure is generated using Chimera (Pettersen et al., 2004) from the crystal structure of groEL-groES of *E. coli* (PDB 1PCQ; Chaudhry, 2003).

The HDOCK server generated multiple models, with the highest-confidence model presented in Figure 15. The model with the highest scores contained a docking score of -245.02, and a confidence score of 0.869. According to HDOCK metrics, a negative docking score indicates a higher possibility for the proteins to bind, while confidence scores above 0.7 empirically reflects that the two molecules are very likely to bind. Based on these criteria, a potential interaction between $IRED_{V8}$ and the interior of the GroEL segment is suggested. To further assess this interaction, the dimensions of $IRED_{V8}$ and the GroEL cavity were compared. The inner cavity of GroEL has a diameter of 45 Å, and the total height of the GroEL homo-oligomer is 145 Å (Marchenkov & Semisotnov, 2009) (Figure 17, A); while $IRED_{V8}$ dimensions were measured at 38.5 Å in diameter, and 90.5 Å in height (Figure 17, B). Considering these estimations and that the proteins usually enter one of the GroEL oligomers at a time, the folded structure of $IRED_{V8}$ could partially fit within one of GroEL's rings. A potential interaction between GroESL and $IRED_{V8}$ may contribute to improved folding and stability during the heterologous production in *C. necator*.

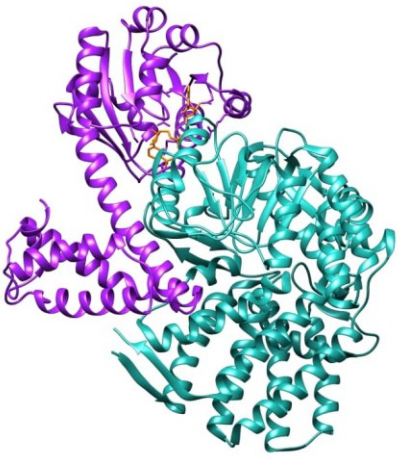

Figure 16. IRED monomer and a segment of GroEL interact in a docking model : The interaction between the monomer of $IRED_{V8}$ (purple protein) and a segment of GroEL (blue protein) is modeled with HDOCK server with a confidence score of 0.8699. NAD^+ cofactor is represented in orange.

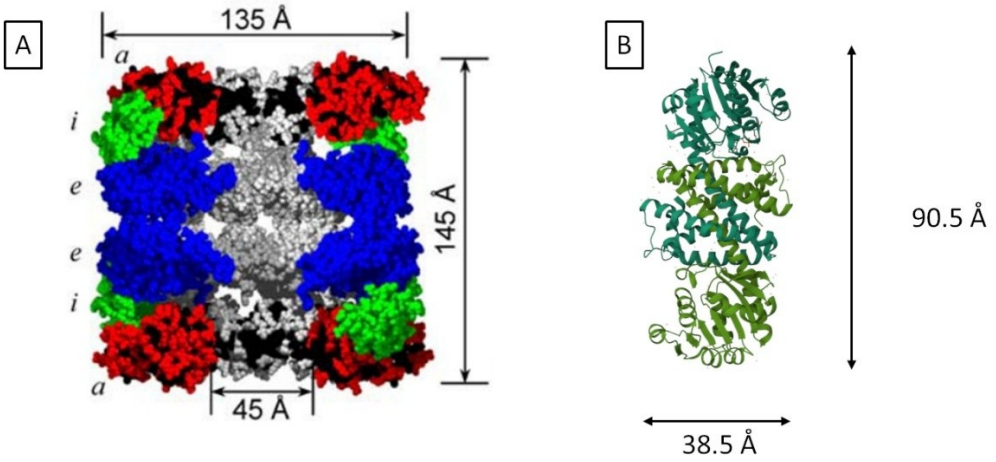

Figure 17. Dimensions of GroEL and IRED : Crystal structure with calculated measurements of GroESL; the image is obtained from the analysis of Marchenkov & Semisotnov (2009) on the PDB structures 1OEL and 1AON (A). Crystal structure of $IRED_{V8}$ (B), distances between atoms are calculated using Chimera (Pettersen et al., 2004) from the PDB structure 6TOE (Stockinger et al., 2021).

However, it is important to note that the docking model and the $IRED_{V8}$ dimensions obtained through *in-silico* analysis provided only a preliminary indication of a hypothetical interaction. The predictions are limited by the use of isolated IRED and GroEL monomers, which do not account for the overall protein complex with GroES; possible steric hinderance between the structures; or the specific mechanisms governing GroESL activity. Therefore, *in vivo* experimentation was essential to confirm these observations.

The plasmids containing $IRED_{V8}$ and GroESL were transformed into *C. necator* to evaluate the *in vivo* effect of chaperonin overexpression in *C. necator* cells. The $ired_{V8}$ gene was previously cloned under a rhamnose-inducible promoter in the broad-host pKR plasmid, and transformed into the wild-type *C. necator* H16, resulting in strain lls365 (pAA56 plasmid, Figure 18, Supplementary B.1 $IRED_{V8}$ production in *C. necator.*). The groESL operon was provided on the pEG19 plasmid from the laboratory of S. Guillouet (Figure 19) and transformed into *C. necator* with different genomic background. The results of protein production will be discussed in detail in the following chapters

3.1.1.2 $IRED_{V8}$ production: Combining GroELS, $IRED_{V8}$ and Δlon *in vivo*.

To further optimize $IRED_{V8}$ production, we investigated another key regulator of protein stability and degradation: the Lon protease. The Lon protease is a highly conserved ATP-dependent serine peptidase, which regulates the cell homeostasis. It primarily degrades misfolded or damaged proteins, and exhibits chaperon-like activity. (Gottesman, 1996; I. Lee & Suzuki, 2008; Phillips et al., 1984). First identified in *E. coli* by Chung & Goldberg (1981) , Lon protease has been extensively studied for its regulatory functions and effects in protein production. Strains like *E. coli* BL21 and BL21(DE) (Studier & Moffatt, 1986) lack of Lon protease and are routinely used for the production of recombinant proteins. Following a similar approach and obtain higher expression levels of heterologous proteins, the Lon protease from *C. necator* H16 was deleted, resulting in the Δlon strain (P. Schoenmakers, personal communication, 2022). To the best of our knowledge, this represents the first reported deletion of the Lon protease in *C. necator*. This modification aimed to decrease proteolytic degradation and enhance heterologous protein stability.

In this context, $IRED_{V8}$ was cloned in a pKR-broad host plasmid backbone (Figure 18, Al-Shameri 2021, personal communication).The plasmid was transformed in the wild-type *C. necator* H16 (WT) and Δlon, obtaining the strains *C. necator* x pAA56 (WT + IRED) and Δlon x pAA56 (Δlon +IRED).

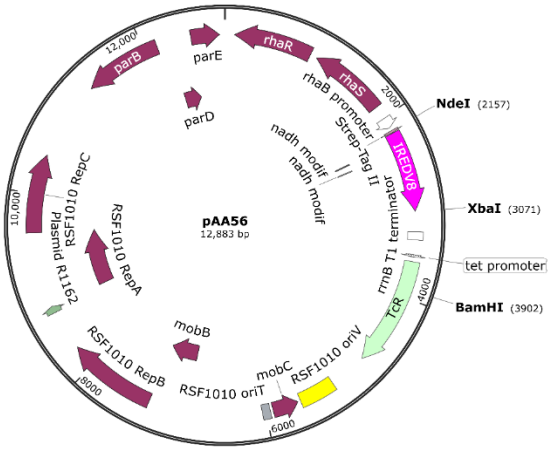

Figure 18 Plasmid map pAA56 containing $IRED_{V8}$. Plasmid was constructed by Al-Shameri 2021, personal communication. Strep-tag II is used. Some restriction enzymes with one recognition site are shown. Plasmid maps is generated with SnapGene®.

The plasmid pEG19, containing the groESL operon was obtained from S. Guillouet lab (Figure 19) and co-expressed in WT and Δlon genetic backgrounds, resulting in the strains: *C. necator* x pAA56 x pEG19 (WT + IRED + GroESL), and Δlon x pAA56 x pE19 (Δlon + IRED + GroESL). This combined strategy was designed to maximize the complementary roles of GroESL and Lon protease: GroESL promotes proper folding and prevents aggregation, while the absence of Lon protease minimizes proteolytic degradation. Together, these modifications were expected to improve $IRED_{V8}$ folding and stability, ultimately enhancing its performance in the enzymatic cascade and maximize product yield.

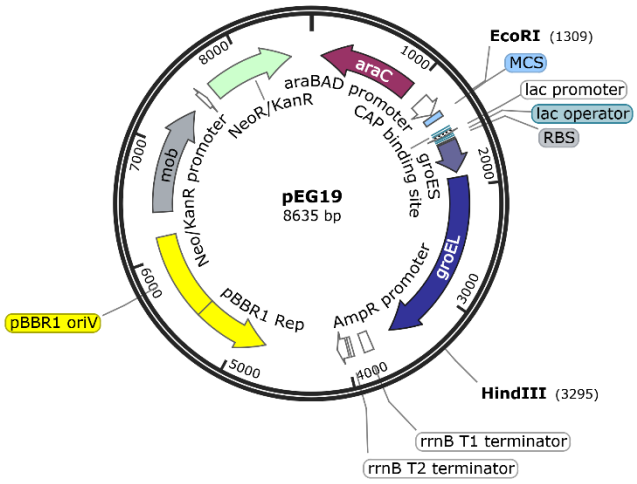

Figure 19 Plasmid map of pEG19 (Marc et al., 2017). Restriction sites for EcoRI and HindIII are indicated. Plasmid maps is generated with SnapGene®.

Preliminary genetic confirmations were performed through PCR by amplifying the rhamnose-inducible system along with the *ired* gene from the pAA56 plasmid. The plasmid was directly extracted from the strain WT + IRED (Figure 21, A). Multiple colonies from each transformation were screened and clones showing a band at the expected size around 2.9 kb were selected for further analysis (Figure 20 A-C, arrows). An additional colony-PCR was conducted to verify the genetic background in the colony 14-Δlon +IRED, and colony 16-Δlon + IRED + GroESL. The presence or deletion of the *lon* gene was assessed by an amplification of the locus. The intact *lon* locus produced a band of 2.5 kb, as observed in the WT strain (Figure 21, A), while a deletion resulted in a shorter band of 820 bp (indicated by the arrows).

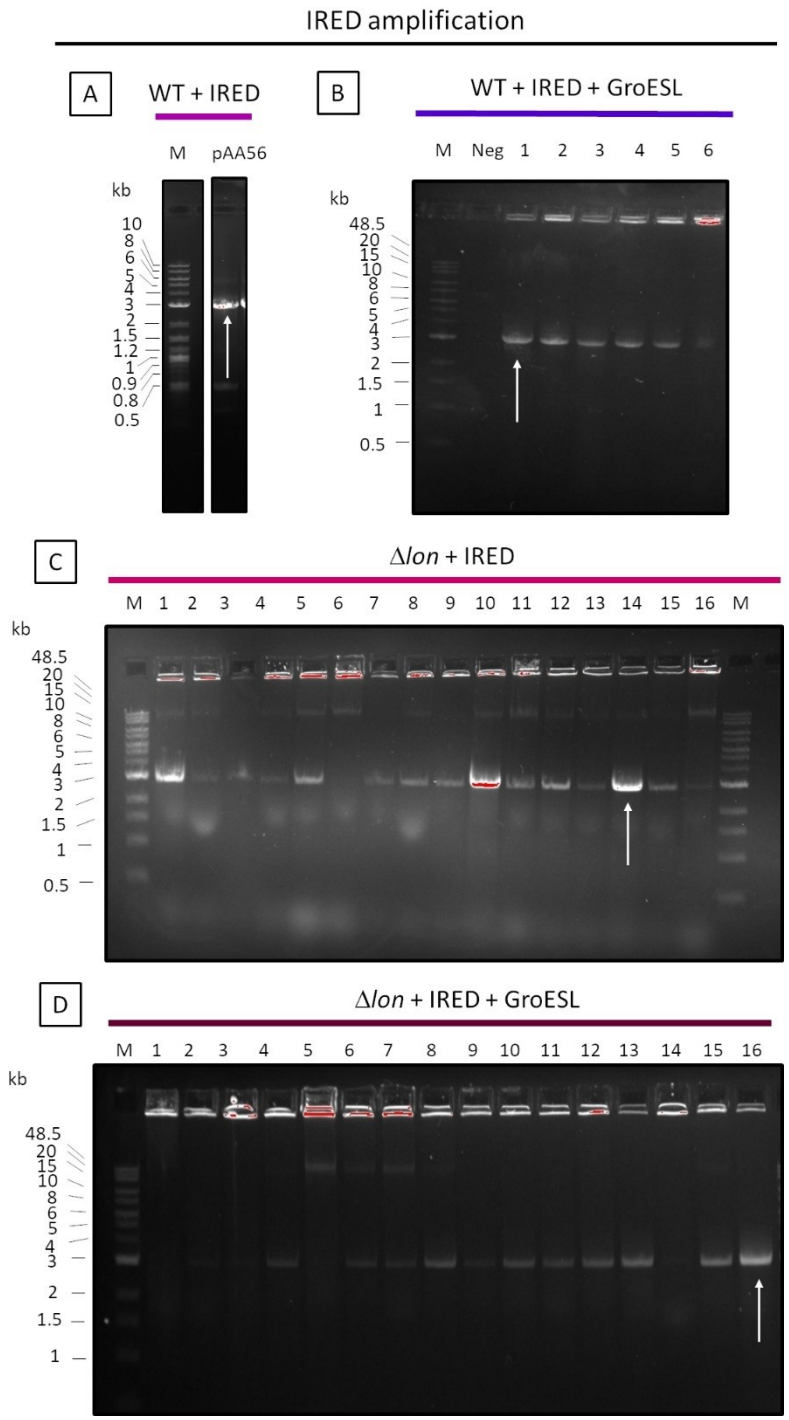

Figure 20. IRED$_{V8}$ amplification in transformed *C. necator* colonies : Presence of *ired* is evaluated by amplifying the rhamnose promoter with *ired* containing the Strep-tag II in the different strains. The segment is amplified by PCR from the extracted plasmid, pAA56, of the strain WT + IRED (A). Colony-PCR is used for screening in the transformations of WT + IRED + GroESL (B), Δlon +IRED (B), and Δlon + IRED + GroESL (C). A band of 2962 bp is expected, selected colonies are indicated by the arrows. (M: Molecular weight of DNA ladder; Neg: negative PCR control without colony; WT + IRED + GroESL: *C. necator* x pAA56 x pEG19; Δlon +IRED: Δlon x pAA56; Δlon + IRED + GroESL: Δlon x pAA56 x pE19)

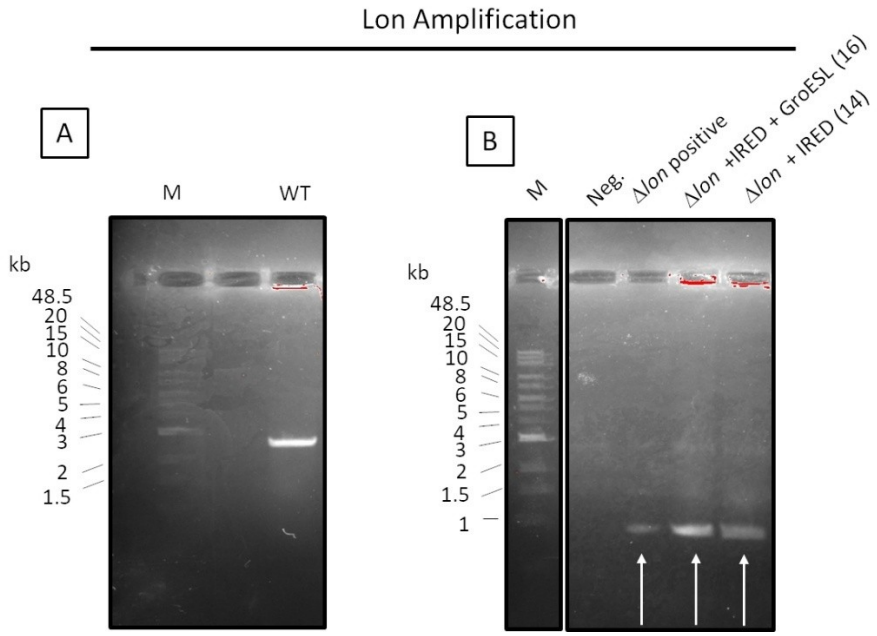

Figure 21. Amplification of Lon protease on selected Δlon transformants : presence of the *lon* gene is verified with a PCR amplification on the strains WT (A); colony 14 of Δlon +IRED transformation and colony 16 of Δlon + IRED+ GroESL transformation (B). A band at 2527 bp is expected for a wild-type *lon* gene, a truncated version of the gene is confirmed with a shorter band at 820 pb (indicated by the arrows) (M: marker, WT: *C. necator* H16, Neg: negative PCR control without colony, Δlon is used as positive control, Δlon +IRED: Δlon x pAA56, Δlon + IRED + GroESL: Δlon x pAA56 x pE19).

The transformed strains, with or without the pEG19 plasmid, were cultivated under heterotrophic conditions using the minimal media FN. This approach allowed us to assess the effects of GroESL overexpression and Lon protease deletion on $IRED_{V8}$ production in a cellular context and to evaluate the predictions from the *in-silico* analysis. Although growth characterization was not performed during these specific tests, some phenotypic traits were empirically observed among the strains. Notably, the precultures of Δlon transformants presented a turbid culture around 16 h, before the WT showed any growth.

For the protein evaluation, the soluble extract of a wild-type *C. necator* H16 strain (WT) was used as a control. In Figure 22 we observed the IRED production for each strain, where 30 µg of total protein was loaded into SDS-PAGE and Western blot. The strain *C .necator* + IRED showed the presence of a band around the expected size for the IRED monomer (35 kDa) corresponding to previous observations (Borlinghaus & Nestl, 2018, Fig. S10). Comparison between the soluble extract of WT and WT + IRED indicates that the protein is only present in the transformed strain (Figure 22, B). The band appears very faint in the SDS-PAGE and is only detectable in the Western blot. Although the same amount of total protein was loaded, the lane in the sample appears more intense in the strain Δlon + IRED. Most likely this is due to an error during the BCA quantification and the concentration for this particular sample was underestimated.

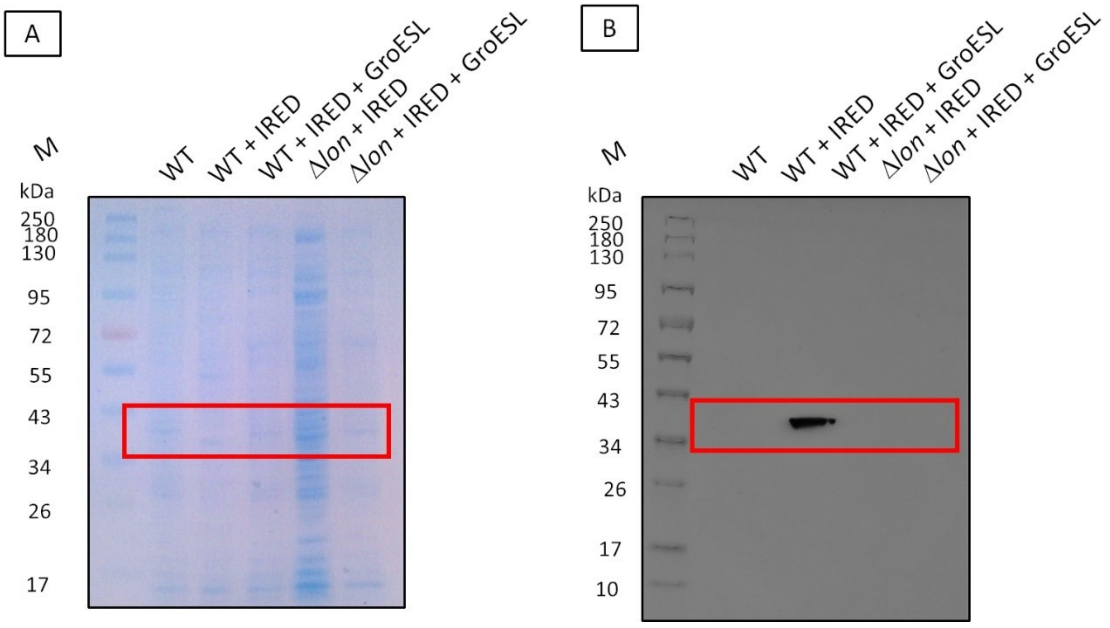

Figure 22. $IRED_{V8}$ is produced in *C. necator* : The soluble extract of 5 strains are analyzed using SDS- Page (A) and Western blot (B), the $ired_{V8}$ gene is fused in N-terminal with a Strep-tag II and revealed with Strep-Tactin® AP. A band corresponding to the IRED monomer is expected at 35 kDa (indicated in red). For each strain, 30 µg of total protein is loaded in the gel. (M: molecular weight of the protein ladder; WT: *C. necator* H16; WT + IRED: *C. necator* x pAA56; WT + IRED + GroESL: *C. necator* x pAA56 x pEG19; Δlon +IRED: Δlon x pAA56; Δlon + IRED+ GroESL: Δlon x pAA56 x pE19).

The enzymatic $IRED_{V8}$ activity was evaluated in the soluble extract using a spectrophotometric assay, where the NADH oxidation was monitored as an indicator of imine reduction. During the enzymatic test, the native oxidoreductases in the soluble extract of *C. necator* interact with the NADH present in the cuvette. After a short time, the reaction stabilizes, and 10 mM of an imine molecule is introduced. In this case, 2-methylpyrrolidinewas used as a suitable substrate for IRED. Once this imine is added, a substantial diminution of NADH is expected, which corresponds to the interaction between the substrate, IRED and the cofactor. The WT strain is included as a negative control to compare the activity of the oxidoreductases natively present in *C. necator*. Two volumes of soluble extract (200 and 400 µL) were tested for each strain, in triplicates. The reaction with 200 µL is illustrated in Figure 23. Following the imine addition, a considerable decrease in the absorbance was observed in WT + IRED compared to the control WT the strain. This suggested that the strain WT + IRED contains an active NADH-dependent enzyme and is oxidizing the cofactor. The remaining strains did not present this behavior, and their enzymatic kinetics was similar as the WT.

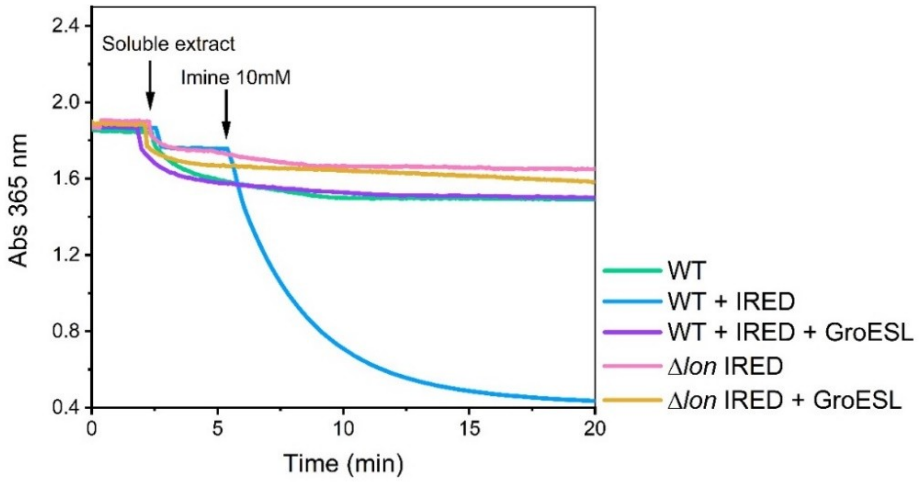

Figure 23. Sample trace activity in the soluble extract of *C. necator* strains : Kinetic data from one replicate of 200 µL of soluble extract. Cofactor oxidation is followed spectrophotometrically at 365 nm for 20 min. The arrows indicate the addition of 200 µL of soluble extract and 10 mM of 2-methyl-1-pyrroline, respectively. The slopes are measured in the linear region of the curve during the 30 s following the addition of each component. The test was performed in 50 mM $KiPO_4$ buffer with 0.5 mM of NADH as cofactor. The cuvette test containing the samples are gassed with N_2 prior the start of the experiment to limit the activity of other oxidoreductases contained in the soluble extract. For activity calculations, the slope is taken during the first 30 s after the addition of the soluble extract and the imine. (WT: *C. necator* H16; WT + IRED: *C. necator* x pAA56; WT + IRED + GroESL: *C. necator* x pAA56 x pEG19; Δlon +IRED: Δlon x pAA56; Δlon + IRED+ GroESL: Δlon x pAA56 x pE19).

The NADH-oxidizing activity of each sample was calculated using the difference between slopes: the: t: t slope obtained after adding the soluble extract was considered as background activity of native *C. necator* oxidoreductases, and it was subtracted from the slope after addition of the imine. This corrected value allowed us to isolate the specific contribution of the imine reductase reaction, and was used to calculate the activity. For the strain WT + IRED, an activity of 88 ± 0.004 mU/mg protein was observed when 200 µL of soluble extract was used, whereas no activity was detected in the other strains (Figure 23).

The activity results in soluble extract, along with the SDS and Western blot, indicated that the production of $IRED_{V8}$ in *C. necator* was achieved in the strain WT + IRED (Figure 22 - Figure 23). In contrast, no detectable protein production was observed in the remaining strains, correlating with the absence of activity during the enzymatic assay. For the strains containing GroESL, we could not confirm the overexpression of GroESL by Western blot, as no affinity tag was present on this protein.

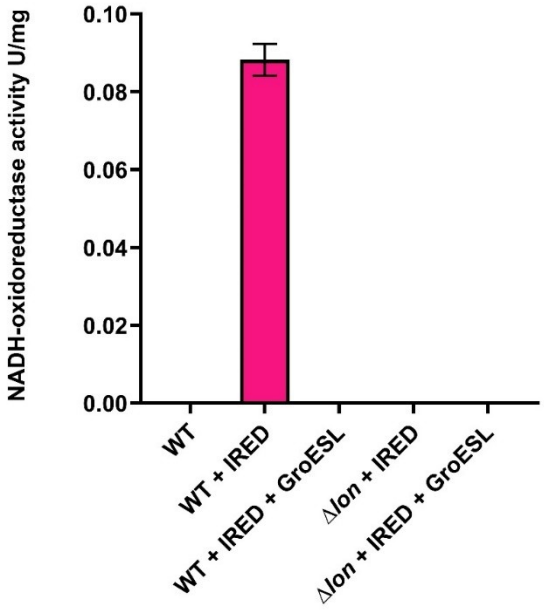

Figure 24. The soluble extract of WT+ IRED oxidizes NADH : The NADH-oxidoreductase activity was evaluated in the soluble extract of the different *C. necator* strains. Means of triplicates are used for all the strains, with the exception of WT + IRED, where duplicates are used. For the soluble extract 200 µL of soluble extract is used. Error bars indicate standard error of the mean (SEM). (WT: *C. necator* H16; WT + IRED: *C. necator* x pAA56; WT + IRED + GroESL: *C. necator* x pAA56 x pEG19; Δlon +IRED: Δlon x pAA56; Δlon + IRED+ GroESL: Δlon x pAA56 x pE19).

The absence of $IRED_{V8}$ production in the strains WT + IRED + GroESL, Δlon +IRED, and Δlon + $\mathrm{IRED_{V8}}$ + GroESL may be attributed to bottlenecks at various levels, including the genetic construction. During the strain construction, antibiotic selection was used to verify the presence of the plasmids in the transformed colonies: 10 µg/mL tetracycline for pAA56 (*ired*-containing plasmid), and 600 µg/mL kanamycin for pEG19 (*groesl*-containing plasmid). Although the colonies grew under the selective pressure, and PCR amplifications were confirmed (Figure 21 and Figure 22), protein production was not detected in the cultivations (Figure 22). To investigate the causes of this disruption, other techniques could be used to assess the genetic constructs. Analysis through RT-PCR could determine if a limitation exists at the transcriptional level by quantifying *ired* mRNA, while full-plasmid sequencing would assess the structural integrity of the pAA56 and pEG19 constructs in *C. necator*. Recent studies have identified bacterial defense mechanisms in *C. necator*, such as restriction-modification or methylation, that could be potential barriers to the expression of heterologous genes (Vajente et al., 2024). Examining the plasmids directly extracted from *C. necator* could provide insights into the $IRED_{V8}$ production challenges.

Given that only one clone per construct was analyzed in this study, the possibility that certain clones may not have fully functional constructs cannot be excluded. To address this, the development of a high-throughput screening method could increase the possibility of identifying those with optimal

production levels. However, even with the correct construct, maintaining multiple plasmids in *C. necator* could introduce additional challenges.

In bacterial systems, plasmid maintenance and replication are known to impose a metabolic burden, as observed in *E. coli* (Ow et al., 2006), potentially compromising cellular fitness and causing diverse physiological effects (San Millan & Maclean, 2017). This burden can be further exacerbated by the presence of multiple antibiotic resistance markers, which have shown to reduce plasmid production (Cunningham et al., 2009). Similarly, the strain WT+ IRED + GroESL harbored two plasmids: 12.8 kp for *ired* expression, with tetracycline resistance; and 8.6 kb for *groesl* expression; with kanamycin resistance. The presence of multiple plasmids could impose a similar metabolic burden that interfered with efficient transcription or translation, particularly as the strain was cultivated in minimal media, which can exacerbate metabolic stress.

In the case of the Δ*lon* strains, the depletion of Lon protease could potentially disrupt cell homeostasis in *C. necator* and affect the heterologous protein production in minimal media. Lon protease plays an important role in controlling protein quality in bacteria and its impact has been studied in various bacteria, exhibiting diverse phenotypes and effects in cellular metabolism. For instance, *E. coli* and *Pseudomonas aeruginosa* strains lacking Lon showed impaired response under antibiotic stress, and cellular morphology was affected leading to disruption of normal growth in *P. aeruginosa* and *Burkholderia glumae* (Brazas et al., 2007; Goo & Hwang, 2021; Matange, 2020). The *E. coli* BL21(DE) strain, which is Lon deficient and contains a T7 RNA polymerase, presented comparable growth to the wild type *E. coli,* however it may exhibit slower growth when burdened with high levels of recombinant protein production (Studier & Moffatt, 1986). Different strategies have been evaluated in this strain to bypass an overexpression system that can impose significant metabolic burden and reduce host viability (Du et al., 2021).

Furthermore, the inherent genome of the *C. necator* H16, characterized by a redundancy, also contributes to a protein cost that could restrict growth efficiency under specific conditions (Jahn et al., 2024). Together, these factors may have hindered the heterologous production of $IRED_{V8}$ in the strains WT + IRED + GroESL, Δlon + IRED+ GroESL. and Δlon + IRED+ GroESL, suggesting the need to optimize the genetic constructs, screening procedure, and cultivation strategies.

3.1.1.3 Enriched $IRED_{V8}$ from *C. necator* is active.

Based on the protein production and activity from the previous screening, only the strain WT + IRED was retained for subsequent experiments. The effect of rhamnose induction was assessed by comparing the induced and non-induced states of WT + IRED in soluble extract.

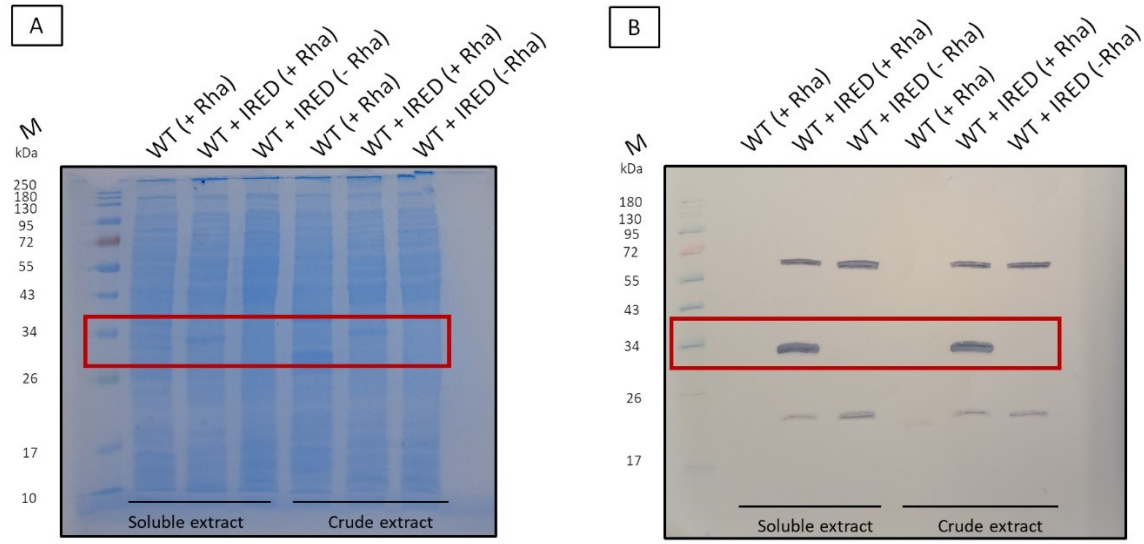

Figure 25. Effect of rhamnose induction on IRED production in *C. necator* : $IRED_{V8}$ production is analyzed in both the soluble extract and the crude extract in WT + IRED, with (+ Rha) and without (- Rha) rhamnose induction. The strain WT (+ Rha) is used as a control. A band corresponding to the IRED monomer is expected at 35 kDa (indicated in red). The crude extract refers to the total protein fraction obtained immediately after cell disruption, while the soluble extract represents the supernatant obtained after centrifugation of the crude extract. (M: molecular weight of the protein ladder, WT: *C. necator* H16, WT + IRED: *C. necator* x pAA56).

A band around 35 kDa, was detected in the crude and soluble extract of the WT + IRED strain when rhamnose was added as inducer, while no protein was detected for the WT control strain (Figure 25-B). The band at 35 kDa corresponds to the expected size of $IRED_{V8}$ monomer, indicating successful protein production in WT + IRED. When WT + IRED strain was not induced, no bands at the monomer size were observed in the SDS-Page nor in the Western blot. However, a different pattern of protein bands was observed in both induced and non-induced conditions compared to Figure 22. In this case. additional bands at approximately 72 kDa and below 26 kDa were detected (Figure 25).

Several hypotheses could explain the unexpected banding pattern observed in the SDS-PAGE and Western blot analyses. The first band at 72 kDa may correspond to the dimeric form of $IRED_{V8}$, potentially stabilized by strong non-covalent interactions that resisted complete denaturation, even in the presence of β-mercaptoethanol. These observations are consistent with the structural properties of IREDs. As dimeric proteins, IREDs contain Rossmann fold, a conserved structural motif essential for binding dinucleotide cofactors, such as NADPH, or in our case, NADH (Caetano-Anollés et

al., 2007; Hanukoglu, 2015; B.-G. Ma et al., 2008). IRED dimerization is typically stabilized by non-covalent interactions such as hydrogen bonds, ionic interactions, and hydrophobic forces at the dimer interface, often involving residues located. near or within the Rossmann fold (Bhattacharyya et al., 2012; Meyer et al., 2020). The stabilizing forces can persist even under partially denaturing conditions, potentially explaining the multiple bands observed in the Western blot.

Interestingly, the 72 kDa band was not detected in Figure 22, suggesting differences in sample preparation. Incomplete protein denaturation, due to insufficient heating or variation in reducing agent concentration, may have contributed to the retention of the $IRED_{V8}$-dimeric form. Other factors, such as elevated protein concentration or the presence of stabilizing cofactors in *C. necator* supernatant could have influenced the stability of IRED dimers and dissociation, as previously reported for other dimeric proteins (Creutznacher et al., 2022). Elevated protein concentration is also known to affect purification efficiency and dimer equilibrium by favoring intermolecular interactions (Janson, 2011). Alternatively, it is possible that the 72 kDa band corresponds to a native protein present in the soluble extract of *C. necator* that is being non-specifically recognized by the Strep-Tactin® AP antibody.

The absence of the 35 kDa band in WT + IRED without rhamnose could be explained by the lack of inducer. Nonetheless, it is possible that WT + IRED produced $IRED_{V8}$ without induction at very low basal levels, insufficient for detection by Western blot. The third band observed below 26 kDa was present in both induced and non-induced strains and could represent a degradation product of $IRED_{V8}$, resulting from proteolysis during or after cell disruption.

With the current data, it is difficult to conclude among the previous hypotheses. Further experiments, including protein identification by mass spectrometry, will be necessary to confirm the identity of the bands at 72 kDa, 35 kDa and below 26 kDa. Moreover, discrepancies in the band patterns between Figures 6 and 9 may be reflecting variable $IRED_{V8}$ production due to strain variability, or other experimental variables.

To further validate IRED activity, we analyzed the soluble extract from these cultures, and the results are presented in the bar chart in Figure 26. No activity was detected in the control strain (WT induced with rhamnose). However, a basal activity of 0.05 U/mg was observed in the WT + IRED strain without rhamnose induction, increasing to 0.18 U/mg when rhamnose was added. This increase in activity aligns with the detection of the monomeric band (~35 kDa) in the Western blot under induced conditions.

The presence of unexpected bands in the non-induced sample, including the 72 kDa band and potential degradation products, may contribute to the basal or parasitic activity detected in the soluble extract of WT + IRED without induction. As previously mentioned, if $IRED_{V8}$ was produced at very low basal levels in WT + IRED in the absence of rhamnose, the activity observed in Figure 26 could be attributed to leaky expression from the rhamnose promoter, sufficient to detect enzymatic activity, but below the detection in Western blot.

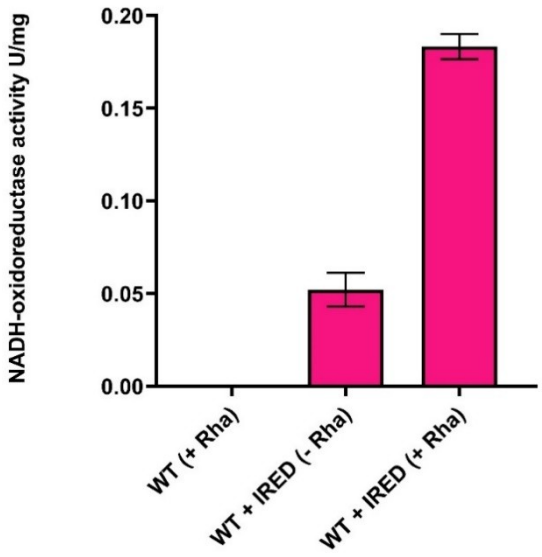

Figure 26. Soluble extract of WT + IRED requires induction for an increased NADH-oxidation : The NADH-oxidoreductase activity was evaluated in the soluble extract of the strain WT + IRED with (+ Rha) or without (- Rha) rhamnose induction. The average activity is obtained using 20 and 50 µL of soluble extract. An activity of 0.05 U/mg is observed when no rhamnose is added and 0.18 U/mg is observed when the strain WT + IRED is induced with 12 mM rhamnose. The activity in the soluble extract is calculated from triplicates and SEM is indicated by the error bars. (WT: *C. necator* H16; WT + IRED: *C. necator* x pAA56).

Additional evaluations were conducted on the strain WT + IRED to purify $IRED_{V8}$ and analyze the enzyme activity. $IRED_{V8}$ purification from *C. necator* was compared with the soluble extract of WT + IRED using SDS-PAGE, Ponceau staining, and Western blotting (Figure 27 A-C). Consistent with previous observations, the monomeric IRED band at the expected size (~35 kDa) was visible in the soluble extract of WT + IRED, with a more intense band observed in the lane corresponding to the eluted $IRED_{V8}$ fraction. Bands at 72 kDa and below 26 kDa were detected in the Western blot of the eluted $IRED_{V8}$ (Figure 26). The similarity in band patterns between the soluble extract (Figure 25) and the eluted $IRED_{V8}$ (Figure 26) suggests that the 72 kDa could be the dimer of IRED. Alternatively, the band at 72 kDa could result from nonspecific protein detection or co-elution during purification, while bands below 26 kDa may represent IRED degradation products or other nonspecific proteins. In contrast, only one band around 35 kDa was observed when $IRED_{V8}$ was initially produced in the soluble extract (Figure 22), which might reflect fluctuation in *ired* expression due to strain variability, plasmid stability or differences during transformation.

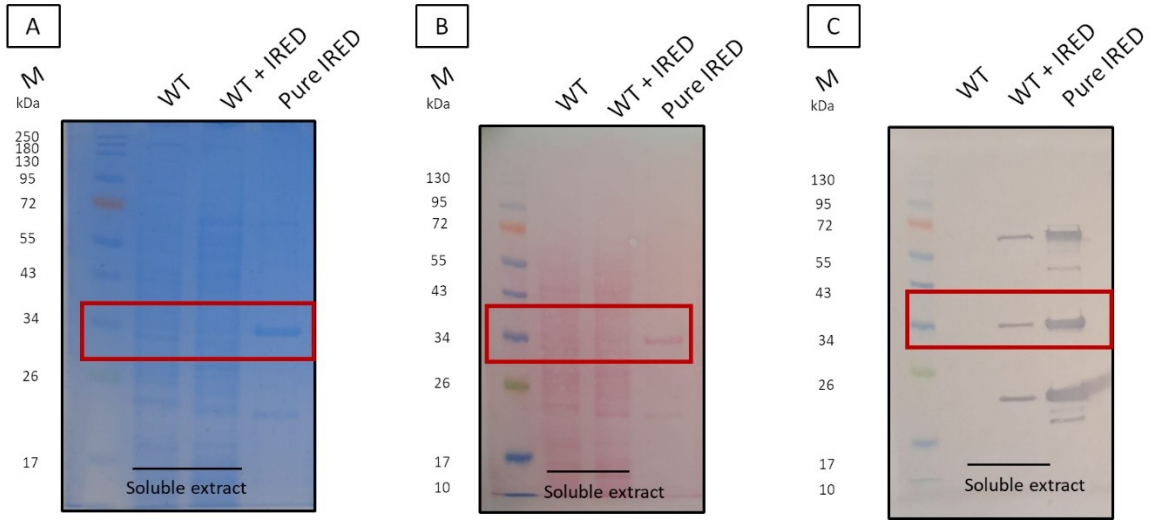

Figure 27. $IRED_{V8}$ is enriched from *C. necator* : The soluble extract and the eluted fraction of WT and WT + IRED is evaluated by SDS-PAGE (A), Ponceau staining (B) and Western blot (C) when the strains are induced with rhamnose. A band corresponding to the IRED monomer is expected at 35 kDa (indicated in red). adder soluble extract, 20 µg of total protein is loaded for each strain, and for the pure protein 4 µg is loaded. (M: molecular weight of the protein adder; WT: *C. necator* H16; WT + IRED: *C. necator* x pAA56).

The eluted fraction (Figure 27, C) was concentrated and exchanged into IRED-storage buffer using an Amicon®, allowing the retention of the band at 35 kDa and 70 kDa while removing the lower protein bands. The activity of the enriched enzyme solution was then compared to $IRED_{V10}$ purified from *E. coli* x pAA44, a strain expressing a variant NADH-dependent IRED with a different plasmid system (AA44 strain, Al-Shameri collection strain, Lauterbach laboratory). As presented in Figure 7, the specific activity of the purified $IRED_{V10}$ was 5.4 ± 0.2 U/mg from *E. coli* and 1.8 ± 0.1 U/mg from the enriched $IRED_{V8}$ from *C. necator*. Although the specific activity from *E. coli* was higher, which aligns with its established use as a robust system for heterologous protein production, the enzyme enriched from *C. necator* was active and functional. These results demonstrate that $IRED_{V8}$ can be effectively produced and enriched from *C. necator*, providing a functional enzyme that can be adapted into its metabolic processes.

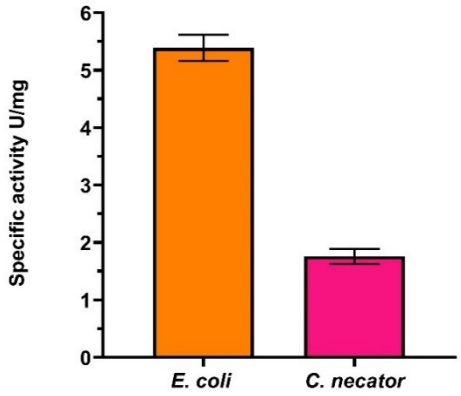

Figure 28. Enriched $IRED_{V8}$ from *C. necator* is active : The enzyme $IRED_{V10}$ is purified from *E. coli* (*E. coli* x pAA44) and $IRED_{V8}$ from *C. necator* (*C. necator* x pAA56), and the activity is tested with the reduction of NADH. The test was performed in 50 mM $KiPO_4$ buffer with 0.5 mM of NADH as cofactor. The means of replicates are shown (n= 12 for *E. coli* and n= 14 for *C. necator*), error bars indicate SEM.

3.1.1.4 Exploring novel IRED candidates: Preliminary study

In addition to $IRED_{V8}$, a selection of putative IREDs was explored as part of a complementary study aimed at catalyzing novel reactions with sterically demanding substrates (Kunth, 2023). This preliminary work focused on the heterologous production, purification and characterization of putative IREDs from the microorganisms: *Myxococcus* sp, *Aspergillus terreus*, *Streptomyces noursei*, *Cupriavidus* sp*, Streptomyces,* and *Myxococcus fulvus*. These uncharacterized IREDs were selected for the potential of their active sites to accommodate bulkier substrates. The genes and proteins sizes are described in Table 16.

Table 16. IREDs candidates : 6 putative IREDs are selected based on the configuration of their active site, which could potentially accommodate larger substrates (B. Nestl, Innophore-industrial partner, 2023). Gene size and estimated protein monomer size is indicated for each IRED.

Uncharacterized IRED	Donor microorganism	Gene size (kb)	Monomeric protein weight (kDa)
IRED 1	*Myxococcus sp.* SCHIC003	1.36	32.19
IRED 2	*Aspergillus terreus*	1.37	31.72
IRED 3	*Streptomyces noursei*	1.32	31.62
IRED 4	*Cupriavidus sp. HPC(L)*	1.34	34.11
IRED 5	*Streptomyces* (unclassified)	1.37	34.07
IRED 6	*Myxococcus fulvus*	1.35	32.86

Synthetic constructs containing the putative IREDs were ordered in pBAD backbones containing a pBAD-promoter, and resistances to ampicillin (Supplementary B.3). The six putative IREDs enzymes were transformed *E. coli* HW191 and produced for initial characterization. The enzymes were purified and analyzed with SDS-PAGE. The gels revealed faint bands around 34 kDa on the purified fractions for IRED 1 and IRED 2 (Figure 29 a and b, respectively). Western blot detection was performed to confirm protein production and bands at the expected size were displayed in IRED 1, 2, and 6 (around 34 kDa). However, the purification was not entirely specific and a contaminant band was present across the eluted samples. Notably, a persistent band around 43 kDa appeared in the crude extracts and throughout some of the eluted fractions in the IRED samples (Figure 29, a-f). This band is higher than the expected size and may result from nonspecific detection of native *E. coli* proteins that remained bound to the purification resin and co-eluted with the band at 34 kDa.

The presence of this contaminant band hindered a complete characterization of the IREDs and indicated the need for further purification optimization. Despite this purification challenge, fractions containing bands around 34 kDa from IRED 1, 2, and 6 were recovered and pooled as follows: eluted fraction 2, eluted fractions 3 + 4, and eluted fractions 5 + 6. Given the exploratory nature of this study, enzymatic activity assays were nevertheless conducted with these fractions to gain information into the catalytic potential of the selected IREDs.

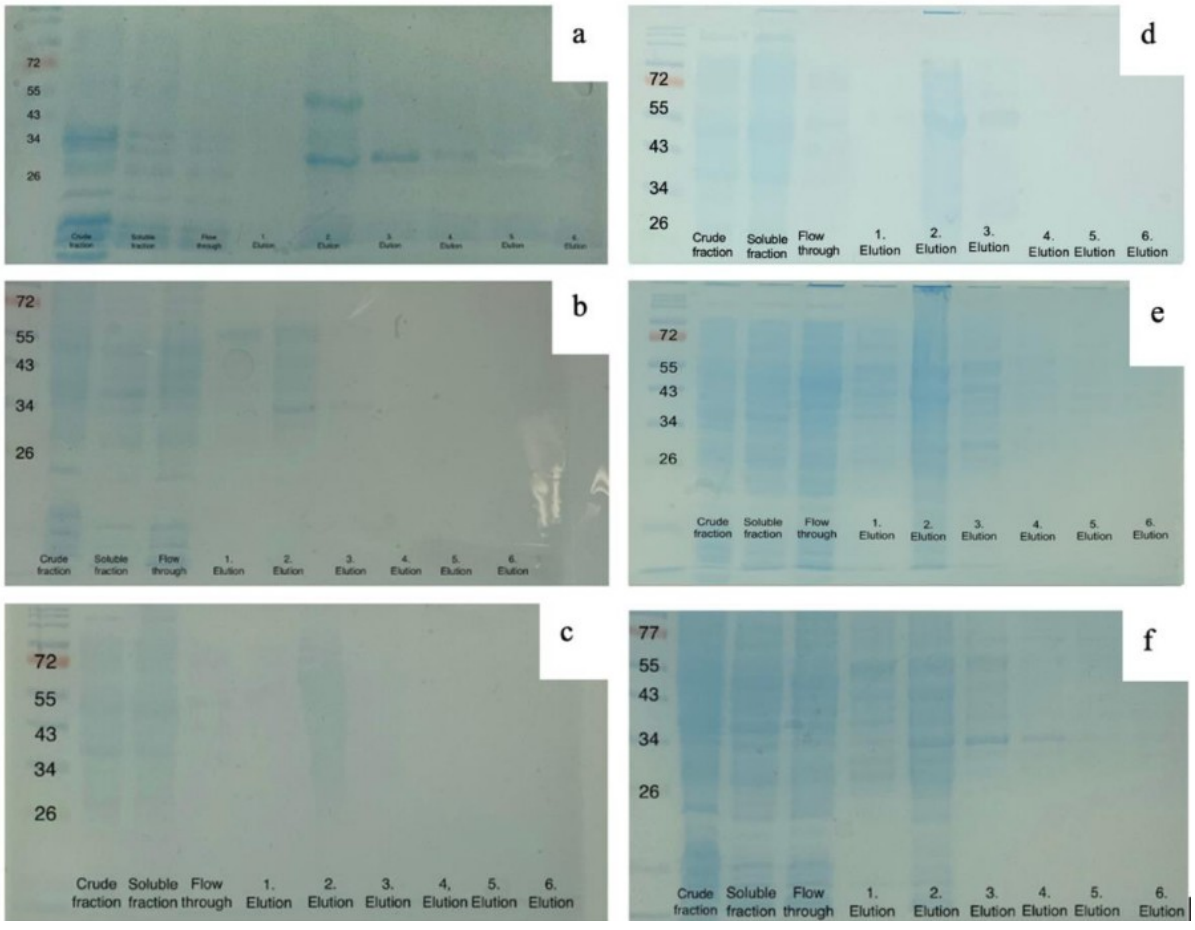

Figure 29. Purification of putative IREDs in SDS-PAGE : The gels contain the samples of a) IRED 1 *Myxococcus sp. SCHIC003*; b) IRED 2 *Aspergillus. terreus*; c) IRED 3 *Streptomyces . noursei*; d) IRED 4 *Cupriavidus sp. HPC(L)* e) IRED 5 *Streptomyces (unclassified)*; f) IRED 6 *Myxococcus fulvus.* The first row on each gel corresponds to the protein ladder, with the protein size indicated in kDa. The wells are loaded from left to right with crude fraction, soluble fraction, flow-through, 1st eluted fraction, 2nd eluted fraction, 3rd eluted fraction, 4th eluted fraction, 5th eluted fraction, and 6th eluted fraction. (Kunth, 2023).

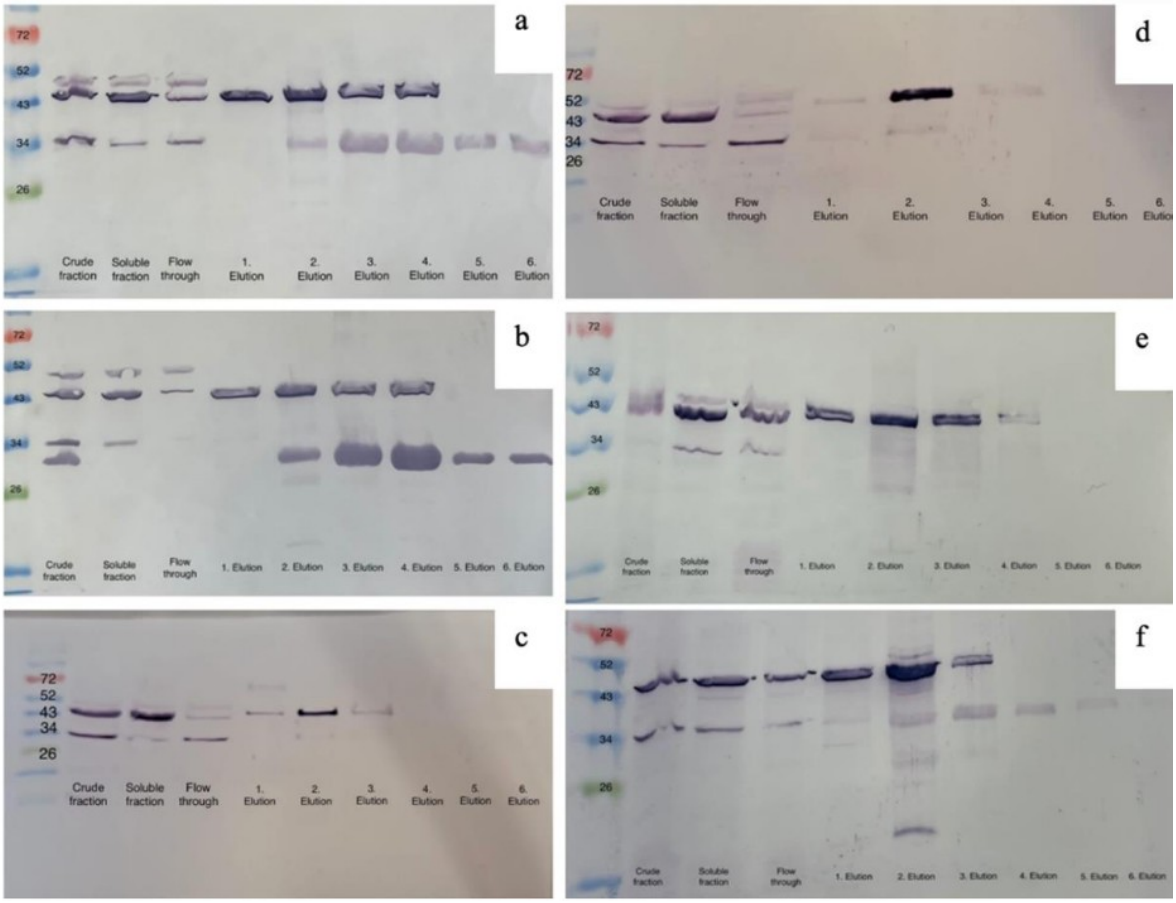

Figure 30. Purification of putative IREDs in Western blot : The gels contain the samples of a) IRED 1 *Myxococcus sp. SCHIC003*; b) IRED 2 *Aspergillus. terreus*; c) IRED 3 *Streptomyces. noursei*; d) IRED 4 *Cupriavidus sp. HPC(L)* e) IRED 5 *Streptomyces (unclassified)*; f) IRED 6 *Myxococcus fulvus.* The first row on each gel corresponds to the protein ladder, with the protein size indicated in kDa. The wells were loaded from left to right with crude fraction, soluble fraction, flow-through, 1st eluted fraction, 2nd eluted fraction, 3rd eluted fraction, 4th eluted fraction, 5th eluted fraction, and 6th eluted fraction. Enzymes are tagged in N-terminal with 6x His-tag and detected using Anti-His/AP Ab (Kunth, 2023).

Enzymatic activity was evaluated with the selected fractions of IRED 1, 2, and 6 using a spectrophotometric assay with the model substrate 2-methyl-1-pyrroline. The IREDs were selected from diverse microorganisms and they present their natural dependence towards the cofactor NADPH. The *in vitro* assay followed NADPH oxidation as an indicator of imine reduction. The analysis indicated potential NADPH oxidation, supporting the classification of the samples as functional IREDs (data not-shown). In addition to 2-methyl-1-pyrroline, the substrate scope of the IREDs was tested with five phenazines. The selected phenazines are structurally larger and more sterically demanding than 2-methyl-1-pyrroline because they contain 4 rings with multiple nitrogen atoms (Figure 31). Phenazines derivatives are *N*-heterocyclic compounds that have drawn interest because of their biological and industrial relevance. In agriculture they are valuable for phytopathogen control (Grahl et al., 2013). In health and pharmaceutical industries, some phenazines are being investigated as anticancer agents and treatments against drug-resistant microbial strains (Cimmino et al., 2013; Halicki et al., 2021). These biological properties make phenazines interesting substrates for IREDs biotransformation.

The activity assays between IRED 1, 2 and 6 and the five phenazines were particularly challenging. The absorption spectra were difficult to interpret due to the sensitivity of phenazines to oxygen in the mix with NADPH (Tokunou et al., 2022; Y. Wang & Newman, 2008), and the presence of multiple reduction sites. These factors may have influenced the reaction conditions and enzyme performance, complicating the analysis (Kunth, 2023). These limitations highlighted the need to optimize the experimental setup in order to accurately assess the catalytic potential of the IREDs with phenazines as substrates. While these initial findings were exploratory, they provided the basis for both expanding the repertoire of IREDs as biocatalysts with different substrates, and for optimizing biotransformation strategies in *C. necator*.

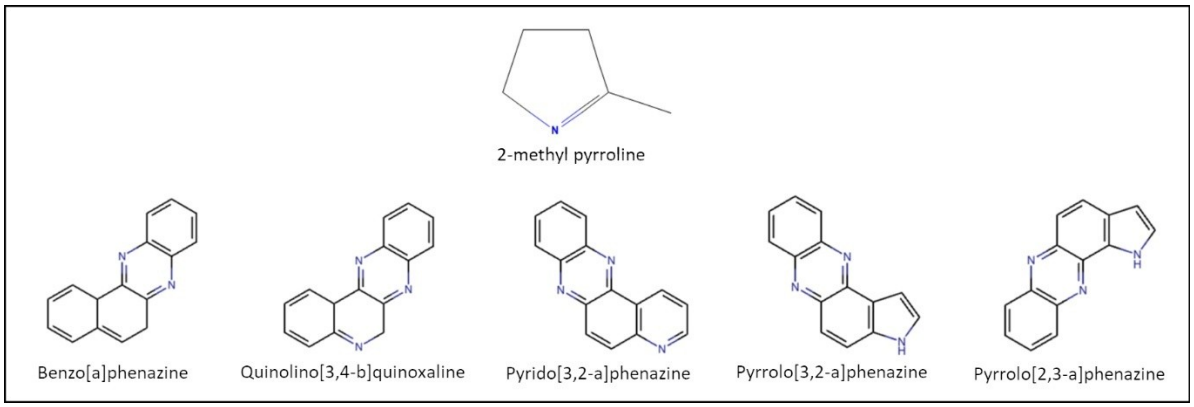

Figure 31. Panel substrate for the putative IREDs : Six substrates were tested in an *in vitro* assay to verify the catalytic activity of the putative IREDs. The molecule 2- methyl pyrroline is used to identify imine reduction activity and the molecules shown below correspond to the tested phenazines. Molecule structures from PubChem, NIH (Adapted from Kunth, 2023).

Encouraged by this study, the purification protocol was optimized and the complete enzyme set is undergoing a new characterization in L. Lauterbach's laboratory. The purification and activity assays were repeated to confirm the observations of IRED 1, 2 and 6; integrate the characterization of the remaining IREDs, and optimize the assay with the phenazines (collaboration with D. Calabrese, unpublished data, 2024). The compatibility of these IREDs with the metabolism of *C. necator* is also being evaluated, and their catalytic performance is being assessed in whole-cell biotransformations (collaboration with P. Schoenmakers, unpublished data, 2024).

3.1.2 *C. necator* produces a variant of Putrescine Oxidase ($PuOx_{M1}$).

Al-Shameri et al. (2019) developed an enzymatic cascade involving a putrescine oxidase variant from *Rhodococcus erythropolis*. Through directed evolution, they engineered the enzyme by substituting the glutamic acid at position 203 with glycine, modifying the access channel to the enzyme's active site pocket. Tests with a panel of diamines demonstrated that this evolved enzyme exhibited increased activity toward non-natural substrates. Building on these findings, Borlinghaus et al. (2019) further optimized the enzyme using semi-rational mutagenesis. They introduced additional mutations to create the $PuOx_{M1}$ variant (L200I/E203S/I206L), which showed enhanced activity toward longer C5 diamine substrates.

In this Chapter, we sought to explore the heterologous production of $PuOx_{M1}$ in *C. necator*. Several strains were obtained and the production of the protein under heterotrophic conditions was analyzed.

3.1.2.1 $PuOx_{M1}$ production and enrichment.

One of our approaches consisted in using the pKR broad-host plasmid system to express the *puox$_{M1}$* gene containing a His-tag® in *C. necator*. During the first attempt for the plasmid construction, a deletion was detected in the regulator gene *rhaS.* The mutation could lead to a premature stop codon, disrupting the correct functioning of the rhamnose regulator. The plasmid pDA2 was constructed exchanging the defective rhamnose promoter with a correct sequence from a pECcas9 plasmid as described Section 2: Materials and methods 2.2.1 DNA Cloning, and detailed by previous works (de la Asunción Vest, 2023). Fragments used for amplification of the pKR plasmid and sequence correction are detailed in Supplementary B.4.2 and plasmid map is presented below (Figure 32).

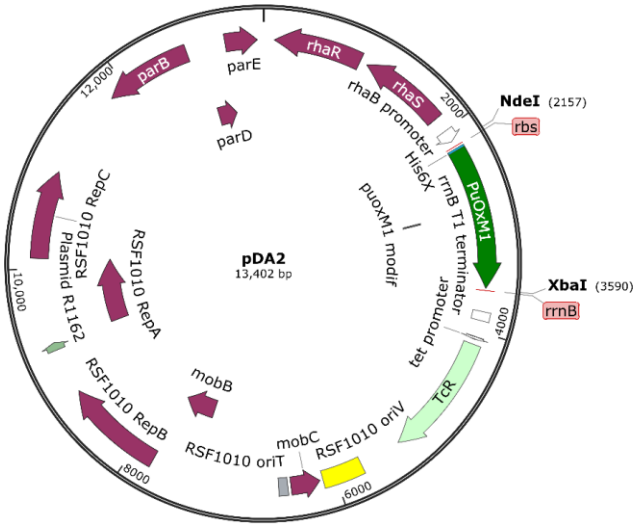

Figure 32. Plasmid map pDA2 containing $PuOx_{M1}$. Hisx6-tag is used. Examples of restriction enzymes are shown. Plasmid maps is generated with SnapGene®.

Plasmid pDA2 was transformed into *C. necator* WT or *C. necator* Δlon and diverse colonies were screened for the presence of the correct promoter with Colony-PCR (Figure 34). The correct amplification resulted in the strains *C. necator* x pDA2 (WT + PuOx) and Δlon x pDA2 (Δlon + PuOx).

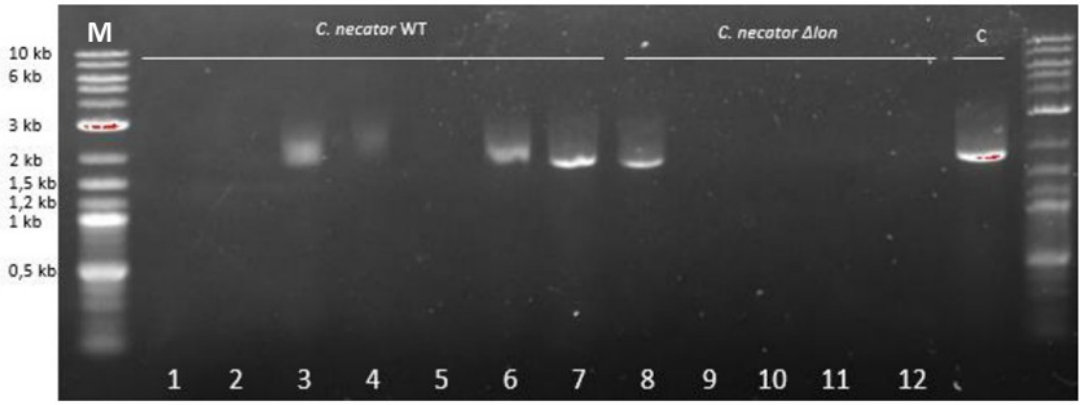

Figure 33. Rhamnose promoter is amplified in transformed *C. necator* colonies : Presence of the corrected rhamnose promoter is evaluated by PCR amplification in transformed WT and Δlon colonies. An amplification of the rhamnose promoter from the pECcas9 plasmid is used as positive control (C). A band of approximately 1.8 kb is expected. (M: Molecular weight of DNA ladder; C: positive control).

The heterologous $PuOx_{M1}$ production was first tested in the soluble extract of WT + PuOx in a small culture. A light band corresponding was identified at the expected size of the $PuOx_{M1}$ monomer (Figure 34, 55 kDa) when the strain WT+ PuOx was cultured in FN medium. However, a secondary band at 34 kDa was also observed. This band was present in the control WT and may result from non-specific binding of the His6-Tag® to native proteins in *C. necator.*

Protein production was scaled up in FN medium to purify $PuOx_{M1}$ from the constructed strains. The purification process was assessed in WT + PuOx (Figure 35) and Δlon + PuOx (Figure 36) using SDS-PAGE and Western blot. The protein $PuOx_{M1}$ carries a His-tag®, and it is expected a molecular weight as a monomer is 54 kDa.

In the SDS-PAGE of the strain WT + PuOx, faint bands were observed in both the flow-through and the elution fraction around the 55 kDa marker (Figure 35, A). This band may correspond to $PuOx_{M1}$ and the weak signal of this band could be due to a low $PuOx_{M1}$ production. To enhance detection and confirm the presence of $PuOx_{M1,}$ Western blot was used to detect the His-tag® (Figure 35, B). In the elution fraction, a single band is observed slightly above the 55 kDa marker, which is not present in the other wells. The slight shift in migration for this band could be attributed to the presence of the His-tag® or features of PuOx that may interact differently with the gel's matrix. However, the difference is minimal, no additional bands were detected in the purified protein, and no corresponding band was present in the negative control (Figure 35, B, E: elution fraction, Neg.: *C. necator* WT).

Additionally, a band was present at the same position in the soluble extract of WT + PuOx (Figure 34). Together, these observations indicated that the band corresponds to $PuOx_{M1}$ and it was purified from WT + PuOx. However, the presence of other bands in the eluted fraction in the SDS-PAGE indicates that the protein was not completely pure and an optimization of the purification protocol is needed.

Similar observations were made for the protein purification in Δlon + PuOx. In the SDS-PAGE, a faint band appeared around the expected size (Figure 36). The visual detection was hindered because of overstaining of the gel with Coomassie Blue, and Western blot was used to confirm the presence of $PuOx_{M1}$. A very faint band was detected in the eluted fraction of Δlon + PuOx around the expected size (Figure 36, B). This suggests a lower protein production of $PuOx_{M1}$ in of Δlon + PuOx in comparison to WT + PuOx (Figure 35).

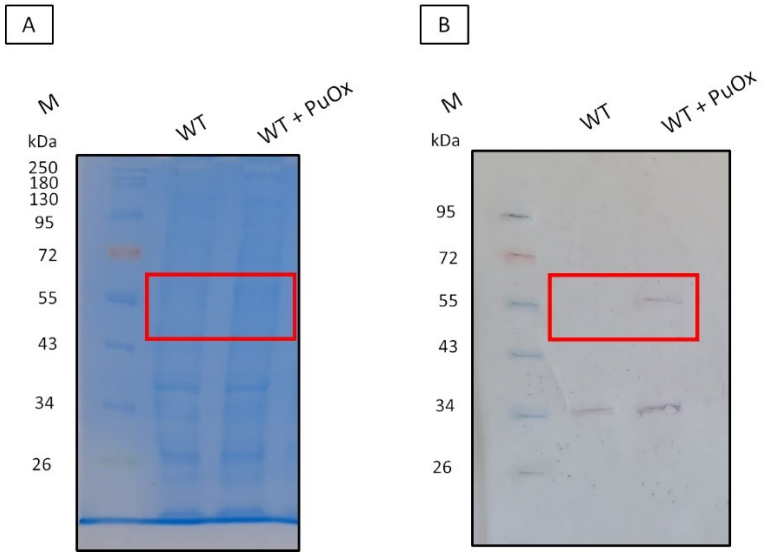

Figure 34. *C. necator* produces $PuOx_{M1}$ in minimal media : $PuOx_{M1}$ production is performed in 50 mL FN media during 48 h. Protein production is induced with 0.2 % rhamnose at an OD_{600} 0.5. The soluble extract is analyzed using SDS-Page (A) and Western blot (B). A band around 54 kDA is expected for $PuOx_{M1}$ monomer, marked with the red rectangle. A total of 20 µg of protein was loaded for each strain. (M: molecular weight of protein ladder, WT: *C. necator* H16, WT + PuOx: WT x pDA2).

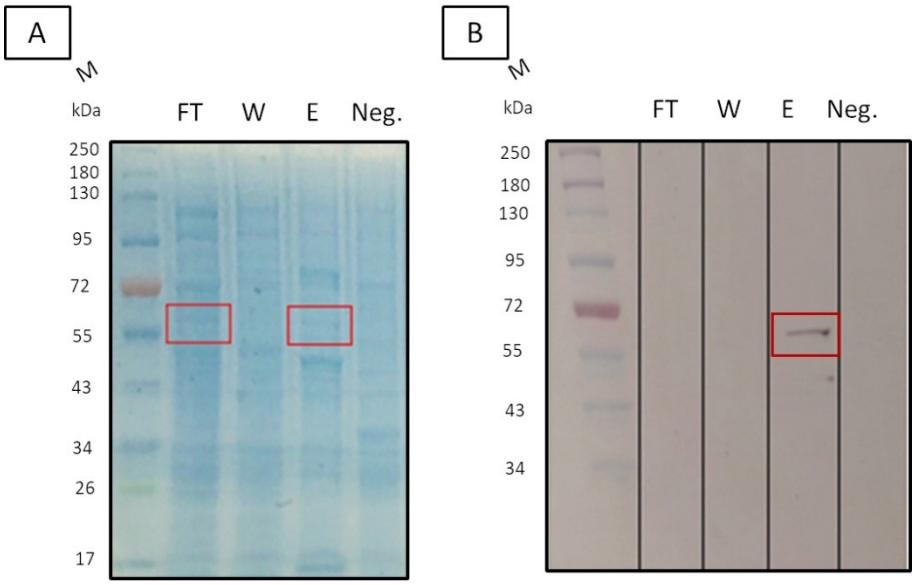

Figure 35. $PuOx_{M1}$ is purified from *C. necator* : WT + PuOx is cultured in 4 L FN medium at 30°C for 48 h with induction at the start of the culture (t_{ind}= 0 h) using 0,2% rhamnose. Purification steps are analyzed by SDS-PAGE (A) and Western blot (B). A band around 54 kDA is expected for $PuOx_{M1}$ monomer, marked with the red rectangle. $PuOx_{M1}$ is tagged at N-terminal with 6x His-tag® and detected using Anti-His/AP Ab (M: molecular weight of protein ladder, FT: flow-through, W: wash , E: elution, Neg. : *C. necator* WT as negative control, WT + PuOx : *C. necator* x pDA2) (Adapted from de la Asunción Vest, 2023).

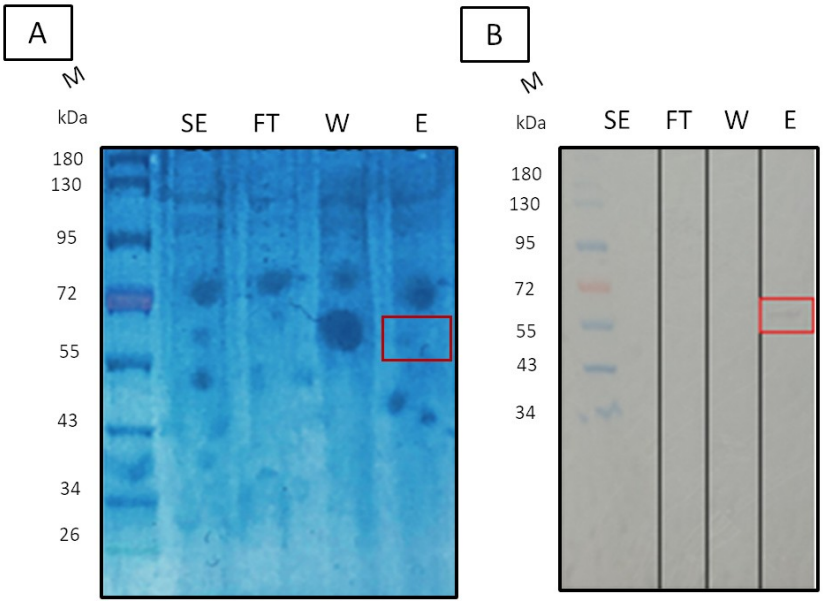

Figure 36. $PuOx_{M1}$ is purified fromΔlon : Δlon + PuOx is cultured in 4 L FN medium at 30°C for 48 h, with induction at the start of the culture (t_{ind}= 0 h) using 0,2% rhamnose. Purification steps are analyzed by SDS-PAGE (A) and Western blot (B). A band around 54 kDA is expected for $PuOx_{M1}$ monomer, marked with the red rectangle (M: molecular weight of protein Ladder, FT: flow-through, W: wash , E: elution, Δlon + PuOx: Δlon x pDA2) (Adapted from de la Asunción Vest, 2023).

3.1.2.2 Exploring the effect of culture duration and induction timing on $PuOx_{M1}$ production in *C. necator.*

To improve $PuOx_{M1}$ production in *C. necator*, we investigated the effect of culture duration and induction timing. First, we examined the impact of cultivation duration. The strains were cultivated under the same conditions as before, except for an extended incubation period of 120 h (5 days) instead of 48 h (2 days). The cultures were then purified, and the SDS-PAGE and Western blot analyses are presented below for the WT + PuOx strain (Figure 37), and Δlon + PuOx (Figure 38).

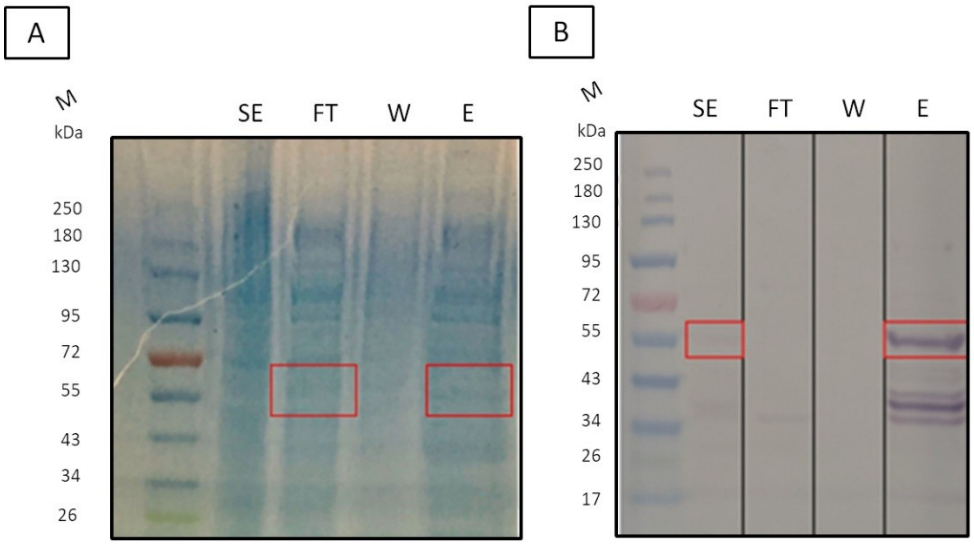

Figure 37. Producing $PuOx_{M1}$ in *C. necator* after 120 h : WT + PuOx was cultured in 4 L FN medium at 30°C with induction at the start of the culture (t_{ind}= 0 h) using 0,2% rhamnose. $PuOx_{M1}$ was purified after 120 h of culture. Purification was analyzed with SDS-PAGE (A) and Western blot (B). A band of 54 kDA was expected for $PuOx_{M1}$ monomer, marked with the red rectangle. (M: molecular weight of protein ladder, FT: flow-through, W: wash , E: elution, WT + PuOx : WT x pDA2) (Adapted from de la Asunción Vest, 2023).

In the SDS-PAGE of the WT + PuOx strain (Figure 37, A)., multiple bands were observed around the region of interest, both in the flow-through fraction and the elution fraction, particularly around the 55 kDa mark. In the Western blot, a band corresponding to the expected size was observed but three additional bands were detected below 43 kDa (Figure 37, B). A similar pattern was observed for the Δlon + PuOx strain. The SDS-PAGE of the eluded fraction presented several bands and intense staining (Figure 38, A). A band around the expected size was present in the eluted fraction of the Western blot, with several bands below (Figure 38, B).

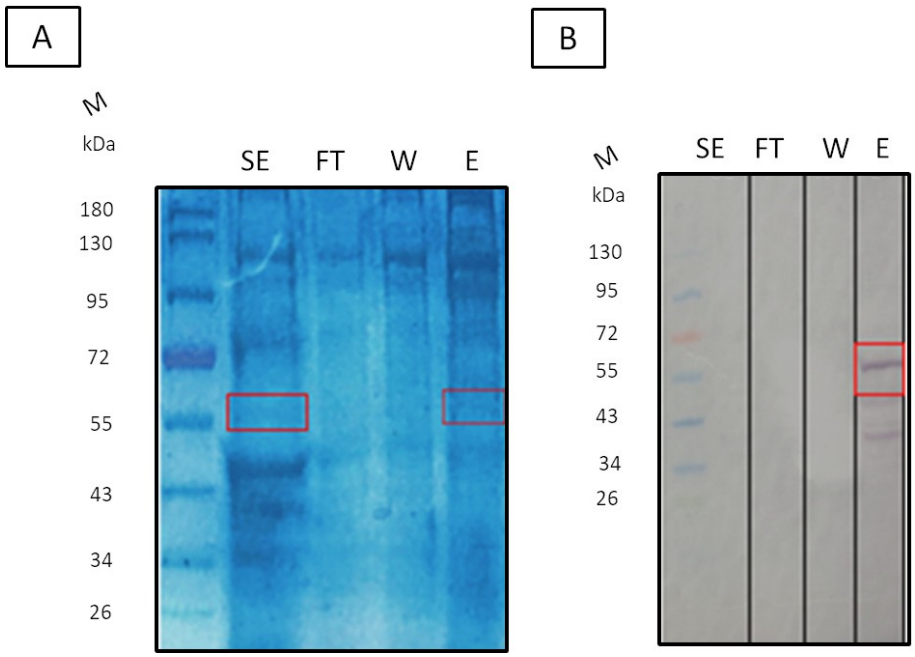

Figure 38. Producing $PuOx_{M1}$ in *C.* Δlon after 120 h : Δlon + PuOx is cultured in 4 L FN medium at 30°C with induction at the start of the culture (t_{ind}= 0 h) using 0,2% rhamnose. $PuOx_{M1}$ is purified after 120 h of culture. Purification is analyzed with SDS-PAGE (A) and Western blot (B). A band of 54 kDA is expected for $PuOx_{M1}$ monomer, marked with the red rectangle. (M: molecular weight of protein ladder, FT: flow-through, W: wash , E: elution, WT + PuOx : WT x pDA2) (Adapted from de la Asunción Vest, 2023)

After 5 days of culture, both strains WT + PuOx and Δlon + PuOx produced a band of the expected molecular weight of 55 kDa (Figure 35-Figure 36, B). The resulted bands were more intense than in the two-day cultures (Figure 37-Figure 38, B), suggesting a higher protein production. Additionally, faint bands were already visible in the soluble extract in Western blots of the five-day cultures, which was not the case for the WT + PuOx strain at two days. However, unspecific bands appeared after five days of cultivation, which were not observed in the two-day cultures (Western blot analysis from Figure 35-Figure 38). These additional bands could be due to protein degradation over an extended cultivation period. Protein degradation is a regulated process in bacteria and it can vary during the different growing phases and different nutritional states. Studies in *E. coli* have shown that proteins are more susceptible for degradation during the stationary phase or during starvation (Nagar et al., 2021; St. John et al., 1979). Extended cultivation in *C. necator* has also led to degradation of native PHB granules and some recombinant proteins (Arhar et al., 2024; Eggers & Steinbüchel, 2013). Alternative, insufficient protease inhibitor during sample preparation could have contributed to the presence of the bands at lower molecular weight (Gorr & Vogel, 2015).

We also investigated the impact of induction timing on $PuOx_{M1}$ production. The strains WT + PuOx and Δlon + PuOx were cultivated under the same conditions as before, but with a modified induction time. In this experiment, induction was performed 24 h after culture initiation (t_{ind}= 24 h). The SDS-PAGE

gels were overexposed during the staining and only the Western blots are presented in Figure 39.In the WT + PuOx strain, no band was detected in the purified fraction in the Western blot (Figure 39, A). In contrast, Δlon + PuOx culture presented a relatively faint band at the 55 kDa mark in the elution fraction (Figure 39, B) and no other bands were observed in the remaining fractions.

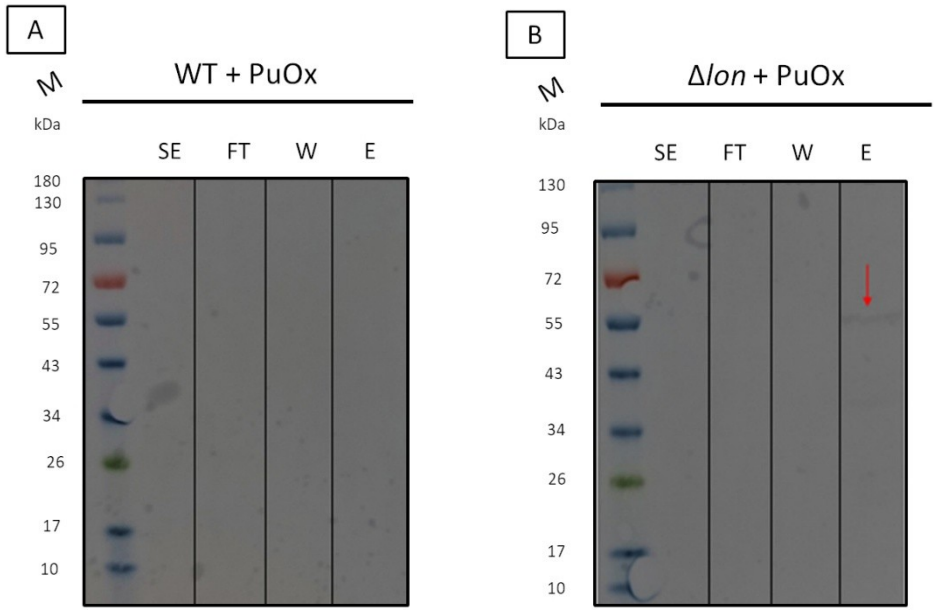

Figure 39. Producing $PuOx_{M1}$ with induction after 24 h : WT + PuOx and Δlon + PuOx are cultured in 4 L FN medium at 30°C with induction 24 h after the start of culture (t_{ind}= 24 h) using 0,2% rhamnose. $PuOx_{M1}$ is purified after 48 h of culture. Purification is analyzed with Western blot from WT + PuOx (A) and Δlon + PuOx (B) (M: molecular weight of protein ladder, FT: flow-through, W: wash , E: elution, WT + PuOx : WT x pDA2, Δlon + PuOx: Δlon x pDA2) (Adapted from de la Asunción Vest, 2023).

Compared to the WT + PuOx cultures induced at t_{ind}= 0 h (Figure 35, Figure 37), the culture induced at t_{ind}= 24 h was unable to produce $PuOx_{M1}$ (Figure 39, A).The Δlon + PuOx strain was able to produce $PuOx_{M1}$ at both induction times t_{ind}= 0 h and t_{ind}= 24 h (Figure 36; Figure 38; and Figure 39, B, respectively). However, inducing 24 h after the start of the culture led in a fainter band in the purified fraction, likely due to the reduced exposure time to rhamnose. When rhamnose was added since the beginning, *C. necator* cells were exposed earlier and longer, ensuring expression activation. Additionally, *C. necator* cells induced at t_{ind}= 24 h might have allocated resources to biomass formation during these first 24 h, rather to protein biosynthesis , as suggested by Mühlmann et al. (2017).

Optimizing cultivation parameters is important for maximizing heterologous protein production in bacterial systems. In *E. coli*, the development of an automated induction profiling has enabled the identification of optimal production conditions for producing a fluorescent protein (Mühlmann et al., 2017). Similarly, in *C. necator* analysis and variations of process parameters has successfully increased biomass and terpene production (Becker et al., 2025). Becker et al. (2025), adjusted cultivation temperature and rhamnose concentrations to enhance production efficiency. While similar strategies

could be applied to improve $PuOx_{M1}$ yields in our system, the primary objective was not simply maximizing protein production but ensuring its functional application. Therefore, as long as a sufficient amount is produced for our intended use, extensive optimization was not a priority.

3.1.2.3 Exploring $PuOx_{M1}$ activity in *C. necator.*

Having analyzed $PuOx_{M1}$ production, the next key aspect was to assess $PuOx_{M1}$ activity. Activity assays for PuOx are commonly based on the detection of H_2O_2 as a byproduct, typically using a peroxidase-coupled system with 2,2'-azino-bis(3-ethylbenzthiazoline-6-sulphonic acid) (ABTS) as a chromogenic substrate (Childs & Bardsley, 1975; van Hellemond et al., 2008). Another strategy involves measuring O_2 consumption with a Clark electrode (Anyanwu et al., 2021; DeSa, 1972). However, the SDS-PAGE gels (Figure 34-Figure 38) revealed that the enzyme purification was not optimal and we decided not to work with the eluted fraction due to the potential presence of contaminants.

An alternative approach was to work with the soluble extract, as previously done for $IRED_{V8}$, to assess $PuOx_{M1}$ activity in an *in vitro* system. However, establishing an assay for PuOx in the soluble extract proved challenging. Measuring H_2O_2 production in the soluble fraction was unsuitable because of the presence of detoxifying enzymes in *C. necator*, such as peroxidase I (*katG*, KEGG database, entry H16_A2777), and superoxide dismutase (*sodA*, KEGG database, entry H16_A0610), which can be upregulated under certain stress conditions (Calvey et al., 2023; S.-E. Lee et al., 2009; Schwartz et al., 2009). The co-expression of peroxidase and superoxide dismutase in *C. necator* could interfere with the standard assay, particularly due to peroxidase activity, which would degrade H_2O_2 and lead to underestimation of PuOx activity.

As an alternative, we adapted a colorimetric method to assess PuOx activity in the soluble extract of *C. necator* using putrescine as a substrate. In the assay, putrescine is oxidized by purified PuOx, generating an unstable aldehyde that spontaneously cyclizes into an imine. The imine subsequently reacts with o-aminobenzaldehyde (o-ABA), forming a detectable colorimetric compound (Bachrach & Reches, 1966; Frydman et al., 1987). This colorimetric method was used by other studies to identify the formation of unsaturated *N*-heterocycles in the presence of purified PuOx from *R. erythropolis* (Anyanwu et al., 2021). We applied the assay in the soluble extract of the WT + PuOx strain. However, unexpected reactions were observed between the o-ABA and putrescine controls, raising questions about the stability of the method and reactivity of o-AB under the tested conditions. This method proved unsuitable for assessing $PuOx_{M1}$ activity in the soluble extract (data not-shown).

Other alternatives for testing activity without purified proteins include the solid-plate assay in a nitrocellulose membrane described by (Alexeeva et al., 2003). However, this assay primarily serves as a screening method for transformed colonies and is still based on H_2O_2 production and detection via peroxidase-coupled assays.

Further activity tests using either purified PuOx would be valuable to complete the protein characterization and determine whether the enzyme is active in *C. necator*.

3.1.3 Summary Chapter 1

Results Summary Chapter 1.

- Several strategies were tested for the heterologous production of NADH-dependent IRED ($IRED_{V8}$), and PuOx variant ($PuOx_{M1}$) in different *C. necator* strains.

$IRED_{V8}$

- Tested *C. necator* clones with GroESL co-expression and/or Δ*lon* did not present $IRED_{V8}$ production or activity in the soluble extract.
- $IRED_{V8}$ was actively produced in WT + IRED strain using the pKR broad-host plasmid and rhamnose induction.
    - The soluble extract presented an oxidoreductase activity of 0.18 ± 0.01 mU/mg.
    - Partially-purified $IRED_{V8}$ from WT + IRED presents a specific activity of 1.8 ± 0.1 U/mg.
    - Preliminary work was initiated for potential IREDs in *E. coli*. Further analyses are required to confirm IRED activity and integrate biotransformations in *C. necator* (Manuscript preparation as coauthor is ongoing)

$PuOx_{M1}$

- $PuOx_{M1}$ was produced in WT + PuOx strain using the pKR broad-host plasmid and rhamnose induction.
- $PuOx_{M1}$ activity assessment was not possible in the soluble extract of WT + PuOx strain.
- $PuOx_{M1}$ purification required further optimization to obtain a pure eluted fraction suitable for characterization.

Chapter 2 Development of the enzymatic cascade in *C. necator* under lithoautotrophic conditions.

The here described research was performed at RWTH Aachen University in collaboration with the INSA Toulouse. The following people were involved:

- **I.A. Castro González**: strain development and testing, sample analysis.
- D. De la Asunción Vest: Bachelor student under I.A. Castro-Gonzalez supervision, cloning and strain development.
- P. Schoenmakers: PhD student, support in sample analysis and strain development.
- J. Hattemer: student, support in sample analysis.

For subchapter 2.1, submitted manuscript:

- **I.A. Castro González**: Conceptualization, Methodology, Investigation, Data Curation, Writing—Original Draft
- P. Pijpstra: Methodology, Investigation
- S Guillouet, N. Gorret, and L Lauterbach: Conceptualization, Supervision, Funding acquisition, Writing—Review and Editing.

Biotransformations are innovative processes for the sustainable production of valuable industrial molecules, such as *N*-heterocycles. Previous works developed and optimized an enzymatic cascade in *E. coli* involving an engineered putrescine oxidase, $PuOx_{M1}$; and an imine reductase, IRED (Borlinghaus et al., 2019). Although the process achieved high product formation, it relied on the addition of expensive cofactors which could affect industrial scalability. To address this limitation, further studies developed an *in vitro* cascade using purified enzymes and introduced the soluble hydrogenase (SH) as a cofactor regeneration system (Al-Shameri et al., 2019, 2020). While these advancements demonstrated the feasibility of H_2 – driven enzymatic cascades, their full integration into whole-cell systems remains a challenge. To address this challenge, we proposed integrating $PuOx_{M1}$ and $IRED_{V8}$ in the lithoautotrophic bacterium *C. necator,* which contains the necessary metabolism to establish H_2-driven biotransformations.

Throughout Chapter 1, we studied the proteins $IRED_{V8}$ and $PuOx_{M1}$, and their heterologous production was demonstrated in different *C. necator* strains. In Chapter 2, we explore the potential of *C. necator* as a biotransformation platform by harnessing its lithoautotrophic metabolism to implement the H_2-driven enzymatic cascade for *N*-heterocycle production. This analysis was done in several steps.

In Subchapter 2.1, we first focused on preculture management for lithoautotrophic growth in *C. necator*. We examined the growth behavior of the wild-type *C. necator* strain in our standard minimal media supplemented with 0.4 % w/v fructose (FN media) or a mix 0.4% w/v glycerol with 0.05% w/v fructose (FGN_{mod}). Afterwards, we evaluated the effect of FN or FGN_{mod} medium on the transition to lithoautotrophic growth and establish a cultivation protocol.

In Subchapter 2.3, the optimized cultivation protocol was extended to engineered *C. necator* strains designed to co-produce $PuOx_{M1}$ and $IRED_{V8}$. Biotransformation assays were conducted under lithoautotrophic conditions to evaluate the *in vivo* performance of the full enzymatic cascade. Additionally, the IRED-catalyzed step was selected for further optimization and comparative analysis between heterotrophic and autotrophic biotransformation setups.

3.1.4 Glycerol-supplemented medium promotes transition of C. necator from heterotrophic to lithoautotrophic growth: Implications for putrescine toxicity studies.

Information from Subchapter 2.1 has been submitted for publication. Therefore, the sections (introduction, results and discussion, and conclusions) are structured in the form of a scientific article following the Journal guidelines. Materials and Methods are integrated in the respective section of this manuscript.

3.1.4.1 Abstract:

- Purpose: Biotransformations in the facultative chemolithoautotrophic bacterium, *Cupriavidus necator*, are gaining attention to obtain valuable industrial molecules. Diverse media elements have to be balanced to combine lithoautotrophic cultivations of *C. necator* and biotransformations. Few studies have focused on the management of precultures and the reported long lag phases in chemolithoautotrophic cultures.

- Methods: A small-scale lithoautotrophic system was adapted with a preculture step in glycerol-containing media to assist the transition towards the lithoautotrophic metabolism. Initial characterization of heterotrophic growth in *C. necator* was conducted by comparing minimal media containing fructose alone versus a combination of fructose and glycerol.

- Results: The presence of glycerol in the preculture medium reduced the lag phase during subsequent lithoautotrophic cultivation compared to precultures grown exclusively on fructose. The optimized system was applied to evaluate the physiological effects of a polyamine molecule, putrescine, in *C. necator*.

- Conclusion: The study provided valuable insights in the development of lithoautotrophic cultivation systems using *C. necator* as a platform organism

3.1.4.2 Introduction

Biotransformations play a crucial role in biotechnology, enabling the production of molecules with applications in pharmaceuticals, drug discovery, environmental technology, and industrial processes (Nag et al., 2024; Shanu-Wilson et al., 2020; Wandrey et al., 2000). Among these, H_2-driven biotransformations have gained increasing attention due to their ability to couple enzymatic reactions with H_2 as energy carrier as shown previously for enzymatic cascade for valuable *N*-heterocycles starting from diamines (Al-Shameri et al., 2019, 2020). These approaches utilized the potential of H_2 from clean energy sources, the ability to regenerate cofactors atom efficient, and the high specificity in enzymatic reactions (Al-Shameri et al., 2023; Lauterbach & Lenz, 2019).

One promising Knallgas bacterium for H_2-driven biotransformations and CO_2-based biosynthesis is Cupriavidus necator. This facultative chemolithoautotrophic bacterium is capable of using CO_2 as its sole carbon source, O_2 as electron acceptor and H_2 as electron donor (Lauterbach & Lenz, 2019; Pohlmann et al., 2006).

Hydrogen oxidation in *C. necator* is facilitated by two distinct energy-converting hydrogenases, both catalyzing the cleavage of H_2 into two protons and two electrons (Lauterbach & Lenz, 2013). The membrane-bound hydrogenase (MBH) transfers electrons derived from H_2 oxidation directly into the respiratory chain, contributing to the proton motive force necessary for ATP synthesis. In contrast, the cytoplasmic, NAD^+-reducing soluble hydrogenase (SH) directly couples the oxidation of H_2 with the reduction of NAD^+ to NADH. The produced NADH subsequently serves as a reducing equivalent for CO_2 fixation via the Calvin-Benson-Bassham cycle, and it contributes to ATP synthesis through electron transfer mediated by NADH-quinone oxidoreductase (Complex I) and other components of the respiratory chain (Lenz et al., 2015) (Lenz et al. 2014).

Traditionally known for its role in polyhydroxyalkanoate (PHA) production (Aliyu Alhafiz et al., 2025), *C. necator* has expanded its biotechnological applications over the years. *C. necator* has been engineered to produce a variety of bioproducts, including isopropanol (Garrigues et al., 2020; Grousseau et al., 2014); acetoin (Windhorst & Gescher, 2019); isobutanol and butanol (H. Li et al., 2012); mevalonate (Garavaglia et al., 2024); sucrose (Nangle et al., 2020); isoleucine and valine (L. Wang et al., 2024), and other products summarized by Y. Wang et al.(2024). Additional studies have demonstrated the feasibility of H_2-driven biocatalysis in resting *C. necator* cells for xylitol production (Jämsä et al., 2024) or isopropanol production (Teetz et al., 2022). Similarly, the use of H_2 as cofactor regeneration system was demonstrated in the asymmetric C=C bond reduction of unsaturated cyclic ketones with high enantiomeric excess in *C. necator* (Assil-Companioni et al., 2019). Despite its biotechnological potential, challenges persist in achieving robust and reproducible cultivation strategies that are compatible with industrial scale applications. In particular, the transition from heterotrophic to lithoautotrophic has been already reported as being slow translating in sometimes very long lag phase (Lambauer & Kratzer, 2022; Sonnleitner et al., 1979)

Previous studies have focused on optimizing *C. necator* cultivations under specific trophic conditions. Repaske et al. (1971) observed that the initial lithoautrophic growth in *C. necator* was dependent on

the availability of bicarbonate ions. More recently, Amer & Kim (2023) evaluated the effect of organic and gaseous substrates in different metabolic conditions in *C. necator*. They investigated the transit from heterotrophy to autotrophy or mixotrophy, and proposed a two-stage system to reduce the lag phase and reach high optical densities in conditions commonly used for PHA production. An optimized protocol developed by Gerlach et al. (2023) allowed the reduction of preculture time and ensure reproductible cultivations in a *C. necator* strain used for homologous overproduction of hydrogenases. However, few studies have directly addressed strategies to minimize the transition time towards lithoautotrophic metabolism, a crucial step for ensuring reproducibility and efficiency in H_2-driven bioprocesses.

In this study, we proposed a gas fermentation strategy incorporating a preculture step in glycerol containing medium to accelerate the adaptation towards lithoautotrophy. Glycerol is a poor carbon source for *C. necator* which induces very slow growth (González-Villanueva et al., 2019). This limited growth promotes CO2 fixation through the Calvin Benson-Bassham cycle (Strittmatter et al., 2022), while affecting key enzymes in the autotrophic metabolism. Transcriptomic analysis suggested that glycerol exposure upregulated the expression of hydrogenase genes (Jugder et al., 2015; Schwartz et al., 1998). Hydrogenase activity has also been reported to be enhanced in the presence of glycerol (Poladyan et al., 2019). We hypothesized that leveraging this metabolic shift during preculture would promote early expression of hydrogenases, facilitating a smoother transition into lithoautotrophy. We first examined the growth of the wild-type strain *C. necator* H16 in minimal media supplemented either with fructose (FN medium), or with a combination of glycerol and fructose (FGN_{mod} medium). These media were then used as precultures and their impact on lithoautotrophic cultivation was evaluated. Our results demonstrated that FGN_{mod} in the preculture phase modified the length of the lag/acceleration phase during lithoautotrophic growth.

The optimized cultivation strategy was subsequently applied to investigate the effect of a polyamine in *C. necator*. Polyamines play essential roles in microbial functions, for example in growth regulation stress responses, and biofilm formation (S. H. Kim et al., 2016; S.-K. Kim et al., 2015; Z. Liu et al., 2021). Besides their native roles, diverse polyamines can be used as biotransformation substrates to obtain pharmaceutical scaffolds (Al-Shameri et al., 2019; Borlinghaus et al., 2019). Polyamines levels in bacteria are tightly regulated to maintain cellular homeostasis (Gevrekci, 2017) and while the addition of natural polyamines such as putrescine did not present a significant impact on bacterial cell growth or membrane stability (Kwon & Lu, 2006), their exogenous presence has not been evaluated in detail in *C. necator*. Understanding the impact of a polyamine such as putrescine in *C. necator* is essential for future applications in engineered biotransformations. The gas fermentation strategy allowed us to evaluate the physiological effects of putrescine in *C. necator*. Growth and cytometry analysis indicated that putrescine is not toxic at high concentrations, but induces an extended lag phase and morphological changes, suggesting a possible stress response in *C. necator*. Our results provided a foundation for evaluating biomolecules in *C. necator*, demonstrating its suitability as a host for H_2 driven biotransformations.

3.1.4.3 Results

Characterization of *C. necator* H16 in FN and FGN_{mod} media.

The growth of *C. necator* H16 wild-type was first analyzed in FN minimal media, containing 4 g L^{-1} fructose. The Cell Growth Quantifier (CGQ, Scientific Bioprocessing) was used to characterize the growth, obtaining a maximal specific growth rate (μ_{max}) of 0.28 ± 0.001 h^{-1} (Figure 40).

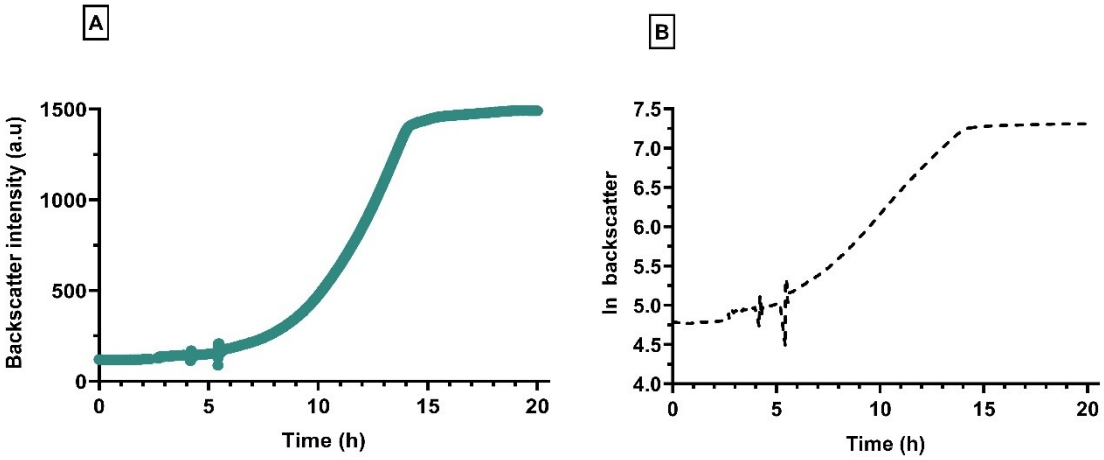

Figure 40. Growth characterization of *C. necator* in FN medium using the CGQ system (A). The μmax is calculated from the natural logarithm (ln) using a linear regression for one sample, with a R^2 = 0.99 (B).

The growth in FGN_{mod} minimal medium was also evaluated as an alternative for the heterotrophic growth. This medium differs from FN in that it contains only 0.5 g L^{-1} fructose and an additional 4 g L^{-1} glycerol. The characterization in FGN_{mod} was performed in triplicates in 500 mL flasks. Two growing phases were identified: a short growth of approximately 5 hours was observed for growth with fructose and the remaining time the strain grew on glycerol (Figure 41, A). The μ_{max} was calculated for each growing phase (Figure 41, B). The WT strain presented a μ_{max} during the short fructose phase of 0.24 ± 0.01 h^{-1}, and in the long glycerol phase of 0.03 ± 0.0003 h^{-1} (Table 17).

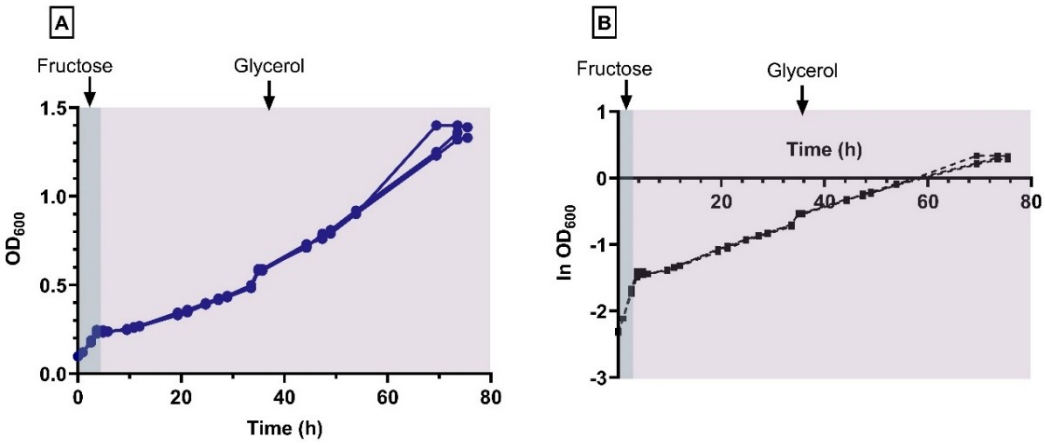

Figure 41. Growth characterization of *C. necator* in FGN_{mod} medium : the growth was followed by measuring the OD_{600} of three replicates. Replicates were inoculated from a single preculture in FN medium (A). The grey area represented growth on fructose, and purple area on glycerol. The µmax was calculated for each replicate from the natural logarithm (ln) using a linear regression, with a R^2 = 0.99 (B).

Table 17. Growth characterization of *C. necator* WT in FN or FGN_{mod} : The maximal growth rate (μ_{max}, h^{-1}) is obtained for each sample, one replicate for FN and three replicates for FGN_{mod}. Two μ_{max} values are indicated for the FGN_{mod} corresponding to the growth in fructose (0.5 g L^{-1}) and glycerol (4 g L^{-1}). The average μ_{max} is indicated for the replicates in FGN_{mod}.

	FN	**FGN_{mod} (fructose/glycerol)**		
Culture No.	1	1	2	3
μ_{max} (h^{-1})	0.28	0.26/ 0.03	0.25/0.03	0.23/0.03
Mean μ_{max} (h^{-1})			0.24/0.03	
Standard error	0.001		0.01/0.0003	

The *C. necator* strain exhibited comparable growth in FN and during the short fructose phase in FGN_{mod}, with a μ_{max} of 0.28 ± 0.001 h^{-1} and 0.24 ± 0.01 h^{-1}, respectively. In contrast, the growth in glycerol in FGN_{mod} was extremely slow, presenting a μ_{max} of 0.03 ± 0.0003 h^{-1}. This slow growth is consistent with the generally low growth rates observed in *C. necator* with glycerol and is attributed to the limited efficiency of its glycerol metabolism (González-Villanueva et al., 2019; Strittmatter et al., 2022).

FGN_{mod} promotes the transition to lithoautotrophic growth in *C. necator* H16.

A customized system for small-scale autotrophic cultivations was developed and implemented by Di Bisceglie et al. (2025) and Weickardt et al.(2025) to characterize the growth and performance of an isopropanol-producing and a PHA-deleted *C. necator* strains during gas fermentation.

The protocol for lithoautotrophic cultivation includes a series of precultures to prepare the metabolism of *C. necator* before entering the gas-growing phase (Figure 42). The protocol was modified using AUT media for the gas fermentation (minimal media containing 2 g L^{-1} NH_4Cl). In the final step of the seed cultivation, we compared minimal media containing either 4 g L^{-1} fructose (FN) or a mixture 4 g L^{-1} glycerol with 0.5 g L^{-1} fructose (FGN_{mod}) as preculture options. The medium FGN_{mod} was developed for the production and purification of MBH and SH (Goris et al., 2011; Lenz et al., 2018). Therefore, FGN_{mod} was selected as an alternative to FN due to its potential to promote hydrogenases production and facilitate the transition to lithoautotrophic metabolism.

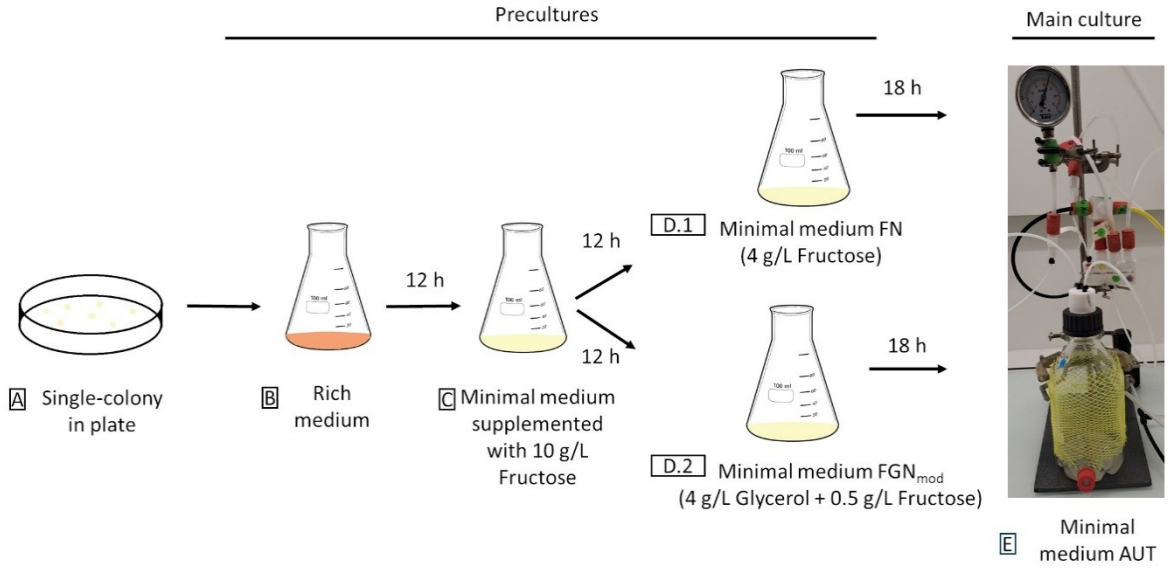

Figure 42. Seed train for lithoautotrophic cultivation of *C. necator*, comparing FN and FGN_{mod} : Diagram with the schematic steps for gas fermentation. A single colony was obtained (A) and used to inoculate 10 mL of the rich medium, TSB without dextrose (B). After 12 h, 25 mL of minimal medium with 10 g L^{-1} of fructose was inoculated (C). The culture was incubated during 12 h and used to inoculate 50 mL FN (D.1) or FGN_{mod} (D.2). Each preculture was used to inoculate 50 mL AUT media for the gas fermentation (E). For each step, 10 % v/v was used as inoculum; the cultures were incubated at 30°C, 140 rpm, the gas fermentation was made in a 1 L bottle to guarantee a larger headspace for gas supply.

Figure 43 illustrates the growth behavior of *C. necator* under lithoautotrophic conditions. All cultures started at an OD_{600} of 0.1 and reached a final OD_{600} between 1.2 and 1.6. Previous studies have established the relationship between biomass concentration and OD_{600} under specific media conditions. In their system, *C. necator* reached a biomass concentration of 2 g_{CDW} L^{-1} which corresponds to an OD_{600} of 1, when the nitrogen source was limited to 1 g/L. The AUT minimal media

contains 2 g/L of nitrogen source and a theoretical maximum biomass concentration of 4 g/L would be expected, corresponding to an OD_{600} of 2. The fact that none of our tested conditions reached this OD suggested that another component may have been limiting the growth. The gas phase was replenished each time the pressure dropped around 0.5 bar, theoretically preventing gas limitation. However, gas transfer efficiency into the liquid phase must also be considered. It is likely that gas transfer was impacting the cultivation, more likely with oxygen as the primary limiting component due to its lower concentration relative to other gases as reported in Di Bisceglie et al. (2025).This growth limitation was consistently observed across the experiments.

To evaluate the difference between the growing conditions, the maximum specific growth rate (μ_{max}, h^{-1}) was calculated for every replicate (Figure 43, D and H) and their means were compared. An average μ_{max} of 0.08 ± 0.02 h^{-1} was obtained when FN was used as preculture medium, and 0.08 ± 0.01 h^{-1} was shown for FGN_{mod} as preculture (Table 18). For an exploratory comparison, a preculture grown in FN was also used to inoculate a lithoautotrophic cultivation, where growth was automatically monitored using the CGQ system. In this case, the bottle was filled with the same initial gas composition, but no atmosphere exchange was made. This cultivation resulted in a μ_{max} of 0.09 ± 0.0003 h^{-1} (data not shown), closely similar to the values obtained by OD measurements indicated in Table 18.

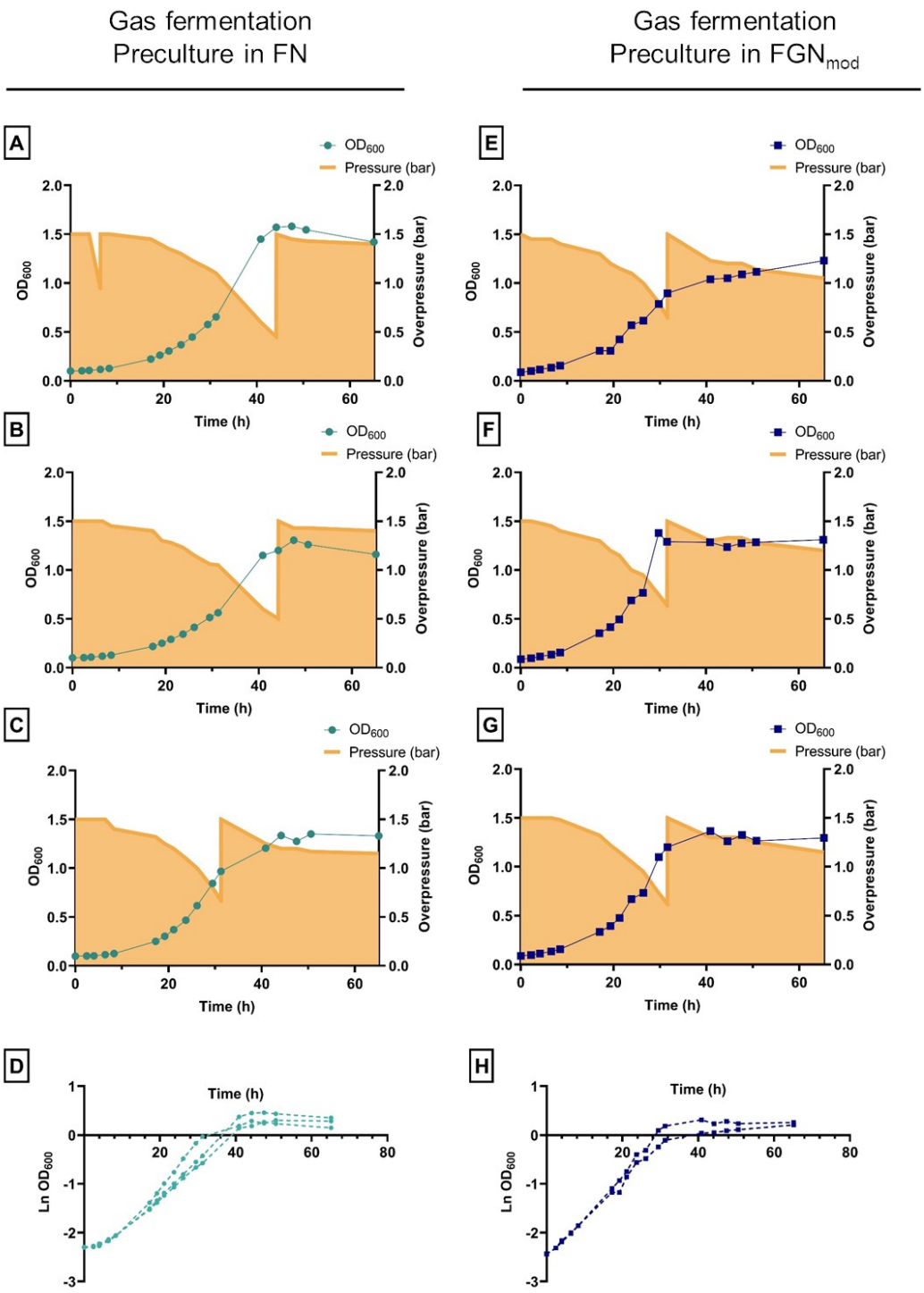

Figure 43. Effect of FGN_{mod} and FN as preculture media on the lithoautotrophic growth of *C. necator* : The bacteria were precultured in minimal media FN (A-D), or FGN_{mod} (E-H) before the lithoautotrophic cultivation. Cultures were performed in triplicate and the growth was followed by measuring absorbance (OD600) and overpressure (bar). The initial gas composition was %H_2:O_2:CO_2, 74:8:18 at an overpressure of 1.5 bar. When the pressure decreased at around 0.5 bar, the atmosphere was exchanged with a new mixture of % H_2:O_2:CO_2, 70:12:18 to ensure sufficient O2 in the medium (Weickardt et al., 2025). The µmax as calculated for each replicate by using the natural logarithm (ln) and linear regression with a R^2 = 0.99 (D and H).

Table 18. Assessment of lithoautotrophic growth in *C. necator* WT following precultivation in FN or modified FGN medium : The maximal growth rate (μ_{max}, h^{-1}) was calculated for each biological replicate, and the mean was compared using an unpaired t-test with a significance level of α= 0.05. No significant difference was observed between the average μ_{max}. The standard deviation was calculated for the replicates.

	Preculture in FN			**Preculture in FGN_{mod}**		
μ_{max} (h^{-1})	0.07	0.07	0.10	0.08	0.09	0.08
Mean μ_{max} (h^{-1})		0.08			0.08	
Standard deviation		0.02			0.01	

Although no significant difference was observed between the μ_{max}, we identified that the strain precultured in FGN_{mod} entered the exponential phase earlier in the lithoautotrophic cultivation compared to the one precultured in FN (Figure 44). When FN was used as preculture, the strain encountered a lag phase of around 4-5 hours whereas the strain pre-grown in FGN_{mod} started growing without lag phase.

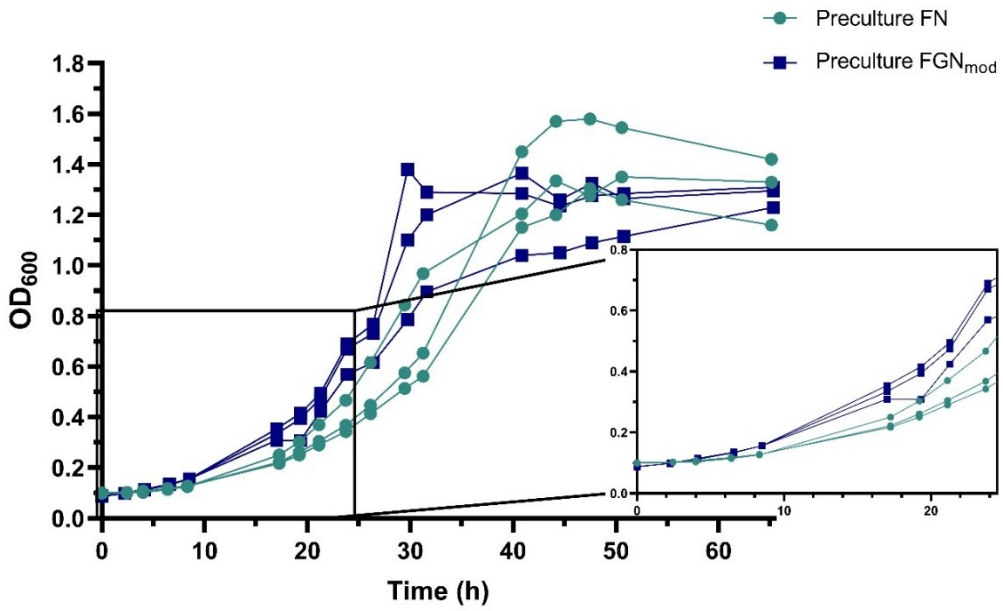

Figure 44. Comparative analysis of chemolithotrophic growth of *C. necator* pre-grown on FN or FGN_{mod} medium : Triplicate cultures were inoculated from a single preculture either on FN or FGNmod medium.

The growth difference might be attributed to the physiological state of the start inoculum which modified the length of the lag/acceleration phase. All replicates were inoculated an OD_{600} of 0.1 after 17 h in preculture. By this time, the inoculum coming from FGN_{mod} entered the growth in glycerol (

Figure 41, A). Glycerol is known as an poor carbon source for *C. necator*, and to compensate the energy deficiency, *C. necator* produces hydrogenases even if no H_2 is present (B. Friedrich & Schwartz, 1993; Strittmatter et al., 2022). When *C. necator* was cultured in 2 g L^{-1} fructose and 2 g L^{-1} glycerol, the hydrogenase activity increased once the bacterium was growing on glycerol (Bürstel, 2013; Friedrich et al., 1981). Furthermore, it has been also shown the importance of *cbbX* genes, coding for Rubisco activases, on growth on glycerol, which is highly dependent on efficient carbon fixation via CBB cycle. Deletion of both *cbbX* copies led to severe reduction in growth and glycerol consumption (Strittmatter et al., 2022). Compared to fructose, growth on glycerol is accompanied by lower intracellular PEP content, which is known to exert feedback control on CBB cycle through the inhibition of CbbR activation function on the *cbb* operon (Bowien & Kusian, 2002). By inducing the hydrogenase production and the activity of RuBisCO with the presence of glycerol in the medium FGN_{mod}, *C. necator* could be better prepared to transition to a lithoautotrophic metabolism and achieved an earlier exponential growth.

Diverse cultivation strategies for *C. necator* have been reported in the literature, with various media available depending on the specific cultivation objectives (Aliyu Alhafiz et al., 2025). Minimal media such as FN and FGN are mainly used for heterotrophic growth (Friedrich et al., 1981; Friedrich, 1982)

while FGN_{mod} medium was designed as a culture medium to purify SH (Goris et al., 2011; Lenz et al., 2018). However, optimization of preculture conditions in *C. necator* remains underexplored. Gerlach et al., (2023) addressed this gap by proposing a sequential preculture approach for cultivation of *C. necator* under heterotrophic conditions. They demonstrated the benefits of a two-step strategy in terms of time and reproducibility. Our study focused on optimizing preculture conditions for gas fermentation. By incorporating FGN_{mod} medium into a three-preculture strategy, we may have accelerated adaptation to lithoautotrophic metabolism and minimized the lag/acceleration phase during gas fermentation. The seed train including FGN_{mod} was retained for subsequent experiments, offering an efficient workflow to study lithoautotrophic cultivations.

The seed train using FGN_{mod} allows the study of putrescine toxicity in *C. necator* during lithoautotrophy.

Having demonstrated that glycerol supplementation during preculture facilitates the transition from heterotrophic to lithoautotrophic growth in *C. necator*, this optimized cultivation protocol was subsequently employed to investigate the physiological impacts of putrescine exposure. Utilizing this strategy enabled a detailed examination of putrescine toxicity under heterotrophic and lithoautotrophic growth conditions. Polyamines such as putrescine, are molecules involved in a variety of cellular processes and their levels are strictly regulated by biosynthetic pathways and cellular uptake (Gevrekci, 2017). Since putrescine supplementation could influence cellular metabolism, it is essential to evaluate its potential effects before integrating it into an enzymatic cascade.

As a control experiment, we first examined the growth behavior of *C. necator* in heterotrophic conditions using FN medium supplemented with increasing concentrations of putrescine. Growth was monitored, and the results are presented in Figure 45. The WT strain exhibited comparable growth pattern across all tested conditions, with a lag phase of approximately 10 hours, consistent with previous characterizations in FN medium (Figure 40). By the end of the cultivation period, cultures supplemented with 0, 2, and 10 mM putrescine reached similar backscatter intensity values, while the culture containing 15 mM putrescine displayed a slightly lower signal Figure 45, A). The μ_{max} was determined for each condition (Figure 45, B) and compared in Table 19. The control condition (0 mM putrescine) exhibited a μ_{max} of 0.3 ± 0.001 h^{-1}, closely matching the 0.28 ± 0.001 h^{-1} obtained during the first FN characterization (Table 17). The growth rates observed with 2, 10, and 15 mM putrescine were similar, indicating that putrescine does not inhibit *C. necator* growth under these conditions (Figure 45).

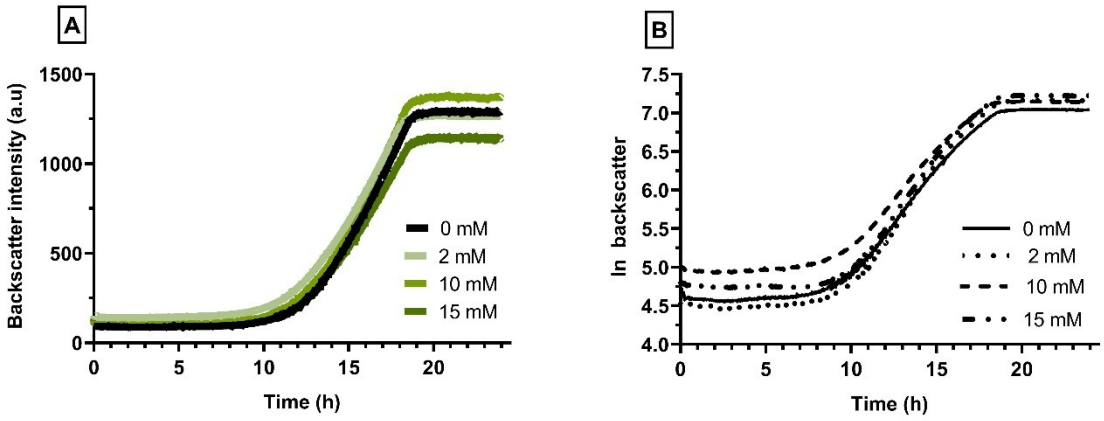

Figure 45. Heterotrophic cultivation of *C. necator* in the presence of putrescine : *C. necator* H16 was cultured in FN medium supplemented with 0, 2, 10 or 15 mM of putrescine for 24 h. Growth was monitored via backscatter light using the CGQ (Scientific Bioprocessing). All cultures were inoculated from a single preculture using FN media (A). The µmax was determined for each replicate from the natural logarithm (ln) using linear regression, with a R^2 = 0.99 (B).

The optimized seed train for lithoautotrophy was then used to assess *C. necator*'s growth in the presence of varying putrescine concentrations. The concentration of putrescine was also increased up to 100 mM under lithoautotrophic conditions to evaluate potential stress responses and physiological adaptations of *C. necator* at elevated polyamine levels. The WT strain was cultivated with 5, 10, or 100 mM putrescine, and growth was monitored by measuring OD_{600} (Figure 46), and the μ_{max} was calculated (Table 19).

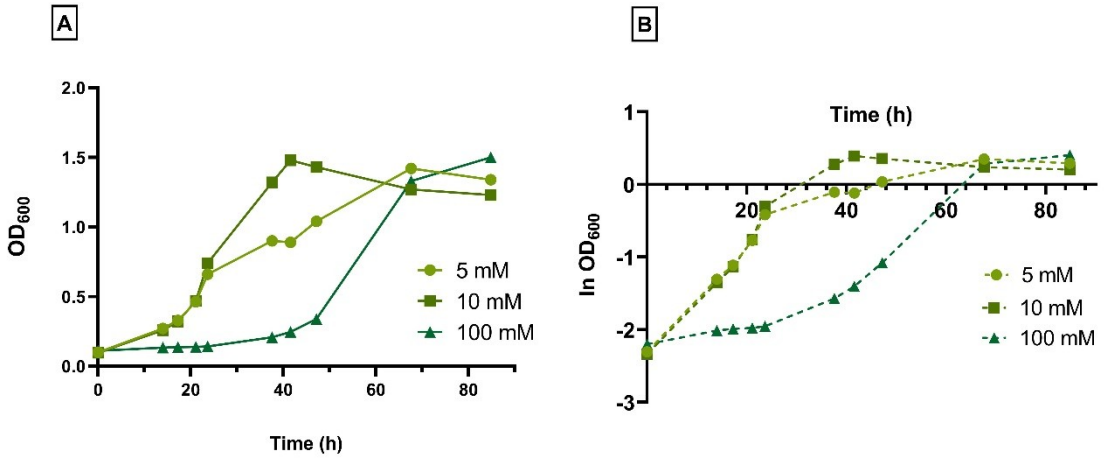

Figure 46. Chemolithoautotrophic cultivations of *C. necator* in the presence of putrescine : *C. necator* was cultivated during gas fermentation with 5, 10 and 100 mM of putrescine. One culture is show for each concentration (A) All cultures were inoculated from a single preculture using FGN_{mod} media. The μ_{max} is calculated for each sample from the natural logarithm (ln) using a linear regression with a R^2 = 0.99 (B).

Table 19. Specific growth rates of *C. necator* during heterotrophic and lithoautotrophic cultivations in the presence of putrescine . The μ_{max} (h^{-1}) was determined for each condition based on the linear growth phase of the gas culture. The μ_{max} at 0 mM* is reported from Table 18.

	Heterotrophic				**Chemolithoautotrophic**			
Putrescine	**0 mM**	**2 mM**	**10 mM**	**15 mM**	**0 mM***	**5 mM**	**10 mM**	**100 mM**
μ_{max} (h^{-1})	0.30	0.24	0.28	0.26	0.08	0.10	0.08	0.06
Standard dev	0.001	0.001	0.001	0.001	0.01	0.18	0.11	0.01

A comparable growth trend was observed when the WT strain was cultured in gas with 5 mM and 10 mM putrescine, exhibiting similar μ_{max} of 0.10 ± 0.18 $h^{-1}$and 0.08 ± 0.11 h^{-1}, respectively. In contrast, exposure to 100 mM putrescine resulted in significantly delayed growth, with a prolonged lag phase of nearly 40 hours. Remarkably, this high concentration of putrescine did not appear to be lethal to *C. necator*, as growth resumed after the lag phase with slightly lower μ_{max} of 0.06 ± 0.01 h^{-1}, and ultimately reached a final OD comparable to the other conditions.

To further characterize the impact of putrescine on cell's physiology, samples were taken at 21, 41 and 68 h and analyzed in terms of viability and morphology. These samples were treated with propidium iodide (PI) to assess the cell's permeability as a marker of viability and analyzed with flow cytometry (Figure 47, A-B). Comparison with the PI-permeable and non-permeable cell controls showed that the WT cells had mostly non permeabilized membranes under all the tested conditions. This indicated that there was no effect on cell's viability during the cultivation in presence of putrescine. However, there was an effect on the morphology of the cells when they were cultured with 100 mM putrescine (Figure 48). We observed that at 21 h the cells had similar size (indicated by the width parameter), but at 41 h and 68 h with 100 mM putrescine, the cells started to elongate as indicated with the shift to longer width values. This change of cell morphology could be a cell–response to stress caused by the high concentration of putrescine in the media, which was no present at 5 or 10 mM of putrescine.

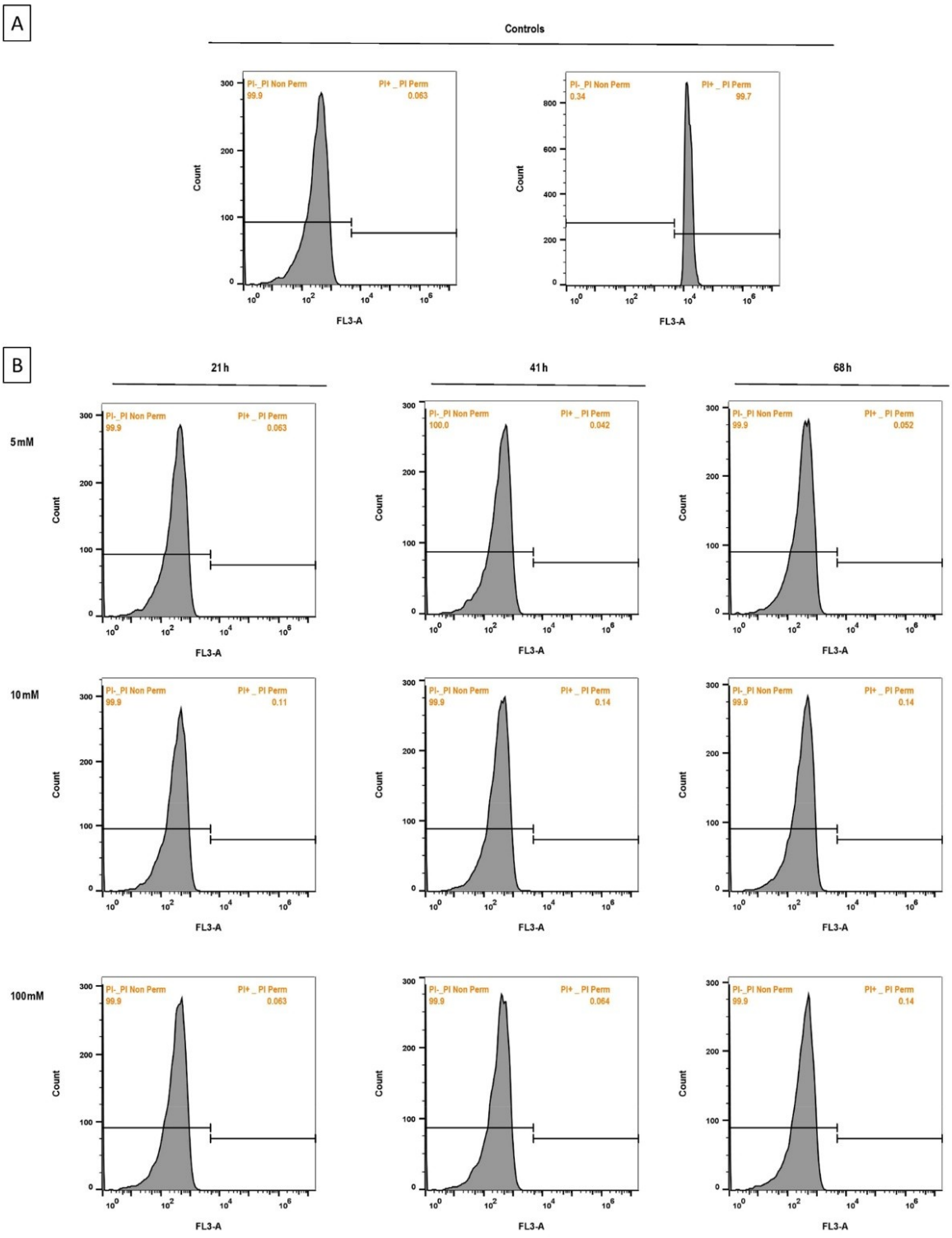

Figure 47. Viability of *C. necator* during chemolithoautotrophic growth with varying concentrations of putrescine : Cell permeability was assessed with propidium iodide staining (FL3 channel) and the single-cell count was plotted in forward scatter (FSC) vs side scatter (SSC). A culture with *C. necator* without putrescine was used as referencing point for PI Non-Permeable (A, left) and a treatment with

isopropanol is used as reference for PI Permeable (A, right). The permeability of cells was studied with 5, 10- and 100-mM putrescine during 21, 41 and 68 h.

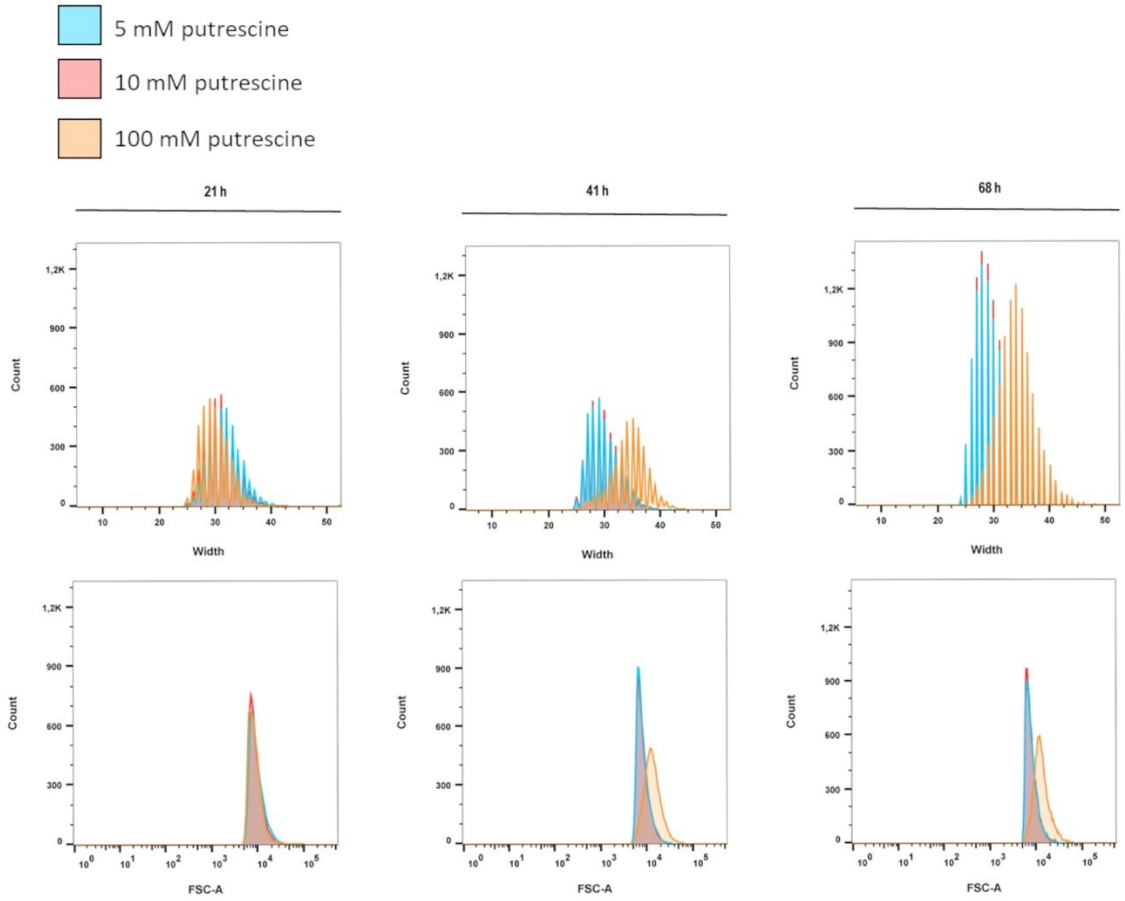

Figure 48. Effect of putrescine on morphology of *C. necator* during chemolithoautotrophic growth with varying concentrations of putrescine : Flow cytometry analysis of cell population based on FSC and pulse width. Cells were analyzed to assess the effect of 5 (blue), 10 (red) and 100 (orange) mM putrescine after 21, 41 and 68 h.

3.1.4.4 Conclusions

The use of glycerol in the preculture phase shown to be an effective strategy to control the start of *C. necator* lithoautotrophic cultures. When the strain was pre-grown in FGN_{mod} medium, *C. necator* was able to transition directly into lithoautotrophic conditions, shortening the lag phase. The optimized cultivation strategy was used to investigate the physiological state of *C. necator* during gas fermentation in the presence of putrescine. Our studies demonstrate that putrescine is not toxic for *C. necator* in the used concentration. However, high putrescine concentrations extended the lag phase in the gas fermentation and reduced slightly the growth rate. The most noticeable impact of high putrescine concentrations was on cell morphology, as cells became elongated, indicating a possible stress response. Putrescine is a relevant polyamine with potential applications in biotransformations

to produce valuable fine chemicals, and these findings provide a foundation for future studies on the integration of putrescine in *C. necator* biotransformations. The impact of putrescine was assessed only under growth, cell viability and morphology. Additional studies of polyamine degradation or effects in metabolic pathways remain to be investigated. Expanding these analyses will be crucial to fully establish *C. necator* as a robust biotransformation platform.

3.1.5 Putrescine transport in *C. necator: in-silico* analysis

Polyamines play important roles in bacterial metabolism, such as structural or regulatory molecules, and alternative nitrogen sources. Krysenko & Wohlleben (2022), summarized various metabolic function of polyamines, and mentioned key transporters required for their assimilation. Polyamine transport systems are required to maintaining intracellular polyamine levels and have been targets for metabolic engineering to enhance putrescine production in *E. coli* (Qian et al., 2009).

In *E. coli*, several transport systems for putrescine have been characterized, notably PotE, a putrescine/ornithine antiporter, and PuuP, a putrescine importer. Additionally, *E. coli* utilizes CadB, a cadaverine/lysine antiporter, which facilitates both the uptake and excretion of cadaverine. CadB operates via a proton motive force and plays a significant role in cellular responses to acidic stress (Soksawatmaekhin et al., 2004). In previous studies, *E. coli* cells expressing *puox* gene from *R. erytropolis* demonstrated the biotransformation of 5 mM, suggesting effective cadaverine trough CadB (Anyanwu et al., 2021).

We assessed the presence of analogous transport systems in *C. necator* with an *in-silico* analysis. Sequencing homology analyses were performed with BlastP, the amino acid sequences of CadB, PotE and PotA from *E. coli* were searched against the *C. necator* H16 genome. Resulting homologous proteins are listed in Table 20.

The blasting analyses predicted protein homologs, indicating the potential for similar diamine transport mechanisms in *C. necator* H16. In addition, search in KEGG database identified the presence of 11 putative spermidine/putrescine transports systems in *C. necator* H16 genome (Table 21).

Furthermore, to evaluate whether putrescine could be consumed by *C. necator*, a new heterotrophic cultivation experiment was performed. In this case, the fructose content (4 g/L) in the FN medium was replaced with the same amount of putrescine, and 50 mL of medium was inoculated with the WT strain at an OD_{600} of 0.1. No growth was observed after almost two days with putrescine as sole carbon source, while WT strain in FN medium presented growth. This result suggests that *C. necator* is unable to utilize putrescine as sole source of carbon for biomass growth.

Table 20. Predicted transport systems for putrescine in *C. necator*: amino acid sequence alignment of CadB, PotE and Pot A from *E. coli* strain in *C. necator* H16 genome . BlastP is performed from NCBI database. The e-value is a statistical measure that estimates the probability of a comparable alignment occurring by chance with the calculated score or higher. Lower e-value indicate a significant similarity between the compared sequences. Protein code from UniPot data base is indicated for *E. coli* proteins. Information from *C. necator* genome is included from KEGG database. Acronyms: acid-polyamine-organocation APC, transporter; amino acid transporter, ATT; ATP-binding cassette, ABC

Origin bacteria	Protein	UniProt code	Protein found in *C. necator* H16	e-value	Information on *C. necator* H16
E. coli K12	Cadaverine/lysine antiporter (CadB)	P0AAE8	Amino acid permease	$4x10^{-8}$	Annotated predicted protein as APC from the AAT family. Located in chromosome 2, locus CAJ97254, gene h16_B2472.
	Putrescine transporter (PotE)	P0AAF1	Amino acid permease	$1x10^{-9}$	Annotated fragment of ABC-type transport system, periplasmic component from APC family Located in chromosome 2.
	Spermidine/putrescine import ATP-binding protein (PotA)	P69874	ABC-type transporter, ATPase component	$4\text{x}10,^{-93}$	Annotated as putative predicted protein. Located in chromosome 1.

Table 21. Putative putrescine transport in *C. necator* : non-exhaustive list of genes related to putrescine transport in *C. necator* H16 with their function. Examples obtained from KEGG database

KEGG Entry	Putative encoded function
H16_B0453	Spermidine/putrescine transport system permease protein
H16_B0454	
H16_B1601	
H16_B1602	
H16_B1830	
H16_B0455	Spermidine/putrescine transport system substrate-binding protein
H16_B1600	
H16_B1828	
H16_B0462	Spermidine/putrescine transport system ATP-binding protein
H16_B1603	
H16_B1829	

3.1.6 Biotransformation from putrescine into pyrrolidine.

New plasmids were constructed to co-express the target genes by two different expression strategies: both genes $ired_{V8}$ and $puox_{M1}$ contained in one single plasmid, or each gene carried on separate plasmids.

To construct one plasmid containing with both genes, the plasmid pDA4 and pAA56 were used (Figure 18, and Figure 32, respectively). Both plasmids have a pKR-backbone and the $puox_{M1}$ was transferred from pDA2 to pAA56. Briefly, a segment containing *rha*B promoter and $puox_{M1}$ from pDA2 was amplified by PCR adding a second XbaI-site in position 5'-terminal. The plasmid pAA56 was digested with XbaI, and ligated with the amplified segment as described in Materials and Methods 2.1 DNA cloning.

The resulted pDA4 plasmid (Figure 49) was transformed in *E. coli*, and colonies were screened. The plasmid was extracted from selected *E. coli* colonies and the $ired_{V8}$ and $puox_{M1}$ sequences were confirmed by sequencing.

The plasmid pDA4 with confirmed sequences was transformed in *C. necator* and colonies were isolated on FN plates containing Tet resistance. Few colonies grew and the plasmid was extracted directly from *C. necator* colonies for verification. For screening, short segments starting from the middle of ired_{V8} (oIC81), and covering the beginning of $puox_{M1}$ (oIC82) were used to verify the correct position of $puox_{M1}$ gene. The colony with the correct position was chosen for growth in selective media and further gas fermentation. The resulting strain was WT x pDA4 (WT + IRED + PuOx).

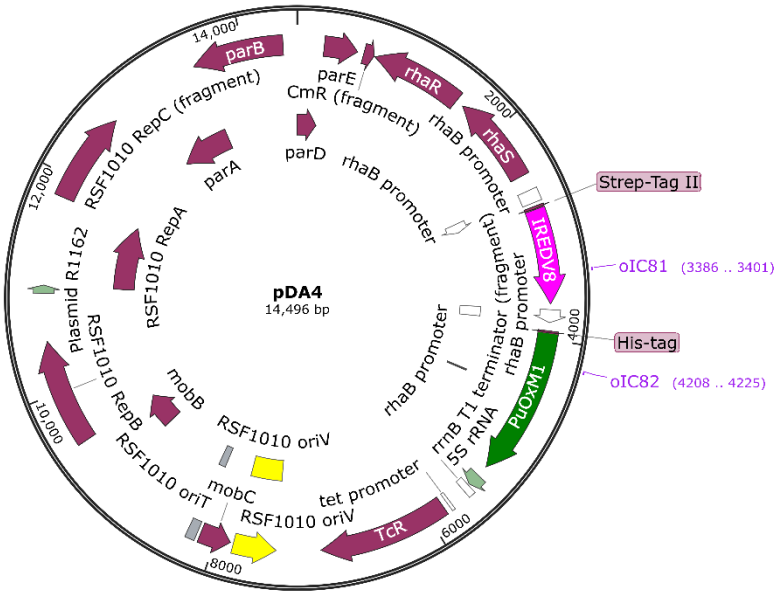

Figure 49. Plasmid map of pDA4. Primers used for screening are shown. $IRED_{V8}$ contains Strep-Tag and $PuOx_{M1}$ contains His-tag.

To obtain a two-plasmid system in one strain, a new plasmid was constructed. As described in Materials and Methods 2.1 DNA cloning, pEG19 (Figure 19) and pBAD18_$PuOx_{M1}$ (Figure 50) were used. The *groEL* gene in pEG19 backbone was exchanged by *puox*$_{M1}$ gene using the restriction sites EcoRI and HindIII present in both constructs. Fragments were extracted from gel and ligated resulting in the new plasmid pDA5 (Figure 51).

The pDA5 plasmid now containing *puox*$_{M1}$ was electroporated simultaneously along with pAA56 in *C. necator*. The transformed colonies were screened towards the resistance to Kan and Tet antibiotics. The resulting strain was WT x pAA56 x pDA5 (WT+ IRED+ PuOx -2)

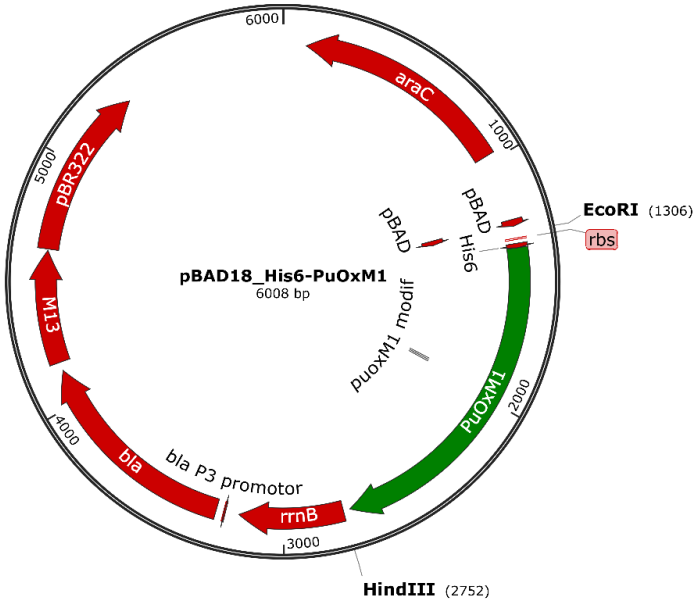

Figure 50. Plasmid map of pBAD18 with $PuOx_{M1}$ (Borlinghaus et al., 2019). Restriction sites for EcoRI and HindIII are indicated. Plasmid maps is generated with SnapGene®.

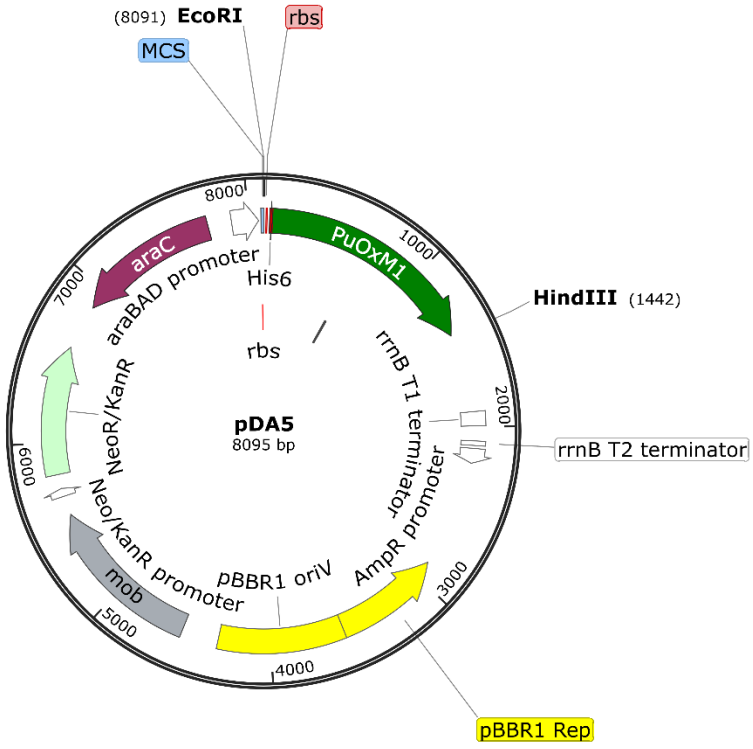

Figure 51. Plasmid map pDA5 containing $PuOx_{M1}$. Restriction sites for EcoRI and HindIII are indicated. Plasmid maps is generated with SnapGene®.

The new strains WT + IRED + PuOx, and WT+ IRED+ PuOx -2 were tested for autotrophic growth and biotransformation of putrescine to pyrrolidine. Seed cultures were prepared before gas fermentation as previously described, with variations on the preculture time and using FGN_{mod} as the final preculture step (Materials and Methods, 2.3.5.1 protocol performed at INSA).

We observed that precultures of the strain WT + IRED + PuOx required 3 days to grow in the first TB preculture. In comparison, the WT and WT+ IRED+ PuOx -2 strains grew overnight in the same media. For gas fermentation, all cultures were inoculated at 0.1 OD_{600} and grew at 30°C. An exception was observed for the strain WT+ IRED+ PuOx -2, which did not present any growth even after three days in gas fermentation. The strain was possibly under high metabolic burden caused by the different plasmids and antibiotics (Kan and Tet), and the strain WT + IRED + PuOx-2 was not further evaluated for biotransformation. Another trial was performed to grow the strain WT + IRED +PuOx-2 in autotrophy using the MIT medium (Di Bisceglie et al., 2025), a variation of minimal medium for *C. necator*. Similar as before, after 44 h of cultivation no growth was observed. Nonetheless, we observed that the strain WT + IRED + PuOx-2 restarted growth when MIT medium was supplemented with 4 g/L fructose. This may suggest that the strain WT + IRED +PuOx-2 had difficulties to grow in the specific gas fermentation setup (Figure 42); however, it was able to restart growing with heterotrophic conditions (Figure S. 3).

Protein expression was induced with 12 mM rhamnose in the remaining strains once they reached an OD_{600} of ~0.6. To optimize protein production, we tested two different temperature and the cultures were grown either at 30°C or 22°C during this phase. After 16 hours, biotransformation was initiated by adding 10 mM putrescine as the substrate, with all cultures maintained at 30°C. Supernatant samples were taken at 0, 16, 24, and 48 hours after putrescine addition to monitor conversion over time (Figure 52, black arrows in panels A-D).

As detailed in Figure 52-E, the strains exhibit similar growth patterns up to the induction point due to their shared genetic background. After induction, the growth patterns varied based on temperature. When maintained at the same temperature, the control strain WT and the strain WT + IRED + PuOx exhibit comparable growth. When the temperature was maintained at 30°C, the strains reached a maximum OD_{600} of approximately 1.3 within 40 hours, followed by a stationary phase that persisted until the end of cultivation. Cultures where the protein production was performed at 22°C showed a slower growth, consistent with the anticipated reduction in metabolic rate at lower temperatures. However, when shifted to 30°C, these cultures continued to grow, eventually reaching a similar maximum OD_{600} of 1.3, with the exception of the WT strain, which reached an OD of 1.6. This difference may reflect the experimental variability of the cultivation, which was also observed in Figure 52.

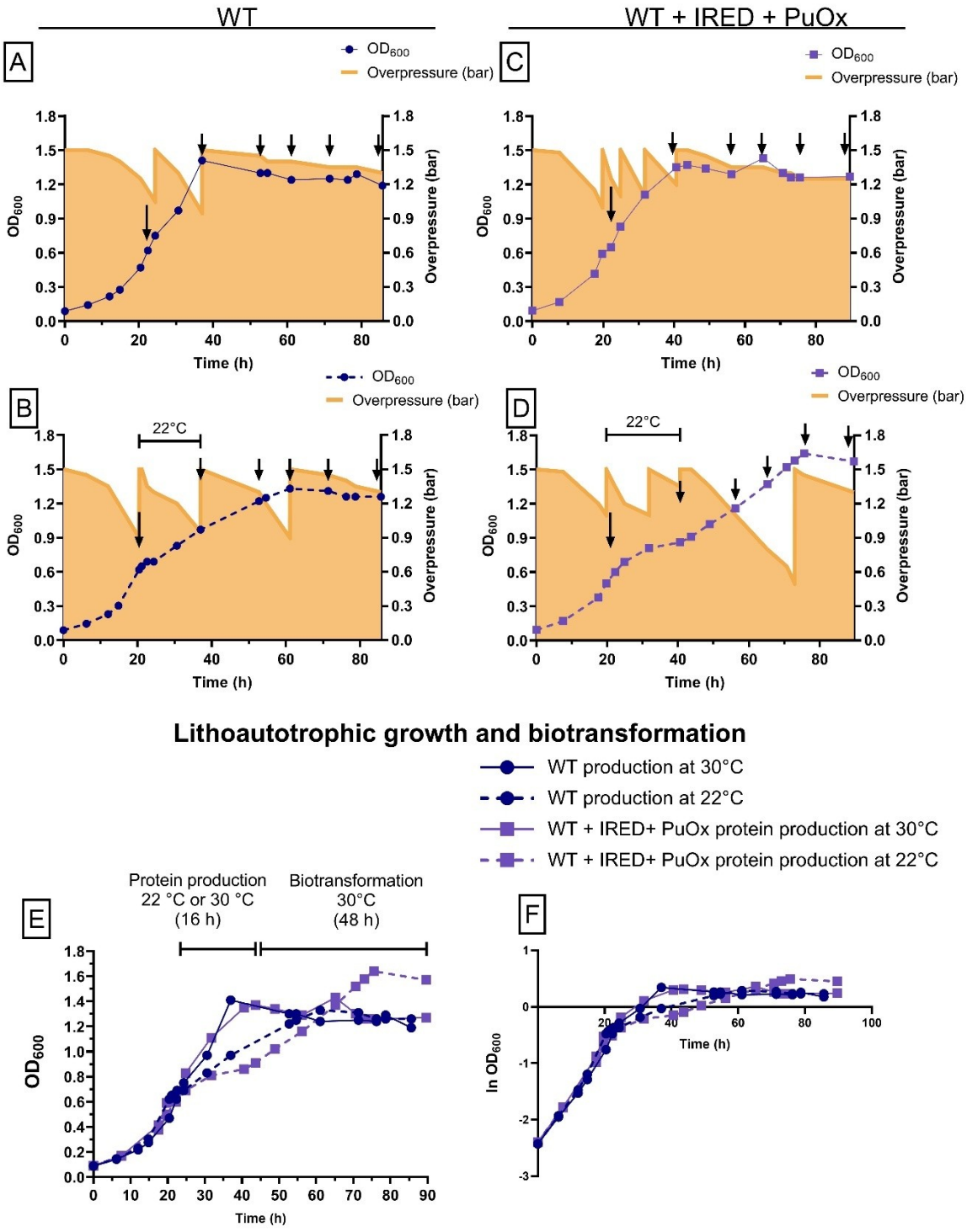

Figure 52. Cultivation of *C. necator* strains to evaluate the lithoautotrophic biotransformation of 10 mM putrescine : The growth of WT and WT + IRED + PuOx is followed by measuring absorbance (OD_{600}) and pressure (bar). The strains are initially grown at 30°C until an OD_{600} of 0.6. The protein production is induced with 12 mM rhamnose, and the temperature is maintained at 30°C (A, C) or shifted to 22°C (B, D) during 16 h. The biotransformation starts by adding 10 mM putrescine and conversion is evaluated during 48 h. Black arrows indicate the start of the protein production, the start of the biotransformation and sampling points, respectively. Temperature change to 22°C is explicitly

labeled and biotransformation occurred at 30°C. The experimental protocol is summarized for all strains (E). (WT: *C. necator* H16, WT + IRED + PuOx: WT x pDA4).

Product analysis was carried out in the supernatant of the samples using GC-MS, and GC-FID No product was detected at any sampling point, neither in the WT control nor in WT + IRED + PuOx (data not-shown). These results indicate that no biotransformation occurred in the strain WT + IRED + PuOx when the cascade started from putrescine.

To investigate potential issues limiting or blocking the cascade in the strain WT + IRED + PuOx, we directed our attention on the individual reactions in whole cells. According to the cascade reaction mechanism, several stages could be assessed: (1) the initial oxidation reaction catalyzed by PuOx, (2) the spontaneous conversion of the aldehyde intermediate to an imine intermediate, or (3) the reduction reaction catalyzed by IRED (Figure 53).

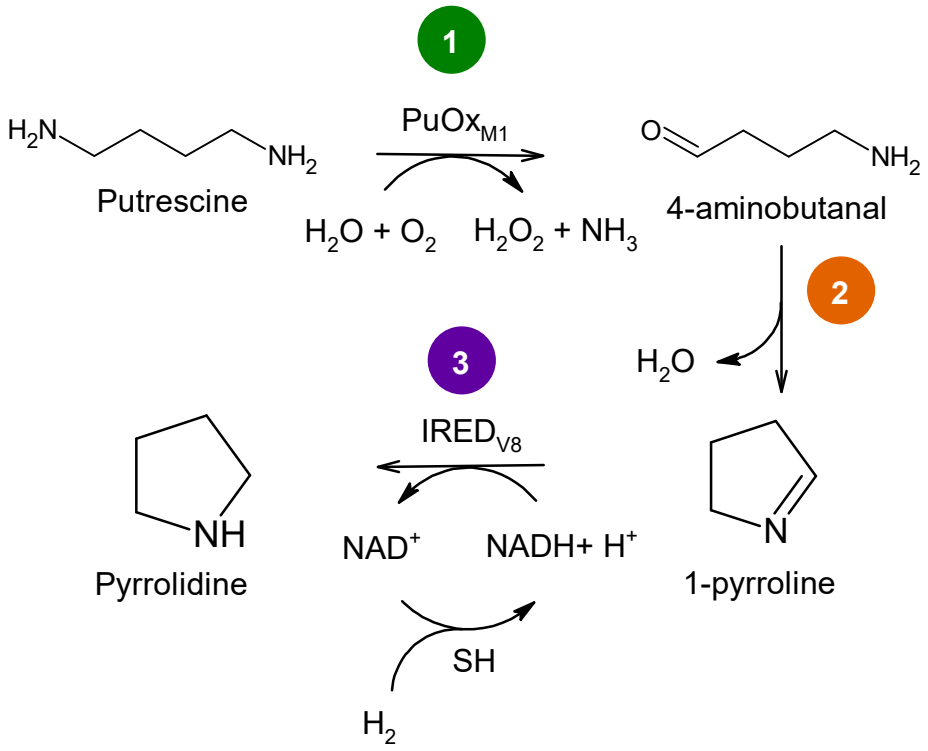

Figure 53. Enzymatic cascade from putrescine to pyrrolidine : the expected biotransformation from putrescine to pyrrolidine in WT + IRED + PuOx strain includes the oxidation of putrescine catalyzed by $PuOx_{M1}$ (2), the spontaneous cyclization to 1-pyrroline (2), and the reduction of 1- pyrrolidine catalyzed by $IRED_{V8}$ (3). The last reaction occurs along with NADH regeneration catalyzed by the soluble hydrogenase (SH) natively present in *C. necator*. Image adapted from Al-Shameri et al. (2019).

The first reaction, the oxidation of putrescine catalyzed by PuOx, generates H_2O_2 as a byproduct. H_2O_2 is a strong oxidizing agent known to cause oxidative stress, potentially disrupting cellular homeostasis

and impairing the cascade's functionality. Investigating redox stress in *C. necator* is complex due to the presence of detoxifying oxidative proteins present in this bacteria, such as catalase, peroxidase, superoxide dismutase (S.-E. Lee et al., 2009; Schwartz et al., 2009). As mentioned in a previous Chapter, the catalase is highly specific for H_2O_2 and would rapidly degrade it which complicates its assessment through traditional quantification methods to evaluate oxidative stress impacts. Moreover, synthesis of H_2O_2 did not presented problems for strain growth during alkane production in *C. necator* (Crépin et al., 2018).

The second reaction, a spontaneous reaction converting the aldehyde intermediate to an imine intermediate, could also be impaired. The equilibrium of this reaction may shift unfavorably, preventing efficient formation of the imine. Analytical challenges further complicate the study of this step, as the intermediates involved are unstable and not all are commercially available (X. Zhang et al., 2017). This instability and the difficulty of synthesis limit experimental approaches.

The third and final reaction of the cascade is catalyzed by IRED. As demonstrated in the Chapter 3.1.1 the reduction of 2-methyl-1-pyrroline to 2-methylpyrrolidineby IRED can be effectively studied *in vitro* using soluble extract. This reaction is particularly advantageous for analysis in whole-cells as both compounds are commercially available, facilitating quantification through established analytical techniques. For the feasibility of this approach, we focused on the study of this particular reaction to gain insights into the cascade’s functionality.

3.1.7 Biotransformation from 2-methyl-1-pyrroline into 2-methyl pyrrolidine.

A new set of lithoautotrophic cultivations was performed in duplicates using the strain WT + IRED + PuOx to evaluate the reduction of 2-methyl-1-pyrroline to 2-methylpyrrolidinecatalyzed by $IRED_{V8}$. The reaction is presented in Figure 54.

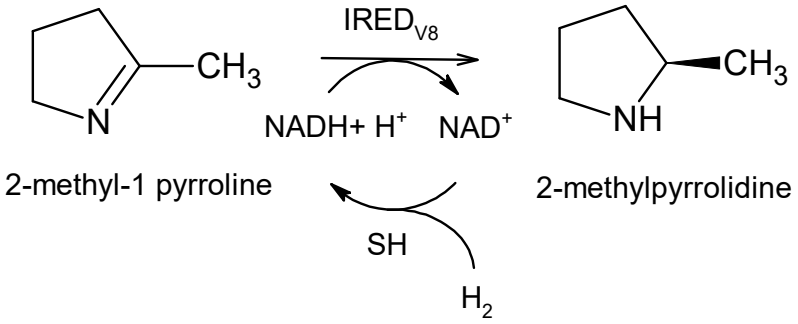

Figure 54. IRED enzymatic reaction in *C. necator* : expected biotransformation from 2-methyl -1 pyrroline to 2-methylpyrrolidine in *C. necator* strains catalyzed by $IRED_{V8}$. Reduction is coupled with NADH regeneration from the native *C. necator* SH reaction.

The cultivation protocol followed the previously established method, with slight modifications. To further explore the effect of temperature, some cultures were maintained at 30°C throughout protein production and biotransformation, while other cultures were shifted to 22°C for the induction step and the initial phase of biotransformation. For cultures with variation at 22°C, temperature was maintained at 22°C during 16 hours before returning to 30°C. When the cultures reached an OD_{600} of 0.5–0.7, induction was carried out using 12 mM rhamnose. Additionally, a shorter induction period of 2-3 hours was tested to ensure sufficient protein production while allowing the reaction with the substrate to start earlier. After 2-3 hours of induction, biotransformation was initiated by adding 10 mM 2-methyl-1-pyrroline as substrate. As in the previous cultivation, supernatant samples were collected to evaluate the biotransformation at 0, 16, 24, and 48 hours after substrate addition. Details of the cultivation conditions are provided in Figure 55.

During the first 25 h of cultivation, the strains exhibited comparable growth (Figure 55, G). Following this phase, a shorter induction period was implemented. When the WT + IRED + PuOx strain was shifted to 22 °C, growth slowed to a specific growth rate of $\mu = 0.02 \pm 0.01\ h^{-1}$. This reduced growth rate persisted throughout the cultivation, even after the temperature was restored to 30 °C at 50 h. From this point the growth rate was $\mu = 0.03 \pm 0.02\ h^{-1}$, and did not recover the μ_{max} typically observed at 30 °C (Table 22). Despite this slower growth under the 22 °C temperature variation, the WT + IRED + PuOx strain achieved a final OD_{600} of approximately 2 after 80 h of cultivation (Figure 55, E-F). This is the optical density expected when using 2 g/L nitrogen source in the medium, and was similarly observed for the WT strain cultivated entirely at 30 °C or subjected to the temperature variation to 22 °C (Figure 55, A, D).

The strain WT + IRED + PuOx presented a similar growth as the WT control when growth was calculated at 30°C (Table 22). It should be noted that under this condition, WT + IRED + PuOx reached a final OD_{600} between 3-5 (Figure 55 C, D), exceeding the theoretical maximum of OD_{600} of 2 when the minimal medium contains 2 g/L of nitrogen source. Given that the WT + IRED + PuOx strain has a wild-type genetic background, it retains the ability to produce and accumulate PHB. *C. necator* is known to accumulate substantial amounts of PHB granules intracellularly at high cell densities, with PHB comprising 60 to 80% of the cell dry weight when grown on a CO_2-gas mix (Lambauer & Kratzer, 2022; Tanaka et al., 1995). This higher OD_{600} could arise from the accumulation of PHB under stress-growing conditions. Interestingly, a relationship between temperature and PHB accumulation in *C. necator* has also been reported in previous studies even with optimal conditions of unlimited growth (Ismail et al., 2024). According to Ismail et al. (2024), higher PHB concentrations were observed at elevated temperatures reaching 30% and 40% of PHA (% cell dry weight) at 35°C and 40°C, respectively. When the *C. necator* strain was grown at the reference temperature of 30°C, a basal accumulation of PHB up to 10% was detected. In our strain WT + IRED +PuOx, a stress-induced PHB production and accumulation at 30°C may have increased the cell light scattering, leading to increased OD_{600} readings. An important factor contributing to metabolic stress could be the plasmid carried by our strain, which encodes IRED and PuOx and has a size of 14.5 kb. This plasmid may exert selective pressure on the strain, diverting cellular resources and potentially driving increased PHB accumulation as a stress response. Conversely, at 22°C, reduced metabolic rates during the 16-hour incubation step may limit growth and PHB accumulation, aligning with the theoretical OD expectations for the nitrogen content in the medium. These hypotheses could be supported through PHB analysis and quantification to validate the observed trends.

The growth rates of the WT and WT + IRED + PuOx strains were compared during the cultivations. Specific growth rates were calculated for the initial 24–636 hours, when the strains were maintained at 30 °C, and during the first hours of induction with rhamnose. This allowed us to assess whether the presence of the plasmid alone had any measurable impact on growth. The results, presented in Table 22, indicate a μ_{max} of 0.092 ± 0.002 for the WT, and 0.081 ± 0.5005 for WT + IRED +PuOx. No significant difference in the growth rates were observed at 30 °C, indicating that the plasmid did not affected growth at 30 ° during the selected period.

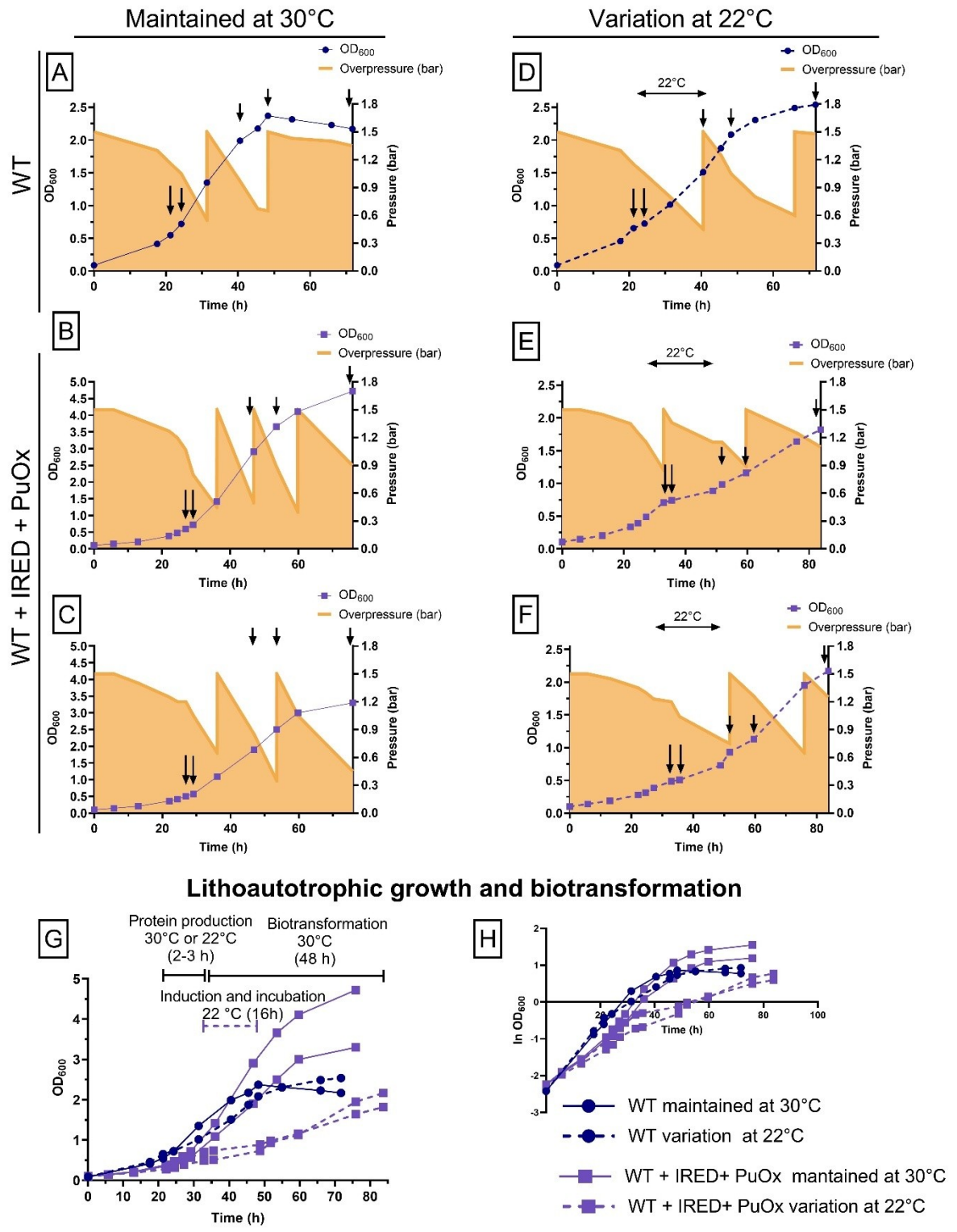

Figure 55 : Cultivation of *C. necator* strains to evaluate the lithoautotrophic biotransformation of 10 mM 2-methyl-1-pyrroline: The growth of WT and WT + IRED + PuOx is followed by measuring absorbance (OD_{600}) and overpressure (bar). The strains are initially grown at 30°C from an OD_{600} of 0.1 until 0.5-0.7. Protein production is then induced with 12 mM rhamnose, and the temperature is maintained at 30°C (A, B, C), or variated to 22°C during 16 h (D, E, F). Duplicates are shown for WT +

IRED + PuOx at 30°C (B, C), and WT + IRED + PuOx at 22°C (E, F). The biotransformation starts after 2-3 hours of induction by adding 10 mM 2-methyl-1-pyrroline and its conversion is evaluated during 48 h. Black arrows indicate the start of the induction, the start of the biotransformation and sampling points, respectively. Temperature change to 22°C is explicitly labeled. The experimental protocol is summarized for all strains (G). The μmax is calculated for each replicate from the natural logarithm (ln) using a linear regression, with a R^2 = 0.98-0.99 (H) (WT: *C. necator* H16; WT + IRED + PuOx: WT x pDA4).

Table 22. Lithoautotrophic growth of *C. necator* strains during 2-methyl-1-pyrroline biotransformation: The maximal growth rate (μ_{max}, h^{-1}) is calculated for each strain during the first 24 to 36 h of culture at 30 °C. The mean and the SEM are indicated. Data is analyzed using an unpaired t--test with Welchs's correction, for a sample size of n=4 for WT, and n=6 for WT + IRED + PuOx. No significant difference ($p<0.05$) is observed.

	WT	**WT + IRED + PuOx**
μ_{max} (h^{-1})	0.100	0.093
	0.093	0.084
	0.087	0.093
	0.090	0.080
	-	0.070
	-	0.066
μ_{max} (h^{-1}) average	0.092	0.081
SEM	0.003	0.005

To evaluate the 2-methyl-1-pyrroline biotransformation, we analyzed the supernatant samples at 0 h, 16 h, 24 h and 48 h after substrate addition (biotransformation time). One set of replicates from the WT + IRED + PuOx strain was analyzed via GC-MS. During the biotransformation time, peaks corresponding to the product, 2-methylpyrrolidine, were observed. Peak identity was confirmed by comparing the mass spectra with database entries but no quantification was possible (data not-shown). The remaining samples were quantified using GC-FID. Substrate and product standards were made from commercial reagents. During substrate analysis and calibration, we observed the presence of two peaks (Figure 56), probably due to the purity of the reagent and the derivatization interaction. Accurate quantification was not possible for the substrate and only product standards were used to quantify the samples.

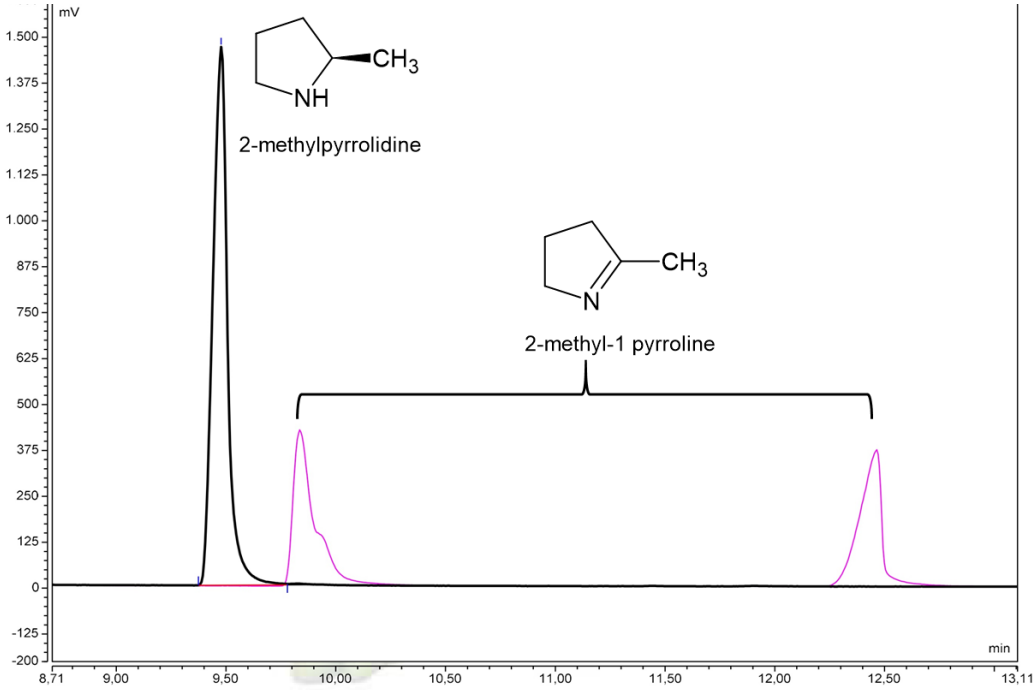

Figure 56. GC-FID Chromatogram of 2-methyl-1-pyrroline (biotransformation substrate) and 2-methylpyrrolidine (biotransformation product).

The lithoautotrophic biotransformation results are presented in Figure 57 and main results are summarized in Table 23. Biotransformation assays demonstrated that WT + IRED +PuOx catalyzed the reduction of 2-methyl-1-pyrroline to 2-methyl pyrrolidine, with no detectable production in the WT control under either temperature condition (Figure 57 A-C) (Supplementary B.6.1 , Figure S. 8-Figure S. 11). Total production over biotransformation time is indicated in Figure 57-A. After 48 h of biotransformation, the WT + IRED +PuOx strain maintained at 30 °C reached a maximum of 80. 4 µM. When the WT + IRED +PuOx strain was incubated at 22 °C and shifted back to 30 °C, a comparable concentration of 70.1 ± 13.5 µM was achieved. Based on the initial 10 mM of substrate, we obtained a conversion of approximately 0.8 % and 0.7 %, respectively.

During the biotransformation, biomass levels varied across strains and cultivations conditions, as illustrated in Figure 55-G. To ensure accuracy, 2-methylpyrrolidineproduction was corrected for biomass dividing the concentration by OD_{600} (Figure 57-B). The WT + IRED +PuOx strain maintained at 30 °C produced a maximum of 29.8 µM/OD after 24 h of biotransformation, followed by a slightly decrease to 24.4 µM/OD at 48 h. In contrast, the strain incubated at 22 °C and shifted back to 30 °C, showed a continuous product accumulation, reaching 34.8± 3.7 µM/OD at 48 h.

Additional calculations were performed to account for theoretical expectations of biomass formation, nitrogen availability, and PHB accumulation. A maximal theoretical OD_{600} value of 2 was set based on the 2 g/L of nitrogen source in the medium. Optical measurements exceeding this theoretical value

were interpreted as potential contributions from PHB accumulation, and were adjusted to a maximum OD_{600} of 2, obtaining a corrected specific production (Figure 57

Figure 57, C). The WT + IRED + PuOx strain maintained at 30 °C presented a progressive production, reaching a maximum of 40.2 µM/OD after 48 h of biotransformation. The highest specific production rate for the strain maintained at 30 °C was observed between 0 h and 16 h, reaching 1.7 µM/OD/h. When the strain was incubated at 22 °C and subsequently shifted to 30 °C, the maximum specific production was 36.4 ± 5.3 µM/OD at 48 h. In this case, the highest specific production rate was 2.02 ± 1.5 µM/OD/h, recorded between 16 h and 24 h, during the 30 °C phase. We observed that for both conditions, the fastest production rates were associated with the 30 °C incubation, and both reached comparable final concentrations after 48 h of biotransformation.

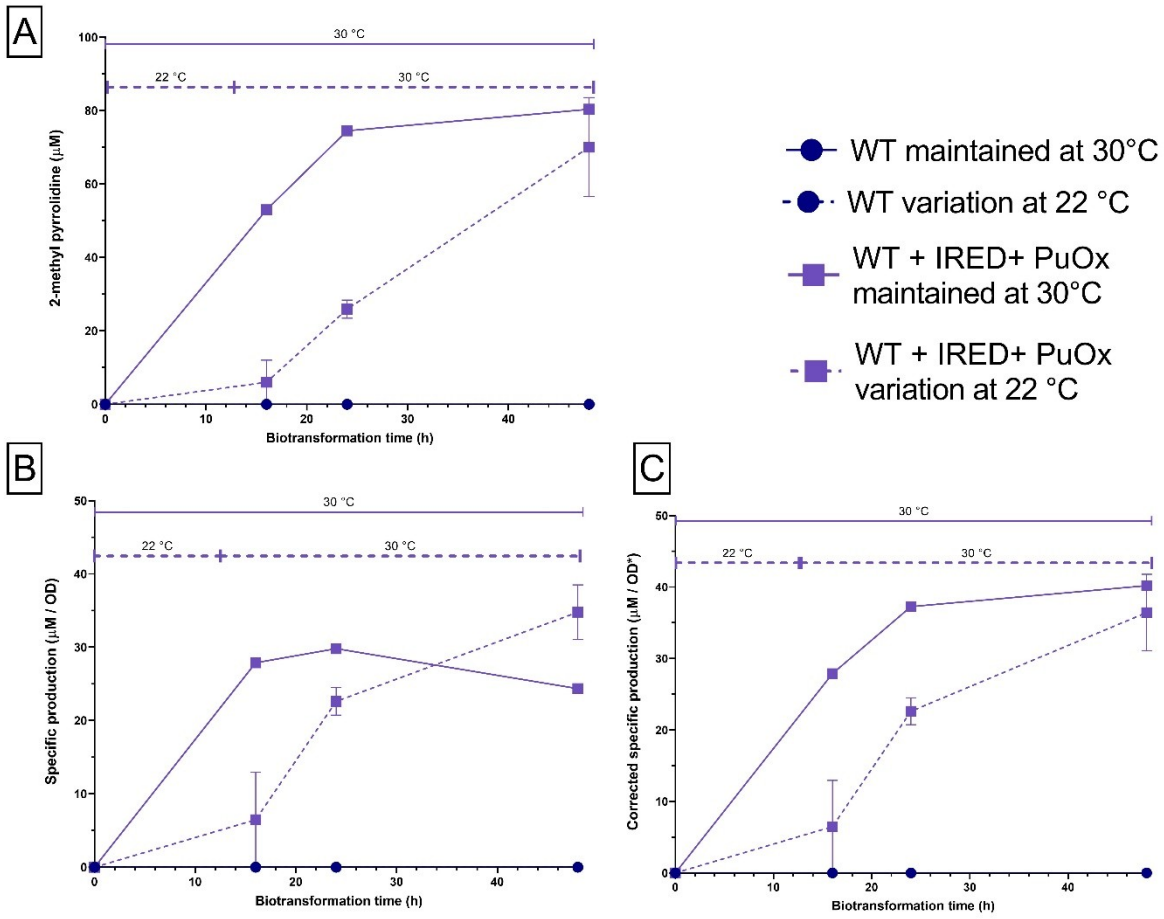

Figure 57. *C. necator* produces 2-methylpyrrolidineunder lithoautotrophic conditions : The strain WT + IRED + PuOx is incubated with 10 mM 2-mehtyl pyrroline as substrate. Samples are quantified with GC-FID at 0, 16, 24 and 48 h after addition of substrate (Biotransformation time). Temperature changed is explicitly labelled for the variation at 22 °C. Total production is plotted for each strain against the biotransformation time (A). Specific production is normalized to OD_{600} for each sample (B). To consider potential contributions from PHB accumulation, the specific production is corrected when the cultures exceeded the theoretical maximal OD_{600} of 2 (C). For WT and WT + IRED + PuOx maintained

at 30 °C n= 1. For WT + IRED + PuOx with variation at 22 °C n=2, and both the mean and the SEM are plotted. (WT: *C. necator* H16; WT + IRED + PuOx: WT x pDA4).

Table 23. Evaluation of IRED biotransformation : $IRED_{V8}$ reaction is evaluated in WT + IRED + PuOx after 48 h of biotransformation. Conversion (%) is based on 10 mM 2-methyl-1-pyrroline as substrate. Specific production (µM/ OD) is corrected when the cultures exceed a theoretical maximal of OD_{600} of 2 to consider PHB accumulation (µM/ OD*) SEM is indicated for n=2 for the variation at 22 °C. All values are calculated during the growth at 30 °C **.

	Maintained at 30 °C	Variation at 22 °C**
Conversion	0.8 %	0.7 %
Specific production (µM/ OD)	29.8	34.8 ± 3.7
Corrected specific production (µM/ OD*)	40.2	36.4 ± 5.4

We expected that the WT + IRED + PuOx strain with the variation at 22 °C would have positive effects on protein production. In *E. coli*, lower temperatures are commonly used in recombinant protein production protocols. Some examples include improved production of soluble protein (Schein & Noteborn, 1988), improved folding through chaperonins (Ferrer et al., 2003), reduced protein aggregation, or degradation (Hunke & Betton, 2003), and improved inducible systems (T.-H. Lin et al., 2024). If similar effects occurred in the WT + IRED + PuOx strain, elevated protein levels during incubation at 22 °C could be expected, potentially contributing to higher production rates and increased final product concentrations. However, comparable values were observed for total 2-methylpyrrolidineproduction and corrected specific production. Notably, the specific production rate was only slightly improved, reaching 2.02 ± 1.5 µM/OD/ h when WT + IRED + PuOx strain was cultivated with the22°C variation, and this increase was only detected after shifting to 30 °C. To verify the effect of temperature over $IRED_{V8}$ production in *C. necator* protein quantification would be required after protein induction. Nevertheless, these results suggest that temperature may have a limited impact on protein levels, but rather an effect on biotransformation kinetics. During the first 16 h biotransformation, when WT + IRED + PuOx was primarily incubated at 22 °C, the specific production rate was 0.4 ± 0.6 µM/OD/ h, approximately five-times lower than when the rate was calculated during the 30 °C phase. Based on this observation, the protocol was simplified and subsequent experiments were conducted entirely at 30 °C, guaranteeing $IRED_{V8}$ activity and biotransformation rate.

The detection of 2-methylpyrrolidine confirmed that $IRED_{V8}$ was both expressed and catalytically active in the strain WT + IRED +PuOx strain under lithoautotrophic conditions. However, the absence of pyrrolidine indicated that the full enzymatic cascade had not occurred, prompting a deeper investigation into the functionality of this strain.

Western blot analyses were performed from 48 h of biotransformation with putrescine (Figure 52), revealing a clear band around 34 kDa in the strain WT + IRED + PuOx. This band was consistent with the size of $IRED_{V8}$ monomer and was observed in both temperature regimes (culture maintained at 30 °C, or culture variation at 22 °C). No band was observed in the WT control (Figure S. 4). In contrast, no band was observed for the expected size of $PuOx_{M1}$ monomer under the same conditions for the WT + IRED + PuOx strain (Figure S. 4-C). The absence of detectable $PuOx_{M1}$ protein possible explains the lack of pyrrolidine formation, as the first step of the enzymatic cascade was not initiated.

Initial gene sequencing of plasmid pDA4 showed that $ired_{V8}$ and $puox_{M1}$ sequences were correct. To investigate problems in gene expression, the plasmid pDA4 was extracted again from WT + IRED + PuOx, and analyzed through full-plasmid sequence. Several mutations were identified along the plasmid. A single base deletion was observed in *rhaS,* creating a premature codon stop in this regulatory gene located upstream $ired_{V8}$. Despite this deletion, $IRED_{V8}$ was produced (Figure S. 4, Figure S. 5), probably because the gene is positioned immediately downstream of the first *rhaB* promoter, where leaky promoter activity may have been sufficient for transcription.

Importantly, a-13 base deletion was identified in the rrnB T1 terminator, along with other base substitutions across the plasmid pDA4 (Supplementary B.5.3 Sequencing pDA4). The rrnB T1 terminator is located downstream $puox_{M1}$, which is the second gene in the plasmid pDA4. Disruption of rrnB1 T1 terminator could have caused longer RNA transcripts extending beyond $puox_{M1}$, altering gene expression or replication conflicts, as observed in other studies (Sohn & Kang, 2005; Wirachman & Grossman, 2024). These mutations likely contributed to disruption in *puox* expression, explaining the absence of $PuOx_{M1}$ protein, and pyrrolidine formation through the enzymatic cascade.

To confirm that $PuOx_{M1}$ could still be produced in *C. necator*, we tested the WT + PuOx strain harboring a pKR-based plasmid carrying only $puox_{M1}$. In this strain, $PuOx_{M1}$ production was successfully detected under lithoautotrophic conditions (Figure S. 7), demonstrating that the enzyme can be produced when the genetic context is appropriate.

As an alternative strategy, we tested a co-culture experiment combining the strains WT + IRED and WT + PuOx under heterotrophic biotransformation with putrescine. No pyrrolidine production was detected by GC-analyses (data-not shown). Further analyses on metabolite exchange and compartmentalization are required to elucidate the underlying constraints of such co-culture system.

We observed challenges in achieving the complete cascade reaction, highlighting the complexity of coordinating multiple genes and enzymatic steps in *C. necator*. Nevertheless, the demonstration of the IRED-catalyzed reaction emphasizes its functionality, and biotransformation potential. As a result, we focused our efforts on optimizing *C. necator* biotransformation catalyzed by $IRED_{V8}$.

3.1.7.1 Optimization of IRED biotransformation in *C. necator*.

In subchapter 2.3, we observed that *C. necator* faced challenges in performing the complete enzymatic cascade, particularly on $PuOx_{M1}$ production and reaction. Despite these challenges, the reaction catalyzed by $IRED_{V8}$ proceeded with low conversion under lithoautotrophic conditions (0.7-0.8 %). IREDs have been extensively study as a biocatalyst and successfully employed in various biotechnological applications. They have gained attention in companies such as Pfizer and Novartis, demonstrating their utility in the large-scale synthesis of pharmaceutical intermediates (Duan et al., 2020; IP.com Prior Art Database, 2017b; E. J. Ma et al., 2021). Based on IRED's industrial importance, and the biotransformation results of 2-methyl pyrrolidine, we directed our attention towards optimizing imine reduction in *C. necator*.

The pKR plasmid backbone presented certain limitations for expression of *ired* and *puox*, prompting us to explore alternative plasmid systems. The pCAT201 plasmid, as presented by Azubuike et al.(2020), emerged as a promising option for electroporation due to its more favorable genetic environment. Additionally, Vajente et al. (2024) conducted an exhaustive study demonstrating the advantages of smaller plasmids, which included improved transformation efficiency and compatibility with non-model organisms. Therefore, we selected the pCAT vector and introduced the $ired_{V8}$ gene as described in Materials and Methods 2.2.1 , to obtain the plasmid pDA6 Figure 58.

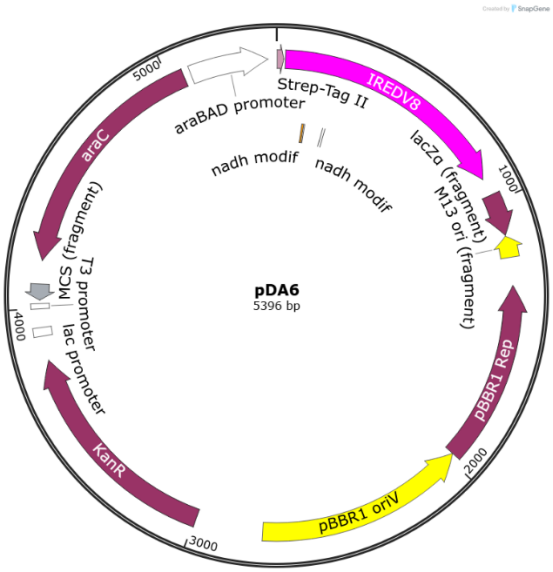

Figure 58. Plasmid map pDA6. Plasmid structure is generated with Snapgene ®.

The plasmid pDA6 was transformed in *E.* coli, and the colonies were screened by PCR-colony with the primers oIC101/oIC102 to amplify $ired_{V8}$. The plasmid was extracted from colonies presenting a band of an approximate size of 949 pb, corresponding to the *ired* gene. Plasmid pDA6 was transformed in *C. necator,* and colonies were isolated in FN plates with Tet. Ten colonies were screened with Colony-PCR with the primers Rha-ired_F/Rha-ired_R for the presence of rhamnose promoter with *ired* gene.

The plasmid was extracted and sequenced from one *C. necator* colony, confirming the strain WT x pDA6 (WT + $IRED_{pcat}$).

Biotransformation of 2-methylpyrrolidine was analyzed in the new strain WT + $IRED_{pcat}$, and compared between heterotrophic and lithoautotrophic conditions. The WT strain without any plasmid, and WT strain carrying an empty pCAT201 backbone (WT + pcat201) were used as controls. The strains were prepared for lithoautotrophic cultivation with a three-step seed train (Table 10). Cultivations were conducted in a different setup for gas fermentation: 60 mL TB or AUT medium contained in 500 mL baffled flasks, no pressure detection was employed in this this particular setup, and safety was prioritized by using non-explosive gas mixture containing 4% O_2, 6% N_2, 80% H_2, and 10% CO_2 (flow rate: 100 mL/min for 8 minutes). All cultures were inoculated to an initial OD_{600} of 0.1 and incubated at 30 °C. The protocol was also simplified by inducing protein production with 0.2 % (v/v) arabinose at an OD_{600} around 0.8-1, while simultaneously adding 10 mM of 2-methyl-1- pyrroline to start the biotransformation.

Supernatant samples from biological duplicates were collected at 0 h, 16 h, 24 h and 48 h after substrate addition (biotransformation time). Protein production was validated in WT + $IRED_{pcat}$ using Western blot, demonstrating protein accumulation over time (Figure S. 12). Production of 2-methylpyrrolidinewas detected in WT + $IRED_{pcat}$ across the biotransformation time, demonstrating that the reaction demonstrating that the reaction is viable under heterotrophic or lithoautotrophic conditions. No product was detected for any condition in the control strains WT and WT + pCAT201, demonstrating that production was caused by $IRED_{V8}$ activity in *C. necator* (Figure 59) (Supplementary B.7.1 , Figure S. 13-Figure S. 19)

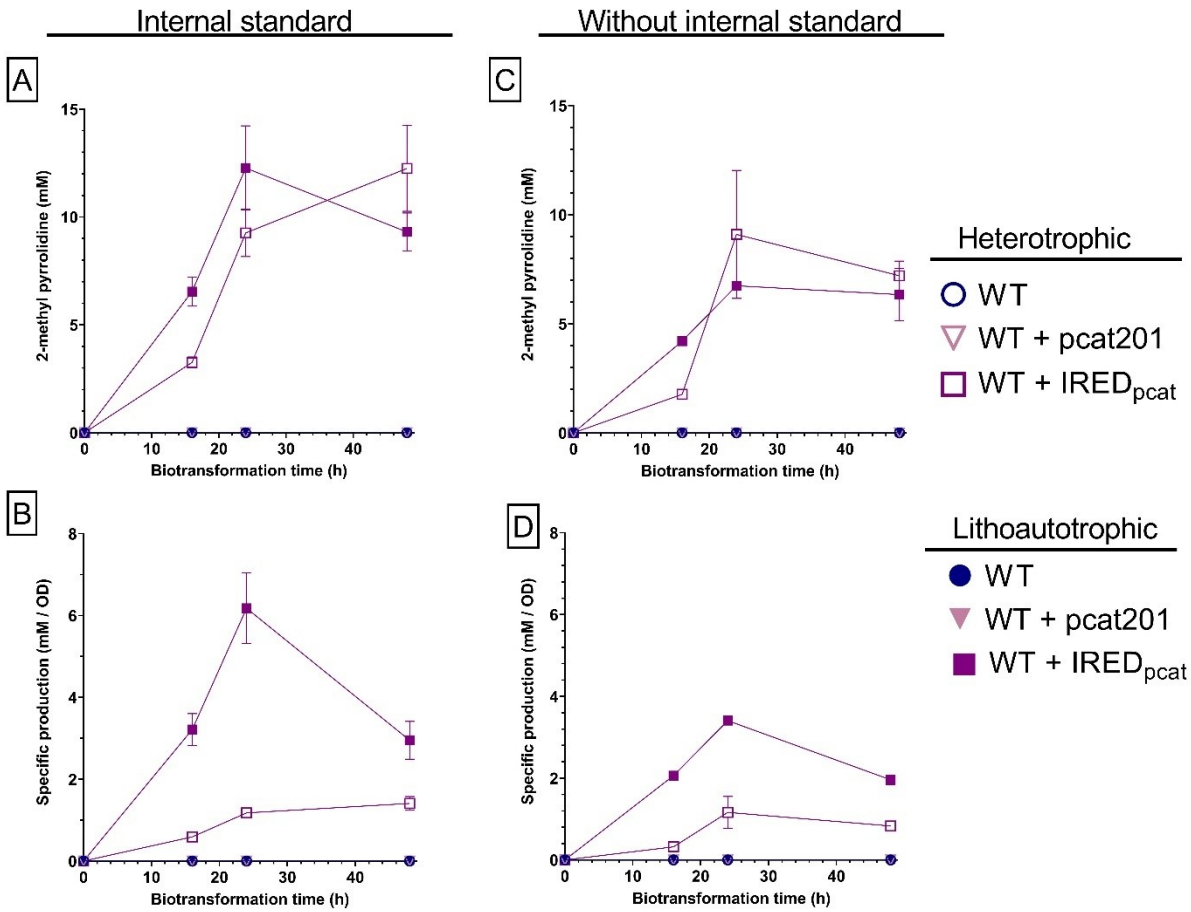

Figure 59. *C. necator* produces 2-methylpyrrolidineunder heterotrophic and lithoautotrophic conditions : Non-explosive gas mixture is used for lithoautotrophic growth. Strains are incubated with 10 mM 2-methyl-1-pyrroline as substrate. Supernatant is evaluated using GC-FID and pyrrolidine as internal standard. Samples are quantified with GC-FID at 0, 16, 24 and 48 h after addition of substrate (Biotransformation time). Samples are quantified considering an internal standard (A, B) or not considering the internal standard (C, D). Total production is plotted against the biotransformation time (A, C). Specific production is normalized with the OD_{600} for each sample (B, D). Biological duplicates are evaluated for each sample. The mean and SEM are plotted. SEM values approximately <0.12, are not visible in the graph. (WT: *C. necator* H16; WT + pcat201: *C. necator* H16 x pCAT201; WT + $IRED_{pcat}$: WT x pDA6).

Quantification of 2-methylpyrrolidinewas performed in GC-FID using 2 mM pyrrolidine as an internal standard (Figure 60). Under both heterotrophic and lithoautotrophic conditions, the use of the internal standard led to overestimated concentrations in WT + $IRED_{pcat}$, exceeding the initial substrate concentration of 10 mM. A maximum production of 12. 3 ± 2mM at 48 h under heterotrophic conditions was observed, while the same maximum was reached earlier, at 24 h, under lithoautotrophic conditions (Figure 59, A) (Figure S. 19). Notably, the peak area of the internal standard showed some variability when 2-methylpyrrolidinewas present in the samples. This variation

could be due to inconsistencies or errors introduced during sample preparation such as extraction or derivatization. These observations suggest that sample preparation protocol may require optimization to improve reproducibility and reliability of quantification with internal standard. Additionally, modifications to the GC program could optimize peak resolution and detection.

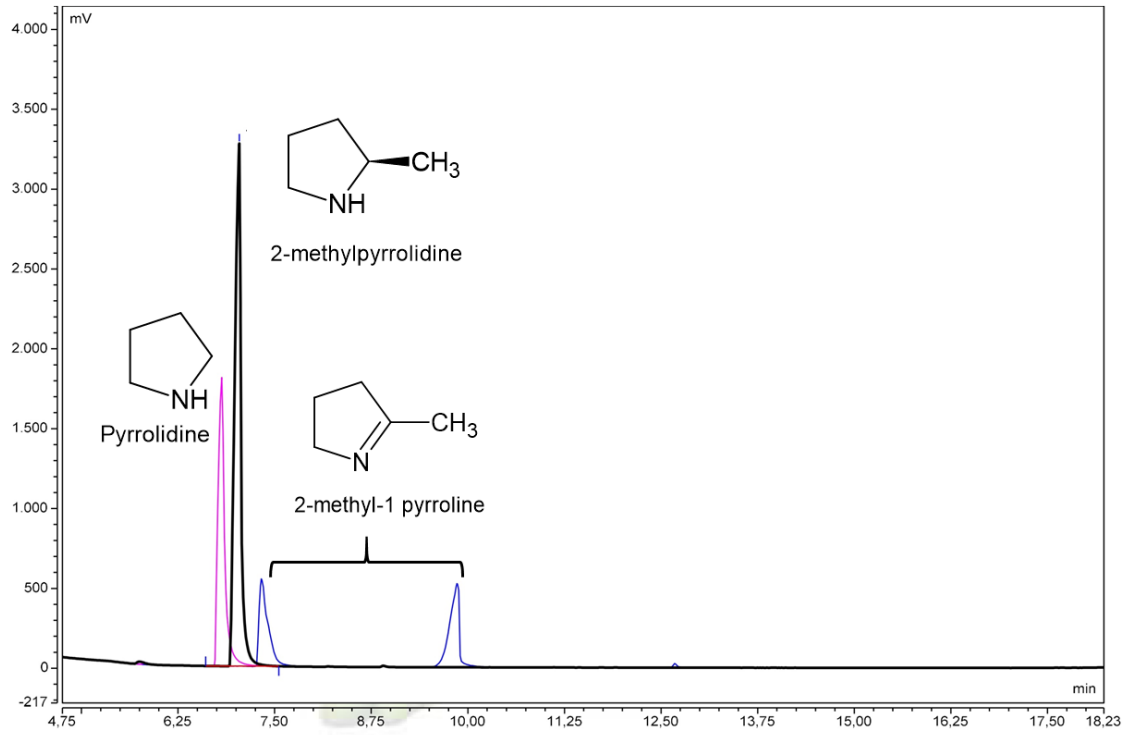

Figure 60. GC-FID chromatogram with 2-methyl-1-pyrroline (biotransformation substrate), 2-methylpyrrolidine (biotransformation product), and pyrrolidine (internal standard)

To assess whether the internal standard introduced quantification bias, the same data were quantified without applying the internal standard correction, yielding concentrations closer to the initial 10 mM substrate (Figure 59, C). The strain WT + $IRED_{pcat}$ reached the maximum production of 9.1 ± 2.9 mM at 24 h under heterotrophic conditions, while a maximum of 6.7 ± 0.03 mM at 24 h was observed in lithoautotrophy.

For both approaches, with and without the internal standard, product concentrations were normalized to biomass by dividing the measured 2-methylpyrrolidine concentration by the OD_{600} for each biotransformation time point (Figure 59, Specific production, C and D). When the internal standard was applied, maximum specific production reached 1.4 ± 0.2 mM/OD at 48 h under heterotrophic conditions, and 6.2 ± 0.9 mM/OD at 24 h under lithoautotrophic conditions. The specific production rate was calculated between 16 h and 24 h, resulting in 0.07 ± 0.02 mM/OD/h under heterotrophic cultures, and 0.4 ± 0.1 mM/OD/h under lithoautotrophic cultures. The specific production rate was five-times higher under lithoautotrophic biotransformation.

When quantification was performed without the internal standard, the maximum specific production was reached at 24 h for both culturing conditions: 1.2 ± 0.4 mM/OD under heterotrophic conditions, and 3.4 ± 0.1 mM/OD under lithoautotrophic conditions. Between 16 h and 24 h, the specific production rate was 0.1 ± 0.07 mM/OD/h under heterotrophic conditions, and twice as high under lithoautotrophic conditions with 0.2 ± 0.003 mM/OD/h. Main results are summarized in Table 24.

Table 24. *C. necator* biotransformation rates to 2-methyl pyrrolidine : biotransformation is compared in WT + $IRED_{pcat}$ under heterotrophic or lithoautotrophic conditions. Quantification in GC-FID is made with or without internal standard. Maximum production (mM), conversion (%), and specific production (mM/OD) are indicated during the biotransformation time. Conversion is based on 10 mM 2-methyl-1-pyrroline as substrate. SEM is indicated for n=2.

	Heterotrophic		Lithoautotrophic	
	Internal Standard	Without Internal Standard	Internal Standard	Without Internal Standard
Time	48 h	24 h	24 h	
Production (mM)	12. 3 ± 2	9.1 ± 2.9	12.3 ± 2	6.7 ± 0.03
Conversion	122.5%	91%	122 .7%	67.4%
Specific production (mM/OD)	1.4 ± 0.2	1.2 ± 0.4	6.2 ± 0.9	3.4 ± 0.1

For both quantification approaches, the specific production rate for WT + $IRED_{pcat}$ was faster under lithoautotrophic conditions. Interestingly, the highest production and specific production were observed at 24 h. This maximum was followed by a decrease at 48 h, regardless of whether the internal standard was considered in the quantification (Figure 59). This pattern suggests that metabolic or physiological factors may influence product stability or synthesis over time. Notably, no intermediate samples were collected between 24 h and 48 h, and concentrations beyond 6.7 ± 0.03 mM may have gone undetected before the decrease in production. After reaching a maximum, the WT + $IRED_{pcat}$ strain may have degraded or re-assimilated 2-methylpyrrolidine, or environmental factors could have affected product stability. Similar declines in production over time have been reported in *C. necator* strains producing 3-hydroxypropionic acid, where product re-assimilation and metabolic shifts during the transition to stationary phase were identified as key contributing factors (Arenas-López et al., 2019; Salinas et al., 2022). In addition, product decreases have been observed in isopropanol production in *C. necator* strains, where the reverse reaction

catalyzed by the alcohol dehydrogenase favored the accumulation of the substrate acetone, particularly under NADPH-limited conditions (S. Guillouet, unpublished data).

Borlinghaus et al. (2019) demonstrated the production of *N*-heterocycles using whole-cell cascade with PuOx and IRED in *E. coli*. The biotransformation was carried out in 12 L volume with 100 mM substrate, and 8 g/L of cell-dry weight, yielding 6 g/L of 3-methylpiperidine after 52 h. In contrast, our optimized IRED system in *C. necator* only includes one enzymatic step. To facilitate a more accurate comparison between our system and values reported in literature, it would advisable to normalize *N*-heterocycle production to cell-dry weight instead of optical density. In our case, we only measured cell-wet weigh at the end of the cultivation, which currently limits direct comparability with other systems.

The small-scale gas fermenter used during this IRED biotransformation is still under development. For the previous setup, the potential influence of PHB accumulation on optical density and production remains to be addressed. Nonetheless, our lithoautotrophic system in *C. necator* achieved between 67-100% conversion in 24 h, demonstrating clear potential for further improvement. Process optimization could be established for scale-up using Design of Experiment (DoE), and monitor parameters such as temperature, pH, substrate concentration, as previously done for *E. coli*-cascade (Borlinghaus et al., 2019). These improvements will enhance reproducibility and scalability of our lithoautotrophic biotransformation process.

Changing plasmid backbone resulted in an effective strategy to improve IRED biotransformation. Following the same approach, new plasmids were designed using the pBAD-based plasmid containing *puox*$_{M1}$, pDA5. The *ired*$_{V8}$ gene, and the predicted NADPH-dependent *ired* genes from other microorganisms (Chapter 3.1.1.4), were cloned in pDA5 using Gibson assembly to create alternative *C. necator* strains. Preliminary tests were conduction under lithoautotrophic conditions with putrescine as substrate to analyze the complete enzymatic cascade. Low pyrrolidine concentrations were detected during gas fermentation with PuOx$_{M1}$ and IREDs candidates (data not-shown, collaboration with P. Schoenmakers, 2024), suggesting that the enzymatic cascade could be viable under further optimization. Validation of these observations is still required.

3.1.8 Summary Chapter 2

Results Summary Chapter 2.

- Glycerol-supplemented medium promoted the transition of *C. necator* from heterotrophic to lithoautotrophic growth and shortened the lag phase.

- Putrescine is not toxic for *C. necator*.
    - In heterotrophic conditions, *C. necator* grew in the presence of 2, 10, 15 mM putrescine.
    - In lithoautotrophic conditions, *C. necator* grew in the presence of 5, 10 and 100 mM. *C. necator*'s cell morphology changed at 100 mM putrescine

- The engineered WT + IRED + PuOx strain did not produce *N*-heterocycles when $ired_{V8}$ and $puox_{M1}$ were co-expressed in the pkr-broad host plasmid. The main obstacle appeared to be the absence of $PuOx_{M1}$ production, blocking the first reaction of the enzymatic cascade

- $IRED_{V8}$ reaction from 2-methyl-1-pyrroline to 2-methylpyrrolidineis possible in WT + IRED + PuOx strain, with 0.8 % conversion under lithoautotrophic conditions.

- IRED biotransformation was optimized using pCAT201-based plasmid in the WT + IRED pcat strain, achieving at least 67 % conversion under lithoautotrophic conditions in a safe-gas mixture.

- Further analyses were initiated with pBAD-based plasmid containing $puox_{M1}$ and *ired* genes from different microorganisms (Chapter 3.1.1.4) in *C. necator*. Low cascade biotransformation starting from putrescine was observed in gas fermentation with $PuOx_{M1}$ and IREDs (data not-shown, collaboration with P. Schoenmakers, 2024)

Section 4: General Discussion, Conclusion and Perspectives.

In our study we explored the potential of *C. necator* as a H_2-driven biotransformation platform for *N*-heterocycles, achieving 2-methylpirrolidine production. We focused on establishing an *in vivo* enzymatic cascade in *C. necator* containing the heterologous oxidoreductases $PuOx_{M1}$ (Borlinghaus et al., 2019), and $IRED_{V8}$ (Borlinghaus & Nestl, 2018), harnessing the cofactor regeneration advantage of the native SH from *C. necator* (Lauterbach et al., 2013). Previous studies have proved that enzymatic cascades using these purified proteins are able to produce *N*-heterocycles *in vitro* (Al-Shameri et al., 2019, 2020), as well as *in vivo* cascades in *E. coli* (Borlinghaus et al., 2019). Our main hypothesis centered that *in vivo* biotransformations in *C. necator* under lithoautotrophic metabolism could produce higher or comparable yields to *E. coli*. We proceeded our analysis with two broader chapters: the first one focusing on heterologous production of $PuOx_{M1}$, and $IRED_{V8}$ under heterotrophic conditions, and the second focusing on the implications of heterologous oxidoreductase on *C. necator* lithoautotrophic metabolism.

4.1 Heterologous oxidoreductases $PuOx_{M1}$ and $IRED_{V8}$ are produced in *C. necator* in heterotrophic and lithoautotrophic conditions.

In Section 3: Chapter 1, we developed several *C. necator* strains producing heterologous $IRED_{V8}$ and $PuOx_{M1}$ in minimal FN of FGN media. Heterologous genes and large operons have been expressed before on *C. necator* for obtention of bioproducts using CO_2 and H_2 fermentations, such as isopropanol production (Garrigues et al., 2020; Grousseau et al., 2014). Other reductases types have also been expressed in *C. necator* for alkane production (Crépin et al., 2016, 2018), or xylitol production (Jämsä et al., 2024). However, the influence of the particular variants $IRED_{V8}$ and $PuOx_{M1}$ oxidoreductases has not yet been assessed together in an *in vivo* chemolithoautotrophic system.

The traditional pkr broad-host plasmid with rhamnose induction (Sydow et al., 2017) was used for expression of $ired_{V8}$ and $puox_{M1}$ genes, individually transformed into *C. necator*.

To optimize heterologous protein production in *C. necator,* we first tested the effect of deleting Lon protease and overexpressing the native GroESL chaperonin on $IRED_{V8}$ production in different *C. necator* strains. Under heterotrophic conditions, $IRED_{V8}$ production was only detected in the WT + IRED strain, suggesting that metabolic stress from multiple genetic modifications may have hindered IRED production in the other strains, or further screening was required.

In the soluble extract of WT + IRED, we clearly detected $IRED_{V8}$ production, and NADH-oxidoreductase activity of 0.08 ± 0.01 U/ mg. The protocol for strain cultivation and cell lysis was optimized, and a new cultivation was performed to assessed the impact of rhamnose regulation. The rhamnose promoter presented a basal activity of 0.05 ± 0.01 U/mg in the soluble extract without induction, which increased to 0.18 ± 0.01 U/mg when the strain was induced. The increased activity in the soluble extract might be due to proper promoter induction, along with a more efficient lysis of *C. necator* cells.

The variation in NADH-oxidoreductase activity in the induced WT + IRED strain (0.88 ± 0.004 U/ mg vs 0.18 ± 0.01 U/mg) was also accompanied with variation in the protein pattern in the Western blot. These results indicate the importance of controlling cultivation, and cell lysis when working with *C. necator* soluble extract, as strain variability and experimental conditions can strongly influence protein production and activity.

In comparison, another heterologous oxidoreductase has been expressed and studied before in the soluble extract of *C. necator*. The hydrogenase from *Hydrogenophilus thermoluteolus*, exhibited higher activity in the soluble extract (2.5 ± 0.1 U/mg) (Preissler et al., 2018). The lower activity observed for $IRED_{V8}$ in soluble extract may be due to the catalytic characteristics of IREDs, typically exhibiting slower reaction rates compared to hydrogenases or central metabolic dehydrogenases.

To further characterized $IRED_{V8}$, enzyme purification was performed. Partially-purified or enriched $IRED_{V8}$ was obtained from *C. necator*, and the activity was tested with the model substrate, 2-methyl-1-pyrroline (Mitsukura et al., 2010). A specific activity of 1.8 ± 0.1 U/mg was observed, increasing 10 times in comparison to the soluble extract (0.18 ± 0.01 U/mg). This increase in specific activity was caused by the enrichment and concentration of the protein. Therefore, we conclude that $IRED_{V8}$ was produced and active in *C. necator*.

We compared $IRED_{V8}$ specific activity to other oxidoreductases expressed in *C. necator*. Preissler et al. (2020), detected a specific activity of around 90 U/mg for NAD^+ reduction for the purified SH from *C. necator* . Similarly, the hydrogenase from *H. thermoluteolus* was purified from *C. necator* resulting in 33.4 U/mg (Preissler et al., 2018). These activities are higher compared to the detected activity of $IRED_{V8}$. However, the *C. necator* strains used in those studies did not have WT genetic background , and were particularly designed for high hydrogenase production. Another example, is the formate dehydrogenase from *Methylorubrum extorquens* expressed in *C. necator,* which showed a specific activity of 80 to 100 U/mg for CO_2 conversion to formate (Ryu et al., 2024). Compared to these cases, $IRED_{V8}$ exhibited lower specific activity, which may be attributed that the enzyme was only partially-purified. Additionally, IRED has a more specialized function in amine reduction, and no directly involved in central metabolism in *C. necator*. Furthermore, IRED depends on NADH availability, and cofactor limitations in *C. necator* may also constrain activity.

The production of $PuOx_{M1}$ was also studied in heterotrophic conditions. Similar as for $IRED_{V8}$, the production of $PuOx_{M1}$ was successful in the soluble extract of the strain WT + PuOx, which contains a pKR backbone and $puox_{M1}$ gene. Purification trials were conducted in both WT + PuOx and Δlon + PuOx strains, and different induction time points and culture duration were evaluated. Partial-purified enzyme was obtained according to the SDS-PAGE gels. We observed that extended heterotrophic cultivation in FN medium probably caused enzyme degradation. After 5 days, fructose in FN medium probably ran out, and the cell had difficulties with nutrition depravation. Induction time also suggested to play a role in $PuOx_{M1}$ production. The induction at the beginning of the culture was better for WT + PuOx, while inducing 24 h after the start of the culture resulted in lower production of purified protein in WT + Δlon. The protein bands were not totally isolated when analyzed in the SDS-PAGE but correctly

detected in Western blot. The enzyme solution was probably contaminated with other soluble proteins from *C. necator*, obtaining only a partially-purified or enriched $PuOx_{M1}$. For these reasons activity assays with purified sample were not performed. Moreover, we encountered difficulties in determining enzymatic activity of $PuOx_{M1}$ in soluble extract due to the unexpected reactions that could appeared with H_2O_2. Reports have demonstrated that *C. necator* possess the necessary detoxifying enzymes for H_2O_2 and no important effects have been observed in other studies (Crépin et al., 2018; S.-E. Lee et al., 2009; Schwartz et al., 2009).

We observed that $IRED_{V8}$ and $PuOx_{M1}$ were enriched and partially purified, thus further optimization is still necessary to obtain purified samples from *C. necator* and characterization of the enzymes. Nevertheless, both heterologous oxidoreductases were successfully produced in the soluble extract in *C. necator*. Particularly, $IRED_{V8}$ demonstrated activity in minimal media in heterotrophic conditions.

In Chapter 2, we analyzed the protein production under lithoautotrophic conditions, using the engineered strain WT + IRED + PuOx. This strain contained the plasmid pDA4, a pKR-based plasmid expressing both $ired_{V8}$ and $puox_{M1}$ genes. However, a mutation was identified on the terminator downstream $puox_{M1}$ which seemed to have prevented the correct transcription of this gene. Therefore, no $PuOx_{M1}$ was produced in WT + IRED + PuOx.

Interestingly, the strain WT + PuOx did not present issues producing $PuOx_{M1}$ under lithoautotrophic conditions. The strain WT + PuOx, contained a pKR-based plasmid with $puox_{M1}$ gene, and $PuOx_{M1}$ protein was detected after growth and protein induction. Autotrophic $PuOx_{M1}$ production suggests that *C. necator* is able to grow, and produce this protein in appropriate genetic constructs.

To the best of our knowledge, this is the first time the oxidoreductases IRED and PuOx are produced in *C. necator* in both heterotrophic and lithoautotrophic conditions, opening possibilities for biotransformations in this bacterium.

4.2 Glycerol-containing medium assists the transition to lithoautotrophic metabolism in *C. necator*, and can be used for biocatalysis applications.

Through Chapter 2, we also investigated the transition from heterotrophic to lithoautotrophic cultivation in *C. necator*. This transition required protocol optimization, and we established a three-step seed train strategy, in which glycerol was used as main carbon source in the final preculture prior to lithoautotrophic growth.

Few studies have focused specifically on *C necator* preculture management to facilitate the transition from heterotrophy to lithoautotrophy. For example, Amer & Kim (2023) assessed the effect of organic, and gaseous substrates in different metabolic conditions. They proposed a two-stage system to reduce lag phase and reach high optical density for in conditions, particularly under conditions optimized for PHA production. Similarly, Gerlach et al. (2023) proposed a protocol for homologous overproduction of hydrogenases, aiming to minimize preculture time. Unlike these studies, our approach focuses on

enabling a progressive and efficient metabolic shift from heterotrophy to strict lithoautotrophy for broader applications, independent of the bioproduct.

Given that *C. necator*'s genetic redundancy has an important metabolic burden (Jahn et al., 2024), transition to lithoautotrophy requires conditions that allow the cells to adapt efficiently. Notably, lag phases during autotrophic adaptation can be extremely long (Lambauer & Kratzer, 2022; Sonnleitner et al., 1979). Amer & Kim (2023) observed up to 22 h delay when altering O_2 and CO_2 pressures. Early work by Repaske et al. (1971), demonstrated that these adaptation delays could be eliminated under certain concentrations of O_2 and CO_2, identifying that initial growth was indirectly related to pCO_2 and directly dependent upon a constant bicarbonate ion concentration.

To favor metabolic conditions for *C. necator*, our strategy introduces glycerol in FGNmod medium before lithoautotrophic cultivation. This simple but effective intervention eliminated the lag phase. Although glycerol is a poor carbon source for *C. necator*, it can still be metabolized. Glycerol consumption mainly depends on *cbb*X genes coding for Rubisco activases, and involved in the CBB cycle (Strittmatter et al., 2022). Moreover, C. necator produces SH even in the absence of H2 (B. Friedrich & Schwartz, 1993; Jahn et al., 2024; Lenz & Friedrich, 1998), which could contribute to faster autotrophic adaptation. The presence of glycerol in FGN_{mod} medium probably promote these responses in *cbb*X genes and upregulating SH production, preparing the inoculum for gas fermentation.

This advancement improves the reproducibility and applicability of lithoautotrophic growth protocol, facilitating the study of biotechnologically relevant biomolecules in *C. necator*. For example, we applied our optimized seed train to assess the effect of putrescine in *C. necator*. Putrescine is a diamine that has been previously used as substrate for the obtention of *N*-heterocycles using a biotransformation cascade in *E. coli* (Borlinghaus et al., 2019). Diamines are usually tightly regulated in bacteria and we investigated if putrescine excess could interfere with the metabolic function or growth of *C. necator*. Remarkably, a concentration of 100 mM putrescine was not lethal to *C. necator*. This high concentration only caused an extended lag phase, slightly lower growth rate, and morphology changes in *C. necator*. Our results added more evidence that this bacterium is an appropriate host for *N*-heterocycle production from diamines substrates. It is important to notice that no putrescine concentration was measured in the supernatant or inside *C. necator* cells during the gas fermentation, and we do not discard the possibility of putrescine degradation or detoxification via other mechanisms in *C. necator*. Further *in-silico* analysis suggested the presence of the necessary proteins for putrescine transport inside *C. necator* cells via putative annotated genes.

4.3 Exploring a new H_2-driven enzymatic cascade in *C. necator*

We explored the production, interaction and activity of the heterologous oxidoreductases $PuOx_{M1}$ and $IRED_{V8}$ with the native SH from *C. necator* in an *in vivo* setup. The strains developed in Chapter 1 were characterized under lithoautotrophy, and new strains were constructed to evaluate simultaneous oxidoreductase interaction towards the synthesis of *N*-heterocycles.

We obtained promising results of $IRED_{V8}$ and $PuOx_{M1}$ production during heterotrophic cultivation, and putrescine tolerance in lithoautotrophic conditions. In initial biotransformation assays in gas fermentation we used the strain WT + IRED + PuOx, which contained both genes on a single plasmid. However, no pyrrolidine product was detected when putrescine was used substrate.

As mention before, protein and genetic analyses were performed in parallel to the biotransformation assay with putrescine. We identified that $PuOx_{M1}$ was not produced in the strain WT + IRED + PuOx, therefore, the first reaction of the enzymatic cascade could not be catalyzed under lithoautotrophic conditions. Nonetheless, we identified that $IRED_{V8}$ was produced in the strain WT + IRED + PuOx, and demonstrated activity in lithoautotrophic cultivation. These results confirmed that half of the enzymatic cascade was functional in *C. necator*, and $IRED_{V8}$ was used to produce 2-methylpyrrolidine.

A separate biotransformation assay was contemplated using the strain WT + PuOx to verify $PuOx_{M1}$ activity in gas fermentation. However, $PuOx_{M1}$ activity catalyzing conversion from putrescine to the intermediate 1-pyrroline was not possible, due to lack of commercial standards, instability of 1-pyrroline for GC analyses (X. Zhang et al., 2017), and challenges interpreting results in the soluble extract.

Genetic bottlenecks were identified for the completion of the enzymatic cascade in the strain WT + IRED + PuOx, and alternatives were proposed. The strain WT + IRED + PuOx-2 was engineered containing the two genes in separate plasmids. However, WT + IRED + PuOx-2 did not grow in one of the gas fermentation setups, probably due to high metabolic burden of the constructs (Cunningham et al., 2009; San Millan & Maclean, 2017).

As an alternative, a co-culture approach combining the strains WT + IRED and WT + PuOx was tested under heterotrophic biotransformation with putrescine. However, no pyrrolidine production was visible, possibly due to limitations in substrate or intermediate transport between the strains. Further analyses, including studies on metabolite exchange and compartmentalization, are required to elucidate the underlying constraints in the co-culture system.

To address the plasmid limitations on the WT + IRED + PuOx strain, new plasmids and strains were constructed. The $puox_{M1}$ gene was cloned in a pBAD-derivative as an alternative backbone resulting in plasmid pDA5. Using pDA5, I initiated the development of new *C. necator* strains where the $puox_{M1}$ gene was inserted before $ired_{V8}$. Additionally, $puox_{M1}$ was co-expressed with the putative IREDs from diverse microorganisms, which are predicted NADPH-dependent (Chapter 3.1.1.4). The constructs were transformed in *C. necator*, resulting in new strains, which would allow us to compare and identify

if IREDs variants are better candidates for the complete cascade. Biotransformation assays were performed with putrescine with the new *C. necator* strains, obtaining low pyrrolidine detection under lithoautotrophic conditions (around 0.1 mM product unpublished data, collaboration with P. Schoenmakers). Experimentation continues in Lauterbach's laboratory to confirm the observations, and improve cascade performance.

This study provided the foundation for the establishment of a H_2-driven enzymatic cascade, supporting *C. necator*, demonstrating the potential as microbial cell factory for lithoautotrophic production of *N*-heterocycles.

4.4 $IRED_{V8}$ is an enzymatic tool for *in vivo* biotransformations in *C. necator*.

Although $PuOx_{M1}$ was not produced in the WT + IRED + PuOx strain, $IRED_{V8}$ was successfully produced during gas fermentation. Moreover, $IRED_{V8}$ activity was detected in this strain with different temperature regimes. The strain WT + IRED + PuOx achieved a lithoautotrophic biotransformation from 2-methyl-1-pyrroline to 2-methylpyrrolidine, with 0.8 % conversion.

To improve IRED efficiency, we focused our efforts on optimizing IRED reaction in *C. necator*. The gene $ired_{V8}$ was cloned in pCAT as alternative backbone, obtaining the strain WT + $IRED_{pcat}$. Advantages of pCAT as a small plasmid have been described before (Azubuike et al., 2020; Vajente et al., 2024).

The WT + $IRED_{pcat}$ strain showed at least 67 % conversion at 24 h during lithoautotrophic biotransformation, being extremely higher than the biotransformation with the same substrate in the strain WT + IRED + PuOx. The strain WT + $IRED_{pcat}$ contains only one plasmid of 5.3 kb length with the $ired_{V8}$ gene. In comparison, the WT + IRED + PuOx contains a plasmid with the two genes, $ired_{V8}$ and $puox_{M1}$, with a length of 14.5 kb. This considerable difference on plasmid size could be deviating resources for the proper protein production.

The biotransformation with WT + $IRED_{pcat}$ was compared to heterotrophic conditions, reaching a conversion of 91 % at 24 h. However, the specific production rate was nearly twice as fast for the lithoautotrophic condition (0.2 ± 0.003 mM/OD/h). Under lithoautotrophy, SH is upregulated, and the NADH recycling is favored (Lauterbach et al., 2013), therefore NADH would be more easily available for $IRED_{V8}$ to utilize as cofactor for the efficient reduction of 2-methyl-1-pyrroline and favorizing enzymatic reaction.

Additionally, we simplified the seed train and the gas input for lithoautotrophic conditions. Our new approach enabled the production of 2-methylpyrrolidine in *C. necator* under non-explosive gas-mixtures, reaching concentrations comparable to those under heterotrophic cultivation. This result suggests that CO_2 could be an alternative substrate from conventional chemical catalysis to produce industrially relevant fine-molecules.

C. necator has been explored as a platform for H_2-driven biotransformations in the presence of O_2, and/or CO_2. Jämsä et al., (2024) used H_2 as a reducing agent for cofactor recycling and produced xylose in *C. necator* resting cells. Teetz et al, (2022) used CO_2 and H_2 from electrolysis byproducts to sustain

C. necator resting cells for isopropanol biosynthesis. Unlike these studies we focus on *in vivo* cultivation through SH cofactor regeneration, integrating relevant heterologous oxidoreductases as new biocatalysis tools in this bacterium. Thereby, we broaden broadening its application scope for *in vivo* enzymatic biotransformations.

Previous studies have described biocatalytic cascades for the production of *N*-heterocycles using *E. coli* as a microbial platform. Borlinghaus et al., (2019) reported a 67% conversion of 3-methylpiperidine from 140 g of substrate in a 20 L bioreactor over 52 hours. Al-Shameri et al. (2019) adapted this enzymatic cascade into an *in vitro* set-up incorporating an NADPH-SH variant as a cofactor regeneration system and gas-permeable membranes. An *in vitro* electrolysis flow-setup was further adapted,, achieving up to 99% conversion of labelled methylated *N*-heterocycles isotopes (Al-Shameri et al., 2020). Although their system demonstrated high conversion, they reported that only 4 % of electrical energy was used for product formation. This limitation was attributed to low gas solubility in water, heat production, and gas transfer over the membrane.

In our study, we circumvented the limitations associated with purified proteins by using *C. necator* as an autotrophic microbial chassis for *in vivo* biotransformation. Using a safe $H_2/O_2/CO_2$ mixture in 60 mL-scale fermenter setup, our engineered strain achieved 67 % conversion to 2-methylpyrrolidine. This conversion is comparable to that obtained in *E. coli* for the production of 3-methylpiperidine (Borlinghaus et al., 2019). Unlike Borlinghaus et al. (2019), we used a smaller scale fermenter, achieving the conversion in 24 h instead of 52 h with *E. coli*. While the target molecules were different, these findings prove the potential of *C. necator* as an autotrophic microbial cell factory.

This study provides a promising outlook for H_2-driven biotransformations in *C. necator*, and opens the possibility for addressing current limitations and exploring advanced engineering strategies.

4.5 Perspectives

Several metabolic and genetic bottlenecks were identified throughout this study, offering new opportunities for further research.

First, an important factor to consider while working with microbial hosts, is cofactor usage and its influence on *C necator* metabolism. Since the selected $IRED_{V8}$ in this study is NADH-dependent, further investigation is needed to understand impact of heterologous IRED on redox balance between NADH/NADPH in *C. necator*. To compare the cascade performance, the native NADPH-dependent IRED from *M. stipitatus* was cloned in the pCAT vector and transformed in *C. necator.* The new plasmids incorporating these changes were constructed and transformations in *C. necator* are undergoing. Biotransformation assays in heterotrophy and lithoautotrophy continue as a joint collaboration with members of Lauterbach's laboratory.

Second, genetic construct design proved to be a limiting factor in implementing the complete enzymatic cascade. Notably, the pkr broad-host plasmid was not optimal for the simultaneous expression of $puox_{M1}$ and $ired_{V8}$, preventing the full cascade activity. Nonetheless, our findings provide

a strong foundation to develop the enzymatic cascade in *C. necator*. As plasmid replacement to a pCAT resulted in improved conversion for $IRED_{V8}$ biotransformation, we constructed additional strains containing *puox* and *ired,* either in pCAT or pBAD backbones as alternatives for the complete enzymatic cascade. Analyses continue on the laboratory to evaluate the performance of new constructs.

In parallel, a preliminary study was performed with IREDs from different microorganisms. Following a similar approach, future research could focus on identifying and characterizing PuOx from diverse sources to refine the performance in the enzymatic cascade.

Another promising strategy to improve the enzymatic cascade could be adaptive laboratory evolution (ALE). ALE could be implemented to target PuOx reaction and force the utilization of NH_3, the byproduct of PuOx reaction, to be the sole nitrogen source in *C. necator*. This strategy aims to drive the metabolic flow more effectively towards diamine oxidation, and into the IRED reaction.

Finally, the complete enzymatic cascade could be extended to access additional target molecules. The project is continuing in the laboratory to produce more complex *N*-heterocycles in *C. necator*. Given the relevance of chiral chemistry, additional experimentation focusing on piperidines enantiomers could enhance the value of the *C. necator* biotransformation platform.

Altogether, our approach states a proof of concept for the heterologous production of IRED and PuOx in *C. necator*, and demonstrates the obtention of small *N*-heterocycles, such as 2-methylpyrrolidine via H_2-driven biotransformation. Further efforts continue in the laboratory to upscale IRED-based biotransformations by increasing substrate concentrations, and expanding the substrate scope. These advancements aim to enable access to chiral *N*-heterocycles molecules, which are highly valuable intermediates for pharmaceutical synthesis. Although downstream processing was not addressed in this study, product extraction with green solvents will be a crucial step to optimize the process for industrial applications, and support the development of sustainable pharmaceutical synthesis using autotrophic microbial cell factories.

Section 5: Bibliography

Abdelshaheed, M. M., Fawzy, I. M., El-Subbagh, H. I., & Youssef, K. M. (2021). Piperidine nucleus in the field of drug discovery. *Future Journal of Pharmaceutical Sciences*, *7*(1). https://doi.org/10.1186/s43094-021-00335-y

Adkins, H., & Billica, H. R. (1948). The preparation of raney nickel catalysts and their use under conditions comparable with those for platinum and palladium catalysts. *Journal of the American Chemical Society*, *70*(2), 695–698. https://doi.org/10.1021/ja01182a080

Alagesan, S., Hanko, E. K. R., Malys, N., Ehsaan, M., Winzer, K., & Minton, N. P. (2018). Functional genetic elements for controlling gene expression in *Cupriavidus necator* H16. *Applied and Environmental Microbiology*, *84*(19). https://doi.org/10.1128/AEM.00878-18

Alexeeva, M., Carr, R., & Turner, N. J. (2003). Directed evolution of enzymes: New biocatalysts for asymmetric synthesis. *Organic & Biomolecular Chemistry*, *1*(23), 4133–4137. https://doi.org/10.1039/B311055A

Aliyu Alhafiz, H., Di Bisceglie, F., Meier, H. P. F., Weickardt, I., Castro González, I. A., García Navarro, J., Schoenmakers, P., Oyen, S. J., Konarzycka-Bessler, M., Gorret, N., Schmidt, S., Schillberg, S., Mann, M., Guillouet, S. E., Kratzer, R., & Lauterbach, L. (2025). *Cupriavidus necator* as a model organism for CO_2-based biotechnology. In *Methods in Enzymology* (Academic Press, p. 32). https://doi.org/10.1016/bs.mie.2025.01.017

Al-Shameri, A., Borlinghaus, N., Weinmann, L., Scheller, P. N., Nestl, B. M., & Lauterbach, L. (2019). Synthesis of N-heterocycles from diamines via H_2-driven NADPH recycling in the presence of O_2. *Green Chemistry*, *21*(6), 1396–1400. https://doi.org/10.1039/C8GC03798A

Al-Shameri, A., Petrich, M.-C., Junge Puring, K., Apfel, U.-P., Nestl, B. M., & Lauterbach, L. (2020). Powering artificial enzymatic cascades with electrical energy. *Angewandte Chemie (International Ed. in English)*, *59*(27), 10929–10933. https://doi.org/10.1002/anie.202001302

Al-Shameri, A., Siebert, D. L., Sutiono, S., Lauterbach, L., & Sieber, V. (2023). Hydrogenase-based oxidative biocatalysis without oxygen. *Nature Communications*, *14*(1), 2693. https://doi.org/10.1038/s41467-023-38227-9

Altschul, S. F., Gish, W., Miller, W., Myers, E. W., & Lipman, D. J. (1990). Basic local alignment search tool. *Journal of Molecular Biology*, *215*(3), 403–410. https://doi.org/10.1016/S0022-2836(05)80360-2

Amer, A., & Kim, Y. (2023). Minimizing the lag phase of *Cupriavidus necator* growth under autotrophic, heterotrophic, and mixotrophic conditions. *Applied and Environmental Microbiology*, *89*(2), e02007-22. https://doi.org/10.1128/aem.02007-22

Anastas, P. T., & Warner, J. C. (1998). Principles of green chemistry. In *Green chemistry: Theory and practice,* (Vol. 29). Oxford University Press.

Andersson, M., Holmberg, H., & Adlercreutz, P. (1998). Evaluation of *Alcaligenes eutrophus* cells as an NADH regenerating catalyst in organic-aqueous two-phase system. *Biotechnology and Bioengineering*, *57*(1), 79–86. https://doi.org/10.1002/(SICI)1097-0290(19980105)57:1<79::AID-BIT10>3.0.CO;2-3

Anyanwu, V. E., Hall, S. J., Stephens, G., & Pordea, A. (2021). Oxidation of cadaverine by putrescine oxidase from *Rhodococcus erythropolis*. *Journal of Chemical Technology & Biotechnology*, *96*(10), 2950–2955. https://doi.org/10.1002/jctb.6851

Arenas-López, C., Locker, J., Orol, D., Walter, F., Busche, T., Kalinowski, J., Minton, N. P., Kovács, K., & Winzer, K. (2019). The genetic basis of 3-hydroxypropanoate metabolism in *Cupriavidus necator* H16. *Biotechnology for Biofuels*, *12*(1), 150. https://doi.org/10.1186/s13068-019-1489-5

Arhar, S., Rauter, T., Stolterfoht-Stock, H., Lambauer, V., Kratzer, R., Winkler, M., Karava, M., Kourist, R., & Emmerstorfer-Augustin, A. (2024). CO_2-based production of phytase from highly stable expression plasmids in *Cupriavidus necator* H16. *Microbial Cell Factories*, *23*(1), 9. https://doi.org/10.1186/s12934-023-02280-2

Assil-Companioni, L., Schmidt, S., Heidinger, P., Schwab, H., & Kourist, R. (2019). Hydrogen-driven cofactor regeneration for stereoselective whole-cell C=C bond reduction in *Cupriavidus necator*. *Chemistry-Sustainability-Energy-Materials*, *12*(11), 2361–2365. https://doi.org/10.1002/cssc.201900327

ATSDR Agency for Toxic Substances and Disease Registry. (1992). *Toxicological profile for Pyridine. Production, Import, Use, and Disposal*. https://wwwn.cdc.gov/TSP/ToxProfiles/ToxProfiles.aspx?id=535&tid=96

Azubuike, C. C., Edwards, M. G., Gatehouse, A. M. R., & Howard, T. P. (2020). Applying statistical design of experiments to understanding the effect of growth medium components on *Cupriavidus necator* H16 growth. *Applied and Environmental Microbiology*, *86*(17). https://doi.org/10.1128/AEM.00705-20

Azubuike, C. C., Gatehouse, A. M. R., & Howard, T. P. (2021). pCAT vectors overcome inefficient electroporation of *Cupriavidus necator* H16. *New Biotechnology*, *65*, 20–30. https://doi.org/10.1016/j.nbt.2021.07.003

Bachrach, U., & Reches, B. (1966). Enzymic assay for spermine and spermidine. *Analytical Biochemistry*, *17*(1), 38–48. https://doi.org/10.1016/0003-2697(66)90005-4

Badger, M. R., & Bek, E. J. (2008). Multiple Rubisco forms in proteobacteria: Their functional significance in relation to CO_2 acquisition by the CBB cycle. *Journal of Experimental Botany*, *59*(7), 1525–1541. https://doi.org/10.1093/jxb/erm297

Baker, S. H., Jin, S., Aldrich, H. C., Howard, G. T., & Shively, J. M. (1998). Insertion mutation of the form I cbbL gene encoding ribulose bisphosphate carboxylase/Oxygenase (RuBisCO) in *Thiobacillus neapolitanus* results in expression of form II RuBisCO, loss of carboxysomes, and an increased CO2 requirement for growth. *Journal of Bacteriology*, *180*(16), 4133–4139. https://doi.org/10.1128/jb.180.16.4133-4139.1998

Balasubramanian, M. (2013). Formation of Completely or Partially Reduced Pyridines and Quinolines. In *Pyridines: From lab to production* (pp. 413–458). Elsevier. https://doi.org/10.1016/B978-0-12-385235-9.00005-9

Bank, R. P. D. (n.d.). *RCSB PDB - 1PCQ: Crystal structure of groEL-groES*. Retrieved January 7, 2025, from https://www.rcsb.org/structure/1pcq

Becker, L., Dietz, E., & Holtmann, D. (2025). Individual process steps optimization of *Cupriavidus necator*-catalyzed production of α-humulene. *Biochemical Engineering Journal*, *215*, 109617. https://doi.org/10.1016/j.bej.2024.109617

Berman, H. M., Westbrook, J., Feng, Z., Gilliland, G., Bhat, T. N., Weissig, H., Shindyalov, I. N., & Bourne, P. E. (2000). The Protein Data Bank. *Nucleic Acids Research*, *28*(1), 235–242. https://doi.org/10.1093/nar/28.1.235

Bhattacharyya, M., Upadhyay, R., & Vishveshwara, S. (2012). Interaction signatures stabilizing the NAD(P)-binding rossmann fold: A structure network approach. *PLOS ONE*, *7*(12), e51676. https://doi.org/10.1371/journal.pone.0051676

Bommareddy, R. R., Wang, Y., Pearcy, N., Hayes, M., Lester, E., Minton, N. P., & Conradie, A. V. (2020). A sustainable chemicals manufacturing paradigm using CO_2 and renewable H_2. *iScience*, *23*(6), 101218. https://doi.org/10.1016/j.isci.2020.101218

Borlinghaus, N. (2019). *Generierung von gesättigten N-Heterozyklen mit Iminreduktasen* [Doctoral dissertation]. http://elib.uni-stuttgart.de/handle/11682/10744

Borlinghaus, N., Gergel, S., & Nestl, B. M. (2018). Biocatalytic access to piperazines from diamines and dicarbonyls. *ACS Catalysis*, *8*(4), 3727–3732. https://doi.org/10.1021/acscatal.8b00291

Borlinghaus, N., & Nestl, B. M. (2018). Switching the cofactor specificity of an imine reductase. *ChemCatChem*, *10*(1), 183–187. https://doi.org/10.1002/cctc.201701194

Borlinghaus, N., Weinmann, L., Krimpzer, F., Scheller, P. N., Al-Shameri, A., Lauterbach, L., Coquel, A., Lattemann, C., Hauer, B., & Nestl, B. M. (2019). Cascade biotransformation to access 3-methylpiperidine in whole cells. *ChemCatChem*, *11*(23), 5738–5742. https://doi.org/10.1002/cctc.201900702

Bowien, B., & Kusian, B. (2002). Genetics and control of CO_2 assimilation in the chemoautotroph *Ralstonia eutropha*. *Archives of Microbiology*, *178*(2), 85–93. https://doi.org/10.1007/s00203-002-0441-3

Boy, C., Lesage, J., Alfenore, S., Gorret, N., & Guillouet, S. E. (2023). Comparison of plasmid stabilization systems during heterologous isopropanol production in fed-batch bioreactor. *Journal of Biotechnology*, *366*, 25–34. https://doi.org/10.1016/j.jbiotec.2023.02.011

Braig, K., Otwinowski, Z., Hegde, R., Boisvert, D. C., Joachimiak, A., Horwich, A. L., & Sigler, P. B. (1994). The crystal structure of the bacterial chaperonin GroEL at 2.8 Å. *Nature*, *371*(6498), 578–586. https://doi.org/10.1038/371578a0

Braig, K., Simon, M., Furuya, F., Hainfeld, J. F., & Horwich, A. L. (1993). A polypeptide bound by the chaperonin groEL is localized within a central cavity. *Proceedings of the National Academy of Sciences of the United States of America*, *90*(9), 3978–3982.

Brazas, M. D., Breidenstein, E. B. M., Overhage, J., & Hancock, R. E. W. (2007). Role of Lon, an ATP-dependent protease homolog, in resistance of *Pseudomonas aeruginosa* to ciprofloxacin. *Antimicrobial Agents and Chemotherapy*, *51*(12), 4276–4283. https://doi.org/10.1128/aac.00830-07

Brigham, C., Gai, C., Lu, J., Speth, D., Worden, R., & Sinskey, A. (2013). Engineering Ralstonia eutropha for Production of Isobutanol from CO2, H2, and O2. In *Advanced Biofuels and Bioproducts* (pp. 1065–1090). https://doi.org/10.1007/978-1-4614-3348-4_39

Buhrke, T., Lenz, O., Porthun, A., & Friedrich, B. (2004). The H*2*-sensing complex of *Ralstonia eutropha*: Interaction between a regulatory [NiFe] hydrogenase and a histidine protein kinase. *Molecular Microbiology*, *51*(6), 1677–1689. https://doi.org/10.1111/j.1365-2958.2003.03933.x

Burgdorf, T., Bömmer, D., & Bowien, B. (2001). Involvement of an unusual mol operon in molybdopterin cofactor biosynthesis in *Ralstonia eutropha*. *Journal of Molecular Microbiology and Biotechnology*, *3*(4), 619–629.

Burgdorf, T., Lenz, O., Buhrke, T., van der Linden, E., Jones, A. K., Albracht, S. P. J., & Friedrich, B. (2005). NiFe-hydrogenases of *Ralstonia eutropha* H16: Modular enzymes for oxygen-tolerant biological hydrogen oxidation. *Journal of Molecular Microbiology and Biotechnology*, *10*(2–4), 181–196. https://doi.org/10.1159/000091564

Bürstel, I. (2013). *Die pleiotrope Maturation der sauerstofftoleranten [NiFe]-Hydrogenasen aus Ralstonia eutropha* [Doctoral dissertation, Mathematisch-Naturwissenschaftliche Fakultät I]. https://doi.org/10.18452/16730

Caetano-Anollés, G., Kim, H. S., & Mittenthal, J. E. (2007). The origin of modern metabolic networks inferred from phylogenomic analysis of protein architecture. *Proceedings of the National Academy of Sciences of the United States of America*, *104*(22), 9358–9363. https://doi.org/10.1073/pnas.0701214104

Calvey, C. H., Sànchez i Nogué, V., White, A. M., Kneucker, C. M., Woodworth, S. P., Alt, H. M., Eckert, C. A., & Johnson, C. W. (2023). Improving growth of *Cupriavidus necator* H16 on formate using adaptive laboratory evolution-informed engineering. *Metabolic Engineering*, *75*, 78–90. https://doi.org/10.1016/j.ymben.2022.10.016

Camacho, C., Boratyn, G. M., Joukov, V., Vera Alvarez, R., & Madden, T. L. (2023). ElasticBLAST: Accelerating sequence search via cloud computing. *BMC Bioinformatics*, *24*(1), 117. https://doi.org/10.1186/s12859-023-05245-9

Candeias, N. R., Branco, L. C., Gois, P. M. P., Afonso, C. A. M., & Trindade, A. F. (2009). More sustainable approaches for the synthesis of *N*-Based heterocycles. *Chemical Reviews*, *109*(6), 2703–2802. https://doi.org/10.1021/cr800462w

Cárdenas-Fernández, M., Roddan, R., Carter, E. M., Hailes, H. C., & Ward, J. M. (2023). The discovery of imine reductases and their utilisation for the synthesis of tetrahydroisoquinolines. *Chemcatchem*, *15*(3), e202201126. https://doi.org/10.1002/cctc.202201126

Chaudhry, C. (2003). Role of the -phosphate of ATP in triggering protein folding by GroEL-GroES: Function, structure and energetics. *The EMBO Journal*, *22*(19), 4877–4887. https://doi.org/10.1093/emboj/cdg477

Chedid, R. B., Melder, J.-P., Dostalek, R., PASTRE, J., & TAN, A. M. (2016). *Process for the preparation of pyrrolidine* (European Union Patent No. EP2872494B1). https://patents.google.com/patent/EP2872494B1/en

Chen, G.-Q. (2009). A microbial polyhydroxyalkanoates (PHA) based bio- and materials industry. *Chemical Society Reviews*, *38*(8), 2434–2446. https://doi.org/10.1039/B812677C

Chen, J. G., Crooks, R. M., Seefeldt, L. C., Bren, K. L., Bullock, R. M., Darensbourg, M. Y., Holland, P. L., Hoffman, B., Janik, M. J., Jones, A. K., Kanatzidis, M. G., King, P., Lancaster, K. M., Lymar, S. V., Pfromm, P., Schneider, W. F., & Schrock, R. R. (2018). Beyond fossil-fuel-driven nitrogen transformations. *Science (New York, N.Y.)*, *360*(6391), eaar6611. https://doi.org/10.1126/science.aar6611

Chichibabin, A. E. (1905). Synthesis of pyridine bases from saturated aldehydes and ammonia. *Zh. Russ. Fiz.-Khim. O-vA.*, *37*, 1229. https://cir.nii.ac.jp/crid/1370849939562886787

Chichibabin, A. E. (1924). Über Kondensationen der Aldehyde mit Ammonik zu Pyridinbasen. *Journal Für Praktische Chemie*, *107*(1–4), 122–128. https://doi.org/10.1002/prac.19241070110

Childs, R. E., & Bardsley, W. G. (1975). The steady-state kinetics of peroxidase with 2,2'-azino-di-(3-ethyl-benzthiazoline-6-sulphonic acid) as chromogen. *Biochemical Journal*, *145*(1), 93–103. https://doi.org/10.1042/bj1450093

Cho, J. S., Kim, G. B., Eun, H., Moon, C. W., & Lee, S. Y. (2022). Designing microbial cell factories for the production of chemicals. *JACS Au*, *2*(8), 1781–1799. https://doi.org/10.1021/jacsau.2c00344

Cho, J. S., Yang, D., Prabowo, C. P. S., Ghiffary, M. R., Han, T., Choi, K. R., Moon, C. W., Zhou, H., Ryu, J. Y., Kim, H. U., & Lee, S. Y. (2023). Targeted and high-throughput gene knockdown in diverse bacteria using synthetic sRNAs. *Nature Communications*, *14*(1), 2359. https://doi.org/10.1038/s41467-023-38119-y

Chung, C. H., & Goldberg, A. L. (1981). The product of the lon (capR) gene in *Escherichia coli* is the ATP-dependent protease, protease La. *Proceedings of the National Academy of Sciences*, *78*(8), 4931–4935. https://doi.org/10.1073/pnas.78.8.4931

Cimmino, A., Andolfi, A., & Evidente, A. (2013). Phenazine as an Anticancer Agent. In S. Chincholkar & L. Thomashow (Eds.), *Microbial Phenazines: Biosynthesis, Agriculture and Health* (pp. 217–243). Springer. https://doi.org/10.1007/978-3-642-40573-0_11

Claassens, N. J., Bordanaba-Florit, G., Cotton, C. A. R., De Maria, A., Finger-Bou, M., Friedeheim, L., Giner-Laguarda, N., Munar-Palmer, M., Newell, W., Scarinci, G., Verbunt, J., de Vries, S. T., Yilmaz, S., & Bar-Even, A. (2020). Replacing the Calvin cycle with the reductive glycine pathway in *Cupriavidus necator*. *Metabolic Engineering*, *62*, 30–41. https://doi.org/10.1016/j.ymben.2020.08.004

Claassens, N. J., Scarinci, G., Fischer, A., Flamholz, A. I., Newell, W., Frielingsdorf, S., Lenz, O., & Bar-Even, A. (2020). Phosphoglycolate salvage in a chemolithoautotroph using the Calvin cycle. *Proceedings of the National Academy of Sciences*, *117*(36), 22452–22461. https://doi.org/10.1073/pnas.2012288117

Claassens, N. J., Sousa, D. Z., dos Santos, V. A. P. M., de Vos, W. M., & van der Oost, J. (2016). Harnessing the power of microbial autotrophy. *Nature Reviews Microbiology*, *14*(11), 692–706. https://doi.org/10.1038/nrmicro.2016.130

Cramm, R. (2009). Genomic view of energy metabolism in *Ralstonia eutropha* H16. *Journal of Molecular Microbiology and Biotechnology*, *16*(1–2), 38–52. https://doi.org/10.1159/000142893

Cramm, R., Pohlmann, A., & Friedrich, B. (1999). Purification and characterization of the single-component nitric oxide reductase from *Ralstonia eutropha* H16. *FEBS Letters*, *460*(1), 6–10. https://doi.org/10.1016/S0014-5793(99)01315-0

Cramm, R., Siddiqui, R. A., & Friedrich, B. (1997). Two isofunctional nitric oxide reductases in *Alcaligenes eutrophus* H16. *Journal of Bacteriology*, *179*(21), 6769–6777. https://doi.org/10.1128/jb.179.21.6769-6777.1997

Crépin, L., Barthe, M., Leray, F., & Guillouet, S. E. (2018). Alka(e)ne synthesis in *Cupriavidus necator* boosted by the expression of endogenous and heterologous ferredoxin–ferredoxin reductase systems. *Biotechnology and Bioengineering*, *115*(10), 2576–2584. https://doi.org/10.1002/bit.26805

Crépin, L., Lombard, E., & Guillouet, S. E. (2016). Metabolic engineering of *Cupriavidus necator* for heterotrophic and autotrophic alka(e)ne production. *Metabolic Engineering*, *37*, 92–101. https://doi.org/10.1016/j.ymben.2016.05.002

Creutznacher, R., Maass, T., Dülfer, J., Feldmann, C., Hartmann, V., Lane, M. S., Knickmann, J., Westermann, L. T., Thiede, L., Smith, T. J., Uetrecht, C., Mallagaray, A., Waudby, C. A., Taube, S., & Peters, T. (2022). Distinct dissociation rates of murine and human norovirus P-domain dimers suggest a role of dimer stability in virus-host interactions. *Communications Biology*, *5*(1), 1–13. https://doi.org/10.1038/s42003-022-03497-4

Cunningham, D. S., Koepsel, R. R., Ataai, M. M., & Domach, M. M. (2009). Factors affecting plasmid production in *Escherichia coli* from a resource allocation standpoint. *Microbial Cell Factories*, *8*(1), 27. https://doi.org/10.1186/1475-2859-8-27

Davis, D. H., Doudoroff, M., Stanier, R. Y., & Mandel, M. (1969). Proposal to reject the genus *Hydrogenomonas*: Taxonomic implications. *International Journal of Systematic and Evolutionary Microbiology*, *19*(4), 375–390. https://doi.org/10.1099/00207713-19-4-375

de Jong, E., Stichnothe, H., Bell, G., & Jørgensen, H. (2020). *Bio-Based Chemicals A 2020 Update*. IEA Bioenergy. https://www.ieabioenergy.com/wp-content/uploads/2020/02/Bio-based-chemicals-a-2020-update-final-200213.pdf

de Jong, E., & van Ree, R. (2009). *IEA Bioenergy Task 42. Biorefineries: Adding value to the sustainable utilisation of biomass*. https://www.ieabioenergy.com/wp-content/uploads/2013/10/Task-42-Booklet.pdf

de la Asunción Vest, D. (2023). *Heterologous production of a putrescine oxidase in Cupriavidus necator* [Thesis for the attainment of Bachelor degree]. RWTH Aachen University.

DeSa, R. J. (1972). Putrescine Oxidase from *Micrococcus rubens*. *Journal of Biological Chemistry*, *247*(17), 5527–5534. https://doi.org/10.1016/S0021-9258(20)81137-5

Desmond, C., Fitzgerald, G. F., Stanton, C., & Ross, R. P. (2004). Improved stress tolerance of GroESL-overproducing *Lactococcus lactis* and probiotic *Lactobacillus paracasei* NFBC 338. *Applied and Environmental Microbiology*, *70*(10), 5929–5936. https://doi.org/10.1128/AEM.70.10.5929-5936.2004

Di Bisceglie, F., García Navarro, J., Lombard, E., Kratzer, R., Kourist, R., & Guillouet, S. E. (2024). *Design and optimization of a small-scale autotrophic cultivation system for hydrogen-oxidizing bacteria*. Manuscript submitted

Di Bisceglie, F., García Navarro, J., Lombard, E., Kratzer, R., Kourist, R., & Guillouet, S. E. (2025). Conceptual Approach for Aerobic Autotrophic Gas Cultivation in Shake Flasks: Overcoming the Inhibitory Effects of Oxygen in *Cupriavidus necator*. *Biotechnology Journal*, *20*(2), e202400641. https://doi.org/10.1002/biot.202400641

Dronsella, B., Orsi, E., Schulz-Mirbach, H., Benito-Vaquerizo, S., Yilmaz, S., Glatter, T., Bar-Even, A., Erb, T. J., & Claassens, N. J. (2025). One-carbon fixation via the synthetic reductive glycine pathway exceeds yield of the Calvin cycle. *Nature Microbiology*, *10*(3), 646–653. https://doi.org/10.1038/s41564-025-01941-9

Du, F., Liu, Y.-Q., Xu, Y.-S., Li, Z.-J., Wang, Y.-Z., Zhang, Z.-X., & Sun, X.-M. (2021). Regulating the T7 RNA polymerase expression in *E. coli* BL21 (DE3) to provide more host options for recombinant protein production. *Microbial Cell Factories*, *20*, 189. https://doi.org/10.1186/s12934-021-01680-6

Duan, S., Feng, X., Gonzalez, M., Bader, S., Hayward, C., Ljubicic, T., Lu, J., Mustakis, J., Maloney, M., Rainville, J., & Zhang, X. (2020). Developing a Multistep Continuous Manufacturing Process for (1R,2R)-2-Amino-1-methylcyclopentan-1-ol. *Organic Process Research & Development*, *24*(11), 2734–2744. https://doi.org/10.1021/acs.oprd.0c00405

Dubaquié, Y., Looser, R., Fünfschilling, U., Jenö, P., & Rospert, S. (1998). Identification of in vivo substrates of the yeast mitochondrial chaperonins reveals overlapping but non-identical requirement for hsp60 and hsp10. *The EMBO Journal*, *17*(20), 5868–5876. https://doi.org/10.1093/emboj/17.20.5868

Eggers, J., & Steinbüchel, A. (2013). Poly(3-Hydroxybutyrate) degradation in *Ralstonia eutropha* H16 Is mediated stereoselectively to (S)-3-hydroxybutyryl coenzyme A (CoA) via crotonyl-CoA. *Journal of Bacteriology*, *195*(14), 3213–3223. https://doi.org/10.1128/JB.00358-13

Enrich-Prast, A., Bastviken, D., Crill, P., Santoro, A. L., Signori, C. N., & Sanseverino, A. M. (2014). Chemosynthesis. In *Reference Module in Earth Systems and Environmental Sciences*. Elsevier. https://doi.org/10.1016/B978-0-12-409548-9.09054-0

Erfani, N., Baharudin, L., & Watson, M. (2024). Recent advances and intensifications in Haber-Bosch ammonia synthesis process. *Chemical Engineering and Processing - Process Intensification*, *204*, 109962. https://doi.org/10.1016/j.cep.2024.109962

Espina, G., Atalah, J., & Blamey, J. M. (2021). Extremophilic oxidoreductases for the industry: Five successful examples with promising projections. *Frontiers in Bioengineering and Biotechnology*, *9*. https://doi.org/10.3389/fbioe.2021.710035

European Commission. (2024, December 11). *Bioeconomy research and innovation*. https://research-and-innovation.ec.europa.eu/research-area/environment/bioeconomy_en

European Commission: Directorate-General for Research and Innovation. (2018). *A sustainable bioeconomy for Europe: Strengthening the connection between economy, society and the environment : updated bioeconomy strategy*. Publications Office of the European Union. https://data.europa.eu/doi/10.2777/792130

Faber, K. (2011). Biocatalytic Applications. In K. Faber (Ed.), *Biotransformations in Organic Chemistry: A Textbook* (pp. 31–313). Springer. https://doi.org/10.1007/978-3-642-17393-6_2

Feng, J., Geng, W.-C., Jiang, H., & Wu, B. (2022). Recent advances in biocatalysis of nitrogen-containing heterocycles. *Biotechnology Advances*, *54*, 107813. https://doi.org/10.1016/j.biotechadv.2021.107813

Ferrer, M., Chernikova, T. N., Yakimov, M. M., Golyshin, P. N., & Timmis, K. N. (2003). Chaperonins govern growth of *Escherichia coli* at low temperatures. *Nature Biotechnology*, *21*(11), 1266–1267. https://doi.org/10.1038/nbt1103-1266

France, S. P., Hepworth, L. J., Turner, N. J., & Flitsch, S. L. (2017). Constructing biocatalytic cascades: In vitro and in vivo approaches to de novo multi-enzyme pathways. *ACS Catalysis*, *7*(1), 710–724. https://doi.org/10.1021/acscatal.6b02979

France, S. P., Howard, R. M., Steflik, J., Weise, N. J., Mangas-Sanchez, J., Montgomery, S. L., Crook, R., Kumar, R., & Turner, N. J. (2018). Identification of novel bacterial members of the imine reductase enzyme family that perform reductive amination. *ChemCatChem*, *10*(3), 510–514. https://doi.org/10.1002/cctc.201701408

France, S. P., Hussain, S., Hill, A. M., Hepworth, L. J., Howard, R. M., Mulholland, K. R., Flitsch, S. L., & Turner, N. J. (2016). One-Pot Cascade Synthesis of Mono- and Disubstituted Piperidines and Pyrrolidines using Carboxylic Acid Reductase (CAR), ω-Transaminase (ω-TA), and Imine Reductase (IRED) Biocatalysts. *ACS Catalysis*, *6*(6), 3753–3759. https://doi.org/10.1021/acscatal.6b00855

Fricke, W. F., Kusian, B., & Bowien, B. (2009). The genome organization of *Ralstonia eutropha* strain H16 and related species of the *Burkholderiaceae*. *Microbial Physiology*, *16*(1–2), 124–135. https://doi.org/10.1159/000142899

Friedrich, B., Heine, E., & Friedrich, C. G. (1981). Nickel requirement for active hydrogenase formation in *Alcaligenes eutrophus*. *Journal of Bacteriology*, *145*(3), 1144–1149. https://doi.org/10.1128/jb.145.3.1144-1149.1981

Friedrich, B., & Schwartz, E. (1993). Molecular biology of hydrogen utilization in aerobic chemolithotrophs. *Annual Review of Microbiology*, *47*, 351–384. https://doi.org/10.1146/annurev.mi.47.100193.002031

Friedrich, C. G. (1982). Depression of hydrogenase during limitation of electron donors and derepression of ribulosebisphosphate carboxylase during carbon limitation of *Alcaligenes eutrophus*. *Journal of Bacteriology*, *149*(1), 203–210. https://doi.org/10.1128/jb.149.1.203-210.1982

Frolov, N. A., & Vereshchagin, A. N. (2023). Piperidine derivatives: Recent advances in synthesis and pharmacological applications. *International Journal of Molecular Sciences*, *24*(3), 2937. https://doi.org/10.3390/ijms24032937

Frydman, R. B., Ruiz, O., Kreisel, M., & Bachrach, U. (1987). Oxidation of N-alkyl and C-alkylputrescines by diamine oxidases. *FEBS Letters*, *219*(2), 380–386. https://doi.org/10.1016/0014-5793(87)80257-0

Fukui, T., Mukoyama, M., Orita, I., & Nakamura, S. (2014). Enhancement of glycerol utilization ability of *Ralstonia eutropha* H16 for production of polyhydroxyalkanoates. *Applied Microbiology and Biotechnology*, *98*(17), 7559–7568. https://doi.org/10.1007/s00253-014-5831-3

Fuss, S., Lamb, W. F., Callaghan, M. W., Hilaire, J., Creutzig, F., Amann, T., Beringer, T., de Oliveira Garcia, W., Hartmann, J., Khanna, T., Luderer, G., Nemet, G. F., Rogelj, J., Smith, P., Vicente, J. L. V., Wilcox, J., del Mar Zamora Dominguez, M., & Minx, J. C. (2018). Negative emissions—Part 2: Costs, potentials and side effects. *Environmental Research Letters*, *13*(6), 063002. https://doi.org/10.1088/1748-9326/aabf9f

Gai, C. S., Lu, J., Brigham, C. J., Bernardi, A. C., & Sinskey, A. J. (2014). Insights into bacterial CO_2 metabolism revealed by the characterization of four carbonic anhydrases in *Ralstonia eutropha* H16. *AMB Express*, *4*, 2. https://doi.org/10.1186/2191-0855-4-2

Gao, B., Yang, B., Feng, X., & Li, C. (2022). Recent advances in the biosynthesis strategies of nitrogen heterocyclic natural products. *Natural Product Reports*, *39*(1), 139–162. https://doi.org/10.1039/D1NP00017A

Garavaglia, M., McGregor, C., Bommareddy, R. R., Irorere, V., Arenas, C., Robazza, A., Minton, N. P., & Kovacs, K. (2024). Stable platform for mevalonate bioproduction from CO_2. *ACS Sustainable Chemistry & Engineering*, *12*(36), 13486–13499. https://doi.org/10.1021/acssuschemeng.4c03561

Garrigues, L., Maignien, L., Lombard, E., Singh, J., & Guillouet, S. E. (2020). Isopropanol production from carbon dioxide in *Cupriavidus necator* in a pressurized bioreactor. *New Biotechnology*, *56*, 16–20. https://doi.org/10.1016/j.nbt.2019.11.005

Gascoyne, J. L., Bommareddy, R. R., Heeb, S., & Malys, N. (2021). Engineering *Cupriavidus necator* H16 for the autotrophic production of (R)-1,3-butanediol. *Metabolic Engineering*, *67*, 262–276. https://doi.org/10.1016/j.ymben.2021.06.010

Gerlach, M.-S., Neubauer, P., & Gimpel, M. (2023). Improved preculture management for *Cupriavidus necator* cultivations. *Biotechnology Letters*, *45*(11–12), 1487–1493. https://doi.org/10.1007/s10529-023-03436-1

Gevrekci, A. Ö. (2017). The roles of polyamines in microorganisms. *World Journal of Microbiology and Biotechnology*, *33*(11), 204. https://doi.org/10.1007/s11274-017-2370-y

Gibbins, J., & Chalmers, H. (2008). Carbon capture and storage. *Energy Policy*, *36*(12), 4317–4322. https://doi.org/10.1016/j.enpol.2008.09.058

Gilio, A. K., Thorpe, T. W., Turner, N., & Grogan, G. (2022). Reductive aminations by imine reductases: From milligrams to tons. *Chemical Science*, *13*(17), 4697–4713. https://doi.org/10.1039/d2sc00124a

Godoy, M. S., Mogilli, B., Fino, D., & Prieto, A. (2020). About how to capture and exploit the CO_2 surplus that nature, per se, is not capable of fixing. *Microbial Biotechnology*, *10*(5), 1216–1225. https://doi.org/10.1111/1751-7915.12805

González-Villanueva, M., Galaiya, H., Staniland, P., Staniland, J., Savill, I., Wong, T. S., & Tee, K. L. (2019). Adaptive Laboratory Evolution of *Cupriavidus necator* H16 for carbon co-utilization with glycerol. *International Journal of Molecular Sciences*, *20*(22), Article 22. https://doi.org/10.3390/ijms20225737

Goo, E., & Hwang, I. (2021). Essential roles of Lon protease in the morpho-physiological traits of the rice pathogen Burkholderia glumae. *PLoS ONE*, *16*(9), e0257257. https://doi.org/10.1371/journal.pone.0257257

Gordon, E. M., Barrett, R. W., Dower, W. J., Fodor, S. P. A., & Gallop, M. A. (1994). Applications of combinatorial technologies to drug discovery. 2. Combinatorial organic synthesis, library screening strategies, and future directions. *Journal of Medicinal Chemistry*, *37*(10), 1385–1401. https://doi.org/10.1021/jm00036a001

Goris, T., Wait, A. F., Saggu, M., Fritsch, J., Heidary, N., Stein, M., Zebger, I., Lendzian, F., Armstrong, F. A., Friedrich, B., & Lenz, O. (2011). A unique iron-sulfur cluster is crucial for oxygen tolerance of a [NiFe]-hydrogenase. *Nature Chemical Biology*, *7*(5), 310–318. https://doi.org/10.1038/nchembio.555

Gorr, T. A., & Vogel, J. (2015). Western blotting revisited: Critical perusal of underappreciated technical issues. *PROTEOMICS – Clinical Applications*, *9*(3–4), 396–405. https://doi.org/10.1002/prca.201400118

Gottesman, S. (1996). Proteases and their targets in Escherichia coli. *Annual Review of Genetics*, *30*, 465–506. https://doi.org/10.1146/annurev.genet.30.1.465

Grahl, N., Kern, S. E., Newman, D. K., & Hogan, D. A. (2013). The Yin and Yang of phenazine physiology. In S. Chincholkar & L. Thomashow (Eds.), *Microbial Phenazines: Biosynthesis, Agriculture and Health* (pp. 43–69). Springer. https://doi.org/10.1007/978-3-642-40573-0_3

Grant, S. G., Jessee, J., Bloom, F. R., & Hanahan, D. (1990). Differential plasmid rescue from transgenic mouse DNAs into Escherichia coli methylation-restriction mutants. *Proceedings of the National Academy of Sciences*, *87*(12), 4645–4649. https://doi.org/10.1073/pnas.87.12.4645

Grousseau, E., Lu, J., Gorret, N., Guillouet, S. E., & Sinskey, A. J. (2014). Isopropanol production with engineered *Cupriavidus necator* as bioproduction platform. *Applied Microbiology and Biotechnology*, *98*(9), 4277–4290. https://doi.org/10.1007/s00253-014-5591-0

Gruber, S., Hagen, J., Schwab, H., & Koefinger, P. (2014). Versatile and stable vectors for efficient gene expression in *Ralstonia eutropha* H16. *Journal of Biotechnology*, *186*, 74–82. https://doi.org/10.1016/j.jbiotec.2014.06.030

Halicki, P. C. B., da Silva Júnior, E. N., Jardim, G. A. de M., Almeida, R. G. de, Vicenti, J. R. de M., Gonçalves, B. L., da Silva, P. E. A., & Ramos, D. F. (2021). Benzo[a]phenazine derivatives: Promising scaffolds to combat resistant Mycobacterium tuberculosis. *Chemical Biology & Drug Design*, *98*(3), 352–362. https://doi.org/10.1111/cbdd.13853

Hanko, E. K. R., Sherlock, G., Minton, N. P., & Malys, N. (2022). Biosensor-informed engineering of *Cupriavidus necator* H16 for autotrophic D-mannitol production. *Metabolic Engineering*, *72*, 24–34. https://doi.org/10.1016/j.ymben.2022.02.003

Hanukoglu, I. (2015). Proteopedia: Rossmann fold: A beta-alpha-beta fold at dinucleotide binding sites. *Biochemistry and Molecular Biology Education*, *43*(3), 206–209. https://doi.org/10.1002/bmb.20849

Hartl, F. U. (1996). Molecular chaperones in cellular protein folding. *Nature*, *381*(6583), 571–580. https://doi.org/10.1038/381571a0

Haszeldine, R. S. (2009). Carbon capture and storage: How green can black be? *Science (New York, N.Y.)*, *325*(5948), 1647–1652. https://doi.org/10.1126/science.1172246

Heath, R. S., Pontini, M., Hussain, S., & Turner, N. J. (2016). Combined imine reductase and amine oxidase catalyzed deracemization of nitrogen heterocycles. *ChemCatChem*, *8*(1), 117–120. https://doi.org/10.1002/cctc.201500822

Heckmann, C. M., & Paradisi, F. (2020). Looking Back: A Short History of the Discovery of Enzymes and How They Became Powerful Chemical Tools. *ChemCatChem*, *12*(24), 6082–6102. https://doi.org/10.1002/cctc.202001107

Hepburn, C., Adlen, E., Beddington, J., Carter, E. A., Fuss, S., Mac Dowell, N., Minx, J. C., Smith, P., & Williams, C. K. (2019). The technological and economic prospects for CO_2 utilization and removal. *Nature*, *575*(7781), 87–97. https://doi.org/10.1038/s41586-019-1681-6

Hoefel, T., Wittmann, E., Reinecke, L., & Weuster-Botz, D. (2010). Reaction engineering studies for the production of 2-hydroxyisobutyric acid with recombinant *Cupriavidus necator* H 16. *Applied Microbiology and Biotechnology*, *88*(2), 477–484. https://doi.org/10.1007/s00253-010-2739-4

Holmes, E. C., Bleem, A. C., Johnson, C. W., & Beckham, G. T. (2024). Adaptive laboratory evolution and metabolic engineering of *Cupriavidus necator* for improved catabolism of volatile fatty acids. *Metabolic Engineering*, *86*, 262–273. https://doi.org/10.1016/j.ymben.2024.10.011

Holzer, A. K., Hiebler, K., Mutti, F. G., Simon, R. C., Lauterbach, L., Lenz, O., & Kroutil, W. (2015). Asymmetric biocatalytic amination of ketones at the expense of NH<sub3</sub> and molecular hydrogen. *Organic Letters*, *17*(10), 2431–2433. https://doi.org/10.1021/acs.orglett.5b01154

Horovitz, A., & Willison, K. R. (2005). Allosteric regulation of chaperonins. *Current Opinion in Structural Biology*, *15*(6), 646–651. https://doi.org/10.1016/j.sbi.2005.10.001

Horwich, A. L., Low, K. B., Fenton, W. A., Hirshfield, I. N., & Furtak, K. (1993). Folding in vivo of bacterial cytoplasmic proteins: Role of GroEL. *Cell*, *74*(5), 909–917. https://doi.org/10.1016/0092-8674(93)90470-B

Houry, W. A., Frishman, D., Eckerskorn, C., Lottspeich, F., & Hartl, F. U. (1999). Identification of in vivo substrates of the chaperonin GroEL. *Nature*, *402*(6758), 147–154. https://doi.org/10.1038/45977

Huber, T., Schneider, L., Präg, A., Gerhardt, S., Einsle, O., & Müller, M. (2014). Direct reductive amination of ketones: Structure and activity of S-selective imine reductases from Streptomyces. *ChemCatChem*, *6*(8), 2248–2252. https://doi.org/10.1002/cctc.201402218

Hunke, S., & Betton, J.-M. (2003). Temperature effect on inclusion body formation and stress response in the periplasm of Escherichia coli. *Molecular Microbiology*, *50*(5), 1579–1589. https://doi.org/10.1046/j.1365-2958.2003.03785.x

Hussain, S., Leipold, F., Man, H., Wells, E., France, S. P., Mulholland, K. R., Grogan, G., & Turner, N. J. (2015). An (R)-imine reductase biocatalyst for the asymmetric reduction of cyclic imines. *ChemCatChem*, *7*(4), 579–583. https://doi.org/10.1002/cctc.201402797

Ibrahim, M. H. A. (2023). *Sistemas para el cocultivo de cepas de Ralstonia eutropha* (Patent No. ES2932307T3). https://patents.google.com/patent/ES2932307T3/es

IEA, I. E. A. (2021). *Bioenergy Annual Report*. https://www.ieabioenergy.com/blog/publications/iea-bioenergy-annual-report-2021/

IEA, I. E. A. (2023, December 6). *Chemicals—IEA*. https://www.iea.org/energy-system/industry/chemicals

International Fertilizer Industry Association. (2014). *Ammonia Production: Moving Towards Maximum Efficiency and Lower GHG Emissions* (In Fertilizer Facts). https://www.fertilizer.org/resource/ammonia-production-moving-towards-maximum-efficiency-and-lower-ghg-emissions/

IP.com Prior Art Database. (2017a). *Imine reductase mediated synthesis of (S, S)-Sertraline* (IP.com Prior Art Database Patent No. Disclosure Number IPCOM000251929). https://priorart.ip.com/IPCOM/000251929

IP.com Prior Art Database. (2017b). *InnovationQ™ Powered by IP.com Prior Art Database*. https://priorart.ip.com/IPCOM/000251929

Ishizaki, A., & Tanaka, K. (1991). Production of poly-β-hydroxybutyric acid from carbon dioxide by *Alcaligenes eutrophus* ATCC 17697T. *Journal of Fermentation and Bioengineering*, *71*(4), 254–257. https://doi.org/10.1016/0922-338X(91)90277-N

Ishizuka, H., Horinouchi, S., & Beppu, T. (1993). Putrescine oxidase of *Micrococcus rubens*: Primary structure and *Escherichia coli*. *Microbiology*, *139*(3), 425–432. https://doi.org/10.1099/00221287-139-3-425

Ismail, S., Giacinti, G., Raynaud, C. D., Cameleyre, X., Alfenore, S., Guillouet, S., & Gorret, N. (2024). Impact of the environmental parameters on single cell protein production and composition by *Cupriavidus necator*. *Journal of Biotechnology*, *388*, 83–95. https://doi.org/10.1016/j.jbiotec.2024.04.009

Jahn, M., Crang, N., Gynnå, A. H., Kabova, D., Frielingsdorf, S., Lenz, O., Charpentier, E., & Hudson, E. P. (2024). The energy metabolism of Cupriavidus necator in different trophic conditions. *Applied and Environmental Microbiology*, *90*(10), e00748-24. https://doi.org/10.1128/aem.00748-24

Jahn, M., Crang, N., Janasch, M., Hober, A., Forsström, B., Kimler, K., Mattausch, A., Chen, Q., Asplund-Samuelsson, J., & Hudson, E. P. (2021). Protein allocation and utilization in the versatile chemolithoautotroph Cupriavidus necator. *eLife*, *10*, e69019. https://doi.org/10.7554/eLife.69019

Jämsä, T., Claassens, N. J., Salusjärvi, L., & Nyyssölä, A. (2024). H_2-driven xylitol production in *Cupriavidus necator* H16. *Microbial Cell Factories*, *23*(1), 345. https://doi.org/10.1186/s12934-024-02615-7

Janson, J.-C. [Editor]. (2011). *Protein Purification: Principles, High Resolution Methods, and Applications, 3rd Edition | Wiley* (3rd ed., Vol. 1). Wiley. https://www.wiley.com/en-es/Protein+Purification%3A+Principles%2C+High+Resolution+Methods%2C+and+Applications%2C+3rd+Edition-p-9781118002193

Jawed, K., Irorere, V. U., Bommareddy, R. R., Minton, N. P., & Kovács, K. (2022). Establishing mixotrophic growth of *Cupriavidus necator* H16 on CO_2 and volatile fatty acids. *Fermentation*, *8*(3), Article 3. https://doi.org/10.3390/fermentation8030125

Jeong, H., Barbe, V., Lee, C. H., Vallenet, D., Yu, D. S., Choi, S.-H., Couloux, A., Lee, S.-W., Yoon, S. H., Cattolico, L., Hur, C.-G., Park, H.-S., Ségurens, B., Kim, S. C., Oh, T. K., Lenski, R. E., Studier, F. W., Daegelen, P., & Kim, J. F. (2009). Genome sequences of *Escherichia coli* B strains REL606 and BL21(DE3). *Journal of Molecular Biology*, *394*(4), 644–652. https://doi.org/10.1016/j.jmb.2009.09.052

Jugder, B.-E., Chen, Z., Ping, D. T. T., Lebhar, H., Welch, J., & Marquis, C. P. (2015). An analysis of the changes in soluble hydrogenase and global gene expression in *Cupriavidus necator* (*Ralstonia eutropha*) H16 grown in heterotrophic diauxic batch culture. *Microbial Cell Factories*, *14*(1), 42. https://doi.org/10.1186/s12934-015-0226-4

Kamathewatta, N. J. B., Nguyen, T. M., Lietz, R., Hughes, T., Taktak Karaca, B., Deay, D. O. I., Richter, M. L., Tamerler, C., & Berrie, C. L. (2021). Probing selective self-assembly of putrescine oxidase with controlled orientation using a genetically engineered peptide tag. *Langmuir*, *37*(24), 7536–7547. https://doi.org/10.1021/acs.langmuir.1c01033

Kanehisa, M. (2019). Toward understanding the origin and evolution of cellular organisms. *Protein Science: A Publication of the Protein Society*, *28*(11), 1947–1951. https://doi.org/10.1002/pro.3715

Kanehisa, M., Furumichi, M., Sato, Y., Matsuura, Y., & Ishiguro-Watanabe, M. (2025). KEGG: Biological systems database as a model of the real world. *Nucleic Acids Research*, *53*(D1), D672–D677. https://doi.org/10.1093/nar/gkae909

Kanehisa, M., & Goto, S. (2000). KEGG: Kyoto encyclopedia of genes and genomes. *Nucleic Acids Research*, *28*(1), 27–30. https://doi.org/10.1093/nar/28.1.27

Kerfeld, C. A., & Melnicki, M. R. (2016). Assembly, function and evolution of cyanobacterial carboxysomes. *Current Opinion in Plant Biology*, *31*, 66–75. https://doi.org/10.1016/j.pbi.2016.03.009

Kerru, N., Gummidi, L., Maddila, S., Gangu, K. K., & Jonnalagadda, S. B. (2020). A review on recent advances in Nitrogen-containing molecules and their biological applications. *Molecules (Basel, Switzerland)*, *25*(8). https://doi.org/10.3390/molecules25081909

Kim, G. B., Kim, H. R., & Lee, S. Y. (2025). Comprehensive evaluation of the capacities of microbial cell factories. *Nature Communications*, *16*(1), 2869. https://doi.org/10.1038/s41467-025-58227-1

Kim, S. H., Wang, Y., Khomutov, M., Khomutov, A., Fuqua, C., & Michael, A. J. (2016). The Essential Role of Spermidine in Growth of *Agrobacterium tumefaciens* Is Determined by the 1,3-Diaminopropane Moiety. *ACS Chemical Biology*, *11*(2), 491–499. https://doi.org/10.1021/acschembio.5b00893

Kim, S., Jang, Y. J., Gong, G., Lee, S.-M., Um, Y., Kim, K. H., & Ko, J. K. (2022). Engineering *Cupriavidus necator* H16 for enhanced lithoautotrophic poly(3-hydroxybutyrate) production from CO_2. *Microbial Cell Factories*, *21*(1), 231. https://doi.org/10.1186/s12934-022-01962-7

Kim, S.-K., Jin, Y.-S., Choi, I.-G., Park, Y.-C., & Seo, J.-H. (2015). Enhanced tolerance of *Saccharomyces cerevisiae* to multiple lignocellulose-derived inhibitors through modulation of spermidine contents. *Metabolic Engineering*, *29*, 46–55. https://doi.org/10.1016/j.ymben.2015.02.004

Kopacz, M. M., Heuts, D. P. H. M., & Fraaije, M. W. (2014). Kinetic mechanism of putrescine oxidase from *Rhodococcus erythropolis*. *The FEBS Journal*, *281*(19), 4384–4393. https://doi.org/10.1111/febs.12945

Kopacz, M. M., Rovida, S., van Duijn, E., Fraaije, M. W., & Mattevi, A. (2011). Structure-based redesign of cofactor binding in putrescine oxidase. *Biochemistry*, *50*(19), 4209–4217. https://doi.org/10.1021/bi200372u

Krieg, T., Sydow, A., Faust, S., Huth, I., & Holtmann, D. (2018). CO_2 to rerpenes: Autotrophic and electroautotrophic α-humulene production with *Cupriavidus necator*. *Angewandte Chemie International Edition*, *57*(7), 1879–1882. https://doi.org/10.1002/anie.201711302

Krysenko, S., & Wohlleben, W. (2022). Polyamine and ethanolamine metabolism in bacteria as an important component of nitrogen assimilation for survival and pathogenicity. *Medical Sciences*, *10*(3), Article 3. https://doi.org/10.3390/medsci10030040

Kumar, R., Karmilowicz, M. J., Burke, D., Burns, M. P., Clark, L. A., Connor, C. G., Cordi, E., Do, N. M., Doyle, K. M., Hoagland, S., Lewis, C. A., Mangan, D., Martinez, C. A., McInturff, E. L., Meldrum, K., Pearson, R., Steflik, J., Rane, A., & Weaver, J. (2021). Biocatalytic reductive amination from discovery to commercial manufacturing applied to abrocitinib JAK1 inhibitor. *Nature Catalysis*, *4*(9), 775–782. https://doi.org/10.1038/s41929-021-00671-5

Kunth, C. (2023). *Enzymatic reduction of sterically challenging imines by novel imine reductases* [Bachelor thesis for the attainment of the degree “Bachelor of Science” in Biology]. RWTH Aachen University.

Kwon, D. H., & Lu, C.-D. (2006). Polyamines increase antibiotic susceptibility in *Pseudomonas aeruginosa*. *Antimicrobial Agents and Chemotherapy*, *50*(5), 1623–1627. https://doi.org/10.1128/AAC.50.5.1623-1627.2006

Lambauer, V., & Kratzer, R. (2022). Lab-Scale Cultivation of Cupriavidus necator on Explosive Gas Mixtures: Carbon Dioxide Fixation into Polyhydroxybutyrate. *Bioengineering (Basel, Switzerland)*, *9*(5), 204. https://doi.org/10.3390/bioengineering9050204

Lau, P. C. K., & Grosse, S. (2013). The fundamentals and fun of biocatalysis. In *Marine Enzymes for Biocatalysis* (pp. 17–69). Elsevier. https://doi.org/10.1533/9781908818355.1.17

Lauterbach, L., & Lenz, O. (2013). Catalytic Production of Hydrogen Peroxide and Water by Oxygen-Tolerant [NiFe]-Hydrogenase during H2 Cycling in the Presence of O2. *Journal of the American Chemical Society*, *135*(47), 17897–17905. https://doi.org/10.1021/ja408420d

Lauterbach, L., & Lenz, O. (2019). How to make the reducing power of H_2 available for in vivo biosyntheses and biotransformations. *Current Opinion in Chemical Biology*, *49*, 91–96. https://doi.org/10.1016/j.cbpa.2018.11.020

Lauterbach, L., Lenz, O., & Vincent, K. A. (2013). H_2-driven cofactor regeneration with NAD(P)+-reducing hydrogenases. *The FEBS Journal*, *280*(13), 3058–3068. https://doi.org/10.1111/febs.12245

Lazdin'sh, I. Ya., & Avots, A. A. (1979). Catalytic methods of obtaining pyridine bases (survey). *Chemistry of Heterocyclic Compounds*, *15*(8), 823–837. https://doi.org/10.1007/BF00509781

Lee, H., Calvin, K., Dasgupta, D., Krinner, G., Mukherji, A., Thorne, P. W., Trisos, C., Romero, J., Aldunce, P., Barrett, K., Blanco, G., Cheung, W. W. L., Connors, S., Denton, F., Diongue-Niang, A., Dodman, D., Garschagen, M., Geden, O., Hayward, B., … Péan, C. (2023). *IPCC, 2023: Climate Change 2023: Synthesis Report. Contribution of Working Groups I, II and III to the Sixth Assessment Report of the Intergovernmental Panel on Climate Change [Core Writing Team, H. Lee and J. Romero (eds.)]. IPCC, Geneva, Switzerland*. Intergovernmental Panel on Climate Change (IPCC). https://doi.org/10.59327/IPCC/AR6-9789291691647

Lee, I., & Suzuki, C. K. (2008). Functional mechanics of the ATP-dependent Lon protease- lessons from endogenous protein and synthetic peptide substrates. *Biochimica et Biophysica Acta*, *1784*(5), 727. https://doi.org/10.1016/j.bbapap.2008.02.010

Lee, S. Y. (1996). Bacterial polyhydroxyalkanoates. *Biotechnology and Bioengineering*, *49*(1), 1–14. https://doi.org/10.1002/(SICI)1097-0290(19960105)49:1<1::AID-BIT1>3.0.CO;2-P

Lee, S. Y., Kim, H. U., Chae, T. U., Cho, J. S., Kim, J. W., Shin, J. H., Kim, D. I., Ko, Y.-S., Jang, W. D., & Jang, Y.-S. (2019). A comprehensive metabolic map for production of bio-based chemicals. *Nature Catalysis*, *2*(1), 18–33. https://doi.org/10.1038/s41929-018-0212-4

Lee, S.-E., Li, Q. X., & Yu, J. (2009). Diverse protein regulations on PHA formation in *Ralstonia eutropha* on short chain organic acids. *International Journal of Biological Sciences*, *5*(3), 215–225.

Lenz, O., Bernhard, M., Buhrke, T., Schwartz, E., & Friedrich, B. (2002). The hydrogen-sensing apparatus in *Ralstonia eutropha*. *Journal of Molecular Microbiology and Biotechnology*, *4*(3), 255–262.

Lenz, O., & Friedrich, B. (1998). A novel multicomponent regulatory system mediates H_2 sensing in *Alcaligenes eutrophus* . *Proceedings of the National Academy of Sciences*, *95*(21), 12474–12479. https://doi.org/10.1073/pnas.95.21.12474

Lenz, O., Lauterbach, L., & Frielingsdorf, S. (2018). O_2-tolerant [NiFe]-hydrogenases of Ralstonia eutropha H16: Physiology, molecular biology, purification, and biochemical analysis. In *Methods in Enzymology* (Vol. 613, pp. 117–151). Elsevier. https://doi.org/10.1016/bs.mie.2018.10.008

Lenz, O., Lauterbach, L., Frielingsdorf, S., & Friedrich, B. (2015). Oxygen-tolerant hydrogenases and their biotechnological potential. In *Biohydrogen* (pp. 61–96). De Gruyter. https://www.degruyterbrill.com/document/doi/10.1515/9783110336733.61/html

Lenz, O., Strack, A., Tran-Betcke, A., & Friedrich, B. (1997). A hydrogen-sensing system in transcriptional regulation of hydrogenase gene expression in Alcaligenes species. *Journal of Bacteriology*, *179*(5), 1655–1663. https://doi.org/10.1128/jb.179.5.1655-1663.1997

Li, H., Opgenorth, P. H., Wernick, D. G., Rogers, S., Wu, T.-Y., Higashide, W., Malati, P., Huo, Y.-X., Cho, K. M., & Liao, J. C. (2012). Integrated Electromicrobial Conversion of CO_2 to Higher Alcohols. *Science*, *335*(6076), 1596–1596. https://doi.org/10.1126/science.1217643

Li, J., Xiong, Q., Mu, X., & Li, L. (2024). Recent advances in ammonia synthesis: From Haber-Bosch process to external field driven strategies. *ChemSusChem*, *17*(15), e202301775. https://doi.org/10.1002/cssc.202301775

Li, Z., Xin, X., Xiong, B., Zhao, D., Zhang, X., & Bi, C. (2020). Engineering the Calvin–Benson–Bassham cycle and hydrogen utilization pathway of *Ralstonia eutropha* for improved autotrophic growth and polyhydroxybutyrate production. *Microbial Cell Factories*, *19*(1), Article 1. https://doi.org/10.1186/s12934-020-01494-y

Li, Z., Xiong, B., Liu, L., Li, S., Xin, X., Li, Z., Zhang, X., & Bi, C. (2019). Development of an autotrophic fermentation technique for the production of fatty acids using an engineered *Ralstonia eutropha* cell factory. *Journal of Industrial Microbiology and Biotechnology*, *46*(6), 783–790. https://doi.org/10.1007/s10295-019-02156-8

Lim, G., Calabrese, D., Wolder, A., Cordero, P. R. F., Rother, D., Mulks, F. F., Paul, C. E., & Lauterbach, L. (2024). H_2-driven biocatalysis for flavin-dependent ene-reduction in a continuous closed-loop flow system utilizing H_2 from water electrolysis. *Communications Chemistry*, *7*(1), 1–7. https://doi.org/10.1038/s42004-024-01288-y

Lin, B., Nowrin, F. H., Rosenthal, J. J., Bhown, A. S., & Malmali, M. (2023). Perspective on intensification of Haber−Bosch to enable ammonia production under milder conditions. *ACS Sustainable Chemistry & Engineering*, *11*(27), 9880–9899. https://doi.org/10.1021/acssuschemeng.2c06711

Lin, B., & Tao, Y. (2017). Whole-cell biocatalysts by design. *Microbial Cell Factories*, *16*(1), 106. https://doi.org/10.1186/s12934-017-0724-7

Lin, K., Elbahloul, Y., & Steinbüchel, A. (2012). Physiological conditions conducive to high cell density and high cyanophycin content in *Ralstonia eutropha* strain H16 possessing a KDPG aldolase gene-dependent addiction system. *Applied Microbiology and Biotechnology*, *93*(5), 1885–1894. https://doi.org/10.1007/s00253-011-3685-5

Lin, T.-H., Cheng, S.-Y., Lin, Y.-F., & Chen, P.-T. (2024). Development of the low-Temperature inducible system for recombinant protein production in *Escherichia coli* Nissle 1917. *Journal of Agricultural and Food Chemistry*, *72*(13), 7318–7325. https://doi.org/10.1021/acs.jafc.4c01075

Lindskog, S. (1997). Structure and mechanism of carbonic anhydrase. *Pharmacology & Therapeutics*, *74*(1), 1–20. https://doi.org/10.1016/S0163-7258(96)00198-2

Liu, C., Colón, B. C., Ziesack, M., Silver, P. A., & Nocera, D. G. (2016). Water splitting–biosynthetic system with CO2 reduction efficiencies exceeding photosynthesis. *Science*, *352*(6290), 1210–1213. https://doi.org/10.1126/science.aaf5039

Liu, Z., Hossain, S. S., Morales Moreira, Z., & Haney, C. H. (2021). Putrescine and its metabolic precursor arginine promote biofilm and c-di-GMP synthesis in *Pseudomonas aeruginosa*. *Journal of Bacteriology*, *204*(1), e00297-21. https://doi.org/10.1128/JB.00297-21

Liu, Z., Shi, S., Ji, Y., Wang, K., Tan, T., & Nielsen, J. (2023). Opportunities of CO_2-based biorefineries for production of fuels and chemicals. *Green Carbon*, *1*(1), 75–84. https://doi.org/doi.org/10.1016/j.greenca.2023.09.002.

Liu, Z., Wang, K., Chen, Y., Tan, T., & Nielsen, J. (2020). Third-generation biorefineries as the means to produce fuels and chemicals from CO2. *Nature Catalysis*, *3*(3), 274–288. https://doi.org/10.1038/s41929-019-0421-5

Lonsdale, T. H., Lauterbach, L., Malca, S. H., Nestl, B. M., Hauer, B., & Lenz, O. (2015). H_2-driven biotransformation of n-octane to 1-octanol by a recombinant *Pseudomonas putida* strain co-synthesizing an O_2-tolerant hydrogenase and a P450 monooxygenase. *Chemical Communications*, *51*(90), 16173–16175. https://doi.org/10.1039/C5CC06078H

Löwe, H., Beentjes, M., Pflüger-Grau, K., & Kremling, A. (2021). Trehalose production by *Cupriavidus necator* from CO_2 and hydrogen gas. *Bioresource Technology*, *319*, 124169. https://doi.org/10.1016/j.biortech.2020.124169

Lu, J., Brigham, C. J., Gai, C. S., & Sinskey, A. J. (2012). Studies on the production of branched-chain alcohols in engineered Ralstonia eutropha. *Applied Microbiology and Biotechnology*, *96*(1), 283–297. https://doi.org/10.1007/s00253-012-4320-9

Lubitz, W., & Ogata, H. (2013). Hydrogenases, Structure and Function. In W. J. Lennarz & M. D. Lane (Eds.), *Encyclopedia of Biological Chemistry (Second Edition)* (pp. 562–567). Academic Press. https://doi.org/10.1016/B978-0-12-378630-2.00205-X

Ma, B.-G., Chen, L., Ji, H.-F., Chen, Z.-H., Yang, F.-R., Wang, L., Qu, G., Jiang, Y.-Y., Ji, C., & Zhang, H.-Y. (2008). Characters of very ancient proteins. *Biochemical and Biophysical Research Communications*, *366*(3), 607–611. https://doi.org/10.1016/j.bbrc.2007.12.014

Ma, E. J., Siirola, E., Moore, C., Kummer, A., Stoeckli, M., Faller, M., Bouquet, C., Eggimann, F., Ligibel, M., Huynh, D., Cutler, G., Siegrist, L., Lewis, R. A., Acker, A.-C., Freund, E., Koch, E., Vogel, M., Schlingensiepen, H., Oakeley, E. J., & Snajdrova, R. (2021). Machine-directed evolution of an imine reductase for activity and stereoselectivity. *ACS Catalysis*, *11*(20), 12433–12445. https://doi.org/10.1021/acscatal.1c02786

Mahram, A., & Herbordt, M. C. (2015). NCBI BLASTP on high-performance reconfigurable computing systems. *ACM Trans. Reconfigurable Technol. Syst.*, *7*(4), 33:1-33:20. https://doi.org/10.1145/2629691

Mann, M. S., Dragovic, Z., Schirrmacher, G., & Lütke-Eversloh, T. (2012). Over-expression of stress protein-encoding genes helps Clostridium acetobutylicum to rapidly adapt to butanol stress. *Biotechnology Letters*, *34*(9), 1643–1649. https://doi.org/10.1007/s10529-012-0951-2

Marc, J., Grousseau, E., Lombard, E., Sinskey, A. J., Gorret, N., & Guillouet, S. E. (2017a). Over expression of GroESL in *Cupriavidus necator* for heterotrophic and autotrophic isopropanol production. *Metabolic Engineering*, *42*, 74–84. https://doi.org/10.1016/j.ymben.2017.05.007

Marc, J., Grousseau, E., Lombard, E., Sinskey, A. J., Gorret, N., & Guillouet, S. E. (2017b). Over expression of GroESL in Cupriavidus necator for heterotrophic and autotrophic isopropanol production. *Metabolic Engineering*, *42*, 74–84. https://doi.org/10.1016/j.ymben.2017.05.007

Marchenkov, V. V., & Semisotnov, G. V. (2009). GroEL-Assisted Protein Folding: Does It Occur Within the Chaperonin Inner Cavity? *International Journal of Molecular Sciences*, *10*(5), Article 5. https://doi.org/10.3390/ijms10052066

Marshall, C. M., Federice, J. G., Bell, C. N., Cox, P. B., & Njardarson, J. T. (2024). An update on the Nitrogen heterocycle compositions and properties of U.S. FDA-approved pharmaceuticals (2013-2023). *Journal of Medicinal Chemistry*, *67*(14), 11622–11655. https://doi.org/10.1021/acs.jmedchem.4c01122

Martin, J., Horwich, A. L., & Hartl, F. U. (1992). Prevention of protein denaturation under heat stress by the chaperonin Hsp60. *Science*, *258*(5084), 995–998. https://doi.org/10.1126/science.1359644

Martínez, A. T., Ruiz-Dueñas, F. J., Camarero, S., Serrano, A., Linde, D., Lund, H., Vind, J., Tovborg, M., Herold-Majumdar, O. M., Hofrichter, M., Liers, C., Ullrich, R., Scheibner, K., Sannia, G., Piscitelli, A., Pezzella, C., Sener, M. E., Kılıç, S., van Berkel, W. J. H., … Alcalde, M. (2017a). Oxidoreductases on their way to industrial biotransformations. *Biotechnology Advances*, *35*(6), 815–831. https://doi.org/10.1016/j.biotechadv.2017.06.003

Martínez, A. T., Ruiz-Dueñas, F. J., Camarero, S., Serrano, A., Linde, D., Lund, H., Vind, J., Tovborg, M., Herold-Majumdar, O. M., Hofrichter, M., Liers, C., Ullrich, R., Scheibner, K., Sannia, G., Piscitelli, A., Pezzella, C., Sener, M. E., Kılıç, S., van Berkel, W. J. H., … Alcalde, M. (2017b). Oxidoreductases on their way to industrial biotransformations. *Biotechnology Advances*, *35*(6), 815–831. https://doi.org/10.1016/j.biotechadv.2017.06.003

Matange, N. (2020). Highly contingent phenotypes of Lon protease deficiency in *Escherichia coli* upon antibiotic challenge. *Journal of Bacteriology*, *202*(3), e00561. https://doi.org/10.1128/JB.00561-19

McCormick, K. (2014). The bioeconomy and beyond: Visions and strategies. *Biofuels*, *5*(3), 191–193. https://doi.org/10.1080/17597269.2014.913882

McGlade, C., & Ekins, P. (2015). The geographical distribution of fossil fuels unused when limiting global warming to 2 °C. *Nature*, *517*(7533), 187–190. https://doi.org/10.1038/nature14016

Meyer, T., Zumbrägel, N., Geerds, C., Gröger, H., & Niemann, H. H. (2020). Structural characterization of an S-enantioselective imine reductase from *Mycobacterium smegmatis*. *Biomolecules*, *10*(8), Article 8. https://doi.org/10.3390/biom10081130

Meylan, F. D., Moreau, V., & Erkman, S. (2015). CO_2 utilization in the perspective of industrial ecology, an overview. *Journal of CO2 Utilization*, *12*, 101–108. https://doi.org/10.1016/j.jcou.2015.05.003

Minx, J. C., Lamb, W. F., Callaghan, M. W., Fuss, S., Hilaire, J., Creutzig, F., Amann, T., Beringer, T., de Oliveira Garcia, W., Hartmann, J., Khanna, T., Lenzi, D., Luderer, G., Nemet, G. F., Rogelj, J., Smith, P., Vicente Vicente, J. L., Wilcox, J., & del Mar Zamora Dominguez, M. (2018). Negative emissions—Part 1: Research landscape and synthesis. *Environmental Research Letters*, *13*(6), 063001. https://doi.org/10.1088/1748-9326/aabf9b

Mitsukura, K., Kuramoto, T., Yoshida, T., Kimoto, N., Yamamoto, H., & Nagasawa, T. (2013). *A NADPH-dependent (S)-imine reductase (SIR) from Streptomyces sp. GF3546 for asymmetric synthesis of optically active amines: Purification, characterization, gene cloning, and expression*. *97*, 8079–8086. https://doi.org/10.1007/s00253-012-4629-4

Mitsukura, K., Suzuki, M., Shinoda, S., Kuramoto, T., Yoshida, T., & Nagasawa, T. (2011). Purification and characterization of a novel (R)-imine reductase from Streptomyces sp. GF3587. *Bioscience, Biotechnology, and Biochemistry*, *75*(9), 1778–1782. https://doi.org/10.1271/bbb.110303

Mitsukura, K., Suzuki, M., Tada, K., Yoshida, T., & Nagasawa, T. (2010). Asymmetric synthesis of chiral cyclic amine from cyclic imine by bacterial whole-cell catalyst of enantioselective imine reductase. *Organic & Biomolecular Chemistry*, *8*(20), 4533–4535. https://doi.org/10.1039/C0OB00353K

Miyahara, Y., Wang, C.-T., Ishii-Hyakutake, M., & Tsuge, T. (2022). Continuous supply of non-combustible gas mixture for safe autotrophic culture to produce polyhydroxyalkanoate by hydrogen-oxidizing bacteria. *Bioengineering*, *9*(10), 586. https://doi.org/10.3390/bioengineering9100586

Montgomery, S. L., Puspanath, A., Heath, R. S., Marshall, J. R., Klemstein, U., Galman, J. L., Woodlock, D., Bisagni, S., Taylor, C. J., Mangas-Sanchez, J., Ramsden, J. I., Dominguez, B., & Turner, N. J. (2020). Characterization of imine reductases in reductive amination for the exploration of structure-activity relationships. *Science Journals — AAAS*.

Morlino, M. S., Serna García, R., Savio, F., Zampieri, G., Morosinotto, T., Treu, L., & Campanaro, S. (2023). Cupriavidus necator as a platform for polyhydroxyalkanoate production: An overview of strains, metabolism, and modeling approaches. *Biotechnology Advances*, *69*, 108264. https://doi.org/10.1016/j.biotechadv.2023.108264

Mühlmann, M., Forsten, E., Noack, S., & Büchs, J. (2017). Optimizing recombinant protein expression via automated induction profiling in microtiter plates at different temperatures. *Microbial Cell Factories*, *16*(1), 220. https://doi.org/10.1186/s12934-017-0832-4

Nag, M., Lahiri, D., Ghosh, S., Sarkar, T., Pati, S., Das, A. P., Ram, D. K., Bhattacharya, D., & Ray, R. R. (2024). Application of microorganisms in biotransformation and bioremediation of environmental contaminant: A Review. *Geomicrobiology Journal*, *41*(4), 374–391. https://doi.org/10.1080/01490451.2023.2261443

Nagar, N., Ecker, N., Loewenthal, G., Avram, O., Ben-Meir, D., Biran, D., Ron, E., & Pupko, T. (2021). Harnessing machine learning to unravel protein degradation in *Escherichia coli*. *mSystems*, *6*(1), e01296-20. https://doi.org/10.1128/mSystems.01296-20

Nagasawa, T., Yoshida, T., Ishida, K., Yamamoto, H., & Kimoto, N. (2011). *Process for production of optically active amine derivative* (United States Patent No. US20110287494A1). https://patents.google.com/patent/US20110287494A1/en

Nakamura, T., Abe, T., Miyashita, Y., Kuroda, H., Ayata, Y., & Akao, A. (2021). *High-purity quinoline derivative and method for manufacturing same* (United States Patent No. US11186547B2). https://patents.google.com/patent/US11186547B2/en

Nangle, S. N., Ziesack, M., Buckley, S., Trivedi, D., Loh, D. M., Nocera, D. G., & Silver, P. A. (2020). Valorization of CO_2 through lithoautotrophic production of sustainable chemicals in *Cupriavidus necator*. *Metabolic Engineering*, *62*, 207–220. https://doi.org/10.1016/j.ymben.2020.09.002

Nelson, D., & Cox, M. (2009). *Principios de bioquímica Lehninger [Lehninger principles of biochemestry, fifth edition]* (5ta ed.). Ediciones Omega, S.a.

Noonan, E., & Vrizzi, S. (2020). *Decoupling economic growth from environmental harm* (No. PE 651.916). EPRS European Parliamentary Research Service.

https://www.europarl.europa.eu/RegData/etudes/ATAG/2020/651916/EPRS_ATA(2020)651916_EN.pdf

OECD. (2009). *The Bioeconomy to 2030*. OECD Publishing. https://doi.org/10.1787/9789264056886-en

Oehlenschläger, K., Schepp, E., Stiefelmaier, J., Holtmann, D., & Ulber, R. (2024). Simultaneous fermentation and enzymatic biocatalysis—A useful process option? *Biotechnology for Biofuels and Bioproducts*, *17*. https://doi.org/10.1186/s13068-024-02519-z

Oh, J.-I., & Bowien, B. (1998). Structural analysis of the fds operon encoding the NAD+-linked formate dehydrogenase of Ralstonia eutropha. *Journal of Biological Chemistry*, *273*(41), 26349–26360. https://doi.org/10.1074/jbc.273.41.26349

Ow, D. S.-W., Nissom, P. M., Philp, R., Oh, S. K.-W., & Yap, M. G.-S. (2006). Global transcriptional analysis of metabolic burden due to plasmid maintenance in *Escherichia coli* DH5α during batch fermentation. *Enzyme and Microbial Technology*, *39*(3), 391–398. https://doi.org/10.1016/j.enzmictec.2005.11.048

Palmeiro-Sánchez, T., O'Flaherty, V., & Lens, P. N. L. (2022). Polyhydroxyalkanoate bio-production and its rise as biomaterial of the future. *Journal of Biotechnology*, *348*, 10–25. https://doi.org/10.1016/j.jbiotec.2022.03.001

Panich, J., Fong, B., & Singer, S. W. (2021). Metabolic engineering of *Cupriavidus necator* H16 for sustainable biofuels from CO_2. *Trends in Biotechnology*, *39*(4), 412–424. https://doi.org/10.1016/j.tibtech.2021.01.001

Panich, J., Toppari, E., Tejedor-Sanz, S., Fong, B., Dugan, E., Chen, Y., Petzold, C. J., Zhao, Z., Yoshikuni, Y., Savage, D. F., & Singer, S. W. (2024). Functional plasticity of HCO_3– uptake and CO_2 fixation in *Cupriavidus necator* H16. *Bioresource Technology*, *410*, 131214. https://doi.org/10.1016/j.biortech.2024.131214

Pettersen, E. F., Goddard, T. D., Huang, C. C., Couch, G. S., Greenblatt, D. M., Meng, E. C., & Ferrin, T. E. (2004). UCSF Chimera—A visualization system for exploratory research and analysis. *Journal of Computational Chemistry*, *25*(13), 1605–1612. https://doi.org/10.1002/jcc.20084

Phillips, T. A., VanBogelen, R. A., & Neidhardt, F. C. (1984). Lon gene product of *Escherichia coli* is a heat-shock protein. *Journal of Bacteriology*, *159*(1), 283–287.

Pohlmann, A., Cramm, R., Schmelz, K., & Friedrich, B. (2000). A novel NO-responding regulator controls the reduction of nitric oxide in *Ralstonia eutropha*. *Molecular Microbiology*, *38*(3), 626–638. https://doi.org/10.1046/j.1365-2958.2000.02157.x

Pohlmann, A., Fricke, W. F., Reinecke, F., Kusian, B., Liesegang, H., Cramm, R., Eitinger, T., Ewering, C., Pötter, M., Schwartz, E., Strittmatter, A., Voss, I., Gottschalk, G., Steinbüchel, A., Friedrich, B., & Bowien, B. (2006). Genome sequence of the bioplastic-producing "Knallgas" bacterium *Ralstonia eutropha* H16. *Nature Biotechnology*, *24*(10), 1257–1262. https://doi.org/10.1038/nbt1244

Poladyan, A., Blbulyan, S., Sahakyan, M., Lenz, O., & Trchounian, A. (2019). Growth of the facultative chemolithoautotroph Ralstonia eutropha on organic waste materials: Growth characteristics, redox regulation and hydrogenase activity. *Microbial Cell Factories*, *18*(1), 201. https://doi.org/10.1186/s12934-019-1251-5

Preissler, J., Reeve, H. A., Zhu, T., Nicholson, J., Urata, K., Lauterbach, L., Wong, L. L., Vincent, K. A., & Lenz, O. (2020). Dihydrogen-driven NADPH recycling in imine reduction and P450-catalyzed oxidations mediated by an engineered O_2 -Tolerant hydrogenase. *ChemCatChem*, *12*(19), 4853–4861. https://doi.org/10.1002/cctc.202000763

Preissler, J., Wahlefeld, S., Lorent, C., Teutloff, C., Horch, M., Lauterbach, L., Cramer, S. P., Zebger, I., & Lenz, O. (2018). Enzymatic and spectroscopic properties of a thermostable [NiFe]-hydrogenase performing H_2-driven NAD+-reduction in the presence of O_2. *Biochimica et Biophysica Acta (BBA) - Bioenergetics*, *1859*(1), 8–18. https://doi.org/10.1016/j.bbabio.2017.09.006

Prywes, N., Phillips, N. R., Tuck, O. T., Valentin-Alvarado, L. E., & Savage, D. F. (2023). Rubisco function, evolution, and engineering. *Annual Review of Biochemistry*, *92*(Volume 92, 2023), 385–410. https://doi.org/10.1146/annurev-biochem-040320-101244

Przybylski, D., Rohwerder, T., Dilßner, C., Maskow, T., Harms, H., & Müller, R. H. (2015). Exploiting mixtures of H_2, CO_2, and O_2 for improved production of methacrylate precursor 2-hydroxyisobutyric acid by engineered *Cupriavidus necator* strains. *Applied Microbiology and Biotechnology*, *99*(5), 2131–2145. https://doi.org/10.1007/s00253-014-6266-6

Przybylski, D., Rohwerder, T., Harms, H., Yaneva, N., & Müller, R. H. (2013). Synthesis of the building block 2-hydroxyisobutyrate from fructose and butyrate by *Cupriavidus necator* H16. *Applied Microbiology and Biotechnology*, *97*(20), 8875–8885. https://doi.org/10.1007/s00253-013-5064-x

Qian, Z.-G., Xia, X.-X., & Lee, S. Y. (2009). Metabolic engineering of *Escherichia coli* for the production of putrescine: A four carbon diamine. *Biotechnology and Bioengineering*, *104*(4), 651–662. https://doi.org/10.1002/bit.22502

Raberg, M., Peplinski, K., Heiss, S., Ehrenreich, A., Voigt, B., Döring, C., Bömeke, M., Hecker, M., & Steinbüchel, A. (2011). Proteomic and transcriptomic elucidation of the mutant *Ralstonia eutropha* G^+ 1 with regard to glucose utilization. *Applied and Environmental Microbiology*, *77*(6), 2058–2070. https://doi.org/10.1128/AEM.02015-10

Ratzka, J., Lauterbach, L., Lenz, O., & Ansorge-Schumacher, M. B. (2011). Systematic evaluation of the dihydrogen-oxidising and NAD+-reducing soluble [NiFe]-hydrogenase from *Ralstonia eutropha* H16 as a cofactor regeneration catalyst. *Biocatalysis and Biotransformation*, *29*(6), 246–252. https://doi.org/10.3109/10242422.2011.615393

Reinecke, F., & Steinbüchel, A. (2009). *Ralstonia eutropha* strain H16 as model organism for PHA metabolism and for biotechnological production of technically interesting biopolymers. *Journal of Molecular Microbiology and Biotechnology*, *16*, 91–108. https://doi.org/10.1159/000142897

Repaske, R., Ambrose, C. A., Repaske, A. C., & De Lacy, M. L. (1971). Bicarbonate requirement for elimination of the lag period of *Hydrogenomonas eutropha* . *Journal of Bacteriology*, *107*(3), 712–717.

Rodríguez, L. E., House, C. H., Smith, K. E., Roberts, M. R., & Callahan, M. P. (2019). Nitrogen heterocycles form peptide nucleic acid precursors in complex prebiotic mixtures. *Scientific Reports*, *9*(1), 9281. https://doi.org/10.1038/s41598-019-45310-z

Rodríguez-Mata, M., Frank, A., Wells, E., Leipold, F., Turner, N. J., Hart, S., Turkenburg, J. P., & Grogan, G. (2013). Structure and activity of NADPH-dependent reductase Q1EQE0 from *Streptomyces kanamyceticus*, which catalyses the R-Selective reduction of an imine substrate. *ChemBioChem*, *14*(11), 1372–1379. https://doi.org/10.1002/cbic.201300321

Rowaihi, I. S. A., Paillier, A., Rasul, S., Karan, R., Grötzinger, S. W., Takanabe, K., & Eppinger, J. (2018). Poly(3-hydroxybutyrate) production in an integrated electromicrobial setup: Investigation under stress-inducing conditions. *PLOS ONE*, *13*(4), e0196079. https://doi.org/10.1371/journal.pone.0196079

Royal Society. (2020). *Ammonia: Zero-carbon fertiliser, fuel and energy store*. Royal Society (Great Britain).

Ryu, H., Nguyen, C. N. M., Kuk Lee, S., & Park, S. (2024). Development of *Cupriavidus necator* H16 as a host for heterologous production of formate dehydrogenase I of *Methylorubrum extorquens*: Possibilities and limitations. *Bioresource Technology*, *394*, 130187. https://doi.org/10.1016/j.biortech.2023.130187

Saggadi, H., Polaert, I., Luart, D., Len, C., & Estel, L. (2015). Microwaves under pressure for the continuous production of quinoline from glycerol. *Catalysis Today*, *255*, 66–74. https://doi.org/10.1016/j.cattod.2014.10.050

Saibil, H. R., Fenton, W. A., Clare, D. K., & Horwich, A. L. (2013). Structure and allostery of the chaperonin GroEL. *Journal of Molecular Biology*, *425*(9), 1476–1487. https://doi.org/10.1016/j.jmb.2012.11.028

Saibil, H. R., & Ranson, N. A. (2002). The chaperonin folding machine. *Trends in Biochemical Sciences*, *27*(12), 627–632. https://doi.org/10.1016/S0968-0004(02)02211-9

Sajeev, S. C., & Deshmukh, R. (2022). *Enzymes Market, by Type (Protease, Carbohydrase, Lipase, Polymerase and Nuclease, Others), by Source (Microorganisms, Plants, Animals), by Reaction Type (Hydrolase, Oxidoreductase, Transferase, Lyase, Other Reaction Types), by Application (Food and Beverages, Household Care, Bioenergy, Pharmaceutical and Biotechnology, Feed, Other Applications): Global Opportunity Analysis and Industry Forecast, 2021-2031*. Enzymes Market Research, 2031. https://www.alliedmarketresearch.com/enzymes-market

Salinas, A., McGregor, C., Irorere, V., Arenas-López, C., Bommareddy, R. R., Winzer, K., Minton, N. P., & Kovács, K. (2022). Metabolic engineering of *Cupriavidus necator* H16 for heterotrophic and autotrophic production of 3-hydroxypropionic acid. *Metabolic Engineering*, *74*, 178–190. https://doi.org/10.1016/j.ymben.2022.10.014

San Millan, A., & Maclean, C. (2017). *Fitness costs of plasmids: A limit to plasmid transmission*. *5*(5), MTBP-0016-2017. https://doi.org/doi:10.1128/microbiolspec.MTBP-0016-2017

Santin, A., Spatola Rossi, T., Morlino, M. S., Gupte, A. P., Favaro, L., Morosinotto, T., Treu, L., & Campanaro, S. (2024). Autotrophic poly-3-hydroxybutyrate accumulation in *Cupriavidus necator* for sustainable bioplastic production triggered by nutrient starvation. *Bioresource Technology*, *406*, 131068. https://doi.org/10.1016/j.biortech.2024.131068

Santolin, L., Sebastian L. Riedel, & Brigham, C. J. (2024). Synthetic biology toolkit of *Ralstonia eutropha* (*Cupriavidus necator*). *Applied Microbiology and Biotechnology*, *108*(1), 450. https://doi.org/10.1007/s00253-024-13284-2

Satagopan, S., & Tabita, F. R. (2016). RubisCO selection using the vigorously aerobic and metabolically versatile bacterium Ralstonia eutropha. *The FEBS Journal*, *283*(15), 2869–2880. https://doi.org/10.1111/febs.13774

Schäfer, C., Bommer, M., Hennig, S. E., Jeoung, J.-H., Dobbek, H., & Lenz, O. (2016). Structure of an actinobacterial-type [NiFe]-hydrogenase reveals insight into O_2-tolerant H_2 oxidation. *Structure*, *24*(2), 285–292. https://doi.org/10.1016/j.str.2015.11.010

Schein, C. H., & Noteborn, M. H. M. (1988). Formation of soluble recombinant proteins in *Escherichia coli* is favored by lower growth temperature. *Bio/Technology*, *6*(3), 291–294. https://doi.org/10.1038/nbt0388-291

Scheller, P. (2016). *Characterization and application of novel imine reductases* [doctoralThesis]. http://elib.uni-stuttgart.de/handle/11682/8849

Schlegel, H. G., Gottschalk, G., & Von Bartha, R. (1961). Formation and utilization of poly-beta-hydroxybutyric acid by Knallgas bacteria (*Hydrogenomonas*). *Nature*, *191*, 463–465. https://doi.org/10.1038/191463a0

Schlegel, H. G., Kaltwasser, H., & Gottschalk, G. (1961). Ein Submersverfahren zur Kultur wasserstoffoxydierender Bakterien: Wachstumsphysiologische Untersuchungen. [A submersion method for culture of hydrogen-oxidizing bacteria: Growth physiological studies]. *Archiv Fur Mikrobiologie*, *38*, 209–222.

Schneider, K., & Schlegel, H. G. (1981). Production of superoxide radicals by soluble hydrogenase from Alcaligenes eutrophus H16. *Biochemical Journal*, *193*(1), 99–107. https://doi.org/10.1042/bj1930099

Schober, M., MacDermaid, C., Ollis, A. A., Chang, S., Khan, D., Hosford, J., Latham, J., Ihnken, L. A. F., Brown, M. J. B., Fuerst, D., Sanganee, M. J., & Roiban, G.-D. (2019). Chiral synthesis of LSD1 inhibitor GSK2879552 enabled by directed evolution of an imine reductase. *Nature Catalysis*, *2*(10), 909–915. https://doi.org/10.1038/s41929-019-0341-4

Schrittwieser, J. H., Velikogne, S., & Kroutil, W. (2015). Biocatalytic imine reduction and reductive amination of ketones. *Advanced Synthesis & Catalysis*, *357*(8), 1655–1685. https://doi.org/10.1002/adsc.201500213

Schwartz, E., Gerischer, U., & Friedrich, B. (1998). Transcriptional regulation of *Alcaligenes eutrophus* hydrogenase genes. *Journal of Bacteriology*, *180*(12), 3197–3204. https://doi.org/10.1128/jb.180.12.3197-3204.1998

Schwartz, E., Henne, A., Cramm, R., Eitinger, T., Friedrich, B., & Gottschalk, G. (2003). Complete nucleotide sequence of pHG1: A *Ralstonia eutropha* H16 megaplasmid encoding key enzymes of H_2-based lithoautotrophy and anaerobiosis. *Journal of Molecular Biology*, *332*(2), 369–383. https://doi.org/10.1016/S0022-2836(03)00894-5

Schwartz, E., Voigt, B., Zühlke, D., Pohlmann, A., Lenz, O., Albrecht, D., Schwarze, A., Kohlmann, Y., Krause, C., Hecker, M., & Friedrich, B. (2009). A proteomic view of the facultatively chemolithoautotrophic lifestyle of *Ralstonia eutropha* H16. *PROTEOMICS*, *9*(22), 5132–5142. https://doi.org/10.1002/pmic.200900333

Scott, K. M., Harmer, T. L., Gemmell, B. J., Kramer, A. M., Sutter, M., Kerfeld, C. A., Barber, K. S., Bari, S., Boling, J. W., Campbell, C. P., Gallard-Gongora, J. F., Jackson, J. K., Lobos, A., Mounger, J. M., Radulovic, P. W., Sanson, J. M., Schmid, S., Takieddine, C., Warlick, K. F., & Whittaker, R. (2020). Ubiquity and functional uniformity in CO_2 concentrating mechanisms in multiple phyla of bacteria is suggested by a diversity and prevalence of genes encoding candidate dissolved inorganic carbon transporters. *FEMS Microbiology Letters*, *367*(13), fnaa106. https://doi.org/10.1093/femsle/fnaa106

Scriven, E. F. V. (2013). *Pyridines: From lab to production*. Academic Press.

Scriven, E. F. V., & Murugan, R. (2005). Pyridine and pyridine derivatives. In Kirk-Othmer (Ed.), *Kirk-Othmer Encyclopedia of Chemical Technology* (1st ed.). Wiley. https://doi.org/10.1002/0471238961.1625180919031809.a01.pub2

Sellés Vidal, L., Kelly, C. L., Mordaka, P. M., & Heap, J. T. (2018). Review of NAD(P)H-dependent oxidoreductases: Properties, engineering and application. *Biochimica et Biophysica Acta (BBA) - Proteins and Proteomics*, *1866*(2), 327–347. https://doi.org/10.1016/j.bbapap.2017.11.005

Shanu-Wilson, J., Evans, L., Wrigley, S., Steele, J., Atherton, J., & Boer, J. (2020). Biotransformation: Impact and application of metabolism in drug discovery. *ACS Medicinal Chemistry Letters*, *11*(11), 2087–2107. https://doi.org/10.1021/acsmedchemlett.0c00202

Shapiro, Z. M., & Moffette, T. R. (1957). *Hydrogen flammability data and application to power loss-of-coolant accident* (No. WAPD-SC-545). Westinghouse Electric Corp., Pittsburgh, PA (United States). Bettis Plant. https://doi.org/10.2172/4327402

Sigler, P. B., Xu, Z., Rye, H. S., Burston, S. G., Fenton, W. A., & Horwich, A. L. (1998). Structure and function in GroEL-mediated protein folding. *Annual Review of Biochemistry*, *67*, 581–608. https://doi.org/10.1146/annurev.biochem.67.1.581

Simon, R., Priefer, U., & Pühler, A. (1983). A broad host range mobilization sustem for in vivo genetic engineering: Transposon mutagenesis in gram negative bacteria. *Bio/Technology*, *1*(9), 784–791. https://doi.org/10.1038/nbt1183-784

Smil, V. (1999). Detonator of the population explosion. *Nature*, *400*(6743), 415–415. https://doi.org/10.1038/22672

Smil, V. (2000). *Enriching the earth: Fritz Haber, Carl Bosch, and the transformation of world food production*. The MIT Press. https://doi.org/10.7551/mitpress/2767.001.0001

Sohn, Y., & Kang, C. (2005). Sequential multiple functions of the conserved sequence in sequence-specific termination by T7 RNA polymerase. *Proceedings of the National Academy of Sciences*, *102*(1), 75–80. https://doi.org/10.1073/pnas.0406581101

Soksawatmaekhin, W., Kuraishi, A., Sakata, K., Kashiwagi, K., & Igarashi, K. (2004). Excretion and uptake of cadaverine by CadB and its physiological functions in Escherichia coli. *Molecular Microbiology*, *51*(5), 1401–1412. https://doi.org/10.1046/j.1365-2958.2003.03913.x

Sonnleitner, B., Heinzle, E., Braunegg, G., & Lafferty, R. M. (1979). Formal kinetics of poly-β-hydroxybutyric acid (PHB) production in *Alcaligenes eutrophus* H16 and *Mycoplana rubra* R14 with respect to the dissolved oxygen tension in ammonium-limited batch cultures. *European Journal of Applied Microbiology and Biotechnology*, *7*(1), 1–10. https://doi.org/10.1007/BF00522473

Sperl, J. M., & Sieber, V. (2018). Multienzyme cascade reactions—Status and recent advances. *ACS Catalysis*, *8*(3), 2385–2396. https://doi.org/10.1021/acscatal.7b03440

St. John, A. C., Jakubas, K., & Beim, D. (1979). Degradation of proteins in steady-state cultures of *Escherichia coli*. *Biochimica et Biophysica Acta (BBA) - General Subjects*, *586*(3), 537–544. https://doi.org/10.1016/0304-4165(79)90044-8

Stockinger, P., Borlinghaus, N., Sharma, M., Aberle, B., Grogan, G., Pleiss, J., & Nestl, B. M. (2021). Inverting the stereoselectivity of an NADH-dependent imine-reductase variant. *ChemCatChem*, *13*(24), 5210–5215. https://doi.org/10.1002/cctc.202101057

Strittmatter, C. S., Eggers, J., Biesgen, V., Pauels, I., Becker, F., & Steinbüchel, A. (2022). The reliance of glycerol utilization by *Cupriavidus necator* on CO_2 fixation and improved glycerol catabolism. *Applied Microbiology and Biotechnology*, *106*(7), 2541–2555. https://doi.org/10.1007/s00253-022-11842-0

Studier, F. W., & Moffatt, B. A. (1986). Use of bacteriophage T7 RNA polymerase to direct selective high-level expression of cloned genes. *Journal of Molecular Biology*, *189*(1), 113–130. https://doi.org/10.1016/0022-2836(86)90385-2

Sydow, A., Pannek, A., Krieg, T., Huth, I., Guillouet, S. E., & Holtmann, D. (2017). Expanding the genetic tool box for *Cupriavidus necator* by a stabilized L-rhamnose inducible plasmid system. *Journal of Biotechnology*, *263*, 1–10. https://doi.org/10.1016/j.jbiotec.2017.10.002

Takeshita, T., & Ishizaki, A. (1996). Influence of hydrogen limitation on gaseous substrate utilization in autotrophic culture of *Alcaligenes eutrophus* ATCC 17697T. *Journal of Fermentation and Bioengineering*, *81*(1), 83–86. https://doi.org/10.1016/0922-338X(96)83127-8

Tanaka, K., Ishizaki, A., Kanamaru, T., & Kawano, T. (1995). Production of poly(D-3-hydroxybutyrate) from CO_2, H_2, , and O_2, by high cell density autotrophic cultivation of *Alcaligenes eutrophus*. *Biotechnology and Bioengineering*, *45*(3), 268–275. https://doi.org/10.1002/bit.260450312

Tang, R., Weng, C., Peng, X., & Han, Y. (2020). Metabolic engineering of *Cupriavidus necator* H16 for improved chemoautotrophic growth and PHB production under oxygen-limiting conditions. *Metabolic Engineering*, *61*, 11–23. https://doi.org/10.1016/j.ymben.2020.04.009

Tang, R., Yuan, X., & Yang, J. (2023). Problems and corresponding strategies for converting CO_2 into value-added products in *Cupriavidus necator* H16 cell factories. *Biotechnology Advances*, *67*, 108183. https://doi.org/10.1016/j.biotechadv.2023.108183

Tang, Y., Xiao, X., Zhang, C., Wang, X., Guo, J., & Liao, X. (2023). A sustainable thermochemical conversion of animal biomass to N-heterocycles. *Collagen and Leather*, *5*(1), 1. https://doi.org/10.1186/s42825-022-00109-z

Tee, K. L., Grinham, J., Othusitse, A. M., González-Villanueva, M., Johnson, A. O., & Wong, T. S. (2017). An efficient transformation method for the bioplastic-producing "Knallgas" bacterium *Ralstonia eutropha* H16. *Biotechnology Journal*, *12*(11). https://doi.org/10.1002/biot.201700081

Teetz, N., Holtmann, D., Harnisch, F., & Stöckl, M. (2022). Upgrading Kolbe electrolysis—Highly efficient production of green fuels and solvents by coupling biosynthesis and electrosynthesis. *Angewandte Chemie International Edition*, *61*(50), e202210596. https://doi.org/10.1002/anie.202210596

Tokunou, Y., Toyofuku, M., & Nomura, N. (2022). Physiological Benefits of Oxygen-Terminating Extracellular Electron Transfer. *mBio*, *13*(6), e01957-22. https://doi.org/10.1128/mbio.01957-22

Tomas, C. A., Welker, N. E., & Papoutsakis, E. T. (2003). Overexpression of groESL in *Clostridium acetobutylicum* results in increased solvent production and tolerance, prolonged metabolism, and changes in the cell's transcriptional program. *Applied and Environmental Microbiology*, *69*(8), 4951–4965. https://doi.org/10.1128/AEM.69.8.4951-4965.2003

UNFCCC. (2016). *The Paris Agreement—Publication |* (Policies and Measures). https://unfccc.int/documents/184656

Vajente, M., Clerici, R., Ballerstedt, H., Blank, L. M., & Schmidt, S. (2024). Using *Cupriavidus necator* H16 to provide a roadmap for increasing electroporation efficiency in nonmodel bacteria. *ACS Synthetic Biology*. https://doi.org/10.1021/acssynbio.4c00380

Valle, A., & Bolívar, J. (2021). *Escherichia coli*, the workhorse cell factory for the production of chemicals. In V. Singh (Ed.), *Microbial Cell Factories Engineering for Production of Biomolecules* (pp. 115–137). Academic Press. https://doi.org/10.1016/B978-0-12-821477-0.00012-X

van Hellemond, E. W., van Dijk, M., Heuts, D. P. H. M., Janssen, D. B., & Fraaije, M. W. (2008). Discovery and characterization of a putrescine oxidase from *Rhodococcus erythropolis* NCIMB 11540. *Applied Microbiology and Biotechnology*, *78*(3), 455–463. https://doi.org/10.1007/s00253-007-1310-4

Vandamme, P., & Coenye, T. (2004). Taxonomy of the genus *Cupriavidus*: A tale of lost and found. *International Journal of Systematic and Evolutionary Microbiology*, *54*(Pt 6), 2285–2289. https://doi.org/10.1099/ijs.0.63247-0

Vaneechoutte, M., Kämpfer, P., De Baere, T., Falsen, E., & Verschraegen, G. (2004). *Wautersia* gen. Nov., a novel genus accommodating the phylogenetic lineage including *Ralstonia eutropha* and related species, and proposal of *Ralstonia* [*Pseudomonas*] *syzygii* (Roberts et al. 1990) comb. Nov. *International Journal of Systematic and Evolutionary Microbiology*, *54*(2), 317–327. https://doi.org/10.1099/ijs.0.02754-0

Vignais, P. M., & Billoud, B. (2007). Occurrence, classification, and biological function of hydrogenases: An overview. *Chemical Reviews*, *107*(10), 4206–4272. https://doi.org/10.1021/cr050196r

Viitanen, P. V., Gatenby, A. A., & Lorimer, G. H. (1992). Purified chaperonin 60 (groEL) interacts with the nonnative states of a multitude of *Escherichia coli* proteins. *Protein Science*, *1*(3), 363–369. https://doi.org/10.1002/pro.5560010308

Vlaeminck, E., Acuña Lopez, P., Uitterhaegen, E., Quataert, K., Delmulle, T., De Winter, K., & Soetaert, W. K. (2024). Pressure fermentation to boost CO_2-based poly(3-hydroxybutyrate) production using *Cupriavidus necator*. *Bioresource Technology*, *408*, 131162. https://doi.org/10.1016/j.biortech.2024.131162

Volova, T. G., Zhila, N. O., Kalacheva, G. S., Brigham, C. J., & Sinskey, A. J. (2013). Effects of intracellular poly(3-hydroxybutyrate) reserves on physiological–biochemical properties and growth of *Ralstonia eutropha*. *Research in Microbiology*, *164*(2), 164–171. https://doi.org/10.1016/j.resmic.2012.10.008

Walsh, C. T. (2015). Nature loves nitrogen heterocycles. *Tetrahedron Letters*, *56*(23), 3075–3081. https://doi.org/10.1016/j.tetlet.2014.11.046

Wandrey, C., Liese, A., & Kihumbu, D. (2000). Industrial biocatalysis: Past, present, and future. *Organic Process Research & Development*, *4*(4), 286–290. https://doi.org/10.1021/op990101l

Wang, J., Yue, Z.-B., Sheng, G.-P., & Yu, H.-Q. (2010). Kinetic analysis on the production of polyhydroxyalkanoates from volatile fatty acids by *Cupriavidus necator* with a consideration of substrate inhibition, cell growth, maintenance, and product formation. *Biochemical Engineering Journal*, *49*(3), 422–428. https://doi.org/10.1016/j.bej.2010.02.005

Wang, L., Yao, J., Tu, T., Yao, B., & Zhang, J. (2024). Heterotrophic and autotrophic production of L-isoleucine and L-valine by engineered *Cupriavidus necator* H16. *Bioresource Technology*, *398*, 130538. https://doi.org/10.1016/j.biortech.2024.130538

Wang, X., Chang, F., Wang, T., Luo, H., Su, X., Tu, T., Wang, Y., Bai, Y., Qin, X., Zhang, H., Wang, Y., Yao, B., Huang, H., & Zhang, J. (2023). Production of *N*-acetylglucosamine from carbon dioxide by engineering *Cupriavidus necator* H16. *Bioresource Technology*, *379*, 129024. https://doi.org/10.1016/j.biortech.2023.129024

Wang, X., Wang, K., Wang, L., Luo, H., Wang, Y., Wang, Y., Tu, T., Qin, X., Su, X., Bai, Y., Yao, B., Huang, H., & Zhang, J. (2023). Engineering *Cupriavidus necator* H16 for heterotrophic and autotrophic production of *myo*-inositol. *Bioresource Technology*, *368*, 128321. https://doi.org/10.1016/j.biortech.2022.128321

Wang, Y., Cui, L., Ding, L., Su, X., Luo, H., Huang, H., Wang, Y., Yao, B., Zhang, J., & Wang, X. (2024). Unlocking the potential of *Cupriavidus necator* H16 as a platform for bioproducts production from carbon dioxide. *World Journal of Microbiology and Biotechnology*, *40*(12), 389. https://doi.org/10.1007/s11274-024-04200-x

Wang, Y., & Newman, D. K. (2008). Redox reactions of phenazine antibiotics with ferric (hydr)oxides and molecular Oxygen. *Environmental Science & Technology*, *42*(7), 2380–2386. https://doi.org/10.1021/es702290a

Wei, H., Wang, W., Chou, Y.-C., Himmel, M. E., Chen, X., Bomble, Y. J., & Zhang, M. (2023). Prospects for engineering *Ralstonia eutropha* and *Zymomonas mobilis* for the autotrophic production of 2,3-butanediol from CO_2 and H_2. *Engineering Microbiology*, *3*(2), 100074. https://doi.org/10.1016/j.engmic.2023.100074

Weickardt, I., Lombard, E., Zhang, A., & Guillouet, S. E. (2025). Comparative characterisation of autotrophic and heterotrophic isopropanol formation by *Cupriavidus necator* in shake flasks. *Journal of Biotechnology*. https://doi.org/10.1016/j.jbiotec.2025.03.011.

Weiler, J. R., Jürgensen, N., Cornejo Infante, M., Knoll, M. T., & Gescher, J. (2024). Strain and model development for auto- and heterotrophic 2,3-butanediol production using *Cupriavidus necator* H16. *Biotechnology for Biofuels and Bioproducts*, *17*(1), 108. https://doi.org/10.1186/s13068-024-02549-7

Weldon, M., & Euler, C. (2025). Physiology-informed use of *Cupriavidus necator* in biomanufacturing: A review of advances and challenges. *Microbial Cell Factories*, *24*, 30. https://doi.org/10.1186/s12934-025-02643-x

Wierckx, N. (2009). *Solvent-tolerant bioconversion, Construction and analysis of phenol producing Pseudomonas putida s12* [Dissertation (TU Delft)]. Delft University of Technology.

Windhorst, C., & Gescher, J. (2019). Efficient biochemical production of acetoin from carbon dioxide using *Cupriavidus necator* H16. *Biotechnology for Biofuels*, *12*(1), 163. https://doi.org/10.1186/s13068-019-1512-x

Wirachman, E. S., & Grossman, A. D. (2024). Transcription termination and antitermination are critical for the fitness and function of the integrative and conjugative element Tn916. *PLOS Genetics*, *20*(12), e1011417. https://doi.org/10.1371/journal.pgen.1011417

Wittenberg, C. L., & Repaske, R. (1958). Studies on the electron transport system in *Hydrogenomonas eutropha*. *Bacteriological Procedures*, *106*.

Wu, K., Yan, J., Liu, Q., Wang, X., Wu, P., Cao, Y., Lu, X., Xu, Y., Huang, J., & Shao, L. (2024). Computational design of an imine reductase: Mechanism-guided stereoselectivity reversion and interface stabilization. *Chemical Science*, *15*(4), 1431–1440. https://doi.org/10.1039/D3SC04636B

Xia, H., Kitazumi, Y., Shirai, O., Ohta, H., Kurihara, S., & Kano, K. (2017). Putrescine oxidase/peroxidase-co-immobilized and mediator-less mesoporous microelectrode for diffusion-controlled steady-state amperometric detection of putrescine. *Journal of Electroanalytical Chemistry*, *804*, 128–132. https://doi.org/10.1016/j.jelechem.2017.09.056

Yabuuchi, E., Kosako, Y., Yano, I., Hotta, H., & Nishiuchi, Y. (1995). Transfer of two *Burkholderia* and an *Alcaligenes* species to *Ralstonia* Gen. Nov.: Proposal of *Ralstonia pickettii* (Ralston, Palleroni and Doudoroff 1973) comb. Nov., *Ralstonia solanacearum* (Smith 1896) comb. Nov. and *Ralstonia eutropha* (Davis 1969) comb. Nov. *Microbiology and Immunology*, *39*(11), 897–904. https://doi.org/10.1111/j.1348-0421.1995.tb03275.x

Yamada, H. (1971). Putrescine oxidase (*Micrococcus rubens*). In *Methods in Enzymology* (Vol. 17, pp. 726–730). Elsevier. https://doi.org/10.1016/0076-6879(71)17126-1

Yamada, H., Tanaka, A., & Ogata, K. (1965). Putrescine oxidase of *Micrococcus rubens*. *Agricultural and Biological Chemistry*, *29*(3), 260–261. https://doi.org/10.1271/bbb1961.29.260

Yamashkin, S. A., & Oreshkina, E. A. (2006). Traditional and modern approaches to the synthesis of quinoline systems by the Skraup and Doebner-Miller methods. (Review). *Chemistry of Heterocyclic Compounds*, *42*(6), 701–718. https://doi.org/10.1007/s10593-006-0150-y

Yan, J., Liu, W., Cai, J., Wang, Y., Li, D., Hua, H., & Cao, H. (2021). Advances in phenazines over the past decade: Review of their pharmacological activities, mechanisms of action, biosynthetic pathways and synthetic strategies. *Marine Drugs*, *19*(11). https://doi.org/10.3390/md19110610

Yan, Y., Tao, H., He, J., & Huang, S.-Y. (2020). The HDOCK server for integrated protein–protein docking. *Nature Protocols*, *15*(5), 1829–1852. https://doi.org/10.1038/s41596-020-0312-x

Yu, X., Niks, D., Mulchandani, A., & Hille, R. (2017). Efficient reduction of CO_2 by the molybdenum-containing formate dehydrogenase from *Cupriavidus necator (Ralstonia eutropha)*. *The Journal of Biological Chemistry*, *292*(41), 16872–16879. https://doi.org/10.1074/jbc.M117.785576

Zhang, B., & Studer, A. (2015). Recent advances in the synthesis of nitrogen heterocycles via radical cascade reactions using isonitriles as radical acceptors. *Chemical Society Reviews*, *44*(11), 3505–3521. https://doi.org/10.1039/C5CS00083A

Zhang, L., Jiang, Z., Tsui, T.-H., Loh, K.-C., Dai, Y., & Tong, Y. W. (2022). A Review on enhancing *Cupriavidus necator* fermentation for poly(3-hydroxybutyrate) (PHB) production from low-cost carbon sources. *Frontiers in Bioengineering and Biotechnology*, *10*. https://doi.org/10.3389/fbioe.2022.946085

Zhang, X., Chingin, K., Zhong, D., Liang, J., Ouyang, Y., & Chen, H. (2017). On the chemistry of 1-pyrroline in solution and in the gas phase. *Scientific Reports*, *7*(1), 7675. https://doi.org/10.1038/s41598-017-08217-1

Zhang, Z., Pan, S.-Y., Li, H., Cai, J., Olabi, A. G., Anthony, E. J., & Manovic, V. (2020). Recent advances in carbon dioxide utilization. *Renewable and Sustainable Energy Reviews*, *125*, 109799. https://doi.org/10.1016/j.rser.2020.109799

Zhila, N. O., Sapozhnikova, K. Y., Kiselev, E. G., Vasiliev, A. D., Nemtsev, I. V., Shishatskaya, E. I., & Volova, T. G. (2021). Properties of degradable polyhydroxyalkanoates (PHAs) synthesized by a new strain, *Cupriavidus necator* IBP/SFU-1, from various carbon sources. *Polymers*, *13*(18), Article 18. https://doi.org/10.3390/polym13183142

Zhu, X.-X., Zheng, W.-Q., Xia, Z.-W., Chen, X.-R., Jin, T., Ding, X.-W., Chen, F.-F., Chen, Q., Xu, J.-H., Kong, X.-D., & Zheng, G.-W. (2024). Evolutionary insights into the stereoselectivity of imine reductases based on ancestral sequence reconstruction. *Nature Communications*, *15*(1), 10330. https://doi.org/10.1038/s41467-024-54613-3

Zingaro, K. A., & Papoutsakis, E. T. (2013). GroESL overexpression imparts *Escherichia coli* tolerance to i-, n-, and 2-butanol, 1,2,4-butanetriol and ethanol with complex and unpredictable patterns. *Metabolic Engineering*, *15*, 196–205. https://doi.org/10.1016/j.ymben.2012.07.009

Zulak, K. G., Liscombe, D. K., Ashihara, H., & Facchini, P. J. (2006). Alkaloids. In *Plant Secondary Metabolites* (pp. 102–136). John Wiley & Sons, Ltd. https://doi.org/10.1002/9780470988558.ch4

Supplementary Information

Supplementary A. Materials and Methods

Table S. 1 Primer List.

Primer	**Sequence 5' to 3'**	**Function**
Rha-ired_F	tatcgataagttaatctttctgcgaattgag	Amplification of rhaR, rhaS, rhaB, and *ired*$_{V8}$. Colony-PCR and sequencing
Rha-ired_R	cgatatcaagttatttcaggaagcgggtcag	
CheckLon_F	ctgcctgccttgatgaatcg	Primers Forward and Reverse for Colony-PCR to verify the presence of *lon* gene in C. necator
CheckLon_R	tttcgttcatgcggccaaag	
oPS28_rhaS	gaattgttcattacgaccagtc	Primer Reverse. Sequencing of *rhaS*
PkrNewrham_Forward-1.	acactatgtaatacggtcattgcataaaaactgttgtaattcattaagcattct	Amplification of pkr with PuOx from pkr_PuO_1. For Gibson Assembly
PkrNewrham_Reverse-1	tcaattcgcagaaagattaaactggcctcctgatgtcg	Primer Reverse. Sequencing of *rhaS*
Rhamnose-Forward-1	attacaacagtttttatgcaatgaccgtattacatagtgtggatttttttcc	Amplification of rhamnose promoter from peCcas9. For Gibson Assembly
Rhamnose-reverse-1	gacgacatcaggaggccagtttaatctttctgcgaattgagatgacgc	
oIC78	aaatctagagatacagcgtgaattttcagg	Primer Forward.

oIC79	ttctgcagtctagattatcagg	Amplification *puox*$_{M1}$ adding XbaI site in 5', for digestion-ligation Primer Reverse. Amplification *puox*$_{M1}$ for digestion-ligation
oIC80_seqRhaS	tccacactatgtaatacggtc	Primer Forward. Sequencing. Annealing *rhaS*
oIC81_seqIRED	agaaggcatcccgctg	Primer Forward. Sequencing. Annealing from half ired sequence
oIC82_seqPuOx	ccgtctacatctcgtcag	Primer Forward. Sequencing. Annealing from half *puox*$_{M1}$ sequence
oIC99	tgacccgcttcctgaaataactagagcggccgccacc	Primer Forward and Reverse Amplification pCAT201 backbone for Gibson Assembly with *ired*$_{V8}$
oIC100	tcgaactgcgggtggctccattaattcctcctgttagcccaaaaaacg	
oIC101	gggctaacaggaggaattaatggagccacccgcag	Primer Forward and Reverse. Amplification *ired*$_{V8}$. For Gibson Assembly with pCAT201
oIC102	cgcggtggcggccgctctagttatttcaggaagcgggtcagaattgcaaagtcatct	

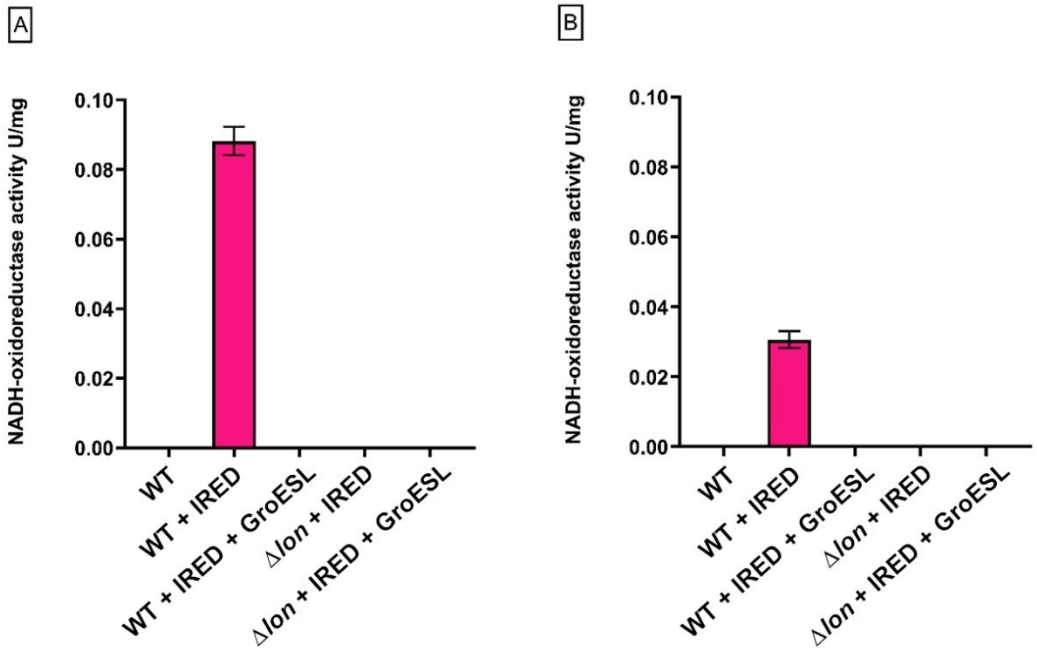

Figure S. 1.Example of IRED activity assay in *C. necator* soluble extract : The NADH-oxidoreductase activity assay setup is tested with different volumes of soluble extract. The activity in the soluble extract of WT + IRED is 0.08 U/mg using 200 µL (A), and 0.03 U/mg using 400 µL is used (B). The activity in the soluble extract is calculated from triplicates and the standard error of the mean is shown. Duplicates are used for WT + IRED in A. (WT: *C. necator* H16; WT + IRED: *C. necator* x pAA56; WT + IRED + GroESL: *C. necator* x pAA56 x pEG19; Δlon +IRED: Δlon x pAA56; Δlon + IRED+ GroESL: Δlon x pAA56 x pE19)

Supplementary B. Results and Discussions

B.1 IRED$_{V8}$ production in *C. necator.*

- Sequence of Strep II-tag-*ired*$_{V8}$ gene. Strep-Tag II is underlined.

Tggagccacccgcagttcgaaaaagccagcatgaaaccgaccctgaccgttattggcgctggccgtatgggctccgcactgattaaagcattcc
tgcaatctggctacacgaccacggtgtgggaatacgagaaagcccgtagcgaaccgctggcaaaactgggcgcacatctggctgatacggtgc
gtgacgccgttaaacgcagcgatattatcgtggttaatgtgattgattatgacgtgtctgatcagctgctgcgccaagacgaagtgacgcgtgaa
ctgcgcggcaaactgctggttcagctgaccagcggttctccggcactggctcgtgaacaggaaacgtgggcgcgccaacatggcattgattatct
ggacggtgcgatcatggccaccccggattttattggccaggcagaatgcgctctgctgtacagtggttccgcggccctgttcgaaaaacaccgtg
ctgtcctgaatgtgctgggcggtgccaccagccatgtcggcgaagatgttggtcatgcctcagcactggacagcgccctgctgtttcagatgtggg
gcaccctgttcggtacgctgcaagcactggctatttctcgcgcagaaggcatcccgctggaaaaaaccacggcgtttatcaaactgaccgaacc
ggtcacccagggtgccgttgcagatgtcctgacccgtgttcagcaaaatcgcctgaccgcagacgctcagacgctggcaagtctggaagctcat
aacgtggcgttccaacacctgctggccctgtgtgaagaacgtaatatccatcgcggtgttgcggatgccatgtactccgttattcgtgaagcggtc
aaagccggccacggtaaagatgactttgcaattctgacccgcttcctgaaataa

- Translated sequence IREDV8 (N32E/R33Y/K37R/L67/I/T71V) (Borlinghaus & Nestl, 2018)

MKPTLTVIGAGRMGSALIKAFLQSGYTTTVWEYEKARSEPLAKLGAHLADTVRDAVKRSDIIVVNVIDYDVSDQLLR
QDEVTRELRGKLLVQLTSGSPALAREQETWARQHGIDYLDGAIMATPDFIGQAECALLYSGSAALFEKHRAVLNVL
GGATSHVGEDVGHASALDSALLFQMWGTLFGTLQALAISRAEGIPLEKTTAFIKLTEPVTQGAVADVLTRVQQNRL
TADAQTLASLEAHNVAFQHLLALCEERNIHRGVADAMYSVIREAVKAGHGKDDFAILTRFLK*

B.2 Enzymatic activity

Extinction cofactor for NADH at 365 nm : 3.3 1/mM/cm

Slopes were measured with the Cary WinUV Software, in the linear region of the curve during the 30 s after addition of each component. Negative slopes are considered as substrate decreases over time and the absolute slope value is retained. For soluble extract, the difference of slopes is used to remove background from soluble extract proteins from the substrate activity. This correction is not required for purified proteins

Calculations were performed used the formula indicated in the respective section of Materials and Methods. In all cases a molecular weight of 33727.41 Da was used (IRED monomer size). Negative activities are considered as no activity.

Statistical analysis for obtention of the mean, standard error of the mean and graphs is performed in the software origin or GraphPadPrism.

Table S. 2. Activity calculations in soluble extract of WT, WT + IRED, WT + IRED + GroESL, Δ*lon* + IRED and Δ*lon* + IRED + GroESL.

Strain	Protein concentration mg/ml	Volume µL	Slope 1 (background)	Slope 2 (substrate addition)	Slope difference (1/min)	Apparent specific activity U/mg
WT	21.52	200	0.1302	0.0199	-0.1103	-0.01553
			0.1841	0.024	-0.1601	-0.02255
			0.1255	0.0212	-0.1043	-0.01469
WT + IRED	18.53		0.0026	0.517	0.5144	0.0026
			0.0017	0.566	0.5643	0.0017
			-	-	-	-
WT + IRED + GroESL	15.98		0.1719	0.0109	-0.161	0.1719
			0.0616	0.0132	-0.0484	0.0616
			0.1433	0.0275	-0.1158	0.1433
Δ*lon* + IRED	12.75		0.0112	0.0159	0.0047	0.0112
			0.0455	0.0152	-0.0303	0.0455
			0.052	0.0148	-0.0372	0.052
Δ*lon* + IRED + GroESL	10.83		0.0383	0.003	-0.0353	0.0383
			0.0297	0.004	-0.0257	0.0297
			0.0543	0.003	-0.0513	0.0543

Table S. 3. Activity calculations in soluble extract of WT, WT + IRED (-Rha), WT + IRED (+Rha).

Strain	Protein concentration mg/ml	Volume µL	Slope 1 (background)	Slope 2 (substrate addition)	Slope difference (1/min)	Apparent specific activity (U/mg)
WT	17.62	20	0.0001	0.0049	0.0048	0.0083
			0.0018	0.0087	0.0069	0.0119
			0.0019	0.0038	0.0019	0.0033
		50	0.0119	0.0058	-0.0061	-0.0042
			0.015	0.0048	-0.0102	-0.0070
			0.0168	0.0068	-0.01	-0.0069
WT + IRED (-Rha)	14.47	20	0.0241	0.0362	0.0121	0.0253
			0.001	0.0427	0.0417	0.0873
			0.012	0.0417	0.0297	0.0622
		50	0.0104	0.0574	0.047	0.0394
			0.0045	0.0762	0.0717	0.0601
			0.0097	0.055	0.0453	0.0379
WT + IRED	20.43	20	0.0047	0.1181	0.1134	0.1682
			0.0035	0.1193	0.1158	0.1718

(+Rha)			0.0086	0.1254	0.1168	0.1732
		50	0.0068	0.3162	0.3094	0.1836
			0.0154	0.3746	0.3592	0.2131
			0.0112	0.3302	0.319	0.1893

Kinetic data is available at the following Sciebo link: https://rwth-aachen.sciebo.de/s/Zla9rrYwOzlT5ty

Table S. 4. Activity calculations in purified IRED from WT + IRED or *E. coli* strain.

Protein	**Protein concentration mg/ml**	**Volume µL**	**Slope 1 (background)**	**Apparent specific activity (U/mg)**
$IRED_{V8}$ purified from WT + IRED	2.66	5	0.0227	1.0344
			0.0344	1.5676
			0.0295	1.3443
		10	0.0648	1.4764
			0.0887	2.0210
			0.0841	1.9162
			0.067	1.5265
			0.0635	1.4468
			0.06	1.3671
		20	0.225	2.5632
			0.2197	2.5028
			0.2297	2.6168
			0.1328	1.5129
			0.1521	1.7327
$IRED_{V10}$ purified from *E.coli* AA44	142	2.5	0.0542	4.6265
			0.0426	3.6364
			0.0652	5.5655
		5	0.118	5.0363
			0.141	6.0179
			0.1262	5.3863
		10	0.2603	5.5548
			0.2611	5.5719
			0.2409	5.1408
		20	0.6013	6.4159
			0.4822	5.1451
			0.6169	6.5824

B.3 Exploring IREDs from different microorganism.

The synthetic constructs were ordered from BioCat GmbH. Each construct contains an *ired* gene from a microorganism with a N-terminal HisA tag in a pBAD backbone. DNA *ired* sequences are given for each microorganism, the position of the His-tag is underlined. One examples of the constructs are given in the image below (Figure S. 2). These IREDs should be naturally NADPH-dependent.

Aspergillus terreus

CCATGGCTAGCTCTCATCATCATCATCATCATGGTATGGCAACCACCACCACCAAACTGACCATCTTCGGTCTG
GGTGCCATGGGCACCGCCATGGCCACCCAGTTCCTGAAACAGGGTCATACCCCGACCGTGTGGAATCGTACC
GCAGCCAAAGCCACCCCGCTGGTTGAACAGGGTGCACATCTGGCAGCAACCATTCCGGCCGCAATTGCCGCA
AGCCCGCTGCTGGTGTTCTGTCTGCTGGATAATGCAGCAGTTGAACAGACCCTGGCAGCCGGCCCGCCGAGTC
TTGCTGGTAAAACCATTCTGAATCTGACCAATGGCACCCCGAGCCAGGCACGCCGCCTGGCAACACTGGCCAG
CGCACGTGGCGCCCGTTATCTGCATGGCGGTATTATGGCAACCCCGGATATGATTGGTGCACCGCATGCAGTT
ATTCTGTATAGCGGTGGCGGCAGTGCAGAAACCTATGCAAGCGTGGAAGGTGTTCTGGCCGTGCTGGGTAGC
GGCAAATATCTGGGCGATGATGCCGGCAGTGCAAGTCTGCATGATCTGGCACTGCTGAGCGGCATGTATGGC
CTGTTCGCAGGCTTCCTGCATGCCACCGCACTGGTGCGCAGTGAAGGTGAAGGCGTGAGCGCAACCGAATTC
CTGGGTCTGCTGGCACCGTGGCTGCAGGCCATGACCGGTTATCTGGGCCTGCTGGCACGCCAGATTGATGAT
GGCGTGTATACCGCACAGACCAGTAATCTGGCCATGCAGCTGGTTGCACTGGAAAATGCCTGTGCAGCCAGC
CGTGAACAGGGCGTTAGTGCCGAAGTTATGCTGCCGCTGAAAGGCCTGGTGGAACGTGCAGTTCGTGAAGGC
CGTGGTGGTCATGATATTAGCAGTCTGATTGATTACTTCAAACGCGATAGCGTTTAATCTAGA

Cupriavidus sp. HPC(L)

CCATGGCTAGCTCTCATCATCATCATCATCATGGTATGAAGACCGTTGCCGTGATTGGCCTGGGTCAGATGGG
TACCACCCTGGCACGCCTGTTCATTGAAGCAGGCATGCAGGTTCGTGTGTGGAATCGCACCCGCAGTAAAGCC
GAACCGCTGGCCAGCCGTGGCGCCATTGTTGCCGCAACCGCCGCAGCCGCAATGGCCGATGCCGAAGCAGTG
GTGATCTGTGTGCATGATTATCGCGCCACCCATGATATTCTGAGTGATGTTGCAGTTAAAAGTGCACTGAAAG
GCAAACTGCTGCTGCAGCTGACCACCGGTAGCCCGCAGGATGCCCGTGATATGGCAGAACTGGCAGCCCGTA
TTGGTGCCGGTTATCTGGATGGCGCCCTGCAGGTTGCACCGGAACAGATGGGTCAGCCGGATACCACCGTGC
TGGTGAGTGGCAGCGGTGAAGATCATGCACTGGCACGCGAACTGCTGGCAGTGCTGGGCGGCAATGTGGTG
TATCTGGGTGAAGATGTGGCCGCCGCCGCAACCATGGATCTGGCAACCCTGAGCTATGTGTATGGTGCCAGC
ATGGGCTTCTTCCAGGGCGCAGCACTGGCACAGGCCGAAGGTCTGGATGTGGGTGTGTATGGTGGTATTGTG
GAAGCCATGAGCCCGAGCTTCGGCGCCTTCCTGCGTCATGAAGGCAATGTGATTGATAATGGCGATTATGCCG
TTAGTCAGAGCCCGCTGAGCATTAGTATTGATGCAACCGGTCGTATTGAACAGGCCATGCGTCAGAAAGGCCT
GCGTAGTGAACTGCCGAGCCTGATTGCCCGTCTGCTGCGCGATGCCGAAGAAGCCGGTTATGGTAATGAAGA
ATTCGCCGCAGTTGCAAAAATTCTGCGCGGTGCCGCAGAACCGGCACCGGTTCGTTAATCTAGA

Myxococcus fulvus

CCATGGCTAGCTCTCATCATCATCATCATCATGGTATGAAGCCGCATATTAGTATTCTGGGCGCCGGTCGCATG
GGTAGCGCACTGGTTAAAGCCTTCCTGCAGAATGAATATACCACCACCGTGTGGAATCGTACCCGTGCACGTT
GTGAACCGCTGGCAGCAGCAGGCGCACGTATTGCAGATAGTGTTCGTGATGCCGTTCAGACCGCCAGCGTGG

TTATTGTTAATGTGAATGATTATGACACCAGCGATGCCCTGCTGCGTCAGGATGAAGTTACCCAGGAACTGCG
CGGTAAAGTTCTGGTGCAGCTGACCAGTGGCAGTCCGAAACTGGCCCGCGAACAGGCCACCTGGGCCAGACG
TCATGGCATTGATTATCTGGATGGCGCCATTATGGCCACCCCGGATCTGATTGGCCGCCCGGATTGCACCCTG
CTGTATGCAGGTCCGAAAGCCCTGTATGATAAACATCAGGCAGTTCTGGCCGCACTGGGCGGCAATACCCAG
CATGTTAGCGAAGATGAAGGTCATGCCAGTGCACTGGATAGTGCCATTCTGTTCCAGCTGTGGGGCAGTCTGT
TCAGTGGCCTGCAGGCCGCAGCAATCTGTCGTGCCGAAGGCATTGCACTGGATGCACTGGGTCCGCATCTGG
AAGCAGTGGCAGCCATGATTCAGTTCAGTATGAAAGATCTGCTGCAGCGCATTCAGAAAGAACAGTTCGGCG
CCGATACCGAAAGCCCGGCCACCCTGGATACCCATAATGTGGCATTCCAGCATCTGCTGCATCTGTGCGAAGA
ACGTAATATTCATCGCGCCCTGCCGGAAGCAATGGATGCCCTGATTCAGACCGCCCGCAAAGCCGGTCATGGC
CAGGATGACTTCAGCGTTCTGGCACGCTTCCTGCGTTAATCTAGA

Myxococcus sp. SCHIC003

CCATGGCTAGCTCTCATCATCATCATCATCATGGTATGAAGCCGACCCTGACCGTTATTGGCGCAGGTCGTATG
GGTAGTGCACTGATTAAAGCATTCCTGCAGAAAGGTTATACCACCACCGTGTGGAATCGTACCCGCAGCCGTA
GCGAACCGCTGGCCAAACTGGGCGCCCATCTGGCAGATACCGTTCGCGATGCAGTGAAACGTAGCGATATTA
TTGTGGTTAATGTTCTGGATTACGATACCAGTGATCAGCTGCTGCGTCAGGATGAAGTTACCCGCGAACTGCG
CGGCAAACTGCTGGTTCAGCTGACCAGCGGCAGCCCGGCCCTGGCAAGAGAACAGGAAACCTGGGCACGCC
AGCATGGCATTGATTATCTGGATGGTGCAATTATGGCCACCCCGGACTTCATTGGCCAGGCCGAATGTGCACT
GCTGTATAGTGGCAGTGCAGCCCTGTTCGAAAAACATCGCGCAGTTCTGAATGTTCTGGGTGGCGCCACCGCC
CATGTGGGCGAAGATGTGGGTCATGCAAGCGCCCTGGATAGTGCCCTGCTGTTCCAGATGTGGGGCACCCTG
TTCGGTACCCTGCAGGCCCTGGCAATTAGTCGCGCCGAAGGCATTCCGCTGGAAAAAACCACCGCCTTCCTGA
AACTGACCGAACCGGTGACCCAGGGCGCCGTTACCGATCTGCTGACCCGTGTGCAGCAGGATCGCCTGACCG
CCGATGAACATACCCTGGCAAGCCTGGAAGCACATAATGTTGCATTCCAGCATCTGCTGGCACTGTGCAAAGA
ACGCAATATTCATCGTGGTGTGGCCGATGCCATGTATAGTGTGATTCATGATGCAGTGAAGGCAGGTCATGGT
AAAGATGACTTCGCCATTCTGACCCGCTTCCTGAAATAATCTAGA

Streptomyces noursei

CCATGGCTAGCTCTCATCATCATCATCATCATGGTATGAGTCGCCATAGCGAACAGAGCGCAGTGACCGTGCT
GGGCCTGGGTCCGATGGGTCGTGCACTGGCCGGTGCCTTCCTGGATGCCGGTCTGCGCACCACCGTGTGGAA
TCGCACCCCGGGCCGCGATGCAGAACTGGTTGCACGCGGTGCAGTGGCAGCCCCGACCGCAGCAGAAGCAG
TGGCAGCAAGCGCCCTGACCGTTGTGTGTGTGGTGAATTATGATGCCGCCGATGCAGTTCTGCGTCCGGATGC
CGTTGCAGATGCACTGAAAGGTCGTACCGTGGTGAATCTGAGTGCAGATACCCCGGATCGTGCCCGCGATAC
CGCACATTGGGCAGCAGAACGCGGCATTGGTTATCTGGATGGCGCCATTATGACCCCGACCACCACCATTGGC
ACCAGTGCCGCAGTGTTCCTGCATAGTGGTCCGGCAGAACTGCATCGCGAACATCGTCCGGTGCTGGAAGCC
CTGGGCGGTAGTCATACCCATCTGGGCGAAGAAATTGGCCGTGCAGCAGCATATGATGTTGCCCTGCTGGAT
GTGTTCTGGACCGCCATGGCAGGCTATGTGCATGCCCTGGCCGTGGCCCGCGCCGAGGGTGTGACCGCAAGA
GAACTGGCCCCGTTCGCCAAAGGCATTGGCGCCATTCTGCCGCCGCTGTTCGATCAGTTCGCCGAAGATGTTG
ATGGCGGCGGCTTCAGTGGCGCAGGCAATCCGCTGACCAGCGCCGTTAGCAGCATGGCACATATTGTGCATA
CCAGTGAAGCCCATGGCATTGATGCAGGTGTTATGCGTGCCGCCGAAGGCATGGCCCGTCGTGCAGTTGGTC
TGGGCCATGGCGAAGATGGCTTCAGTCGCCTGGCAGAAGTTCTGGTGCGCCGTTAATCTAGA

Unclassified *Streptomyces*

CCATGGCTAGCTCTCATCATCATCATCATCATGGTATGGGCAAACAGAGTGTTACCGTTATTGGTCTGGGTCCG
ATGGGTCAGGCCATGGTGAATACCTTCCTGGATAATGGCCATGGTGTGACCGTGTGGAATCGTACCGCCGCA
AAAGCAGAAGCACTGGTGGCACGTGGTGCCGTGCTGGCCCCTACCGTTGAAGCAGCACTGGGTGCCAATGAA
CTGATTGTGCTGAGTCTGACCGATTATGATGCAGTGTATGCAGTTCTGGAACCGGTTACCGATGCCCTGAGTG
GCAAAGTGATTGCAAATCTGAGTAGTGATACCCCGGATAAAGCCCGTCAGGCCGCCACCTGGGCAGCAGAAC
ATGGTGCCAAACATCTGACCGGCGGTGTGCAGGTTCCGCCGCCTCTGATTGGTAAACCGGGCAGCGCCACCT
ATTATAGCGGTCCGAAAGATGTGTTCGATGCCCATGAAGATACCCTGAAAGTTCTGACCGATGCCGATTATCG
CGGCGAAGATGCCGGTCTGGCAGCCATGTATTATCAGGCACAGATGACCATCTTCTGGACCACCATGCTGAGT
TATTATCAGACCCTGGCACTGGGTCGTGCCAATGGCGTTACCGCAAAAGAACTGCTGCCGTATGCAACCATGA
TGACCAGCATGATGCCGCACTTCCTGGAACTGTATGCACAGCATGTGGATAGTGCCGATTATCCGGGCGATGT
GGATCGTCTGGCAATGGGCGCAGCAAGCGTGGATCATGTGCTGCATACCCATCGCGATGCCGGCGTTAGCAC
CGTTCTGCCGGCAGCCGTTGCCGAAATCTTCAAAGCAGGTATGGAAAAAGGCTTCGCAGAAAATAGCTTCAG
CAGCCTGATTGAAGTTCTGAAAAAACCGACCGCATAATCTAGA

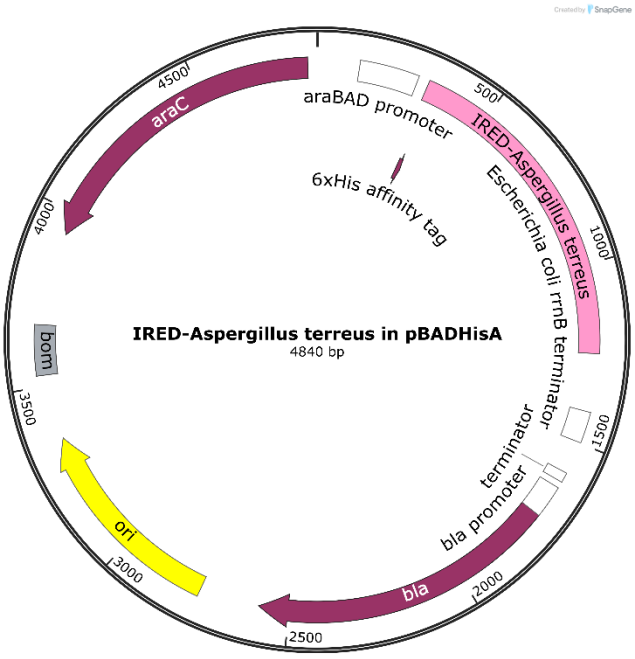

Figure S. 2. Example of synthetic construct containing IRED from *A. terreus*. All other constructs contain the similar backbone, only changing the gene of interest indicated in light pink. Plasmid maps is generated with SnapGene®.

B.4 $PuOx_{M1}$ production and enrichment

B.4.1 Sequence of His6-tag-*puox*$_{M1}$.

- His-tag is underlined

CATCACCATCACCATCACGGATCCCCTACTCTCCAGAGAGATGTTGCAATCGTCGGCGCCGGCCCCTCTGGCCT
GGCAGCGGCAACCGCGCTGCGCAAGGCCGGCTTGTCCGTCGCCGTGATCGAAGCACGCGATCGTGTCGGAG
GCCGCACGTGGACCGACACCATCGACGGCGCAGTCCTGGAGATCGGCGGCCAGTGGGTCTCCCCCGACCAGA
CTGCTCTGATCTCCTTGCTCGACGAACTCGGCCTGAAGACTTTCGAGCGCTACCGCGAGGGCGAGTCCGTCTA
CATCTCGTCAGCAGGCGAGCGGACTCGATACACGGGCGATTCCTTCCCCACGAACGAGACCACCAAGAAGGA
GATGGACCGTCTCATCGACGAGATGGACGATCTCGCAGCGCAGATCGGCGCCGAGGAGCCGTGGGCACATC
CCCTCGCCCGCGATCTCGACACAGTCTCCTTCAAGCAGTGGCTGATCAATCAGTCCGACGACGCCGAGGCCCG
TGACAACATCGGCCTCTTCATCGCGGGTGGTATGCTCACCAAGCCCGCCCACTCGTTCTCCGCCCTACAGGCCG
TACTCATGGCCGCTTCCGCAGGCTCGTTCTCCCACATTGTGGACTCTGACTTCCTTCTCGACAAGCGAGTGATC
GGCGGAATGCAGCAGGTATCTATCCGCATGGCGGAGGCCCTCGGTGACGACGTCTTCCTCAACGCACCCGTG
CGTACGGTGAAGTGGAACGAATCCGGTGCAACGGTGTTGGCGGACGGCGACATTCGCGTCGAGGCAAGCCG
AGTGATCCTGGCCGTACCACCCAACCTCTACTCCCGGATCTCCTACGATCCCCCGCTGCCGCGTCGTCAGCACC
AGATGCATCAGCATCAGTCTCTCGGCCTCGTCATCAAGGTGCACGCCGTGTACGAGACGCCTTTCTGGCGCGA
AGACGGCCTCTCCGGCACCGGCTTCGGCGCGTCCGAGGTAGTGCAGGAGGTGTACGACAACACCAACCACGA
GGACGATCGCGGCACCCTGGTCGCTTTTGTCTCCGACGAGAAGGCCGACGCGATGTTCGAGCTTTCCGCCGA
GGAGCGTAAGGCCACGATTCTGGCCTCACTCGCCCGCTACCTGGGCCCGAAGGCCGAAGAGCCGGTTGTGTA
CTACGAATCCGACTGGGGCTCGGAGGAATGGACCCGCGGTGCGTACGCGGCGAGCTTCGATCTCGGCGGCCT
GCACCGCTACGGCGCGGATTCCCGCACGCCCGTCGGACCGATCCACTTCTCGTGCTCCGACATCGCAGCCGAG
GGATACCAGCACGTGGACGGTGCCGTTCGGATGGGTCAGCGCACCGCCGCCGACATCATCGCCCGCAGCAAG
GCCTGA

- Translated $PuOx_{M1}$ (L200I/I2006L/E203S)

GSPTLQRDVAIVGAGPSGLAAATALRKAGLSVAVIEARDRVGGRTWTDTIDGAVLEIGGQWVSPDQTALISLLDEL
GLKTFERYREGESVYISSAGERTRYTGDSFPTNETTKKEMDRLIDEMDDLAAQIGAEEPWAHPLARDLDTVSFKQW
LINQSDDAEARDNIGLFIAGGMLTKPAHSFSALQAVLMAASAGSFSHIVDSDFLLDKRVIGGMQQVSIRMAEALG
DDVFLNAPVRTVKWNESGATVLADGDIRVEASRVILAVPPNLYSRISYDPPLPRRQHQMHQHQSLGLVIKVHAVYE
TPFWREDGLSGTGFGASEVVQEVYDNTNHEDDRGTLVAFVSDEKADAMFELSAEERKATILASLARYLGPKAEEPV
VYYESDWGSEEWTRGAYAASFDLGGLHRYGADSRTPVGPIHFSCSDIAAEGYQHVDGAVRMGQRTAADIIARSK
A*

B.4.2 Construction of pDA2 with corrected *rhaS* and *puox*$_{M1}$

Sequencing was performed with primer ops28_rhaS in the first version of pKR plasmid containing $PuOx_{M1}$. A base was missing in this version, causing a premature stop codon. The correction was made in plasmid pDA2, and the modification is highlighted in red. Nucleotide sequence for RhaS is indicated in bold.

TCGCGACCTTCTCGTTACTGACAGGAAAATGGGCCATTGGCAACCAGGGAAAGATGAACGTGATGATGTTCA
CAATTTGCTGAATTGTGGTGATGTGATGCTCACCGCATTTCCTGAAAATTCACGCTGTATCTTGAAAAATCGAC
GTTTTTTACGTGGTTTTCCGTCGAAAATTTAAGGTAAGAACCTGACCTCGTGATTACTATTTCGCCGTGTTGAC
GACATCAGGAGGCCAGT**ATGACCGTATTACATAGTGTGGATTTTTT(T)CCGTCTGGTAACGCGTCCGTGGCG**
ATAGAACCCCGGCTCCCGCAGGCGGATTTTCCTGAACATCATCATGATTTTCATGAAATTGTGATTGTCGAAC
ATGGCACGGGTATTCATGTGTTTAATGGGCAGCCCTATACCATCACCGGTGGCACGGTCTGTTTCGTACGCG
ATCATGATCGGCATCTGTATGAACATACCGATAATCTGTGTCTGACCAATGTGCTGTATCGCTCGCCGGATC
GATTTCAGTTTCTCGCCGGGCTGAATCAGTTGCTGCCACAAGAGCTGGATGGGCAGTATCCGTCTCACTGGC
GCGTTAACCACAGCGTATTGCAGCAGGTGCGACAGCTGGTTGCACAGATGGAACAGCAGGAAGGGGAAAA
TGATTTACCCTCGACCGCCAGTCGCGAGATCTTGTTTATGCAATTACTGCTCTTGCTGCGTAAAAGCAGTTTG
CAGGAGAACCTGGAAAACAGCGCATCACGTCTCAACTTGCTTCTGGCCTGGCTGGAGGACCATTTTGCCGAT
GAGGTGAATTGGGATGCCGTGGCGGATCAATTTTCTCTTTCACTGCGTACGCTACATCGGCAGCTTAAGCAG
CAAACGGGACTGACGCCTCAGCGATACCTGAACCGCCTGCGACTGATGAAAGCCCGACATCTGCTACGCCA
CAGCGAGGCCAGCGTTACTGACATCGCCTATCGCTGTGGATTCAGCGACAGTAACCACTTTTCGACGCTTTTT
CGCCGAGAGTTTAACTGGTCACCGCGTGATATTCGCCAGGGACGGGATGGCTTTCTGCAATAACGCGAATCT
TCTCAACGTATTTGTACGCCATATTGCGAATAATCAACTTCGTTCTCTGGCCGAGGTAGCCACGGTGGCGCATC
AGTTAAAACTTCTCAAAGATGATTTTTTTGCCAGCGACCAGCAGGCAGTCSCTGTGGCTGACCGTTATCCGCAA
GA

B.5 Biotransformation from putrescine into pyrrolidine

B.5.1 WT + IRED + PuOx-2 growth

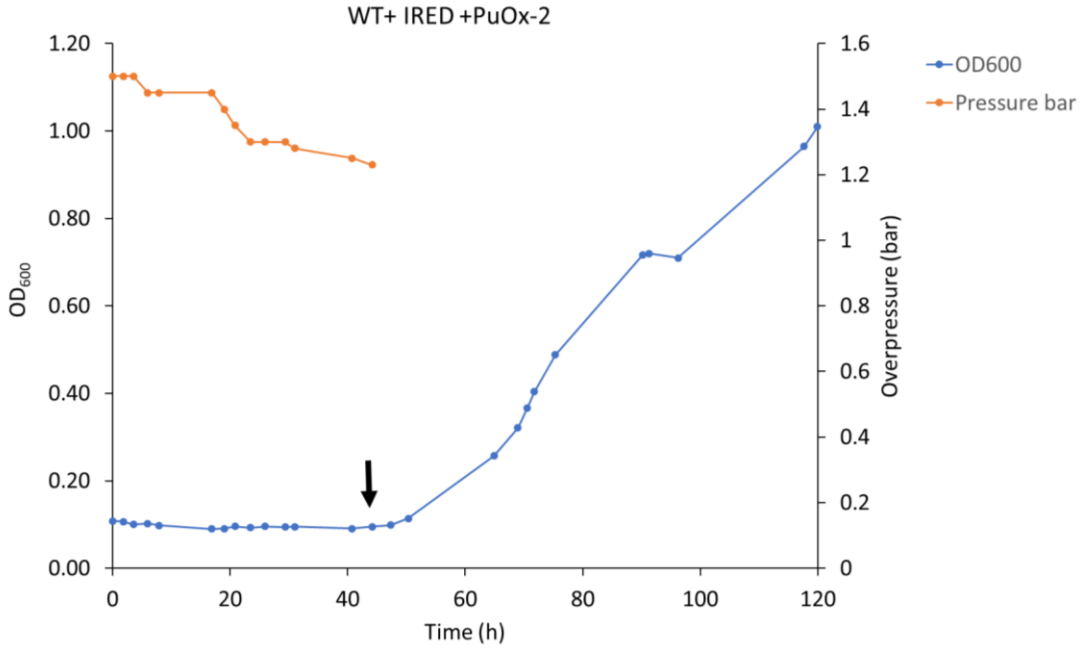

Figure S. 3. Growth of *C. necator* strain with two plasmids under lithoautotrophic and heterotrophic conditions: WT + IRED + PuOx- 2 strain contains $IRED_{V8}$ in pkr based plasmid and $PuOx_{M1}$ in pbad-based plasmid (WT x pAA56 x pDA5: WT + IRED + PuOx- 2). The strain is first cultured under lithoautotrophic

conditions in MIT medium and gas mixture. The arrow indicates addition of 4 g/L fructose. After the arrow, no pressure was measured, and no more gas was added.

B.5.2 Protein assessment in WT + IRED + PuOx

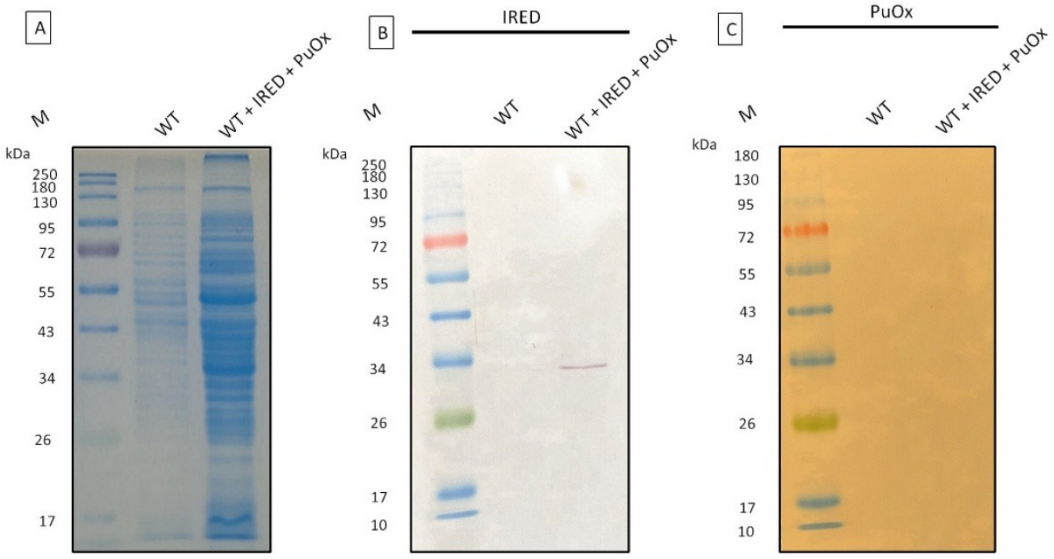

Figure S. 4. IREDV8 and PuOxM2 in WT + IRED + PuOx during lithoautotrophic biotransformation with putrescine : Analysis of gas fermentation maintained at 30 °C, and 48 h biotransformation with putrescine. SDS-PAGE (A). Western blot for detection of Strep-tag II of IREDV8, a band corresponding to the monomer at 34 kDa is expected. Western blot for detection of His6-tag of $PuOx_{M1}$, a monomer at 54 kDa is expected (B). (M: molecular weight of the protein ladder; WT: *C. necator* H16; WT + IRED + PuOx: WT x pDA4).

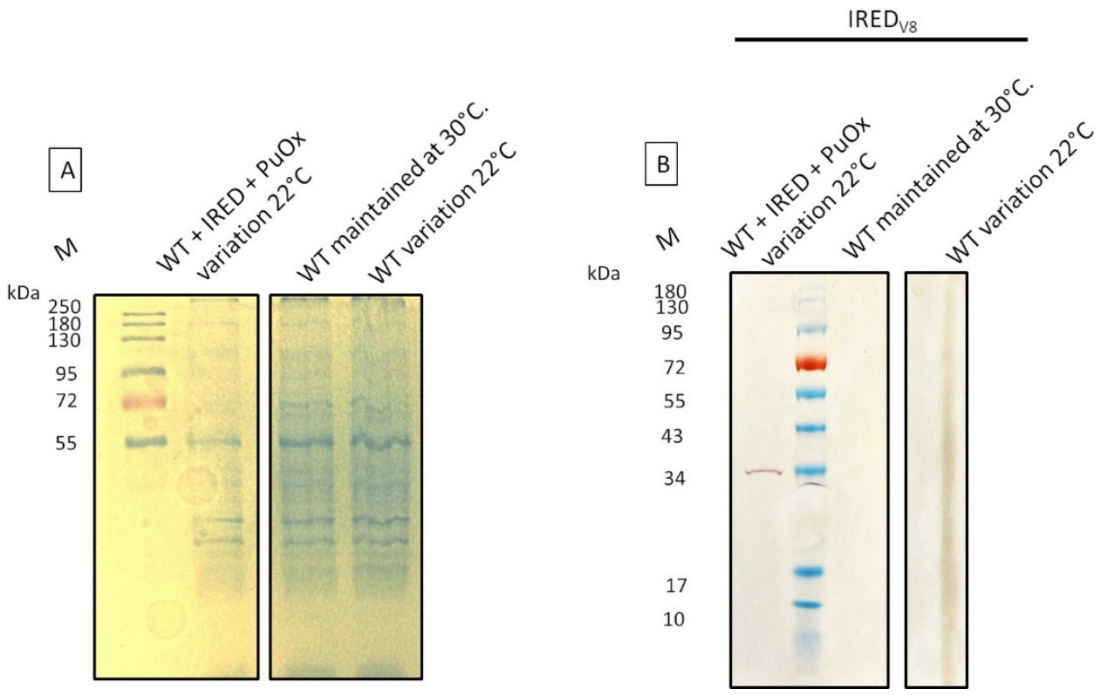

Figure S. 5. IRED$_{V8}$ production in *C. necator* during lithoautotrophic biotransformation with putrescine : SDS-PAGE (A). Western blot for detection of Strep-tag II of IRED$_{V8}$, a band corresponding to the monomer at 34 kDa is expected (B). (M: molecular weight of the protein ladder; WT: *C. necator* H16; WT + IRED + PuOx: WT x pDA4).

B.5.3 Sequencing pDA4

Main mutations are shown in pDA4 after plasmid-sequencing:

- Beginning of *rhaS* in: premature stop codon is highlighted in red

ATGACCGTATTACATAGTGTGGATTTTTTCCGTCTGGTAACGCGTCCGTGGCGA**TAG**

- rrnB T1 terminator : upper sequence is the expected sequence, below the sequence in Pda4 Missing 13 nucleotides are indicated with —

caaataaaacgaaaggctcagtcgaaagactgggcctttcgttttatctgttgtttgtcggtgaacgctctcctgagtaggacaaat
caaataaaacgaaagact----------gggcctttcgttttatctgttgtttgtcggtgaacgctctcctgagtaggacaaat

B.5.4 WT + PuOx growth and protein production

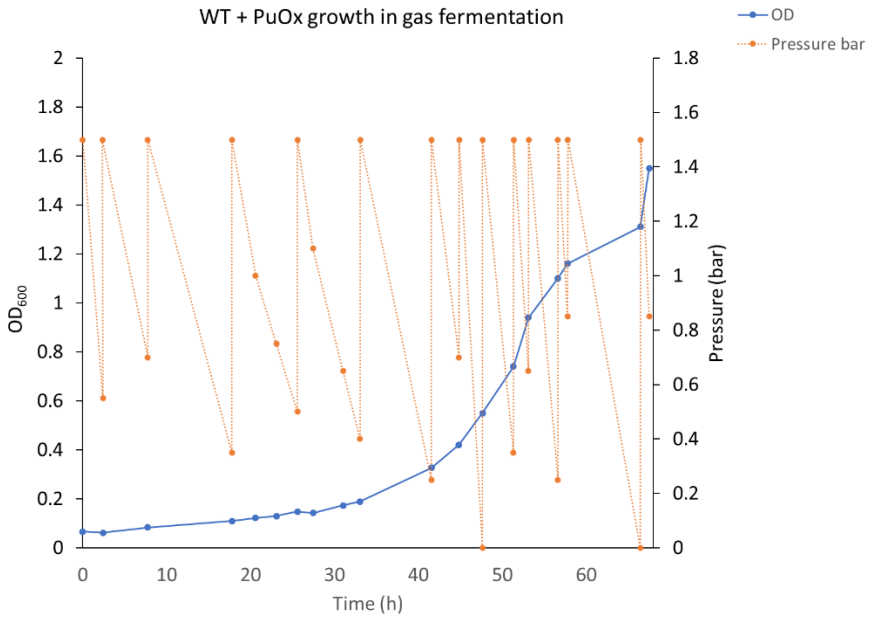

Figure S. 6. Growth characterization in gas fermentation of WT + PuOx strain.

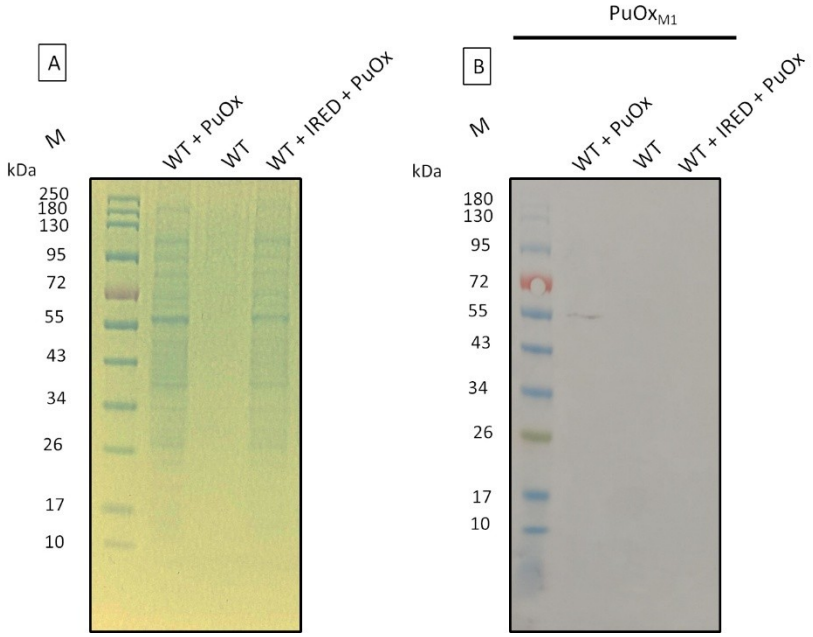

Figure S. 7. $PuOx_{M1}$ production in C. necator strains : $PuOx_{M1}$ production was analyzed in the strain WT + PuOx during lithoautotrophic growth and protein induction, and in the strain WT + IRED + PuOx after 48 h lithoautotrophic biotransformation with pyrrolidine. All cultures were performed at 30 °C. SDS-PAGE (A). Western blot for detection of His6-tag of PuOxM1, a monomer at 54 kDa is expected (B). (M: molecular weight of the protein ladder; WT + PuOx: WT x pDA2; WT: *C. necator* H16; WT + IRED + PuOx: WT x pDA4).

B.6 Biotransformation from 2-methyl-1-pyrroline into 2-methyl pyrrolidine

B.6.1 GC Chromatograms for lithoautotrophic biotransformation in WT + IRED + PuOx.

Supernatants from WT and WT + IRED + PuOx strains were collected at 0, 16 , 24 and 48 h after beginning of biotransformation. Two different temperature regimes were applied: gas fermentation entirely at 30 °C, or variation at 22 °C during 16 h. The biotrasnformation was started with addition of 10 mM 2-methyl-1-pyrroline. Two peaks are observed for 2-methyl-1-pyrroline around 9.8 and 12.5 min. One peak was detected for 2-methylpyrrolidine around 9.5 min.

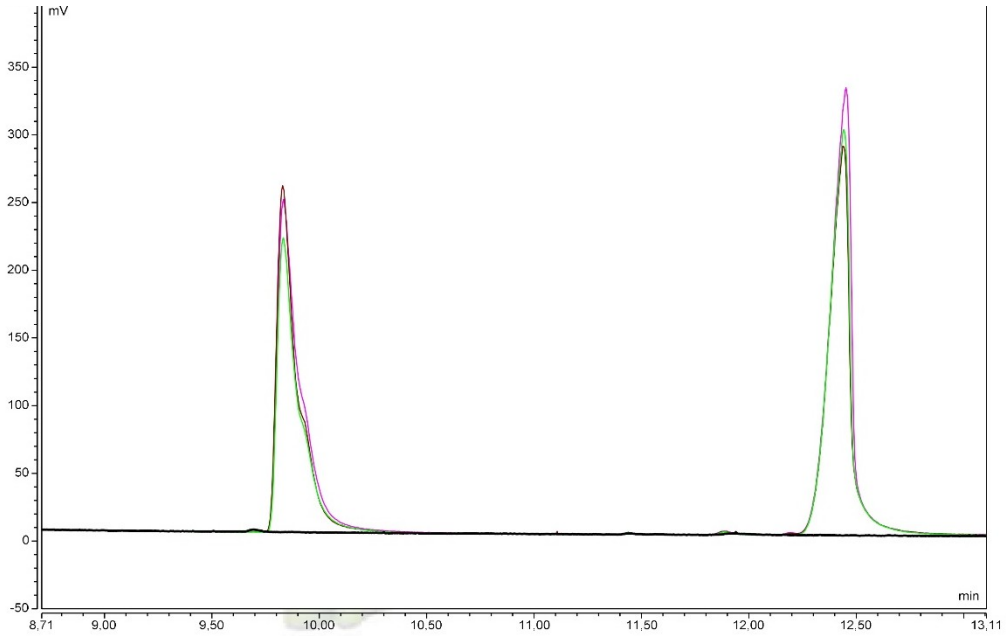

Figure S. 8. GC-FID Chromatogram of WT strain with cultivation at constant temperature 30 °C. Different biotransformation time points are analyzed. Color code: black,0 h ; pink, 16 h; brown 24 h; green, 48 h. One sample is shown.

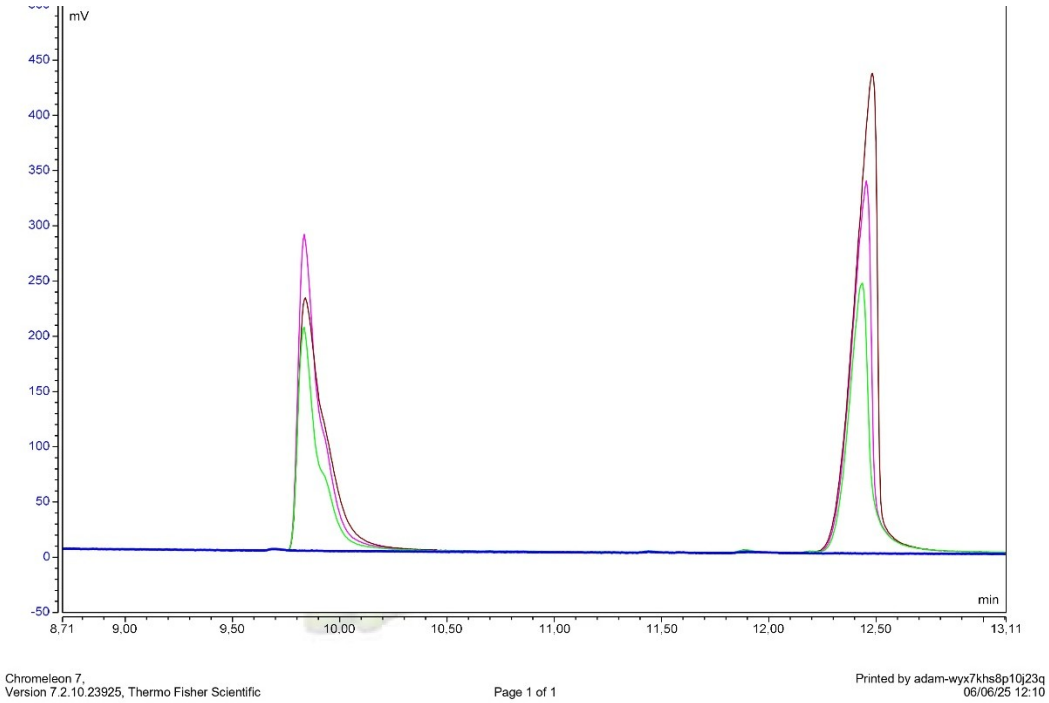

Figure S. 9. GC-FID Chromatogram of WT strain with variation of temperature at 22 °C, and continuing at 30 °C. Different biotransformation time points are analyzed. Color code: blue,0 h ; pink, 16 h; brown 24 h; green, 48 h. One sample is shown.

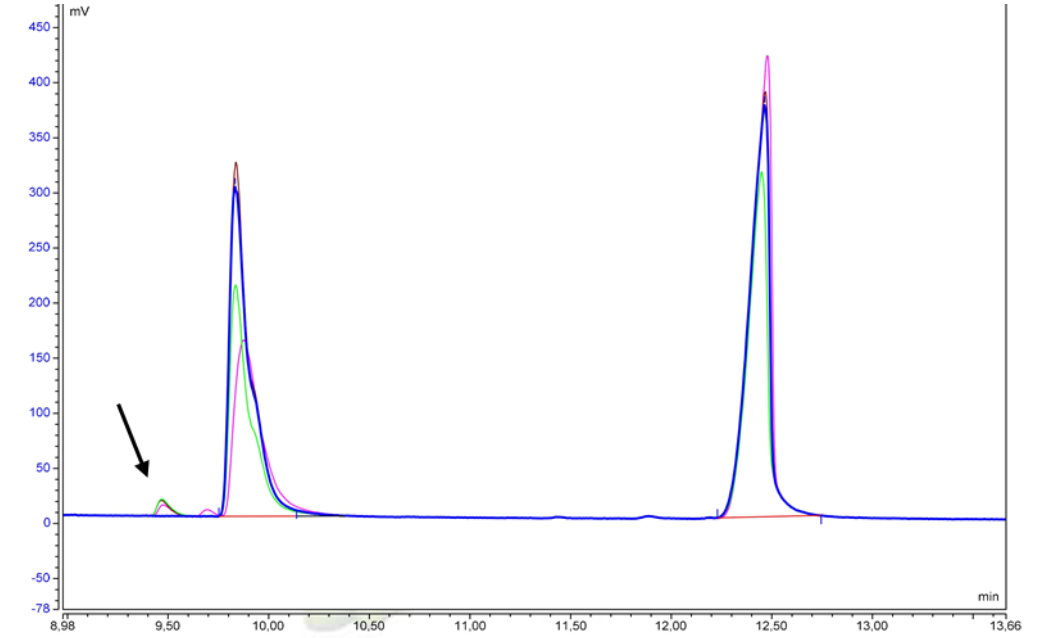

Figure S. 10. GC-FID Chromatogram of WT + IRED + PuOx strain with cultivation at constant temperature 30 °C. Different biotransformation time points are analyzed. Color code: black,0 h ; pink, 16 h; brown 24 h; green, 48 h. One sample is shown. Product detection is indicated with an arrow.

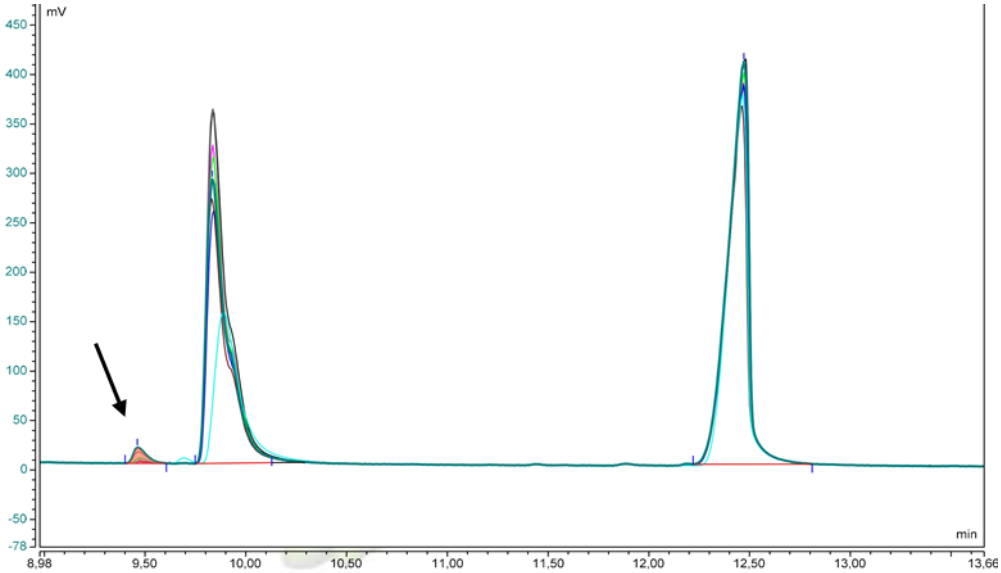

Figure S. 11.GC-FID Chromatogram of WT + IRED + PuOx strain with variation of temperature at 22 °C, and continuing at 30 °C. Different biotransformation time points are analyzed. Color code: blue and pink 0 h ; green and grey, 16 h; dark blue and red 24 h; light blue and aqua, 48 h. Duplicates are shown.

B.7 Optimization of IRED biotransformation

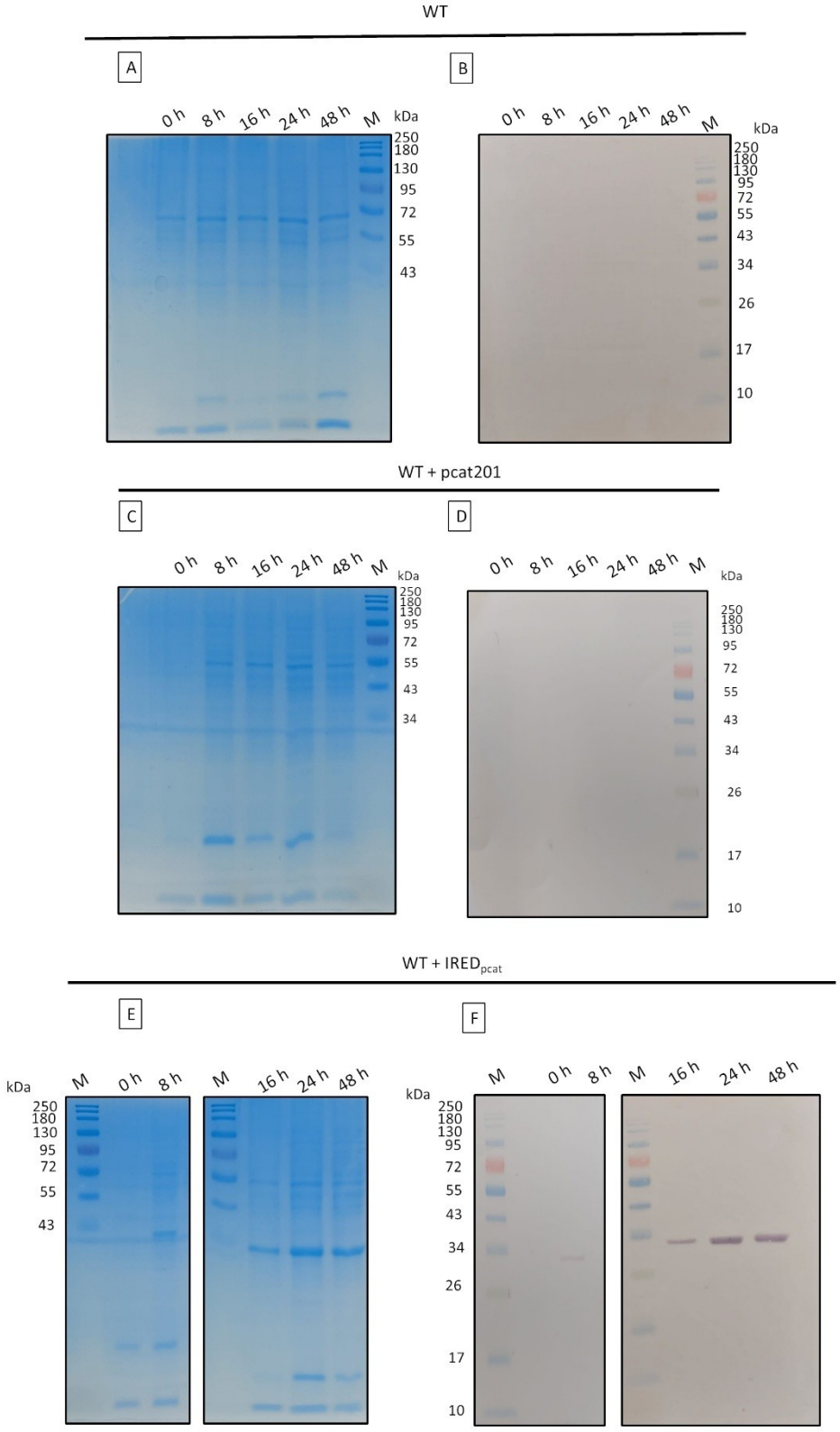

Figure S. 12.Optimized IRED$_{V8}$ production in *C. necator* in gas fermentation : C. necator strains are analyzed with SDS-PAGE (A, C, E) and Western blot (B, D, F). A band corresponding to the IRED

monomer is expected at 35 kDa. (WT: *C. necator* H16; WT + pcat201: *C. necator* H16 x pCAT201; WT + $IRED_{pcat}$: WT x pDA6).

B.7.1 GC Chromatograms for lithoautotrophic biotransformation in WT + $IRED_{pcat}$.

Supernatants from WT, WT + pcat201, and WT + $IRED_{pcat}$ strains were collected at 0, 16 , 24 and 48 h after beginning of biotransformation in heterotrophic or lithoautotrophic cultivation. The biotrasnformation was started with addition of 10 mM 2-methyl-1-pyrroline. One peak around 6.8 min corresponds to pyrrolidine as internal standard. One peak around 7 min corresponds to 2-methylpyrrolidine. Two peaks are observed for 2-methyl-1-pyrroline around 7.3, and 9.9 min.

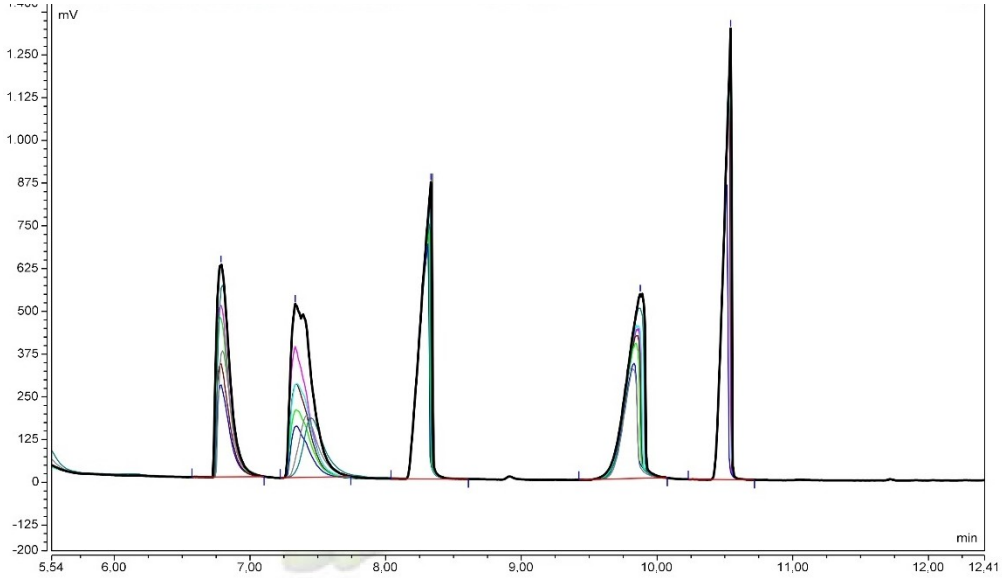

Figure S. 13. GC-FID Chromatogram of WT strain in heterotrophic conditions (TB medium) . Different biotransformation time points are analyzed. Color code: black and blue,0 h ; pink and brown, 16 h; green and light blue 24 h; grey and aqua, 48 h. Duplicates are shown.

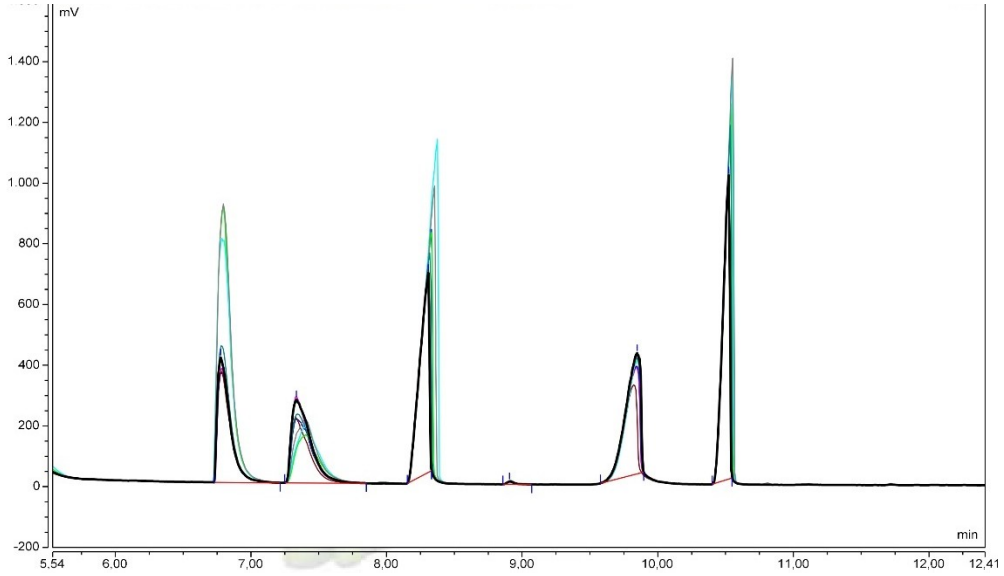

Figure S. 14. GC-FID Chromatogram of WT + pcat201 strain in heterotrophic conditions (TB medium). Different biotransformation time points are analyzed. Color code: black and blue,0 h ; pink and brown, 16 h; green and light blue 24 h; grey and aqua, 48 h. Duplicates are shown.

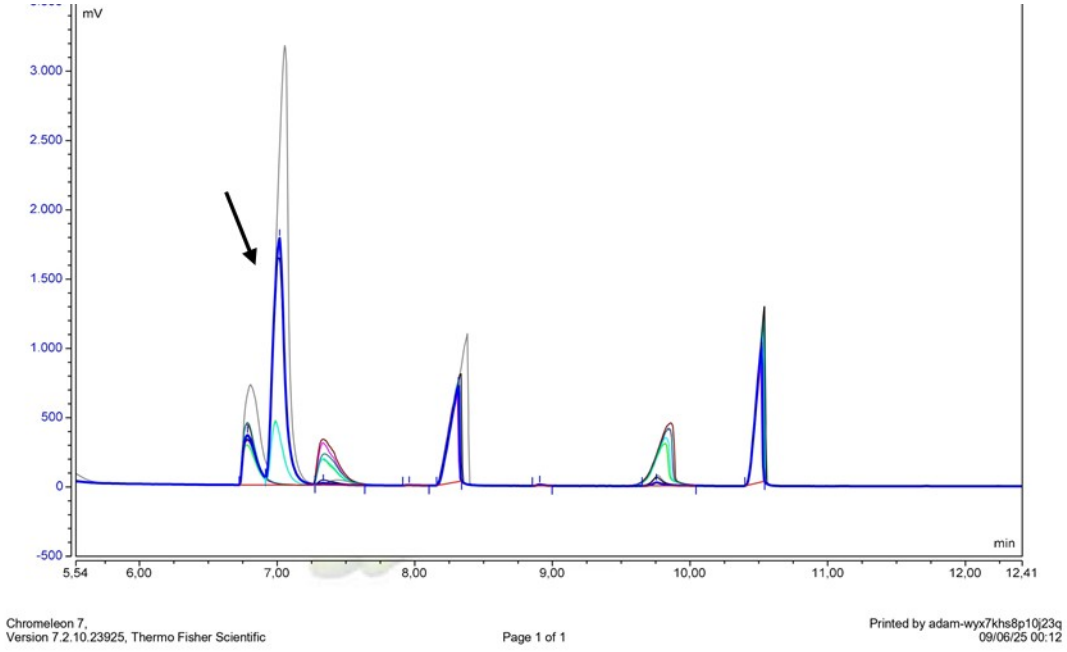

Figure S. 15. GC-FID Chromatogram of WT + $IRED_{pcat}$ strain in heterotrophic conditions (TB medium). Different biotransformation time points are analyzed. Color code: pink and brown,0 h ; green and light blue, 16 h; grey and black 24 h; dark blue and aqua, 48 h. Duplicates are shown. Product is indicated with an arrow.

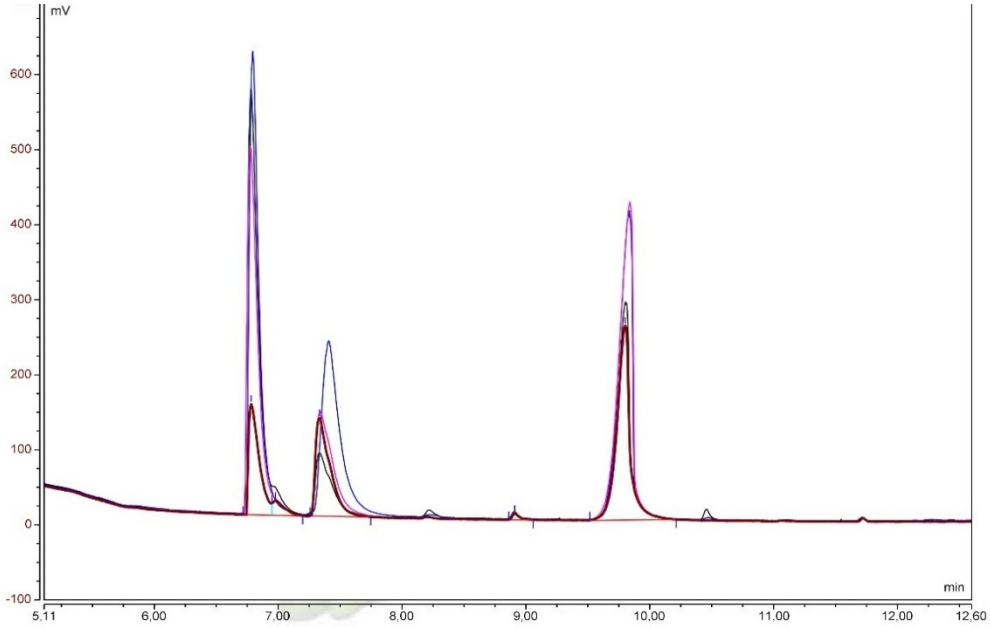

Figure S. 16. GC-FID Chromatogram of WT strain in lithoautotrophic conditions (AUT medium with gas mixture). Different biotransformation time points are analyzed. Color code: black,0 h ; blue, 16 h; pink, 24 h; brown, 48 h. One sample is shown.

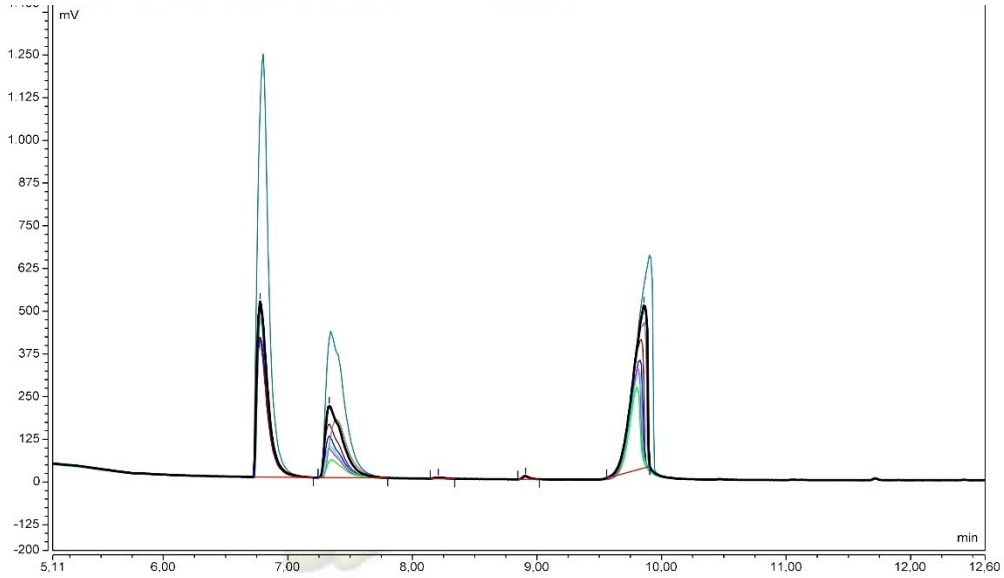

Figure S. 17. GC-FID Chromatogram of WT + pcat201 strain in lithoautotrophic conditions (AUT medium with gas mixture). Different biotransformation time points are analyzed. Color code: black and blue,0 h ; pink and brown, 16 h; green and light blue 24 h; grey and aqua, 48 h. Duplicates are shown.

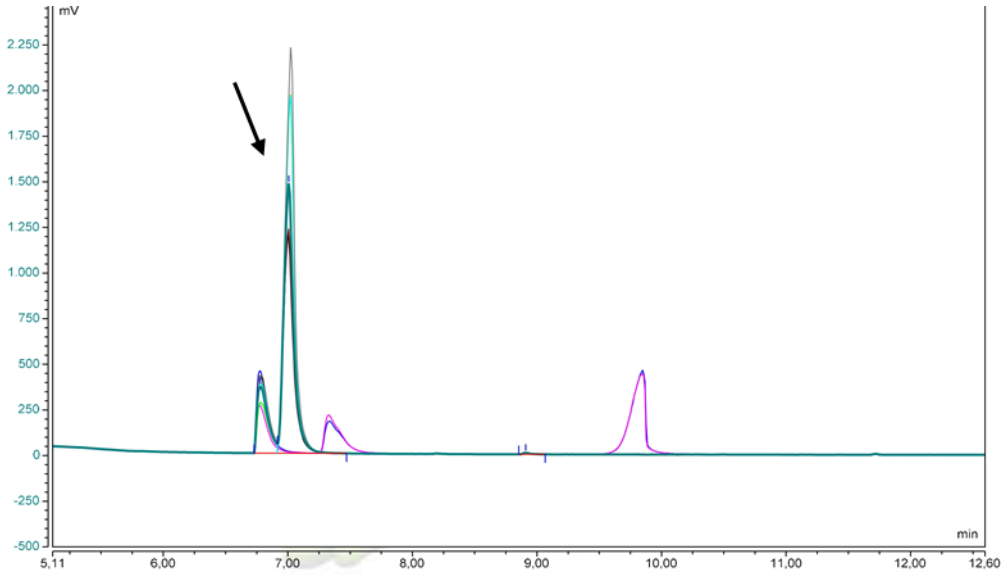

Figure S. 18. GC-FID Chromatogram of WT + $IRED_{pcat}$ strain in in lithoautotrophic conditions (AUT medium with gas mixture). Different biotransformation time points are analyzed. Color code: blue and pink,0 h; red and brown, 16 h; green and light blue 24 h; grey and aqua, 48 h. Duplicates are shown. Product is indicated with an arrow.

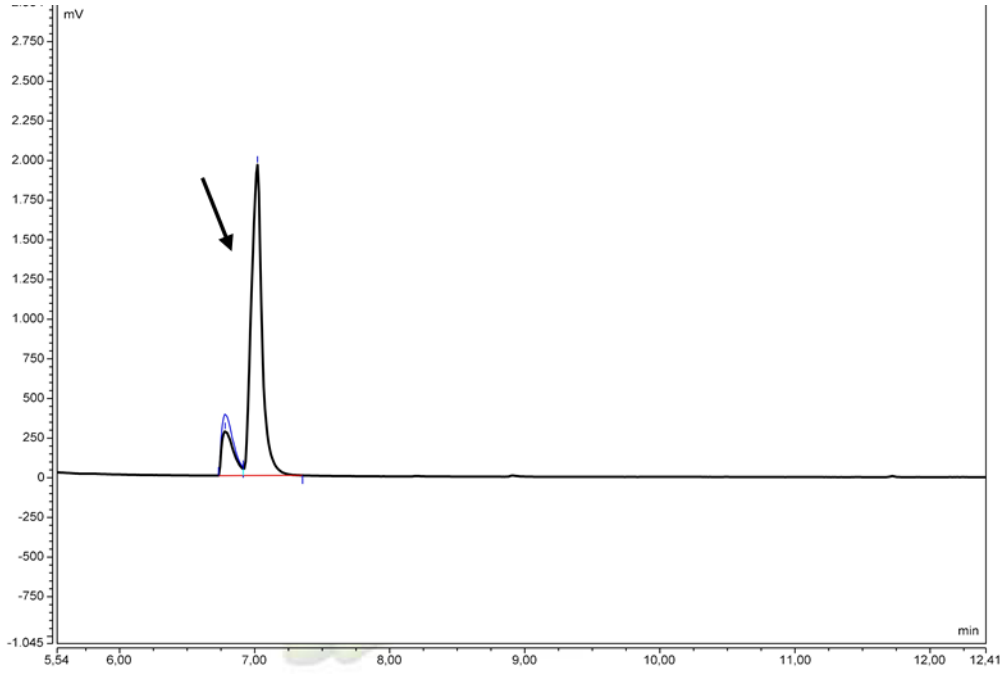

Figure S. 19. GC-FID Chromatogram of WT + $IRED_{pcat}$ strain in in lithoautotrophic conditions (AUT medium with gas mixture). Full conversion is observed 24 h after start of biotransformation. Only product is detected and no substrates peaks. Product is indicated with an arrow.

B.8 Data storage and online data.

- Raw data from GC-FID is stored in the university cloud Sciebo NRW, with the link:

https://rwth-aachen.sciebo.de/s/vJuz8ygkKlipXlL

- All plasmids sequences are further accessible in the university cloud Sciebo NRW, with the link:

https://rwth-aachen.sciebo.de/s/Xa00oUN8fPmLnxs

- Bachelor's theses are accessible in the university cloud Sciebo NRW, with the link:

https://rwth-aachen.sciebo.de/s/LkTGMnkyqP5Y3WW (de la Asunción Vest, 2023)

https://rwth-aachen.sciebo.de/s/p8qfRJMj3fqAtoG (Kunth,2023)